

ELECTRIFIED VEHICLE TRACTION MACHINE DESIGN WITH
MANUFACTURING CONSIDERATIONS

ELECTRIFIED VEHICLE TRACTION MACHINE DESIGN WITH
MANUFACTURING CONSIDERATIONS

by

Rong Yang, B.Sc., M.Sc.

A Thesis Submitted to the School of Graduate Studies in Partial Fulfilment of the
Requirements for the Degree of Doctor of Philosophy

McMaster University

October 2016

谨以此献给我的父亲母亲

To My Parents

Abstract

This thesis studies the brushless permanent magnet synchronous (BLPM) machine design for electric vehicle (EV) and hybrid electric vehicle (HEV) application. Different rotor topologies design, winding design, and multiphase designs are investigated and discussed.

The Nissan Leaf interior permanent magnet (IPM) traction machine has been widely analyzed and there is much public domain data available for the machine. Hence, this machine is chosen as a representative benchmark design. First, the Nissan Leaf machine is analyzed via finite element analysis (FEA) and the results confirmed via published experimental test data. The procedure is then applied to all the following machine designs and results compared. Then the Nissan Leaf machine rotor is redesigned to satisfy the performance specification with sinusoidal phase current in the full range for the same performance specification and permanent magnet material. Afterword, a comparative study assessing the design and performance attributes of the Nissan Leaf IPM machine, when compared to a surface permanent magnet (SPM) machine designed within the main Nissan Leaf machine dimensional constraints. The study illustrates and concludes that both the IPM and SPM topologies have very similar capabilities with only subtle differences between the design options. The results highlight interesting manufacturing options and materials usage.

The grain boundary diffusion processed (GBDP) magnets are proposed to reduce the rare earth material content in the permanent magnet machines, especially subject to high load and high temperature operating scenarios by preventing or reducing the onset of demagnetization. The design and analysis procedure of BLPM machine with GBDP magnets are put forward. In the end, the Nissan Leaf IPM machine is taken as an example to verify the analysis procedure. and the results illustrates that IPM machines with GBDP magnets can realize torque and maintain efficiency at high loads while being less prone to demagnetization.

A new multi-phase synchronous reluctance machine (SRM) with good torque performance and conventional voltage source inverter is introduced for traction machine applications. Although the torque density is low compared with BLPM machine, the SRM machine gets rid of permanent magnets and achieve low torque ripple compared with switched reluctance machine when the asymmetric inverter is replaced with conventional voltage source inverter.

The concentrated windings are designed and studied with both IPM and SPM rotor according to the Nissan Leaf machine requirements of performance and dimension to investigate how the concentrated windings affect the machine performance and manufacturability and cost. 9-, 12-, 15- slot concentrated windings' stator share the same slot area with the Nissan Leaf machine distributed winding and the performance are evaluated and compared.

Multi-phase concentrated windings machines with IPM and SPM rotor are designed and analyzed based on the Nissan Leaf machine specification and dimension constraints. The performance of 2×3-phase, 5-phase, 9-phase machine at low speed and top speed are studied and the advantages and disadvantages are compared in terms of torque quality, efficiency, and power electronic requirements.

Acknowledgments

First and foremost, I would like to thank my supervisor, Dr. Ali Emadi, for his support, guidance, and patience on me and my research work. It has been a great honor to be one of his Ph.D. students. I am proud of being part of the Canada Excellence Research Chair in Hybrid Powertrain Program and appreciate all the knowledge and experience gained through several projects. It is the best thing ever happened to my life to join Dr. Emadi's group and work with him.

I would also like to thank Dr. Stephen Veldhuis. He gave me lots of precious suggestions and instruction on my research, especially on manufacturing parts. Dr. Veldhuis sees the best in people, encourages them, supports them, and guides them to what they want to achieve. I am grateful for working with him and being involved MMRI research group.

I would also like to express my special thanks to Dr. Nigel Schofield. This thesis would have been more difficult without his help and guidance. Dr. Schofield is warm-hearted, very knowledgeable, critical thinking, and ready to assist when I have unanswered questions. I learned a lot from his insightful comments and careful thinking. I would also like to thank Dr. Fengjun Yan, for his stimulating discussions throughout my Ph.D. program.

I am grateful to my colleagues in the Canada Excellence Research Chair in Hybrid Powertrain Program. Special thanks to Dr. Berker Bilgin, Dr. Yinye Yang, Dr. James (Weisheng) Jiang for their support and sharing expertise and assisting with the projects I am working on. Special thanks go to Jianning Dong, Hao Ge, Sandra Castano, Michael Kasprzak, Trevor Hadden, Hannah Koke, Fei Peng, Yu Miao, and everyone in the Lab for being working and spending great times together.

I am also grateful to all my friends at McMaster University. It is you who make my life in Canada so wonderful. Special thanks to Linyan Liu for her encouragement and support over the years. I will all my friends every luck in their life and career.

My deepest gratitude goes to my parents for their continuous love and unwavering support. My very special thank you goes to my brother for supporting me and helping me look after my parents. It is to them that I would like to dedicate this thesis.

This research was undertaken, in part, thanks to funding from the Canada Excellence Research Chairs Program and the Natural Sciences and Engineering Research Council of Canada Discovery Grant Program.

Table of Contents

Abstract	iv
Acknowledgments.....	vi
Table of Contents	viii
List of Figures	xii
List of Tables.....	xvii
Nomenclature.....	xx
Declaration	i
Chapter 1 Electrified Vehicle Powertrains	1
1.1 Introduction	1
1.2 Literature Review	7
1.2.1 Interior versus Surface-mounted Permanent Magnets Machines	7
1.2.2 Grain Boundary Diffusion Processed Magnet	8
1.2.3 Distributed Windings versus Concentrated Windings	10
1.2.4 Multiphase Machines	14
1.3 Research Contributions	16
1.4 Thesis Outline	17
Chapter 2 Electrified Vehicle Traction Machines	19
2.1 Introduction	19
2.2 Fundamentals of Rotating Electric Machines	19
2.2.1 Factors Effecting Magnetic and Electrical Loading.....	22
2.2.2 Permanent Magnets	24
2.3 Basic Brushless Permanent Magnet Machine Analysis.....	27

2.3.1	Machine Model	27
2.3.2	BLPM Traction Machine Design Considerations	32
2.4	Traction Machine Design Considerations.....	35
2.4.1	Pole and Slot Combinations	35
2.4.2	Rotor Topology	36
2.4.3	Machine Losses and Efficiency.....	38
2.5	Traction Machine Manufacturing Considerations	42
2.5.1	Overview of the Electric Machine manufacturing	43
2.5.2	Lamination Manufacturing Process	44
2.5.3	Stator Windings Manufacturing	48
2.5.4	Magnet Manufacturing	50
2.5.5	System Cost Analysis for Traction Machine.....	51
2.6	Summary	52
Chapter 3 Benchmark Machine Studies.....		53
3.1	Introduction	53
3.2	Overview of Nissan Leaf Machine	53
3.3	Nissan Leaf Machine FEA Model Creation.....	58
3.4	Validation of Nissan Leaf Machine FEA Model.....	65
3.5	Assessment Criteria	68
3.6	Design Parameter Studies	72
3.6.1	DC-Link Voltage.....	72
3.6.2	Temperature	75
3.6.3	High Back-EMF Precaution	77
3.7	Summary	79

Chapter 4 Rotor Design for Volume Manufacturing	81
4.1 Introduction	81
4.2 Comparative Study of Modified and Original Benchmark Machine.....	81
4.3 Comparative Study of PM Traction Machine Topologies for EV's.....	84
4.3.1 SPM Rotor Design	86
4.3.2 Comparative Studies	95
4.3.3 Design and Comparison of two example machines	101
4.3.4 Manufacturing Comparison of Two Example Machines	107
4.4 Rotor Stress Analysis.....	108
4.5 Zero Magnet Machine Designs.....	114
4.6 Comparative study of IPM with conventional and GBDP Magnet	123
4.6.1 Design process of PM machines with GBDP magnets.	124
4.6.2 GBDP Magnet Modelling Process and Specification	126
4.6.3 Results and comparison.....	129
4.7 Summary	133
Chapter 5 Stator Design for Volume Manufacturing.....	135
5.1 Introduction	135
5.2 Fundamentals of Stator Windings.....	135
5.3 Winding Layout procedure	139
5.3.1 Terminologies Needs for Winding Layout.....	139
5.3.2 Assumptions for the Winding Layout Procedure	141
5.3.3 Integer Slot Winding Layout Procedure.....	141
5.4 Comparative Study between Concentrated and Distributed Windings for EV's.....	146
5.5.1 Winding Connection Design	146

5.5.2 Preliminary Design of Concentrated Winding Machines.....	147
5.5.3 Concentrated Winding SPM Machine Design and Performance	153
5.5 Aluminum Stator Winding Design	160
5.6 Comparative Study between Stranded and Bar Wound Windings for EV's	162
5.7 Summary	163
Chapter 6 Multiphase Machine Design and Study	165
6.1 Introduction	165
6.2 2×3-Phase Machine Design with Distributed Winding	165
6.3 Five-Phase Machine Design with Concentrated Winding	172
6.3.1 Winding Connection Design for 5-phase Machine	172
6.3.2 Preliminary Design of 5-phase Machine	173
6.3.3 Final Design of 5-phase machine	177
6.4 Nine-Phase Machine Design with Concentrated Winding	181
6.4.1 Winding Connection Design for 9-phase Machine	181
6.4.2 Preliminary Design of 9-phase Machine	182
6.4.3 Final Design of 9-phase machine	185
6.5 Distributed Winding Multiphase SPM Machine Design	189
6.6 Summary	194
Chapter 7 Conclusions, Future Research Work and Publications	195
7.1 Conclusion	195
7.2 Future Research Work	197
7.3 Publications	198
References	199

List of Figures

Fig. 1.1. World motor vehicle production [8].	3
Fig. 1.2. Top 10 motor vehicle producing countries 2015 [8].	3
Fig. 1.3. Conceptual illustration of a hybrid powertrain (From Fig. 5.1 in [9])	5
Fig. 1.4. Three typical types of HEV (Modified from Fig. 2, Fig. 3, and Fig. 4 in [10])	5
Fig. 1.5. GM permanent magnet machine applied in Chevy Spark [14]	6
Fig. 1.6. Rare earth metal prices compared with gold (% of January 2008 price) [26]	9
Fig. 1.7. Typical concentrated and distributed windings connections for U phase (8 poles, 3 phases).	11
Fig. 1.8. Structure of EVs propulsion drive system.	15
Fig. 2.1. Idealized electric machine.	20
Fig. 2.2. Magnetic load condition.	23
Fig. 2.3. Hysteresis loop of a typical permanent magnet material.	25
Fig. 2.4. BLPM machines with IPM and SPM rotor topologies.	28
Fig. 2.5. BLPM machine vector diagram.	30
Fig. 2.6. Influence of direct-axis inductance on field-weakening capability.	34
Fig. 2.7. Surface-PM and IPM machine rotor topologies.	37
Fig. 2.8. Magnet eddy current loss investigation.	41
Fig. 2.9. FEA Based Magnet eddy current loss calculation.	41
Fig. 2.10. Main manufacturing process of electric machines [77].	43
Fig. 2.11. Stator laminations [78].	46
Fig. 2.12. Examples of spiral-laminated stator cores.	47
Fig. 2.13. Akita's model of a joint-lapped core [81]	47
Fig. 2.14. Mecrow's segmented lamination for easy insertion of pre-wound coils [82]	47
Fig. 2.15. Part of stator yoke, pre-pressed coil, and tooth in SMC from Jack [83].	47
Fig. 2.16. Examples of stator with special tooth tips [84].	48
Fig. 2.17. Comparison of the coils with a semi-closed and open slot [85].	48
Fig. 2.18. Winding the coils of a joint-lapped core from Akita [81].	49
Fig. 2.19. Interior stator machine with concentrated winding [86].	49

Fig. 2.20. Two needle-wound coils of the outer-rotor prototype motor [78].....	49
Fig. 2.21. Microstructure of sintered permanent magnet material.....	51
Fig. 3.1. Efficiency map of 2012 Nissan Leaf Machine [91].	56
Fig. 3.2. Inverter efficiency map [91].....	56
Fig. 3.3. Combined inverter and motor efficiency map [91].	57
Fig. 3.4. Continuous test results [91].	57
Fig. 3.5. Winding connection of Nissan Leaf Machine.	58
Fig. 3.6. Coil connection of 2011 Nissan Leaf Machine.	58
Fig. 3.7. Nissan Leaf machine and its 2D model in JMAG.	60
Fig. 3.8. Flux lines distribution in 1/8 and 1/4 model under same operation condition. ..	60
Fig. 3.9. Normalized back-EMF and remanence of N28AH in different temperatures at 10,000rpm.	61
Fig. 3.10. Demagnetization curve of N28AH.	61
Fig. 3.11. Demagnetization curve of N28AH as defined in JMAG.....	62
Fig. 3.12. Estimated winding length of 2011 Nissan Leaf Machine.....	64
Fig. 3.13. Locked rotor test results and simulation results.	65
Fig. 3.14. Nissan Leaf machine back-EMF comparison between test data and FEA results at 20°C.	66
Fig. 3.15. Peak phase current comparison between test data and FEA simulation.....	67
Fig. 3.16. Torque, power, and speed specification of Nissan Leaf machine.	69
Fig. 3.17. Cogging torque waveform.	69
Fig. 3.18. DC-link voltage of the Nissan Leaf electric vehicle.....	74
Fig. 3.19. Battery current of the Nissan Leaf electric vehicle.	74
Fig. 3.20. Open circuit EMF of lithium-ion battery.....	75
Fig. 3.21. Nissan Leaf machine FEA and ORNL test results at a fixed DC-link voltage of 375V.....	75
Fig.3.22. DC-link current during fault.	79
Fig. 3.23. Nissan Leaf powertrain system without and with DC/DC converter.	80
Fig. 4.1. Geometry comparison of Nissan Leaf machine and the modified one.....	82

Fig. 4.2. Torque performance comparison of Nissan Leaf machine and the modified one with sinusoidal phase current.....	83
Fig. 4.3. Power performance comparison of Nissan Leaf machine and the modified one with sinusoidal phase current.....	83
Fig. 4.4. Design process of SPM rotor.....	88
Fig. 4.5. Example SPM machine FEA design results.....	88
Fig. 4.6. Rotor model and its force analysis	93
Fig. 4.7 Stator Comparison of IPM and SPM.....	94
Fig. 4.8. IPM machine torque segregation at base and top speed.....	98
Fig. 4.9. Nissan Leaf IPM and SPM machine inductance comparison.....	98
Fig. 4.10. Lines of equal vector magnetic potential and flux-density contours for Nissan Leaf IPM and modified model.....	100
Fig. 4.11. Flux weakening range comparison of SPM design and Nissan Leaf IPM.	105
Fig. 4.12. Performance results comparisons between IPM and SPM machines at 10,000rpm.	106
Fig. 4.13. Torque-current comparisons between IPM and SPM machines with 311kA/m coercivity permanent magnet at 2100rpm, 180°C.	107
Fig. 4.14. Forces acting on general element in a rotating solid disc.....	108
Fig. 4.15. 12-slot SR machine with sine wave current excitation.....	117
Fig. 4.16. 15-slot SR machine with square wave current excitation.....	118
Fig. 4.17. 12-slot SR machine with square wave current excitation.....	119
Fig. 4.18. Torque comparison of SR machines.....	120
Fig. 4.19. Structure comparison between Nissan Leaf machine and synchronous reluctance machine.....	121
Fig. 4.20. GBDP and demagnetization curves comparison between GBDP and without GBDP[135].	124
Fig. 4.21. Flow chart for the design process of permanent magnet machines using GBDP permanent magnets.	125

Fig. 4.22. Intrinsic and normal curves for a permanent magnet at 120 and 180 degrees centigrade and an example recoil permeability curve.....	127
Fig. 4.23. Coercivity definition of grain boundary magnet (Unit: kA/m, 180°C).....	127
Fig. 4.24. Grain boundary magnet programming flowchart.	129
Fig. 4.25. Geometry and specifications of the IPM machines model [91].	131
Fig. 4.26. Permanent magnet working points when current peak value is 100A and 200A.	132
Fig. 4.27. Demagnetization ratio when current peak value is 100A and 200A.	134
Fig. 5.1. Stator Winding classification.....	136
Fig. 5.2. Filed solution at 2100 rpm of different slot numbers with 8 poles, 8 turns per coil, 151mm stack length at the edge of demagnetization.	138
Fig. 5.3. Flowchart of integer slot winding layout procedure.....	142
Fig. 5.4. Back-EMF of 9-, 12-, 15-slot IPM and SPM machine at 2100rpm.....	150
Fig. 5.5. Phase voltage and magnetic flux density distribution of 9-slot IPM and SPM machine at 2100rpm, full load.	151
Fig. 5.6. Phase voltage and magnetic flux density distribution of 12-slot IPM and SPM machine at 2100rpm, full load.	152
Fig. 5.7. Phase voltage and magnetic flux density distribution of 15-slot IPM and SPM machine at 2100rpm, full load.	153
Fig. 5.8. Structure comparison between Nissan Leaf machine and 9-slot concentrated winding machine.	155
Fig. 5.9. Structure comparison between Nissan Leaf machine and 12-slot concentrated winding machine.	156
Fig. 5.10. Structure comparison between Nissan Leaf machine and 15-slot concentrated winding machine.	157
Fig. 5.11. Machine slot geometries.....	161
Fig. 5.12. Options for bar wound winding.....	162
Fig. 6.1. 2×3 phase machine winding set.....	167
Fig. 6.2. Winding connection of 2.....	167

Fig. 6.3. Winding connection relationship of 2	167
Fig. 6.4. Inverter comparison between 3- and 2	168
Fig. 6.5. Five phase winding set.	173
Fig. 6.6. Winding Connection of 5 phase 15 slot concentrated winding.	173
Fig. 6.7. Back-EMF comparison between 5-phase IPM and SPM machine at 2100rpm.	175
Fig. 6.8. Phase voltage and magnetic flux density distribution comparison between 10- slot, 5-phase IPM and SPM machine at 2100rpm, full load.	176
Fig. 6.9. Phase voltage and magnetic flux density distribution comparison between 15- slot, 5-phase IPM and SPM machine at 2100rpm, full load.	177
Fig. 6.10. Torque profile comparison between modified Nissan Leaf machine and 5 phase machines at 2100rpm, full load.....	180
Fig. 6.11. Nine phase winding set.....	182
Fig. 6.12. Back-EMF comparison between 9-phase IPM and SPM machine at 2100rpm.	184
Fig. 6.13. Flux density distribution comparison between 9-phase IPM and SPM machine at 2100rpm, full load.....	185
Fig. 6.14. Phase voltage and flux density distribution of 9-phase, 21 turns, 200mm stack length SPM machine at 2100rpm.....	188
Fig. 6.15. Seven phase winding set.....	189
Fig. 6.16. Geometry and winding connection of 5-, 7-, 9- phase SPM machine with...	190

List of Tables

Table 3.1. Details of 2012 Nissan Leaf machine [89-96].	55
Table 3.2. Comparison of phase current between Nissan Leaf machine test results and FEA simulation.	67
Table 4.1. Magnet comparison of Nissan Leaf IPM and the Modified Design.	82
Table 4.2 Property of popular sleeve materials and the recommending ranges.	90
Table 4.3 Property of carbon fiber.	90
Table 4.4. The mechanical properties of the iron steel, permanent magnet and sleeve.	90
Table 4.5 Mechanical performance comparison of SPM machines with different sleeves.	93
Table 4.6 Performance comparison between IPM and SPM at base and at top speed (N36Z and 4.5mm magnet thickness).	93
Table 4.7 Mechanical and electrical performance comparison of SPM machines with different magnet and sleeves thickness. (N28AH for magnet material and 12 turns)	95
Table 4.8. Details of Nissan Leaf IPM and example SPM machine design; distributed winding.	97
Table 4.9 Performance information of Nissan leaf IPM over whole speed range.	103
Table 4.10 Performance information of modified Nissan leaf IPM over whole speed range.	104
Table 4.11 Performance information of SPM design candidate over whole speed range.	104
Table 4.12. Mass comparison between IPM and SPM at base and at top speed.	105
Table 4.13 Three-phase concentrated winding connection for 12-slot machine.	115
Table 4.14. Five-phase connections for the 15 slots.	116
Table 4.15. Design parameters comparison between Nissan Leaf machine and synchronous reluctance machine.	122
Table 4.16: Performance comparison between grain boundary magnet motor and conventional motors.	131

Table 5.1. Comparison between single and double-layer concentrated windings [46][85].	137
Table 5.2. Coil angle, in and out direction for each coil.....	143
Table 5.3. Coil angle, in and out direction for each coil after applying Equation 4.8.	144
Table 5.4. Chosen coils for phase A.	144
Table 5.5. Winding layout of the 48-slots, 8-poles, 3-phases machine.	145
Table 5.6 Three phase concentrated winding connection for 9 slot machine.....	146
Table 5.7 Three phase concentrated winding connection for 15-slot machine.....	147
Table 5.8. Performance comparison among 9-slot, 12-slot and 15-slot IPM machine with concentrated winding at base speed (120°C).....	148
Table 5.9. Performance comparison among 9-slot, 12-slot and 15-slot SPM machine with concentrated winding at base speed (120°C).....	149
Table 5.10. Design parameter comparison between 3 phase 9 slot, 12 slot and 15 slot SPM machine with concentrated winding.	158
Table 5.11. Performance comparison among 9 slot, 12 slot and 15 slot SPM machine with concentrated winding at base and at top speed (120°C).	159
Table 5.12. Comparison between copper and aluminum wire slot.....	161
Table 5.13. Performance comparison between stranded and bar wound distributed winding IPM machine at corner and top speed (120°C).....	164
Table 6.1. Performance comparison between 3-phase and 2×3-phase IPM machine with distributed winding at base and top speed (120°C).	168
Table 6.2. Redesign of 2×3-phase IPM machine with distributed winding (120°C).....	169
Table 6.3. Performance comparison between 3-phase and 2×3 phase SPM machine with distributed winding at base and top speed (120°C).	170
Table 6.4. Redesign of 2×3-phase SPM machine with distributed winding (120°C).....	171
Table 6.5 Five phase concentrated winding connection for 10-slot machine.....	172
Table 6.6. Performance comparison between 10-slot and 15-slot 5-phase preliminary design with concentrated winding at corner speed (120°C).	174

Table 6.7. Design parameter comparison between 5-phase 10-slot and 15-slot SPM machine with concentrated winding.	178
Table 6.8. Performance comparison between 5 phase 10 slot and 15 slot SPM machine with concentrated winding at base and at top speed (120°C).	178
Table 6.9. Material usage comparison between 5 phase 10 slot and 15 slot SPM machine with concentrated winding (kg).	180
Table 6.10. Nine phase concentrated winding connection for 9 slot machine.	181
Table 6.11. Performance comparison between 9-slot 9-phase preliminary design with concentrated winding at 2100rpm (120°C).	183
Table 6.12. Design parameter comparison for 9-phase, 9-slot SPM machine with concentrated winding.	186
Table 6.13. Performance comparison between 9 phase 9 slot SPM machine with 8 turns and 11 turns at base and at top speed (120°C).	186
Table 6.14. Performance comparison between 9 phase 9 slot SPM machine with 200mm and 209mm stack length at base and at top speed (120°C, 21 turns).	187
Table 6.15. Material usage comparison between 200mm and 209mm stack length of 9-phase SPM machine with concentrated winding (kg).	187
Table 6.16. Material usage comparison between 5-, 7- and 9- phase SPM machine with single layer integer slot distributed winding (kg).	190
Table 6.17. Design parameter comparison for 5-, 7- and 9-phase SPM machine with distributed winding.	192
Table 6.18. Performance comparison between 5-, 7- and 9-phase SPM machine with distributed winding at base and at top speed (120°C).	192
Table 6.19. Performance comparison between 5-, 7- and 9-phase SPM machine with distributed winding at base and at top speed (120°C).	193

Nomenclature

Symbol	Meaning	Unit
B_{ave}	Average airgap flux density	T
I_c	Current carried in the stator winding per conductor	A
L	Active axial stack length	mm
B	Magnetic load	T
Q	Electric load	A
ω_r	Mechanical rotational speed	rad/s
m	Mass	kg
J	Inertia	kg·m ²
ρ	Material density	kg/m ³
B_r	Remanence	T
H_c	Coercivity	kA/m
R_s	Phase winding resistance	Ω
L_s	Phase synchronous inductance	H
i_s	Phase current	A
ψ_{PM}	PM flux space phasor	T
L_d	d-axis inductance	H
L_q	q-axis inductance	H
ω_e	Electrical angular speed	rad/s
δ	Load angle	degree
γ	Current excitation angle	degree
k_0	Back-EMF coefficient	p.u.
I_s	Phase RMS current	A
P	Power	w
N_s	Number of stator slots	p.u.
P	Number of poles	p.u.

m	Number of phases	p.u.
k_e	Eddy current loss coefficient	p.u.
k_h	Hysteresis loss coefficient	p.u.
k_α	An excess loss coefficient	p.u.
D	Current density	A/mm ²
n	Time harmonic order	p.u.
f	Fundamental frequency	p.u.
A_{copper}	Copper area	mm ²
T_t	Electric machine torque	Nm
C_τ	Electric machine torque coefficient	p.u.
R_1	Stator resistance	Ω
R_2	Rotor resistance referred to stator	Ω
R_c	Loss resistance	Ω
V_{dc1}	DC-link voltage at Converter 1 terminals	V
I_{dc}	DC-link current	A
ρ_{cu}	Copper resistivity	$\mu\Omega\text{m}$
ρ_{cu}	Copper density	kg/m ³
ρ_{al}	Aluminum density	kg/m ³
ρ_{mag}	Magnet density	kg/m ³
ρ_s	Lamination steel density	kg/m ³
E	Young's modulus	GPa
E_{mag}	Young's modulus of magnet	GPa
E_s	Young's modulus of steel	GPa
γ_{mag}	Poisson's ratio of Magnet	p.u
γ_s	Poisson's ratio of steel	p.u
σ_t	Tensile force	N
σ_m	Centrifugal force generated by magnet	N

$\varepsilon_{\Delta T}$	Strain caused by thermal stress	p.u
α	Thermal expansion coefficient	$^{\circ}\text{C}^{-1}$
ε_{pre}	Strain caused by the interference fit	p.u
ε_m	Strain caused by the centrifugal force of magnets	p.u
$\varepsilon_{t[\max]}$	Strain generated by centrifugal force of sleeve	p.u
δ	Interference for press fit	mm
i_{sd}	d - axis stator current	A
i_{sq}	q - axis stator current	A
p	Number of pole pairs	p.u
V_s	Stator phase terminal voltage	V
ω_{\max}	Achievable top speed within the power specification	rad/s
k_{wn}	Winding factor	p.u
k_{dn}	distribution factor	p.u
k_{pn}	Short pitch factor	p.u

Declaration

No portion of the work referred to in this thesis has been submitted in support of an application for another degree or qualification of this or any other place of learning.

Chapter 1

Electrified Vehicle Powertrains

1.1 Introduction

Hybrid electric vehicles (HEVs) and electric vehicles (EVs) have emerged as promising alternative solutions in the transportation sector to reduce or replace the dependency on fossil fuels and combat emissions [1-4]. Electric machines (EMs), which convert the electrical energy and vice versa to mechanical energy to propel or brake the vehicle respectively, are key components optimizing the functionality and performance of vehicles [3-4]. Compared with other applications, traction motors require specific characteristics, such as high torque and power density, high efficiency, low torque ripple, noise and vibration, high starting torque, high reliability, low cost, etc. [5-7]. Due to the overall distinguished performance, permanent magnet (PM) machines have become one of the most prominent traction machines widely applied in hybrid and electric vehicles.

Electric machine design is a challenging task since electromagnetic, thermal, and mechanical phenomena are coupled and need to be considered at the same time. A lot of design variables and design choices make it difficult to search an optimal design. Additional complexity is the conflict between performance and manufacturability. For example, thinner steel lamination, more accurate lamination shape and tighter air-gap width are helpful with high performance, while each attribute will increase the manufacturing difficulties and cost. When involving performance and manufacturing together, the electric machine design process must be a multi-disciplinary task which challenges design knowledge and engineering experience.

Over the years, numerical modeling tools and design optimization methods have been successfully applied to predict, validate and optimize designs in engineering. For example, finite element numerical simulation, lumped parameters analysis, differential evolution optimization to name a few techniques. Unfortunately, none of these considers manufacturing and cost systematically. Furthermore, due to lack of constraints of manufacturability and cost, some optimization results are unrealistic in industrial application.

Manufacturing is a difficult topic to assess without the cost structure of the manufacturing process, as an understanding of the component supply chain. Indeed, the automotive market is a highly cost sensitive sector where small commodity changes can have a disproportionate effect if it impacts on the manufacturing company's existing tooling and techniques. HEV's and EV's are disruptive technologies to existing automotive manufacturers since the new powertrain components are still at an early stage of technological development.

The automotive industry is one of the world's most important economic sectors with production volume increasing since the 1950s, as shown in Fig. 1.1. There are more than 800 million cars and light trucks on the road around the world since 2007 [8]. Although the consumption of cars slows down in the developed and BRIC (Brazil, Russia, India and China) countries, the continually increasing market demand challenges the research and development of vehicle powertrains.

According to Fig.1.2, the production of the top 10 motor vehicle producing countries contributes more than one third of the total volume all over the world. So it can be envisaged that the mass production of traction machines will be realized in these countries in the near future. Therefore, the study of traction machine design targeting low mass production cost is an interesting topic of great benefit to be automotive industry.

As well as the development of HEV's and EV's, the production volume of traction machines will expand following the whole vehicle market around the world. Large production volumes make every cost item count. Similar to other components in conventional combustion engine vehicles, minimized cost will be the most important constraint besides the system performance requirements. While HEV's and EV's current

only form a small part of this market, any future more to these new powertrain technologies will require.

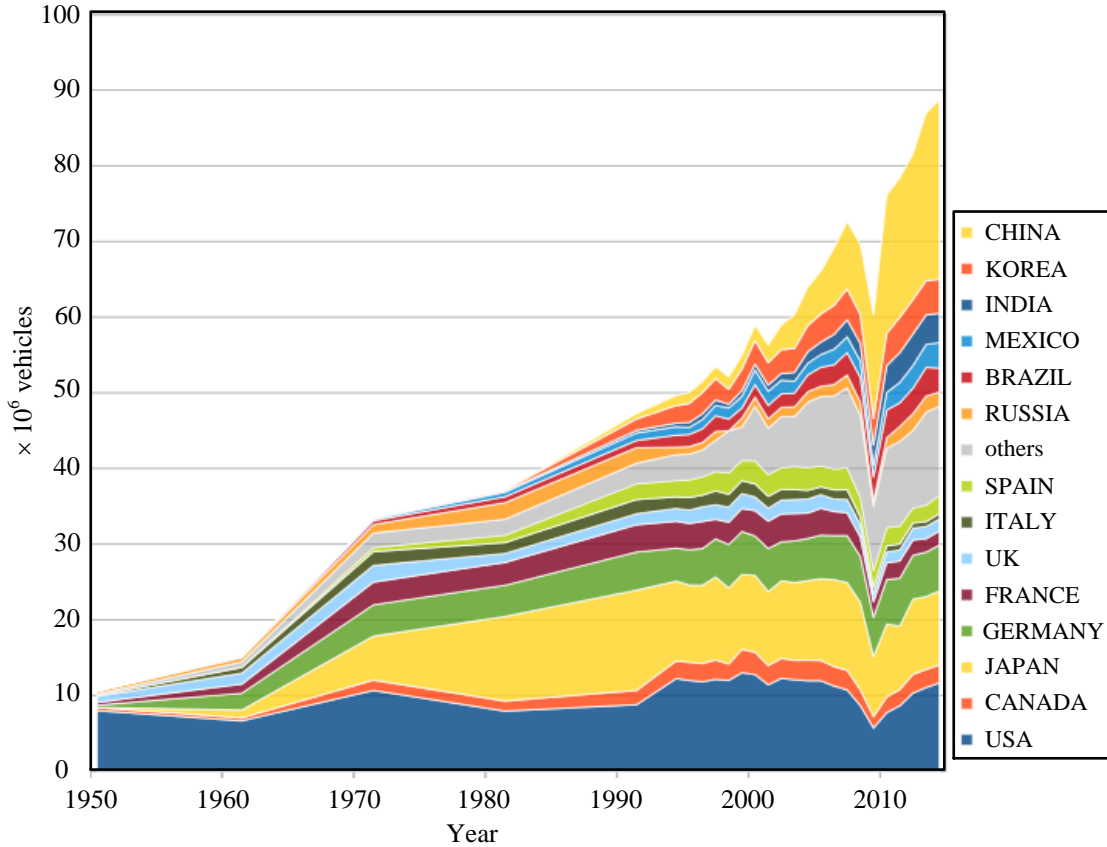


Fig. 1.1. World motor vehicle production [8].

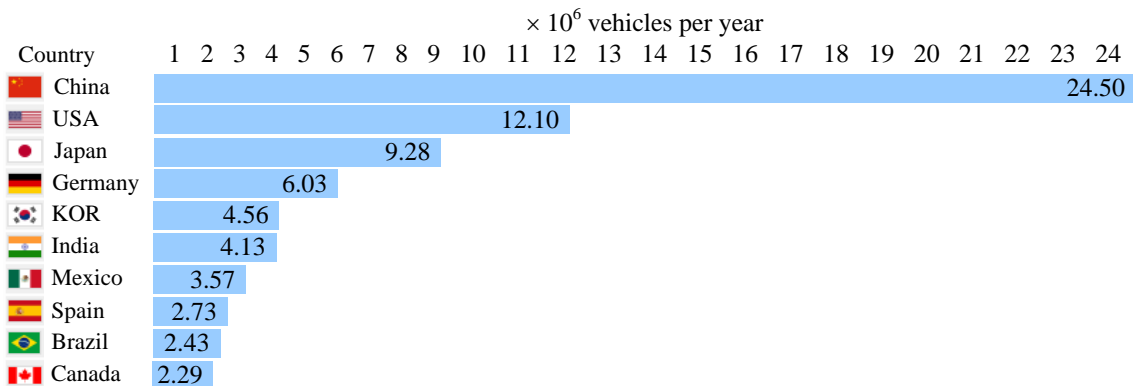


Fig. 1.2. Top 10 motor vehicle producing countries 2015 [8].

A hybrid electric vehicle is a vehicle fitted with an internal combustion engine (ICE) and an electric machine (EM). Here, the electrical element of the powertrain is regarded as a secondary power source to a primary power source (engine) and it is desirable to optimize the power source operations so that the functionality and performance of the HEVs is ensured. By regenerating braking-energy, component down-sizing or right-sizing and making the engine always run in the best operating area, fuel economy improvements are realized. The main issues for HEV include the running condition judgment and control strategy, optimization and management of the energy source, real-time optimization of engine and motor, energy management of the battery packs and control of braking energy recovery [2].

Generally, the powertrain includes the energy source and the energy converter or power source. If there are two or more energy sources, the powertrain will be called hybrid powertrain which has several different power flow routes as shown in Fig. 1.3. Based on how the gasoline and electric power sources are utilized in the vehicle, the HEV can be classified into three types: (a) series hybrid, (b) parallel hybrid and (c) split hybrid, where their typical structures are shown in Fig. 1.4.

These three different configuration HEVs perform differently and encounter different control problems. Series hybrids obtain regenerative power from the vehicle kinetic or potential energy and allow the engine to work under its most efficient conditions. However, the more transfer links lead to more power losses. The control part of the Series hybrids can be realized easily by turning on the ICE when the battery state of charge (SOC) is low, and run it at optimal efficiency until the battery SOC is high. Compared with series hybrids, parallel hybrids have lower energy conversion losses and greater level of flexibility in configuration, component sizing, and control because the engine power is directly transferred to the driving wheels. Generally, the small secondary power source, which means ICE and EM do not operate simultaneously, make the controller focus on timing of engine start/stop and the execution of regenerative braking while the large secondary power source determines complicated control so that the overall efficiency of ICE and EM is optimal. Split hybrids are the combination of series hybrids and parallel hybrids. All kinds of optimal design and control strategy can be used in this

type. But the structure is complex and cost is high, especially for those with planetary gears [2].

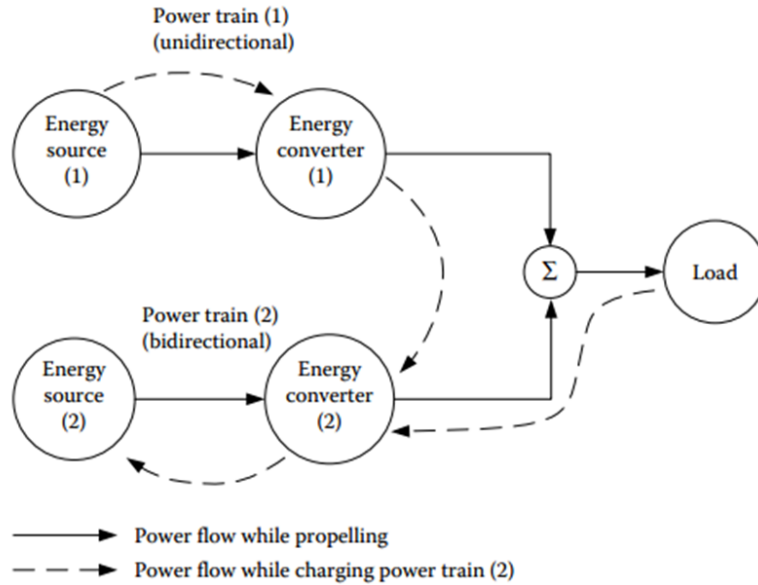


Fig. 1.3. Conceptual illustration of a hybrid powertrain (From Fig. 5.1 in [9])

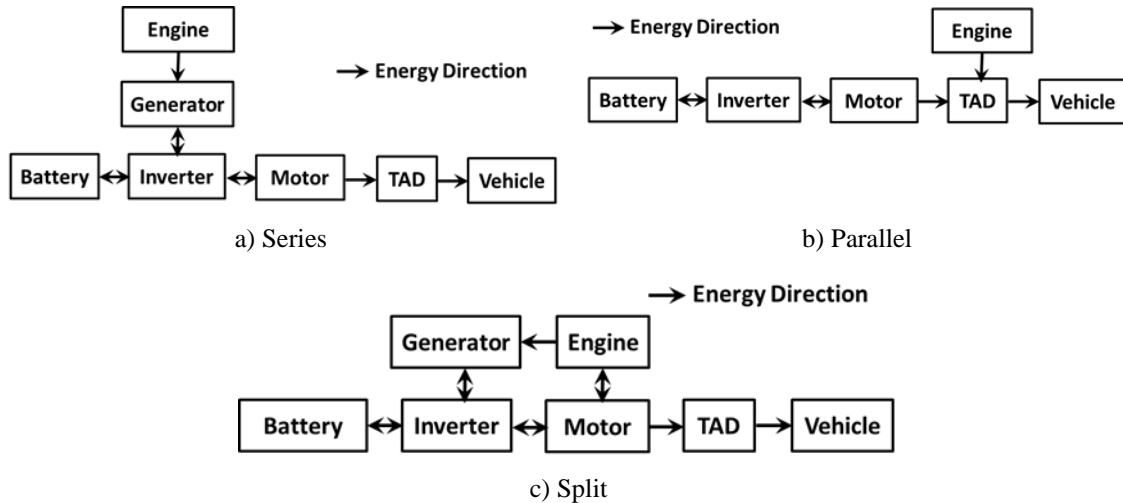


Fig. 1.4. Three typical types of HEV (Modified from Fig. 2, Fig. 3, and Fig. 4 in [10])

Configurations, combining with road conditions, determine the fuel economy, engine efficiency, electric path efficiency, control strategies, numbers and sizes of components. According to the results in [11], both parallel and split configurations have higher fuel economy than series configuration in the highway driving conditions. The split configuration possesses high fuel efficiency not only in urban driving but also in highway driving. Therefore, most of the full-hybrid passenger cars adopt the split configurations, such as the Toyota Prius, Toyota Lexus, GM, Chrysler and Ford Fusion Hybrid [12]. A comprehensive research, careful analysis and in-depth trade-off decisions must be done before selecting a HEV powertrain configuration. Although the powertrain configurations have been mature in the commercial area, they still attract many researchers studying on the performance of different configurations and trying to find the more fuel-efficient engines and transmissions [13].

An important element in the HEV or EV powertrain is the electric traction machine, the design considerations of which are the primary focus of this research study. Fig. 1.5 illustrates the GM Chevy Spark vehicle powertrain and location of the main vehicle traction machine. The figure also shows an exploded view of the traction machine which is an interior permanent magnet machine as will be discussed further in this thesis.

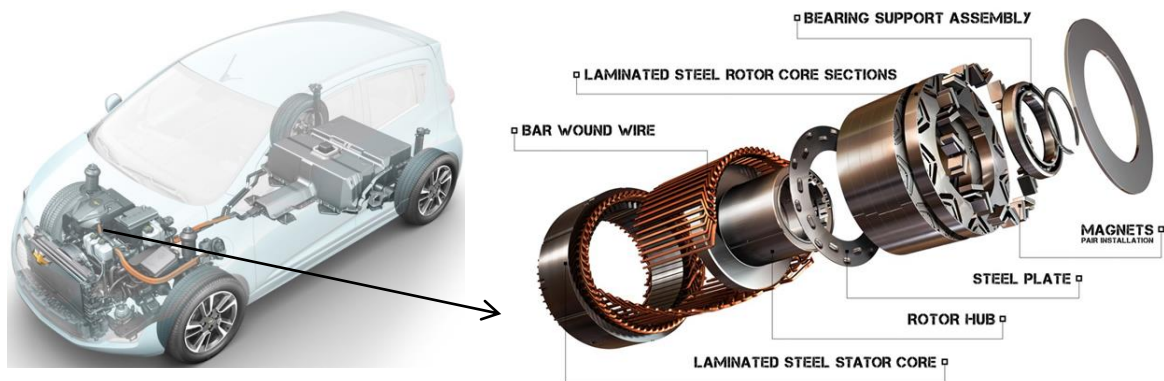


Fig. 1.5. GM permanent magnet machine applied in Chevy Spark [14].

1.2 Literature Review

1.2.1 Interior versus Surface-mounted Permanent Magnets Machines

IPM machines appear to be the favored topology choice for electric vehicle traction machine applications because of their widely quoted benefits of saliency torque contribution, minimum magnet mass, superior demagnetization withstand, wide flux-weakening capability and high operational efficiencies, to list the often quoted attributes [15, 16].

Due to the same inductance on the direct- and quadrature-axes, there is essentially no reluctance torque generated by SPM machines, although they can operate in a flux-weakening mode if appropriately designed [17-19]. Both rotor topologies have been explored with distributed and concentrated stator windings [16-19] with various justifications for either implementation, the IPM being widely regarded as the preferred choice.

Jahns et al [19] designed IPM and SPM machines with fractional-slot concentrated windings (FSCW) against the same vehicle traction specification, same slot-pole combination and same materials, presenting results in terms of flux weakening capability, overload capability, efficiency, loss, demagnetization, etc. However, the airgap and active axial lengths were varied, diluting the comparison. The results show that the IPM machine design needed slightly less permanent magnet material but required a higher phase current with similar machine torque and efficiencies over the whole speed range. Pellegrino et al [20] compared an IPM and SPM machine, but with different winding configurations and airgap diameter. Chlebosz and Ombach [21] studied the demagnetization properties of IPM and SPM traction machines and concluded that SPM machines required permanent magnets with higher coercivity or demagnetization withstand. However, the compared machines had different pole numbers, magnet material and geometries, hence the conclusions cannot be deemed general.

Although studies have compared the two rotor topology options for brushless PM machines, the compared designs always tend to have varied machine parameters, making a quantifiable comparison difficult, if somewhat arbitrary, and closely linked to the personal preference of the machine designer. To-date, no study has directly identified and justified the technical aspects of the two rotor topologies. This thesis aims to address this deficiency via the comparison of a published electric vehicle traction machine design having a distributed stator winding and an IPM rotor, as detailed in Chapter 3 with an SPM rotor while maintaining the mechanical air-gap and stator lamination as discussed in Chapter 4.

1.2.2 Grain Boundary Diffusion Processed Magnet

Permanent magnets play an important role in terms of performance and cost. Their configuration, geometry, volume, material properties and location, including associated flux barriers are essential in determining machine performance. Adversely, the rare earth permanent magnets are a significant portion in the total cost of the traction motor despite being only one tenth of the total machine mass (typically) [22]. This minimizing rare earth permanent magnet material in a design can significantly reduce the machine cost [23]. In addition, manufacturing processes applied to magnets can lead to the degradation of machine performance due to changes in localized magnet material properties. For instance, the excess ends of magnets are usually ground to keep magnets and rotor the same axial length. Here, the grinding process can damage the coating and change the localized permeability of the magnets. Hence, some grain-boundary magnets are manufactured to a prescribed length so that the grinding process can be eliminated [23].

The price and procurement of rare earth materials may restrict the development and expansion of permanent magnet (PM) machines. Grain boundary diffusion processed magnets contain less Dysprosium, a small contributory element to the total magnet material volume, but also the element that contributes a higher cost than neodymium. HEV and EV traction machines require high heat resistant magnets since they operate under high-temperature and high load conditions. Adding heavy rare earth (HRE)

materials such as Dysprosium (Dy) and Terbium (Tb) is a universal method applied to improve the demagnetization due to high temperature of the magnet [24]. However, the price of the rare earth magnet material has increased exponentially in recent years [25]. In his book [25], Walter T. Benecki points out that the neodymium price will be relatively stable while the Dysprosium price will still be expensive in coming decades. Fig. 1.6 shows the Dy and Neodymium (Nd) prices compared with gold from 2008 to 2014. After the rare earth crisis in 2010, the Nd and Dy prices grew exponentially [26]. Then the permanent magnet price gets better but still varies depends on the Nd and Dy cost. Therefore, it is necessary to design PM machines with less Dy material; hence the application of grain boundary diffusion processed magnets can provide a good solution.

It is hard to predict what will happen in next 30 years. Both the mechanical stress and unstable price for the permanent magnet material may limit the development of permanent magnet machines. So both the grain boundary diffusion processed magnet and the non-magnet machine design are introduced to reduce the rare earth material application or to get rid of permanent magnet in electric machines. The use of grain boundary material will be explored as part of the rotor design discussions of Chapter 4.

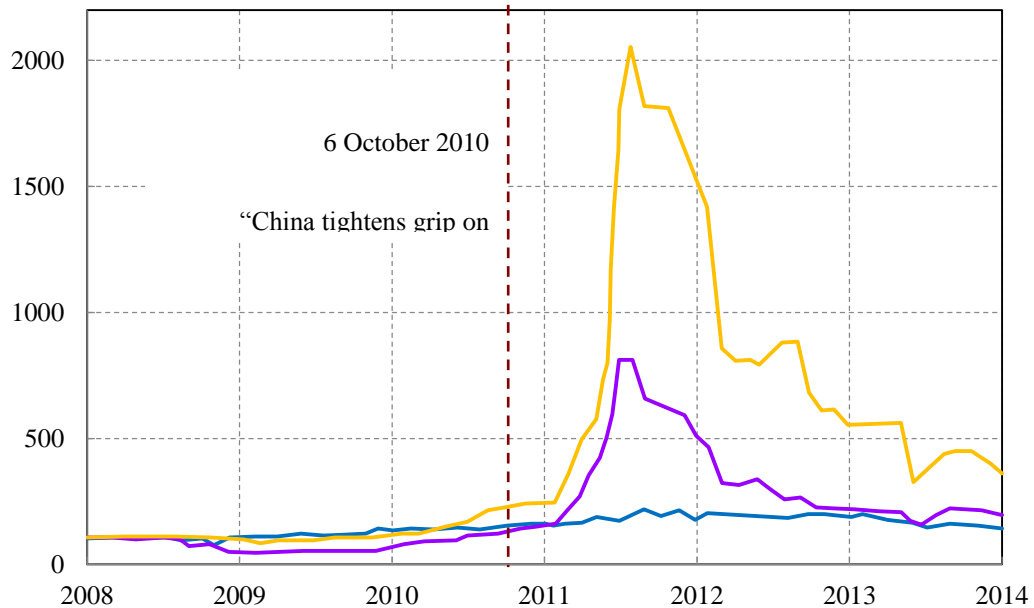


Fig. 1.6. Rare earth metal prices compared with gold (% of January 2008 price) [26].

1.2.3 Distributed Windings versus Concentrated Windings

The most common winding configurations for radial field electric machines can be classified as distributed and concentrated windings shown in Fig 1.7. In this thesis, both the integer slot and fractional slot distributed windings are denoted as distributed windings (wound around more than one tooth) and the concentrated windings refer to the non-overlapped concentrated windings (wound around one tooth). Concentrated and distributed windings have their own advantages and disadvantages. It is often quoted that the benefits for concentrated windings are [27-29]:

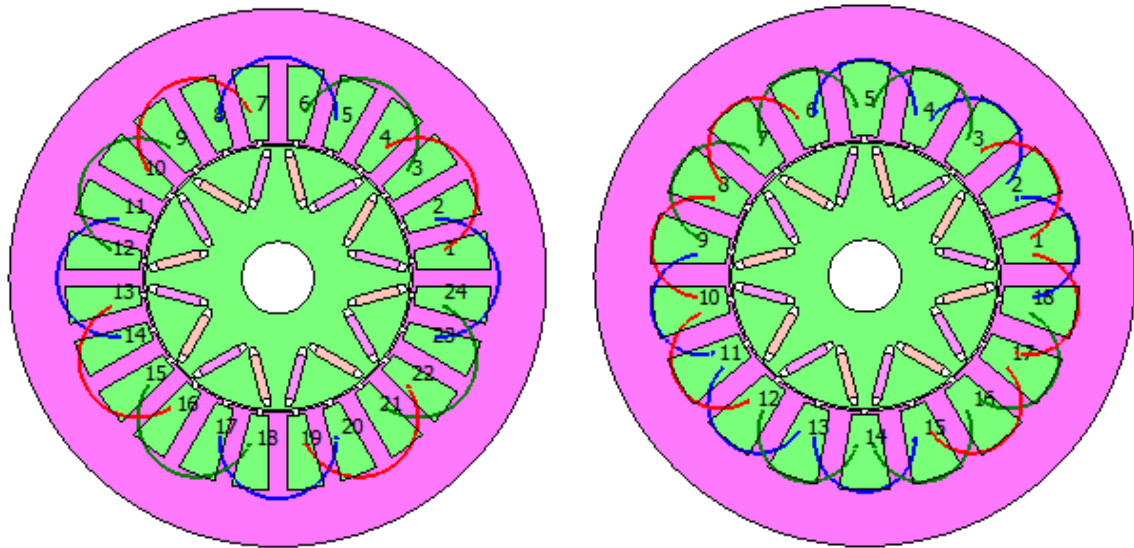
- (a) Shorter end-turns, which leads to smaller copper loss and copper mass.
- (b) Higher copper fill factors, especially for segmented stator, which provides higher torque and power density and potential lower manufacturing cost.
- (c) Low mutual coupling which results in better fault tolerance, especially for single layer concentrated windings.

However, concentrated windings have a number of drawbacks that include:

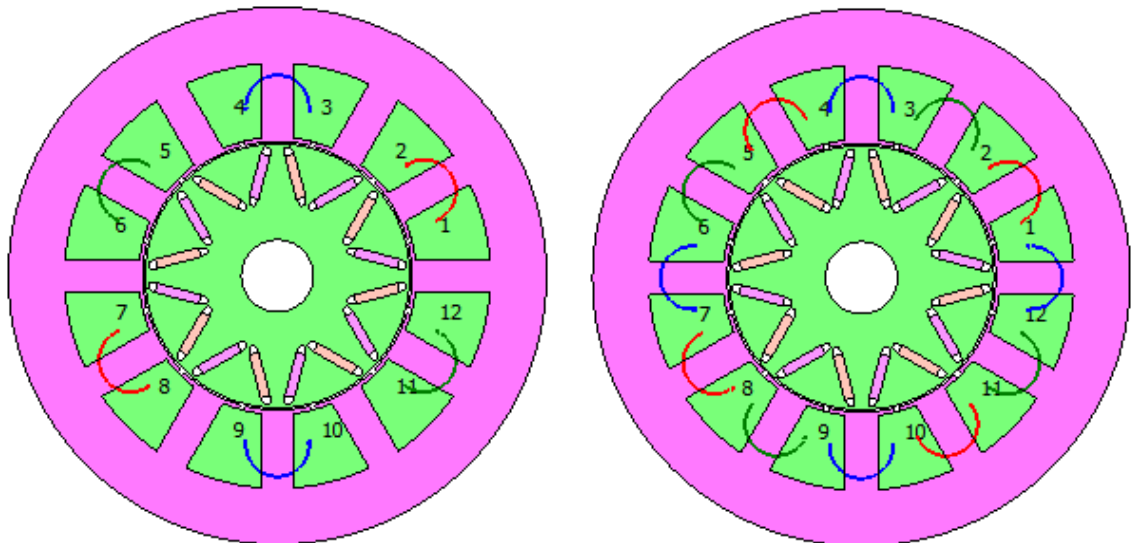
- (a) Higher parasitic effects, which generally leads to higher noise and vibration.
- (b) Unbalanced magnetic forces.
- (c) Excitation torque ripple.
- (d) Higher rotor loss (including rotor core loss, magnet loss, and sleeve loss for conductive sleeve) due to higher localized field distribution on rotor.

Higher d-axis inductance reduces the reluctance torque for IPM machines and the field weakening range, but increases the flux weakening capability for SPM machines [27]. Based on the particular features of concentrated windings, concentrated windings are popular in low speed, small power machine applications. The studies in [28, 29] shows that concentrated windings with either IPM or SPM rotors can generate higher torque than the distributed windings machines in the low speed application. However, the stator iron loss, rotor slot ripple loss and permanent magnets eddy current loss are all higher than distributed winding in the high speed flux weakening region [30].

The research of concentrated windings for EV traction machine applications can be dated back to 1990s [31], unfortunately it showed that the concentrated IPM produced lower



(a) 24 slot single layer integer slot distributed winding (b) 18 slot double layer fractional slot distributed winding



(c) 12 slot single layer non-overlapped concentrated winding (d) 12 slot double layer non-overlapped concentrated winding

Fig. 1.7. Typical concentrated and distributed windings connections for U phase (8 poles, 3 phases).

torque in the constant torque region and yielded smaller constant power range than distributed SPM machines. Although the application for EV traction machine does not look promising, there are still plenty of researchers studying on concentrated windings

and its application in other areas. Soulard [32] investigated the pole-slot combinations for PM machines with concentrated windings and provided the winding factor table for normal slot-pole combination. The paper also concluded the high least common multiple (LCM) between slot and pole numbers lead to the low cogging torque and the concentrated windings have lower torque ripple than the one slot per pole per phase distributed windings. However, those general conclusions did not consider the specific machine and application constraints. From Table I in [33-35], the winding factor for 9-slot/8pole is 0.945 while the 12-slot/8pole combination is 0.866, which suggests that the 9-slot/8pole machine will provide higher torque than the machine with 12-slot/8pole combination. Nevertheless, the result presented in Chapter 5 show that with the same rotor, slot area, stack length, winding layer, number of turns, air-gap length and demagnetization limit, the average output torque at full voltage, base speed for the 9-slot/8pole with 340A peak phase current excitation is 197.1Nm, while for the 12-slot/8pole with same peak phase current, it is 250.6Nm. This has also been reported by other researchers, for example, Jussila [32]. Jahns et al. [35] claimed that the classical steady stator phasor or d-q analysis is not suitable for analysis of concentrated winding machine topologies due to their deviation from the sinusoidal conventional distributed windings, which explained that the torque production is not just determined by the winding factor in the concentrated winding machine. They proposed a closed form analysis for the SPM machine with concentrated windings. A 36-slot/42-pole, 6kW SPM machine was selected to verify the analytical model.

Up to date, the research on concentrated windings for traction application is still continuing. Jahns et al [36] compared the concentrated and distributed windings with same IPM rotor cross section, airgap length and similar ampere-turns, but with scaled stack active axial length to meet the peak power requirements of a benchmark specification. The results show that the machine with concentrated winding obtains higher efficiency in the high speed region due to lower stator loss while the machine with distributed winding has smaller rotor core loss. The choice can be made based on the specific requirement. Furthermore, they also proposed that the concentrated windings have higher d-axis inductance and extend the constant power working region for SPM [19, 38]. The results in [39, 40] also proved that the concentrated winding machines have

higher d-axis inductance than the integer slot distributed winding machine with the same constraints. Conversely, when compared to fractional slot distributed windings, concentrated windings do not have merit in terms of d-axis inductance according to [41, 42]. A fractional slot distributed IPM machine design has been proposed to replace induction machines in a tram application, reducing the number of machines in the system by increasing the machine power density by 1.5 times [43]. For the number of layers of concentrated winding, Lester and Nicola pointed out that the single layer concentrated winding layout is more suitable for the machines with large air-gaps, for example, SPM machines, due to high magneto motive force (MMF) harmonics. On the contrary, a double layer concentrated winding layout can be applied to the machines with smaller air-gap, for instance, IPM machines, because of their low MMF harmonics [44-46]. The heat dissipation of concentrated winding is also a challenging task for the machine designer. Compared with distributed windings, the slot area of concentrated windings is bigger and the hotspot temperature is higher [42]. As stated in [47], the cooling method and current density should be considered in the machine design and optimization stage.

Different with the literatures mentioned above, this thesis mainly focuses on the comparative study between the proposed concentrated winding machines and the benchmarked Nissan Leaf integer slot distributed winding IPM machine with same rotor structure, same thermal management method, and performance constraints. Meanwhile, the concentrated winding and distributed windings are applied to the same SPM rotor to study the performance difference. The performance specification is the pre-requisite and the manufacturability and cost difference between concentrated and distributed windings under the same constraints are another important respect.

This thesis therefore makes comparisons of topologies based on consistent volumetric, thermal and performance constraints, a study that has not been comprehensively repeated.

1.2.4 Multiphase Machines

Multiphase machines have the advantages in high power and high tolerance drive systems. Recently, the multiphase machines have also attracted attention in electric vehicle applications [48].

The structure of the traction machine and its drive system in EVs is shown in Fig. 1.8. In the EV application, the electric source of the traction motor is battery. In order to make sure the inverter works in the high efficiency region no matter the voltage change of the battery, a DC/DC converter is adopted to keep the DC link voltage steady and stable. Between the converter and inverter, a capacitor is applied to store the fluctuation of energy. For the traditional three phase machines, there are three voltage source inverter (VSI) legs. If the number of phase is increased, the current rating for each inverter legs will reduce for the same power requirement. The switching loss should remain roughly constant through the control complexity may increase due to more phases and switches. The conventional three phase VSI can be directly applied to the $N \times 3$ (N is positive integer) phases machine. From the machine side, multiphase can increase the fault tolerance capability and, importantly, reduce the excitation torque ripple, an important system design goal. So far, multiphase machines have been widely applied in ship, aircraft and high power propulsion due to the advantages mentioned above [48-50].

For multiphase machines, current harmonics of orders less than the phase number, when coupled with the corresponding spatial MMF harmonics, will produce useful torque and relatively small loss, noise and torque ripple. Therefore, concentrated and full-pitched stator winding structure is preferable for multiphase machines, for which, it is also possible to increase the power density of the drive by minimizing the supply waveform [51]. The implementation and dynamic simulation of induction motor with 3 and 5 phases are completed and it shows that the machine with 5 phases has lower torque ripple compared to 3 phases [52]. The influence of phase numbers on drive and loss are compare for 3 phase and 9 phase machines in EV applications in [48].

Slot-pole combinations and their effects on winding factors, rotor loss, cogging torque and radial forces for 3-, 5- and 7-phase machines are discussed in [54]. Here, 18-slot-12-

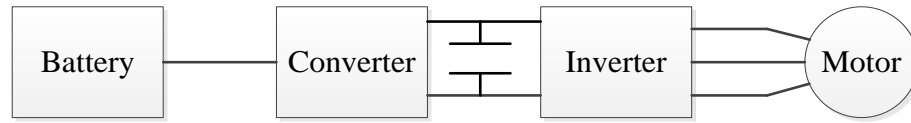


Fig. 1.8. Structure of EVs propulsion drive system.

pole-3-phase, 15-slot-12-pole-5-phase, 20-slot-12-pole-5-phase, and 14-slot-12-pole-7-phase machines are reported as examples to verify the average output torque, rotor loss, torque ripple, cogging torque and radial forces by finite element analysis (FEA) and prove that combinations with winding factors higher than 0.9 produce much more rotor losses comparing to those with winding factors between 0.75 and 0.9. In addition, the combinations generating low cogging torque generally have high winding factor and high rotor loss. The drive model of 3 phase and 2×3 phase and its application results are investigated in [55]. Here, 72-slot-6-pole and 108-slot-6-pole machine for 3-phase and 2×3-phase connections as examples to verify the control model and compare results with FEA predictions. The machine is induction and used for ship propulsion.

EV is a road vehicle which involves an electric propulsion system. With this broad definition in mind, EVs may include battery electric vehicles, hybrid electric vehicles and fuel cell electric vehicles. Utilize the Direct Torque Control (DTC) and Predictive Torque Control (PTC) to the five phase machine and get the required performance [56]. The multiphase technology has been used for many years on ships and split the very high power values that would be the case for three phases. For rail vehicles, the multiphase systems are sporadically used and limited to withstand the different levels of catenary voltage. In road vehicles, the electrification is today commonly implemented with three phase solutions and it seems that the multiphase have yet to penetrate this sector [57-59].

This thesis considers machines having more than 3-phases, specifically Chapter 6 discusses 2×3, 5-, 7- and 9-phase design with concentrated and distributed winding and with IPM and SPM rotor topologies.

1.3 Research Contributions

The manufacturability and manufacturing cost for prototype and volume production are always considered in the traction machine design stage. The studies reported in this thesis present an improved comparison of machine topologies that previously presented and also offers new topologies for future consideration.

An SPM machine is designed according to the Nissan Leaf IPM machine benchmark design with a distributed winding and show to satisfy the performance requirements, a conclusion that is against popular opinion, particularly when the machine is working in the flux weakening region.

This thesis contributes to electric vehicle systems by introducing a new multi-phase synchronous reluctance machine (SRM) with good torque performance and operation from a conventional voltage source inverter for traction machine applications. As far as the author is aware there has been no published data on 5-phase SRM design for traction machine applications. A major obstacle to this has been the high noise and vibration and low torque density of the synchronous machines. However, in the proposed SRM, the asymmetric inverter is replaced with conventional voltage source inverter to achieve low torque ripple compared with switched reluctance machine.

Many people have investigated stator slot and rotor pole combinations for concentrated windings. But no author has completed a thorough assessment of the suggested combinations against specific machine volume and performance constraints. This thesis presents several results for machine designs against a reference benchmark and suitable for EV traction applications. The material and manufacturing cost are also considered.

IPM machines have complicated rotor designs, not really discussed in literature for all operating points. This thesis considers designs suitable for full sinusoidal excitation current over the whole speed operation range. The choice and influence of IPM rotor topologies has been published in Journal.

1.4 Thesis Outline

This Chapter has presented a general overview of the EV powertrain and literature review of traction machine design to-date to introduce the subject area, electric machine design and topics currently existing worldwide. The discussion is not presented as a comprehensive review of the industry, but as an introduction to the main topic area of this thesis.

Chapter 2 discusses the fundamentals of traction machine modeling and design, some considerations to the manufacturing processes.

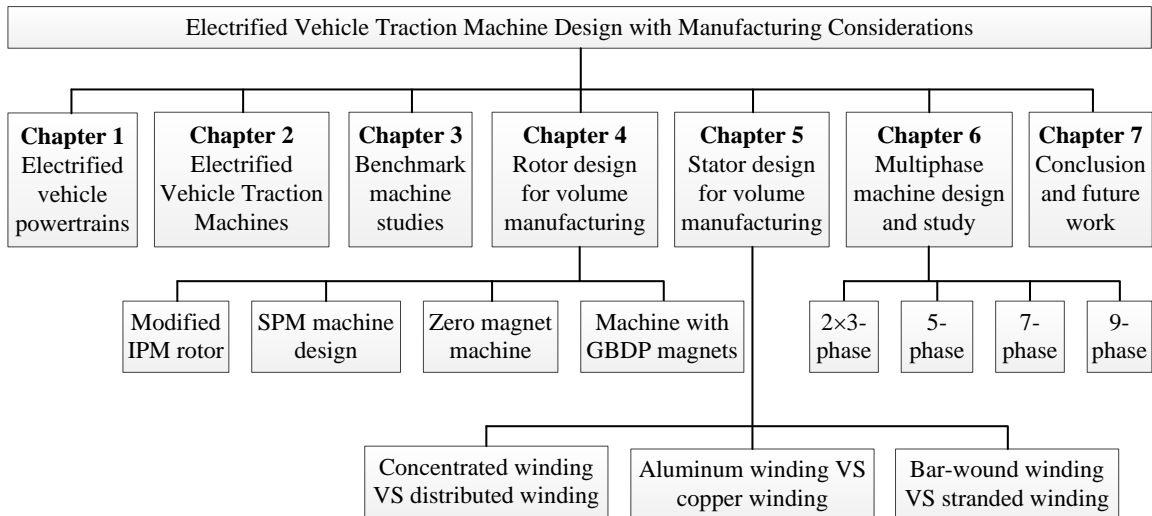
In Chapter 3, a commercial IPM traction machine used in the Nissan Leaf is described and modeled against published performance specifications. Since there is much published data available for this machine and drive system from Oakridge National Laboratory, an independent US test establishment, the machine is used to form a benchmark against which subsequent designs can be validated without the necessity of expensive prototyping and test validation. Chapter 3 also establishes the relevant performance criteria against which subsequent designs are assessed.

Chapter 4 discusses the design of rotor topologies for the benchmarked Nissan Leaf Machine application. The Nissan Leaf machine rotor is redesigned with the same magnet material and rotor dimensional constraints and the performance compared. The comparative study results between SPM and IPM machines are presented. The zero magnet designs of synchronous reluctance machine and switched reluctance machine are presented. Grain boundary diffusion processed permanent magnet material is analyzed and applied in the PM machine to obtain the best design specifications.

Different winding designs are presented in Chapter 5. Concentrated windings and distributed windings are discussed from both design and manufacturing aspects. The FEA analysis is adopted to evaluate the machine performance. An aluminum stator winding is also designed and studied to show the advantages and disadvantages compared to copper stator windings. Finally, the bar wound winding is designed and investigated to compare its merits and demerits with respect to the stranded winding of the Nissan Leaf machine design.

Multiphase machines with concentrated and distributed windings are designed and studied in Chapter 6. The 2×3-phase connection is tried in the modified Nissan Leaf IPM machine with distributed winding and the performance compared to the stranded 3-phase connection. The 5-phase, 10- and 15- slot concentrated winding machines are designed to meet the specifications of Nissan Leaf machine and the benefits and drawbacks are discussed. The 9-phase, 9-slot concentrated winding machine is designed to meet the Nissan Leaf machine and is assessed.

Finally, Chapter 7 concludes the thesis research findings, main achievements and presents recommendations for future work.



Chapter 2

Electrified Vehicle Traction Machines

2.1 Introduction

In this Chapter, the traction machine design fundamentals and manufacturing issues are discussed. The intent of this Chapter is to establish the necessary background for following Chapters and to introduce various components of the machine design process for study of the Nissan Leaf IPM machine as a benchmark machine for the later chapters. This chapter presents analytical sizing equations, guidelines for selection of the number of poles and slots and magnetic circuit materials. The primary focus of the chapter is on permanent magnet synchronous machines (PMSMs) including fundamental of design, manufacturing, benchmark machine, assessment criteria and design parameter studies.

2.2 Fundamentals of Rotating Electric Machines

The main components of a rotating machine are the rotor and stator. There is a gap between rotor and stator, which is denoted as the airgap, as shown in Fig. 2.1 and 2.2. The structure of an idealized electric machine is shown in Fig. 2.1. Assuming B_{ave} is the average airgap flux density, I_c the current carried in the stator winding per conductor and L the active axial stack length, the force acting on one conductor is calculated from first principles as:

$$F = B_{ave} I_c L \quad (2.1)$$

thus, the force acting on Z conductors is:

$$F = B_{ave}(ZI_c)L \quad (2.2)$$

The torque acting on the winding is:

$$T = B_{ave}(ZI_c)L\frac{D}{2} \quad (2.3)$$

The average airgap flux density, B_{ave} varies over the range 0.3T to 1.2T, depending on the magnetic strength from rotor and stator sides [60]. The quantity (ZI_c) can vary from machine to machine, but can be defined in terms of a specific electric loading, Q , where:

$$Q = \frac{ZI_c}{\pi D} \quad (2.4)$$

where Q is a more limited quantity and varies from 10 to 100A/mm² for typical industrial machines [60]. But in special machines, Q can go higher depending on winding mechanical design, cooling medium and techniques.

Thus, the general torque expression for first order sizing exercises becomes:

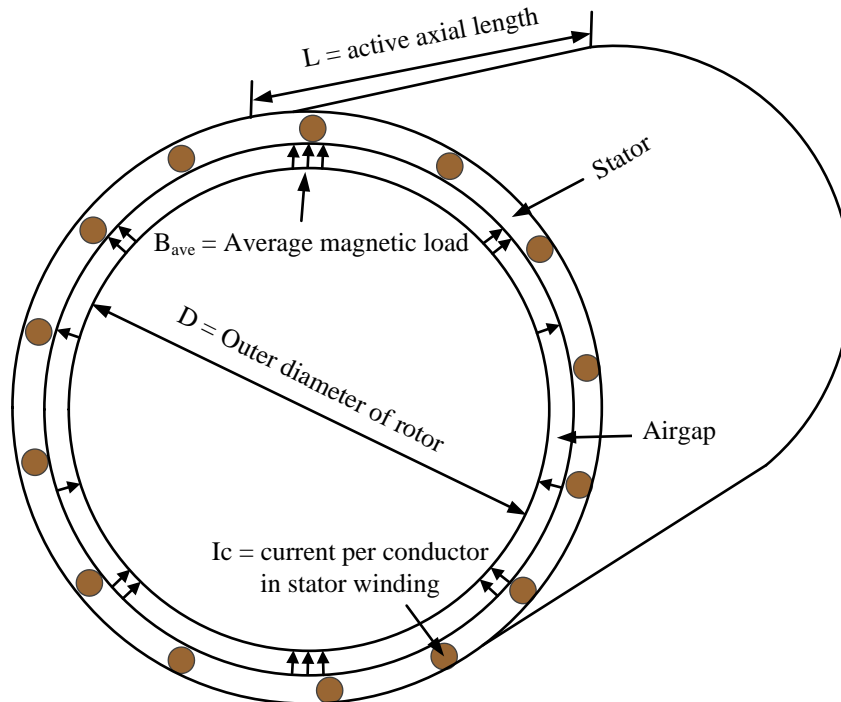


Fig. 2.1. Idealized electric machine.

$$T = \frac{\pi}{2} D^2 L B_{ave} Q \quad (2.5)$$

where B_{ave} is the specific magnetic loading, Q is the specific electrical loading.

The power conversion is given by:

$$P = T \omega_r \quad (2.6)$$

where ω_r is in mechanical radians per second.

Impact observations can be drawn from this simple analysis:

- (a) Torque is proportional to rotor volume while B and Q are approximately constant for a class of machine and independent of machine dimensions.
- (b) Torque is generally independent of the number of pole-pairs. Poles being more related to the speed of machine or volumetric considerations.
- (c) High torque can often require large diameters, i.e. so called “torque motors”, which do not always have continuous requirements or only low speed requirements.

The actual choice of D and L often depends on the torque-to-inertia ratio required to satisfy system dynamics.

Since the inertia of a cylinder is:

$$J = \frac{\pi}{32} D^4 L \rho \quad (2.7)$$

where ρ is the material density in kg/m^3 .

The, torque-to-inertia is:

$$\frac{T}{J} = \frac{\frac{\pi}{2} D^2 L B_{ave} Q}{\frac{\pi}{32} D^4 L \rho} = \frac{16}{D^2 \rho} B_{ave} Q \quad (2.8)$$

So the torque-to-inertia is inverse in proportion to the square of rotor outer diameter. Hence fast acting servo type motors always prefer long-thin rotor length-diameter proportions. Conversely, for drives requiring constant speed, the larger inertia may be an advantage by smoothing out the effect of any torque pulsations thus minimizing corresponding speed fluctuations.

(d) An alternative approach is to derive an expression for the stress per unit area of the rotor surface. From the Equation 2.5, force on the rotor surface is $2T/D$ and surface area of rotor is πDL . Therefore, the force per unit rotor surface area is:

$$\frac{F}{\pi DL} = \frac{2T}{\pi D^2 L} = B_{ave} Q \quad (2.9)$$

2.2.1 Factors Effecting Magnetic and Electrical Loading

In reality, the magnetic loading is usually limited by either saturation of the iron leading to large magnetizing MMF requirements or losses in the iron leading to poor efficiency and high temperature rise. In addition, PM machines can be limited by the magnetic properties of the PM. For example, saturation/loss limited machine:

If B_{ave} is the average magnetic loading in the airgap, the stator tooth flux density is given by:

$$B_t = \frac{B_{ave} \lambda_t}{w_t} \quad (2.10)$$

where the tooth width, w_t , and slot width, λ_t , are as illustrated in Fig. 2.2.

Therefore, if B_t is limited to around 1.7T to 1.8T, then for typical slot/tooth geometries B_{ave} is limited to 0.5T to 0.7T.

B_{ave} can be increased only if the slot width is decreased, but this then reduces the available winding slot area and hence electrical loading. Some machines are designed with no teeth, so called “airgap winding” machines. Such windings eliminate the restriction due to teeth, but effectively increase the magnetic airgap between the stator and rotor; hence require increased MMF. However, this is useful in reducing losses in teeth and magnetic cogging torque produced due to changes in airgap or magnetic circuit reluctance.

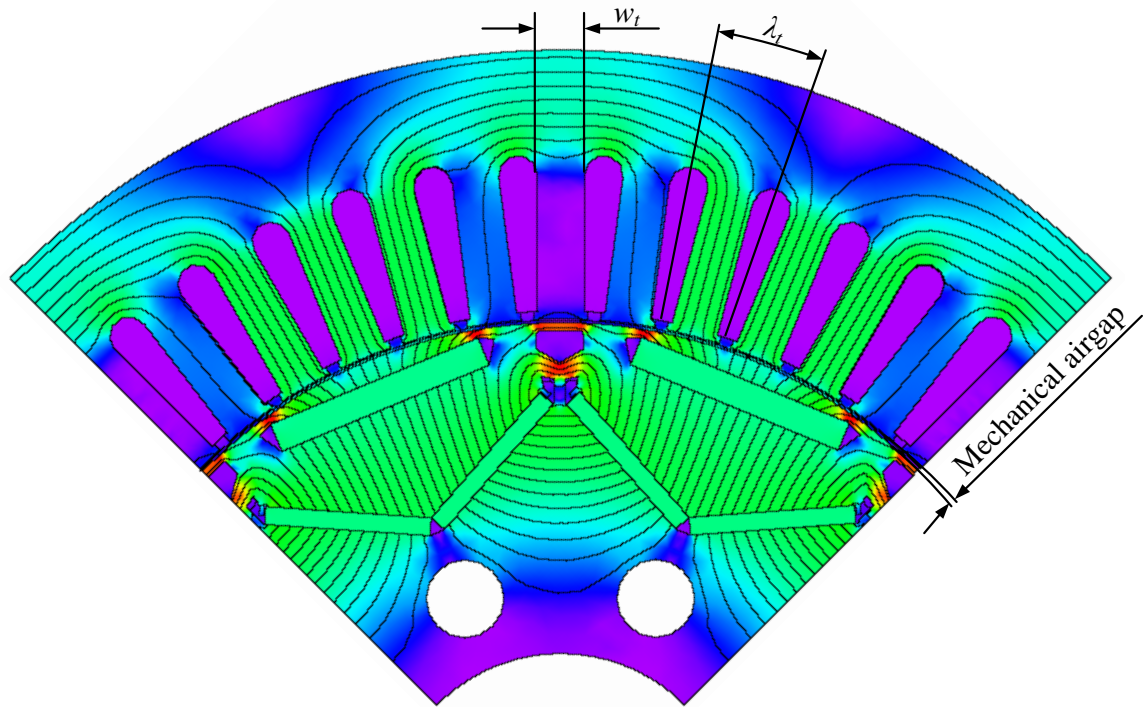


Fig. 2.2. Magnetic load condition.

The rating of any machine is related to the losses internal to the machine and how effectively the losses can be removed to maintain the machine constituent components within their thermally rated limits. The electric loading is a significant contributing factor to machine loss and can quite often determine the thermal performance of the machine. Also, the winding wire insulation (per turn) and other insulations e.g. slot liners, inter-phase and end-winding insulators, and insulating resins, are usually the most likely materials to degrade due to over temperature.

Thermal modeling is used to calculate temperature variations within each component of the machine to ensure that they are operated within their thermal design limits.

Heat can be removed from a machine by a number of techniques that ultimately fix the electrical loading for a given design. The degree of cooling in terms of complexity and cost often relates to the application, final product cost, available volume envelope, etc. The most common (through not exhaustive) techniques can be summarized as:

(a) Simple natural ventilation.

- (b) Force air cooled ventilation, e.g. vacuum cleaners has a small, but nevertheless, a very high rate of take-off air for cooling. Machines have finned cases to increase external surface area and provide a guide for air flow.
- (c) External water cooled jackets. This is common in automotive, but cooling fluid may be at 60°C at the cooling inlet if taken from the vehicle/engine system.
- (d) Internal cooling pipes and fluid media. Aircraft and automotive fuel are often used to directly cool fuel pumps. Direct oil cooling of windings.

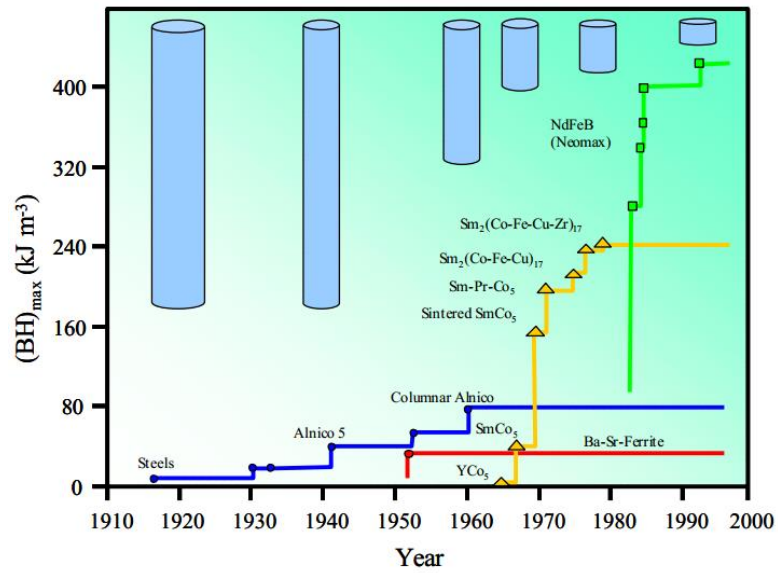
Insulations are classified according to their temperature capability as well as voltage insulation properties. It is usually the temperature factor that ultimately leads to failure due, for example, to over temperature operation during mechanical (system) or electrical faults.

Further, it is important to understand the application duty of the machine. To help clarify and assist in standardizing between manufacturers and users internationally recognized standards set out specific duty regimes.

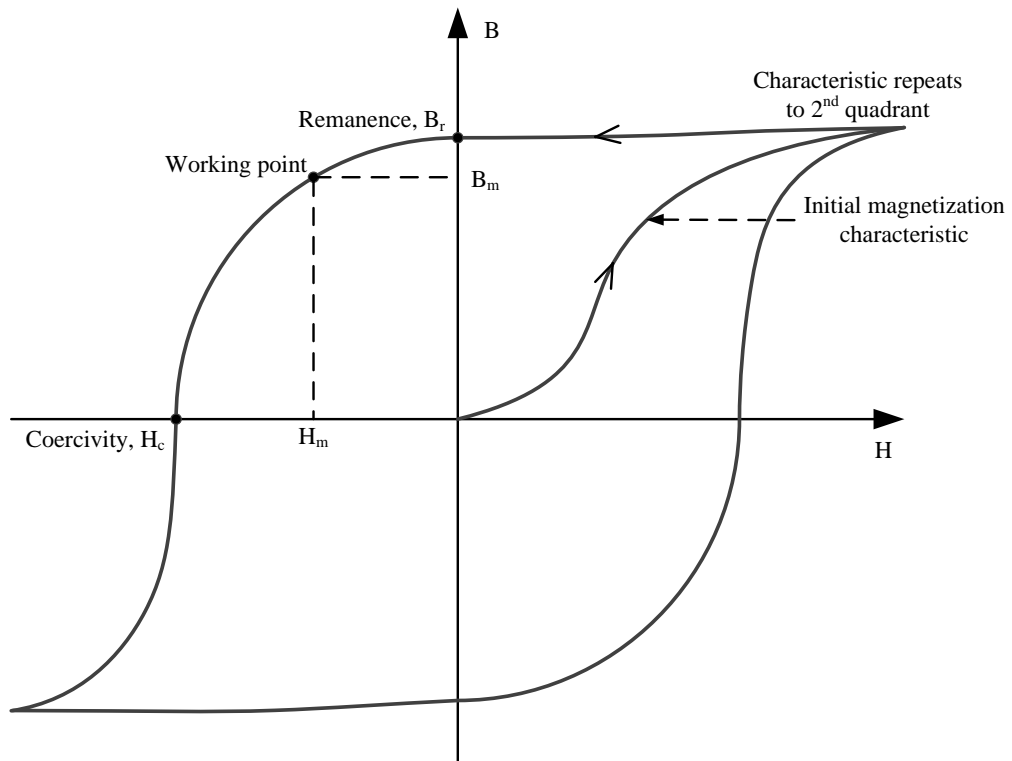
2.2.2 Permanent Magnets

Permanent magnet materials have experienced a significant technological developments from 1970's with the emergence of so-called rare earth materials, i.e. Samarium-Cobalt (SmCo) and Neodymium-Iron-Boron (NdFeB), as illustrated in Fig.2.3 (a) highlighting the improvement in “Energy product” during the 20th century. These material developments have fostered new electrical machine developments particularly in application areas where machine power or torque density is critical design requirement, i.e. in the automotive, aerospace and marine sectors.

Permanent magnets are characterized by having a large area hysteresis loop and are therefore generally known as HARD magnetic materials as opposed to SOFT magnetic materials such as mild steel, iron, lamination steels etc., that ideally have small loop areas to minimize hysteresis loss. Fig. 2.3 (b) illustrates a typical hysteresis loop for a



(a) Development of permanent magnet materials [61].



(b) Typical hysteresis B-H loop of a permanent magnet material.

Fig. 2.3. Hysteresis loop of a typical permanent magnet material.

permanent magnet material defining the main terminologies that will be used later in the thesis discussions.

Permanent magnet machine (device) design hinges around the characteristic of Fig. 2.3 (b) and in determining the working point of a magnetized material. As usual with magnetic circuits, the three dimensional complex field patterns often require sophisticated finite element modeling techniques for greater standard of accuracy, although much useful work can be done by assuming a simple magnetic circuit type approach and using linear or graphical modeling techniques.

2.3 Basic Brushless Permanent Magnet Machine Analysis

2.3.1 Machine Model

Brushless permanent magnet (BLPM) machines generally have two types of rotor topologies:

- a) interior permanent magnet (IPM) rotor, where magnets are buried within the rotor iron [62, 63];
- b) the surface-mounted permanent magnet (SPM) rotor, where magnets are mounted on the rotor surface.

The rotor structures of IPM and SPM machines are illustrated in Fig. 2.4 (a) and (b) respectively.

The magnets, which have a relative permeability close to unity, appear as an air gap to the stator magneto-motive force. Therefore, for the IPM machine, since the magnets are on the rotor direct axis and the quadrature axis paths have a larger iron contents, the direct axis reactance is less than the quadrature axis reactance, which results in rotor saliency [64]; for SPM machine, the reluctance between the stator and the rotor is essentially uniform and hence the direct axis reactance and quadrature axis reactance can be regarded as same. Fig. 2.4 illustrates the two rotor topologies within the same stator arrangement, as will be studied in later Chapters.

It has been reported that BLPM machines have relatively high efficiency, high torque, and high power density for low speed operation because the excitation provided by PMs is current free and lossless, while PM machines inherently have a short constant power range since the fixed flux magnets limit its extended speed range [65-69]. However, the PM material is electrically resistive (approximately 70 times that of copper) and hence the rotor PM segments in high performance machines are axially laminated to reduce eddy currents. This feature will be discussed later in Chapter 4.

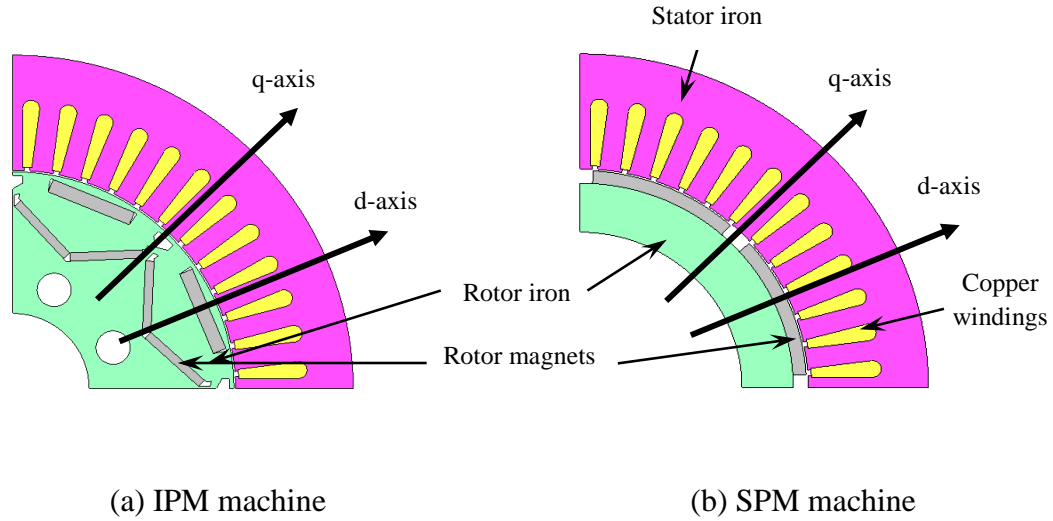


Fig. 2.4. BLPM machines with IPM and SPM rotor topologies.

To investigate general machine operational characteristics, a linear electro-magnetic model of a BLPM machines can be considered. The model is implemented in a classical linear two axis approach and simplified with some assumptions. Firstly, the magnetic saturation is neglected, which results in constant equivalent circuit inductances and magnet flux-linkage. Then, both the stator winding distribution and machine inputs are assumed to be sinusoidal so that the air gap space harmonics and switching harmonics during power electronic converter are neglected. In this way, the machine parameters which have significant influence on the machine power capability over a wide speed range can be determined, which clearly identifies the machine design procedure. These considerations are generally appropriate for the SPM, but need some care for the IPM, since the magnetic circuit and hence machine parameters are no longer linear due to magnetic saturation and cross-field effects. Notwithstanding this comment, thus analysis is still useful to develop the basic operational concepts and design ideas.

Since there are no electrical circuits on the rotor of BLPM machines, the machine per phase voltage equation comprises of the stator voltage equation [64]:

$$V_s = R_s i_s + \frac{d}{dt} (L_s i_s + y_{PM}) \quad (2.11)$$

where R_s is the phase winding resistance, L_s is the phase synchronous-inductance, i_s and ψ_{PM} are phase current and PM flux space phasor respectively.

The voltage equation in the synchronously rotating reference frame can be split into direct and quadrature parts:

$$V_{sd} = R_s i_{sd} + L_d \frac{di_{sd}}{dt} - \omega_e L_q i_{sq} - \omega_e \psi_{PMq} \quad (2.12)$$

$$V_{sq} = R_s i_{sq} + L_q \frac{di_{sq}}{dt} + \omega_e L_d i_{sd} + \omega_e \psi_{PMd} \quad (2.13)$$

where the subscripts d and q represent d -axis and q -axis components, ω_e is electrical angular speed.

For steady-state operation, the time derivative terms can be equated to be zero. The voltage equations, based on the machine vector diagram shown in Fig. 2.5, are expressed as follows:

$$V_s \sin \delta = R_s I_s \sin \gamma + \omega_e L_q I_s \cos \gamma \quad (2.14)$$

$$V_s \cos \delta = R_s I_s \cos \gamma - \omega_e L_d I_s \sin \gamma + \omega_e k_o \quad (2.15)$$

where δ is load angle, γ is current excitation angle, k_o the back-EMF coefficient and I_s the phase RMS current.

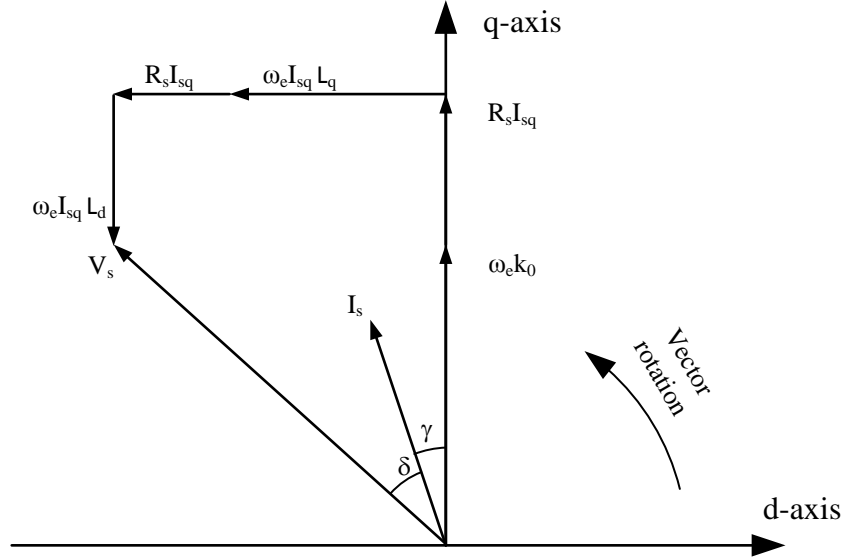


Fig. 2.5. BLPM machine vector diagram.

Therefore, the electrical angular speed can be calculated from:

$$\omega_e = \left(\frac{-b + \sqrt{b^2 + 2ac}}{2a} \right)$$

$$a = (k_o - L_d I_s \sin \gamma)^2 + (L_q I_s \cos \gamma)^2 \quad (2.16)$$

$$b = 2R_s I_s \left(k_o \cos \gamma + \frac{L_q - L_d}{2} I_s \sin 2\gamma \right)$$

$$c = (R_s I_s)^2 + V_s^2$$

Rotor speed is calculated from:

$$\omega_r = \frac{\omega_e}{p} \quad (2.17)$$

where p is the number of pole pairs.

The total power, including copper loss and electro-mechanical power, is calculated from:

$$P = 3(V_{sq}I_{sq} + V_{sd}I_{sd}) \quad (2.18)$$

By neglecting copper loss, which is reasonable for highly efficient machines, the electro-mechanical power as a function of the machine parameters, phase current magnitude and current excitation angle can be expressed as:

$$P_e = 3\omega_e \left(k_o I_s \cos \gamma + \frac{L_q - L_d}{2} I_s^2 \sin 2\gamma \right) \quad (2.19)$$

Hence, the electro-magnetic torque is derived as:

$$T_e = 3p \left(k_o I_s \cos \gamma + \frac{L_q - L_d}{2} I_s^2 \sin 2\gamma \right) \quad (2.20)$$

This torque equation illustrates the main torque combinations in BLPM machines, one arising from the interaction of current and permanent magnet excitation:

$$\text{Excitation torque component} = 3pk_o I_s \cos \gamma \quad (2.21)$$

and one arising from the interaction of machine phase current and the variation winding reluctance expressed in terms of the direct- and quadrature-axis inductance, the saliency or reluctance torque:

$$\text{Reluctance torque component} = 3p \left(\frac{L_q - L_d}{2} \right) I_s^2 \sin(2\gamma) \quad (2.22)$$

In constant torque region, for any magnitude of stator phase current, there is an optimum current excitation angle which leads to maximum electro-magnetic torque. As the speed increases, this angle is chosen for maximum torque operation until the maximum phase voltage constrained by the DC link is reached and then machine enters to the field-weakening region. At the maximum voltage constraint with the increment of machine speed, the current excitation angle rises from the optimum value to 90 degrees. Hence, for BLPM machines where there is no physical field current excitation, field weakening is achieved by supply of a negative component of d-axis stator current vector, which is progressively increased to reduce the machine flux.

Therefore, for SPM machine, L_d equals to L_q , hence the torque is maximized when the current excitation angle equals to zero and the current excitation angle progressively increased to field weaken the machine. For IPM machines, the optimum current excitation angle is obtained by differentiating the electro-magnetic torque with respect to the current excitation angle and equating the result to zero:

$$\frac{dT_e}{d\gamma} = 3p \left[(L_q - L_d) I_s^2 \cos(2\gamma) - k_o I_s \sin \gamma \right] = 0 \quad (2.23)$$

Solving for the differentiating equation yields:

$$\gamma_{opt} = \sin^{-1} \left(\frac{-C + \sqrt{C^2 + 8}}{4} \right) \quad (2.24)$$

where $C = \frac{k_o}{(L_q - L_d) I_s}$.

Again, speeds above the full-load base speed at full stator voltage are achieved by advancing the current excitation angle from its optimum value towards the maximum of 90°E.

The above discussion will be illustrated in the machine analysis procedure and subsequent results in Chapters 3 to 5.

2.3.2 BLPM Traction Machine Design Considerations

When designing a BLPM traction machine, special attention is required to ensure that the machine has reasonable field-weakening capability within the drive system rated voltage and current constraints.

In order to achieve an extended constant power above the voltage constrained base speed, the expression of rotor speed, Equ. (2.17) and (2.18) are analyzed. According to [68], the copper loss of stator winding of traction machines is generally a relatively small proportion of the shaft output power and the resistive voltage drop is also negligible. Hence, the phase resistance in Equ. (2.17) is neglected to assess the main design

parameters impacting on extended speed operation. The simplified rotor speed is expressed as:

$$\omega_r = \frac{|V_s|}{p\sqrt{(k_o - L_d I_s \sin \gamma)^2 + (L_q I_s \cos \gamma)^2}} \quad (2.25)$$

Above base speed, the current excitation angle is increased towards 90 degrees, hence the maximum achievable speed is given by:

$$\omega_{r,(\max)} = \frac{|V_{s,(\max)}|}{p[k_o - L_d I_{s,(\max)}]} \quad (2.26)$$

Therefore, according to Equ. (2.26), the machine maximum speed limit primarily depends on four parameters:

- (a) the supply voltage limit,
- (b) the phase current limit,
- (c) the back-EMF coefficient and
- (d) the direct-axis inductance.

More importantly, it can be noticed that if the machine is designed such that:

$$k_o = L_d I_{s,(\max)} \quad (2.27)$$

the maximum achievable speed is theoretically infinite (in this loss-less scenario).

It is worth noting at this point that according to Equ. (2.28) maximum speed is influenced by the ratio of back-EMF coefficient and $L_d I_s$ production. The quadrature axis inductance does not contribute to extended speed capability. This is a widely miss-conceived assumption in many current publications in the literature that machines must be salient if they have to realize a traction torque-speed characteristic. It may be a point that in being salient the direct-axis inductance is increased above that of an SPM design, however, this is not generally of use in a practical design of high current loads due to reduction of inductance with saturation. This discussion will be continued in Chapter 3 and 4 where an SPM design is proposed compared against a reference benchmark IPM design.

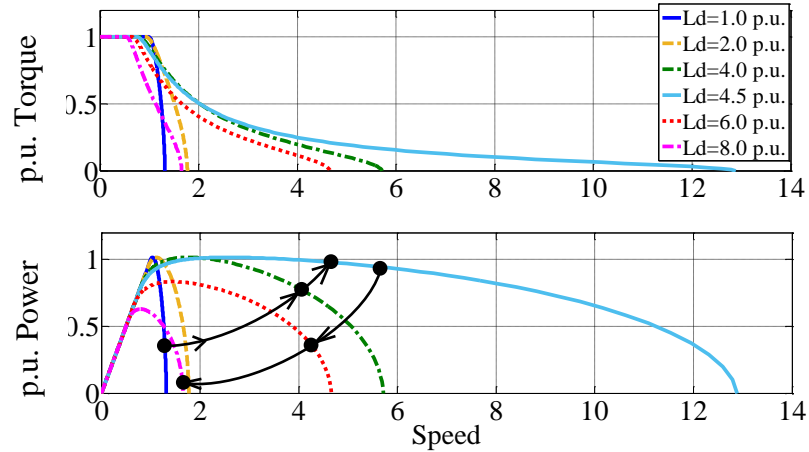


Fig. 2.6. Influence of direct-axis inductance on field-weakening capability.

Fig. 2.6 illustrates the impact on field-weakening capability due to increasing direct-axis inductance, L_d . With the increase of direct-axis inductance from 1.0 to 4.5 per unit (p.u.), the machine field-weakening capability is improved. Although the machine base speed is shifted to a lower value, the power characteristic has been extended to match a traction requirement. However, for any further increase in the direct-axis inductance, for example, from 4.5 to 6.0 then 8.0 p.u., the value of the $L_d I_s (max)$ product will be higher than the value of k_o , resulting in a fall-off in both the peak power capability and the extended speed capability, due to the dominance of the winding impedance voltage drop. This feature will also be observed in Chapters 3 to 5 where particular designs have limited high speed capability.

By comparing the influences of the four parameters of Equ. (2.26) on the machine torque-speed and power-speed performance, the following conclusions are made:

- (a) the increase in the supply voltage constraint will neither improve machine field-weakening capability nor rated operating performance;
- (b) increasing the direct-axis inductance effectively facilitates field-weakening within the voltage and current constraints, but this results in some small reduction in the torque and power performance at 1.0 p.u. speed [61];
- (c) this issue can be solved by increasing the phase current constraint slightly or adjusting the value of the back-EMF coefficient [61].

2.4 Traction Machine Design Considerations

2.4.1 Pole and Slot Combinations

Traditionally, both integer-slot and fractional-slot motors are used in the construction of BLPM machines. The number of slots-per-pole-per-phase is defined as:

$$q = \frac{N_s}{mP} \quad (2.28)$$

where N_s is the number of stator slots, P is the number of poles and m is the number of phases.

The winding is referred to as an integer-slot type if q is an integer number. Otherwise, the winding is referred to as a fractional-slot type. An attractive class of fractional-slot windings where the number of slots-per-pole-per-phase less than or equal to 0.5, allows for single tooth wound windings, as will be discussed in Chapter 5.

Integer-slot windings, in general, offer the highest values of winding factors and typically can benefit from existing and well developed induction motor winding practices and manufacturing equipment. However, the resulting long and overlapping end windings as well as the low values of attainable slot fills associated with integer-slot windings should be carefully considered [32]. Practical fractional-slot tooth wound (concentrated windings), in general, offer reduced length non-overlapping end windings, increased slot fill and overall simplicity of the winding [42]. These qualities are beneficial for high efficiency and high volume production machines. However, the resulting low fundamental winding factor [34], associated rich harmonic content of the stator MMF [35] and potential high core loss [43], should be carefully considered in the selection of fraction-slot windings. Some attractive slot-pole combinations may result in MMF sub-harmonics that can lead to significant rotor losses.

In the design of high performance machines, it is common to consider additional criteria such as vibrations and acoustic noise in the selection of slot-pole combinations [33]. In radial flux machines, the air-gap field has a significant radial component that results in

radial air-gap stresses that are significantly larger than the tangential stresses that produce useful torque. The mode of the spatial distribution of the radial stress waveform is a function of the number of slots and poles. Selection of the number of slots and poles has a significant impact on the radial stator stress distribution [32]. For instance, machines with 12/10 and 9/6 slot-pole combinations produce resultant stator forces respectively. A motor with 9/8 slot-pole combination leads to an unbalanced force distribution. However, it is the impact of unbalance on the motor bearings and load that is import, and that applies to any load. In general, the mechanical structure of the stator is more susceptible to mechanical deformations resulting from stresses with low modes [33]. If not properly mitigated, these deformations can lead to increased vibrations and acoustic noise during normal operation. Topologies that have inherently low radial force modes, such as 12/10, may benefit from stator lamination designs with increased yoke thicknesses, closed stator slots, or other means of increasing stator structural stiffness that will reduce unwanted stator deformations and acoustic noise. It should be mentioned that these changes typically have a negative impact on torque density and manufacturing cost. These features will be explored in Chapter 5.

2.4.2 Rotor Topology

In permanent magnet machines, a wide selection of rotor topologies is available. Two main classes of machines have already been identified based on the two basic rotor topologies, namely, surface permanent magnet (SPM) and interior permanent magnet (IPM) machines. Examples of rotor topologies belonging to the class of SPM and IPM are provided in Figs. 2.1 (a) and (b), and (c) through (f), respectively. An example of a generic SPM machine is provided in Figs. 2.7 (a). Torque quality (both cogging and on-load ripple) and back-EMF distortion performance of the generic SPM motor can be improved by properly shaping (chamfering) the surface of the magnet such that it results in an air-gap flux density waveform that approximates a sinusoidal distribution, an example topology illustrated in Fig. 2.7 (b). However, a shaped magnet, Fig. 2.7 (b), is in general more expensive since it requires additional material to support increased airgap

and additional machining to shape the magnets. IPM rotors are shown in Figs. 2.7 (c) through to (f). These topologies offer potential benefits associated with rotor saliency, an additional reluctance torque component and claimed improved field-weakening performance [16-18], although this feature will be discussed in detail in Chapter 4. IPM rotors shown in Figs. 2.7(c), (d) and (f) benefit from simple rectangular magnet shapes and are typically used with high energy rare earth magnets. On the other hand, multi-layer and spoke IPM topologies shown in Figs. 2.7 (e) can take advantage of lower-cost alternative magnet materials such as bonded rare-earths and ceramic ferrites. Furthermore, the rotor topologies shown in Figs. 2.7 (d), (e) and (f) have an additional design flexibility to increase the air-gap flux density by focusing (concentrating) the PM flux. It should be mentioned that Fig. 2.7 provides only a basic overview of a large number of rotor topologies that are available. Selection of the proper topology depends on the specific target application. For example, SPM motors are predominantly used in servo applications where torque linearity and quality are of high concern. On the hand, various IPM topologies are most commonly found in traction and industrial applications, where high-speed field weakening performance is of importance.

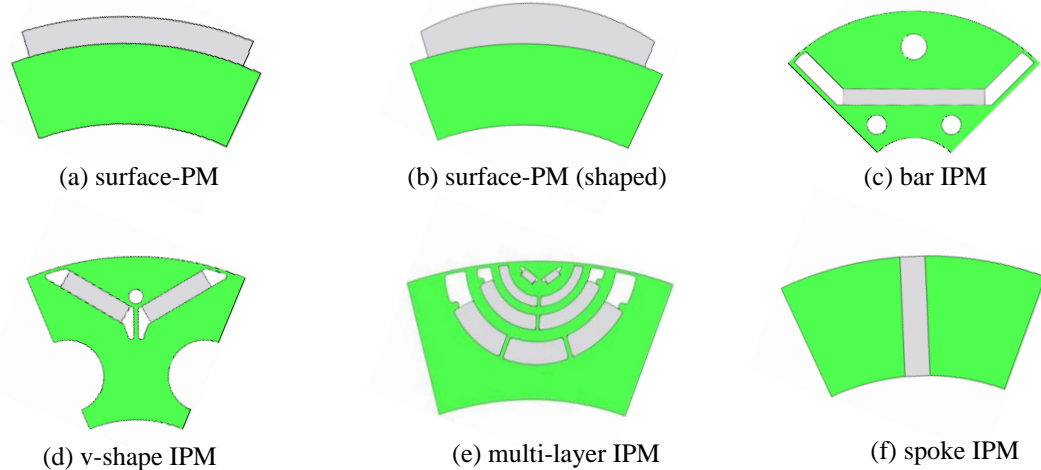


Fig. 2.7. Surface-PM and IPM machine rotor topologies.

2.4.3 Machine Losses and Efficiency

Electric machine losses lead to practical performance limitations related to temperature rises of the insulation and permanent magnet systems. Efficiencies attainable in electric machines are mainly limited by the electric (conductor) and magnetic materials used to carry electric currents and magnetic fluxes, respectively. Therefore, understanding and quantifying the main loss mechanisms in such materials is crucial in the design of high performance electric machines.

(a) Winding Loss

Joule, ohmic or copper losses in the stator winding depend on the winding RMS current and resistance. Stator winding DC resistance per phase can be calculated using the basic geometric parameters related to the stack length, mean end winding (end-turn) length, conductor area and material resistivity.

In addition to the loss in the DC component of the resistance, the stator winding will contain frequency dependent losses that are related to the skin and proximity effects of conductors of finite diameter placed in alternating magnetic fields. While leakage fields in the slots of an electric machine are typically small, their frequencies can be significantly high, especially for high speed machines and machines excited with PWM drives. High frequency induced ohmic losses are highly dependent on the following three factors: slot-opening dimensions, conductor diameter and transposition within the slot, and winding inductance (that provides smoothing of PWM current ripples).

Thus, a factor, k_{AC} , can be used to multiply the DC resistance to take account of higher frequency effects associated with conductor skin effect [69].

$$R_{ph(AC)} = k_{AC} \left(\frac{\rho l_{total}}{\text{conductor area}} \right) \quad (2.29)$$

For the machines considered in subsequent Chapters higher frequency losses in conductors assumes negligible due to the use of multi-stranded, transposed winding conductor per coil turn. This precludes the discussion on bar-wound winding topologies

in Chapter 5 which mention higher frequency conductor loss, but does not calculate them due to the detrimental effect of the winding implementation.

For an n-phase machine, the total armature winding copper or Joule losses can be calculated using the following equation:

$$P_{cu} = nI_{ph(rms)}^2 R_{ph(AC)} \quad (2.30)$$

where r_s is the winding resistance per phase computed at the correct operating temperature.

(b) Core Loss

Electromagnetic core losses induced by time-varying fields in laminated electric steels are typically calculated in the post-processing stage of the electromagnetic analysis and are based on the combination of calculated core flux density values and data obtained from loss measurements performed by manufacturers on lamination material samples. Measured specific core loss data is fitted to a fixed coefficient Steinmetz expression that is given as follows [70]:

$$P_{core} = k_h f B^\alpha + k_e f^2 B^2 + k_\alpha f^{1.5} B^{1.5} \quad (2.31)$$

where k_e is the eddy current loss coefficient, k_h is the hysteresis loss coefficient and k_α is an excess loss coefficient used to improve the curve fitting process.

The fixed coefficient model provided in Equ. (2.30) is limited to a narrow set of frequencies. An improvement to this classical model assumes that the hysteresis power coefficient, α , is equal to 2, the excess loss coefficient, k_α , to be equal to zero, and accounts for variation in loss with both frequency and flux density. On the other hand, tooth-yoke junction and tooth-tip regions experience both radial and tangential rotating (distorted elliptic) field components. It should be mentioned that in a typical machine stator teeth and yokes account for the majority of the core losses.

Loss measurements on electric steels used in the laminations of electric machines are typically performed assuming AC pulsating field components. Improvements can be introduced by accounting for DC (constant) bias fields and incremental losses in the

measurements. In addition, further improvements in the measurements are possible by accounting for the above mentioned rotational field components in the measurement [71].

(c) Magnet Loss

Permanent magnet losses in the rotor are produced by alternating field components that are not synchronized to the rotor rotation. Alternating field components in the rotor structure can be attributed to permeance variation produced by stator lamination slotting (in semi-closed and open slots), space-harmonics produced by armature winding layouts, and time-harmonics produced by either the power supply or a combination of the power supply-motor interaction. The eddy-current loss is the dominant loss component, while magnet hysteresis in the magnet material is typically considered insignificant [72].

To analyze the magnet eddy current loss for IPM machines, the investigation of the loss origin is carried out shown as in Fig. 2.8. Those three sources of loss are all analyzed through Finite Element Analysis (FEA) in JMAG. Since concentrating on the motor structure and no control added in the simulation, the slot harmonics is the main reason of the magnet eddy current loss.

The discretized Steinmetz model, shown in Equation (2.32) [70], is adopted to calculate the magnet eddy current loss:

$$W_{eddy\ current\ loss} = \int \sum K_e D \cdot (nf)^2 \cdot \{B_{r,n}^2 + B_{\theta,n}^2\} dv \quad (2.32)$$

where K_e is loss coefficient, D is current density, n is time harmonic order, f is fundamental frequency, $B_{r,n}$ is the n -th harmonics of the radial components of the flux density, and $B_{\theta,n}$ is the n -th harmonics of the peripheral components of the flux density. The calculation process is shown in Fig. 2.9. The 3D simulation is the prerequisite of the calculation and all data of the elements on the magnets are needed to be exported to carry out the calculation.

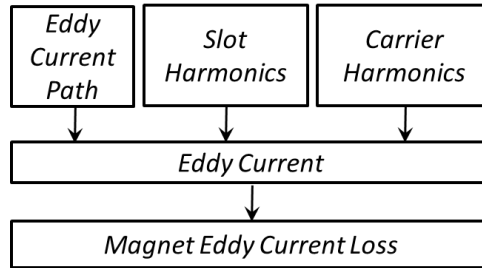


Fig. 2.8. Magnet eddy current loss investigation.

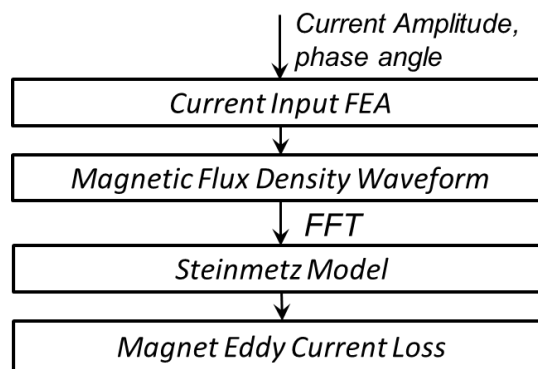


Fig. 2.9. FEA Based Magnet eddy current loss calculation.

(d) Windage and friction

This is estimated from the machine geometry, i.e. airgap and rotor dimensions, rotor chamber air flows etc. and the machine bearings. Typically, windage and frictional losses are relatively small by design compared to other mechanisms, as will be seen in the design calculations of Chapter 3 to 5.

2.5 Traction Machine Manufacturing Considerations

This section reviews the popular techniques and recent developments in electric machine manufacturing, including prototype, low volume and high volume. Manufacturing methods for the main parts of electric machines, assembly and how they affect performance are discussed, as well some indication of the cost issues.

Early in 1970s, design for manufacturability (DFM), was developed, as design concept and studied by many scholars, such as, R. H. J. Warnecke, D. M. Anderson, and Geoffrey Boothroyd [74-76]. The assembly-oriented design manner, like Boothroyd method and Dewhurst method, and assemblability Evaluation Method (AEM) developed by Hitachi, have achieved great success in reducing product cost [74]. Later on, concurrent engineering was put forward to encourage designers consider manufacturing factors at the design stage, including conceptual design, embodiment design and detailed design [75]. Now this topic is still focused by some researchers. Peter Groche, Wolfram Schmitt, etc. [76] integrated manufacturing-induced properties in product design and formulating mathematical optimization algorithms to obtain the design result. Distinguished with the conventional Design for Assembly (DFA) and Design for Manufacture, they considered the manufacturing-induced properties before design and carried out the optimization process in design.

Although the DFM idea have been presented and approved for more than 40 years, it is hard for designers to give specific method to let others learn or inherit in a short time. Since design and manufacturing process change significantly for various products, the concrete implementation is out of the scope of this thesis.

In addition, manufacturing constraints during machine design process need consideration. Although steel lamination can be manufactured to 0.1 mm, the general thickness for IPM machines is 0.35 mm since the cost will be much larger for the thinner lamination. Air-gap width for IPM machines range from 0.3 mm to 1.0 mm, which is much larger than induction machine (IM) and switched reluctance machine (SPM) since the rotor with permanent magnet inside has a large magnetic force which makes the assembly more difficult. The tolerance of each part should be controlled no smaller than 0.01mm since the manufacturing cost will increase exponentially with high manufacturing precision.

Given the potential for high manufacturing volumes for automotive applications, as discussed in Section 1.1, many techniques have been investigated to try to simplify the manufacturing process for electric machines.

2.5.1 Overview of the Electric Machine manufacturing

As the wide application of electric machines, IMs have well established manufacturing techniques and automated product lines for mass production. Fig. 2.10 shows the main manufacturing steps of IMs [77]. The stator and rotor are the two main parts which will be manufactured separately while they also share some common manufacturing process, for instance, lamination stamping and stacking, machining, coating, and test. Finally, the



Fig. 2.10. Main manufacturing process of electric machines [77]. stator and rotor will be assembled together and some related tests will be done to make sure the electric machines are qualified.

The electric machines manufacturing process varies with the product volume. Usually, a prototype will be fabricated in a workshop without product line. In that case, the winding, stacking and assembly will be done manually. So the labor cost and some design factors like winding factor, slot filling factor and air-gap width, are all linked in some way or another to the machine design. The cost of electric machines can be divided into fixed and variable costs. The fixed cost is the cost that does not change as the product volume changes, while the variable cost depends on the specific electric machine geometry, tolerance requirements, volume and materials selected etc. Variable costs including raw material, manufacturing overhead, direct labor, indirect manufacturing, supplies and depreciation of equipment and facilities, and so on. The main components for electric machines manufactured in high volumes are the:

- (a) Lamination manufacturing process
- (b) Lamination selection
- (c) Permanent magnets, and
- (d) Stator windings.

2.5.2 Lamination Manufacturing Process

In general, the cost of manufacturing laminations decided by the amount of steel cost and the stamping machine. To fully use the material on the steel strip, the width of the stamped steel strip is just a little larger than the outer diameter of the lamination. If the width of the steel rolls was fixed, the design result would be slightly adjusted to reduce the cost. In addition, the punching machine can be purchased based on the production quantity, efficiency requirement, precision target, and cost. The error of punch increases as the process times, which needed to be controlled in a certain area to make sure the similarity of the lamination so that they can be attached to a rotor or a stator. Some punching machine can manufacture a lamination by one punch while smaller one just punch a part and need several steps to complete one. So the cost of punching machine and changing worn punch head needs to be compared. Besides, the lamination in a prototype is often manufactured by wire-electrode cutting, hence the cost for cutting is higher than the material.

Firstly, the steel sheet is unrolled and cut to smaller strips according to the outer diameter of the laminations and the new steel strip is rolled again to form steel strip rolls separately. Then the laminations are stamped from the steel strips and the error mainly determined by the punch. The shape error of slots putting magnet is strictly controlled in case the slot can't fit the magnet. In actual production conditions, motor companies have more than two suppliers for one part to avoid the risk from one supplier and the stack of lamination also imparts another part of error. Thus each slot has tolerance to assemble the magnet with tiny shape differences.

In general, the cost of manufacturing laminations decided by the amount of steel cost and the stamping machine. To fully use the material on the steel strip, the width of the stamped steel strip is just a little larger than the outer diameter of the lamination. If the width of the steel rolls was fixed, the design result would be slightly adjusted to reduce the cost. In addition, the punching machine can be purchased based on the production quantity, efficiency requirement, precision target, and cost. The error of punch increases as the process times, which needed to be controlled in a certain area to make sure the similarity of the lamination so that they can be attached to a rotor or a stator.

If manufacturing of electric machines is considered in early design stage, the designer will obtain reasonable design. The automatic winding method, laminated or spiral-laminated cores needs smaller slot fill factor compared with the manual winding, segmented or soft magnetic composite (SMC) cores, and open slots.

Typical thickness of lamination in traction motors ranges from 0.2mm to 0.35mm.

Depending on volume, stator laminations can be manufactured in complete or in sections, as illustrated in Fig. 2.11 [78]. For high volume manufacture, various researchers and companies have considered a number of techniques. For example, punching the tooth profile on a straight strip and then winding this strip to form the stator, as illustrated in Fig. 2.12 [79, 80]. Alternatively, tooth sections are individually stamped and these then assembled to form the complete stack, two examples of which are shown in Fig. 2.13 [81] and Fig. 2.14 [82].

Soft magnetic composites (SMCs) are also used for stator manufacture. The material can be compressed into a 3-dimensional design giving the machine designer some additional freedom to implement the magnetic field. However, SMC materials have a lower

magnetic performance when compared to laminated structures from thin sheet silicon steels and are hence not usually considered for high power traction applications. Fig. 2.15 shows components from a sectionalized SMC machine proposed by Jack [83]. While Fig. 2.16 and 2.17 shows other examples of stator assembly concepts [84, 85].

Welding is a widespread method for securing stator cores with the drawbacks of requiring manual loading of laminations and maintenance activity. But the welding also plays an important role in iron loss since it will change the electrical properties of silicone steels. This process has a significant impact on the eddy current, so care is needed in the weld application.

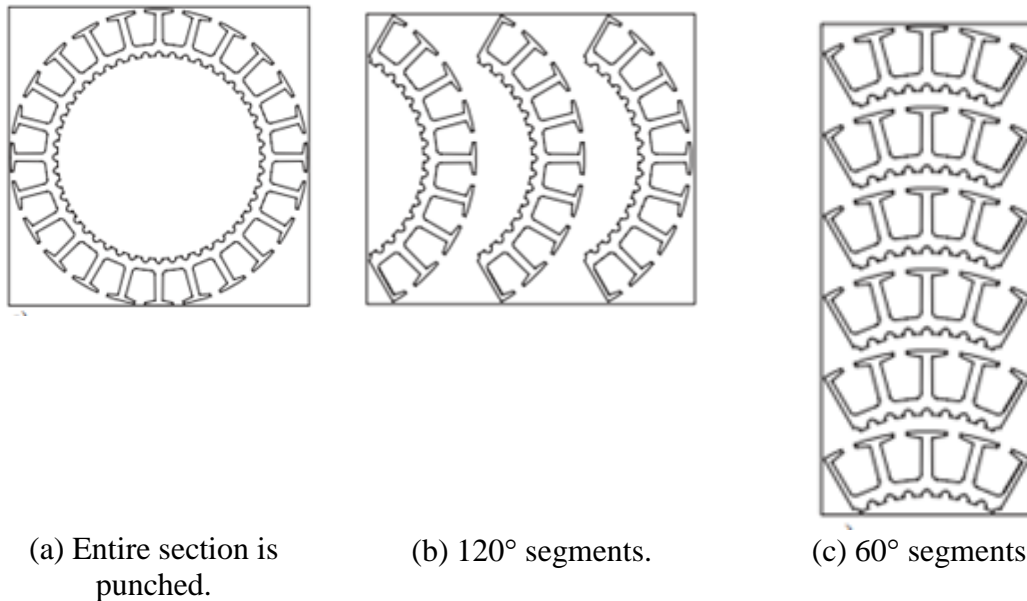
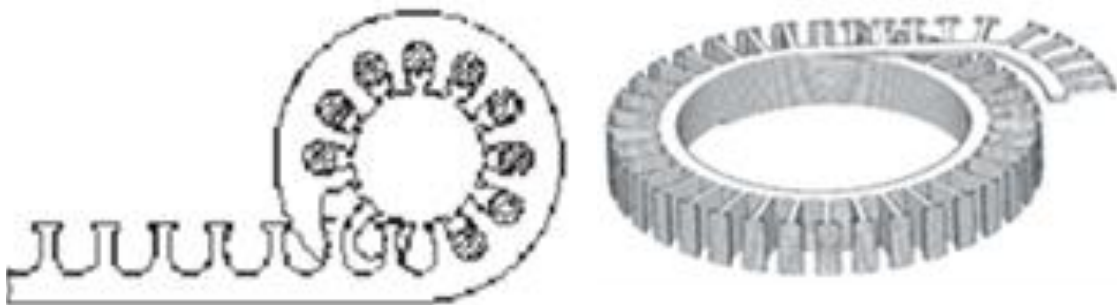


Fig. 2.11. Stator laminations [78].



- (a) Outer stator from Mitsuhiro [79]. (b) Inner stator from Lee [80].
 Fig. 2.12. Examples of spiral-laminated stator cores.

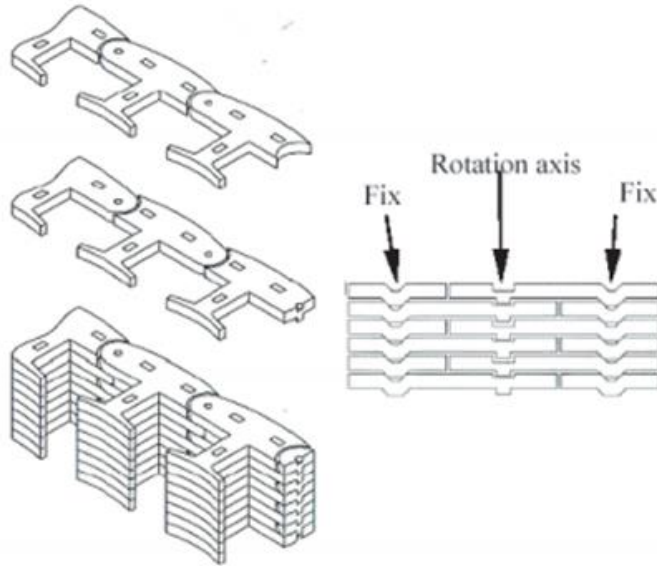


Fig. 2.13. Akita's model of a joint-lapped core [81].



Fig. 2.14. Mecrow's segmented lamination for easy insertion of pre-wound coils [82]



Fig. 2.15. Part of stator yoke, pre-pressed coil, and tooth in SMC from Jack [83].

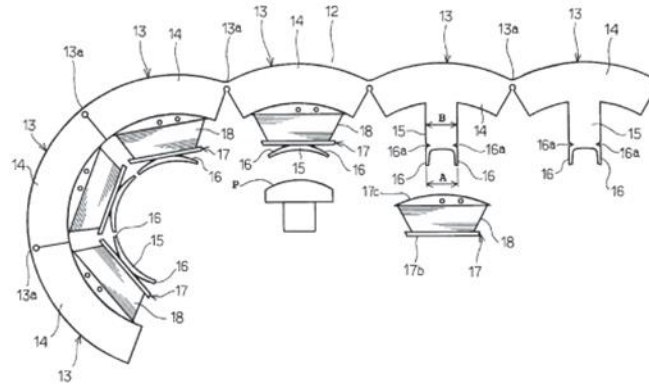


Fig. 2.16. Examples of stator with special tooth tips [84].

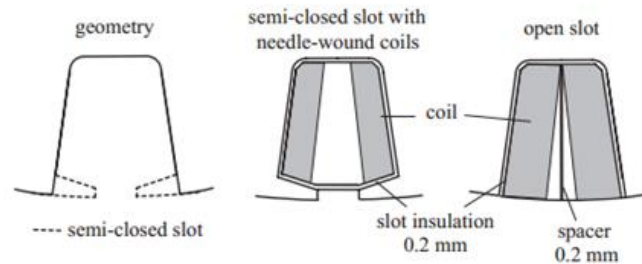


Fig. 2.17. Comparison of the coils with a semi-closed and open slot [85].

2.5.3 Stator Windings Manufacturing

Windings can be classified into stator windings and rotor windings based on the winding positions on the machine. From the perspective of manufacturing process, windings can be single-wrap winding, multiple-wrap winding, distributed winding, concentrated winding, etc. Although winding wires have their own insulations, insulation paper or other insulation materials are overspread in the slots or between the winding layers to isolate electrical transfer. Slot wedges are also used as the insulation part. In application, insulation is the most vulnerable part and fails very often. Some machine maintenance companies can heat the stator with failed insulation and take out the windings then insert the new insulation layers and then rewind the windings. Both concentrated and distributed windings can be automatically wound and inserted to the stator slots. Fig. 2.18 shows how a concentrated winding machine winds on each tooth for an open stator lamination. While Fig. 2.19 shows a complete stator for an external rotor SPM machine for a washing

machine application. For this application, machine power density is less of criteria than fully automated manufacture as car is witnessed by the relatively poor slot packing factor required for slot needle winding tool as shown in Fig. 2.20.

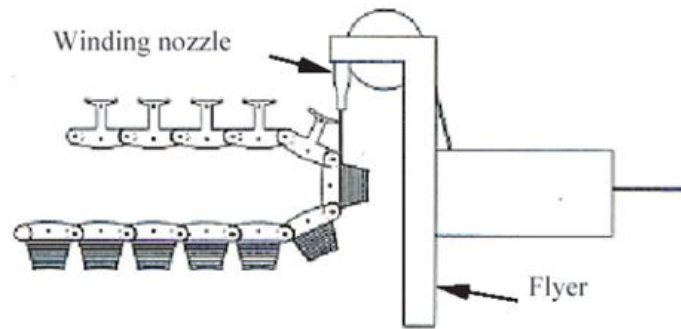


Fig. 2.18. Winding the coils of a joint-lapped core from Akita [81].

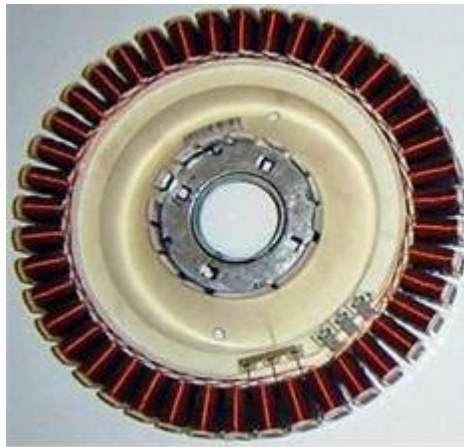


Fig. 2.19. Interior stator machine with concentrated winding [86].



Fig. 2.20. Two needle-wound coils of the outer-rotor prototype motor [78].

2.5.4 Magnet Manufacturing

Powder metallurgy and melt-spinning are two major techniques to produce permanent magnets. The anisotropic, fully dense magnets are manufactured through powder metallurgy while isotropic bonded magnets are obtained by melt-spinning. Magnets fabricated by these two conventional methods have the same elements distribution. However, due to the skin effect, the eddy current only appears on the surface of the magnets. Grain boundary magnets, which have different rare earth metal element distribution, are introduced to lower the cost. Only the four surfaces perpendicular to the magnetization direction needed to diffuse the rare-earth elements, like Dy atoms. Nevertheless, the grain boundary diffusion process costs more than the powder metallurgy and melt-spinning. It is also a trade-off between the reduction of rare-earth element (Dy) and the grain boundary diffusion process cost.

In spite of only one tenth of the weight in the motor, magnets play an important role in permanent magnet machines. The cost of magnet usually increases to one third of the whole motor. The decrease of magnet material, especially the rare earth element can obviously help reduce the motor cost. In addition, the fabrication of magnets also leads to the change of magnet performance. For instance, the excessive end of the magnet is usually grinded to keep the magnet and rotor in same length. However, the grinding process will damage the coating and change the permeability of the magnet. Some grain-boundary magnets are manufactured to a certain length so that the grinding process can be waived.

Sintered rare earth magnets, NdFeB and SmCo, have very uncontrolled structures once processed, as illustrated by the microstructure pictures captured at McMaster University for a typical NdFeB sample in Fig. 2.21. This uncontrolled structure requires some level of surface treatment (coating) or banding in SPM designs to guarantee mechanical integrity, as discussed in Chapter 4.

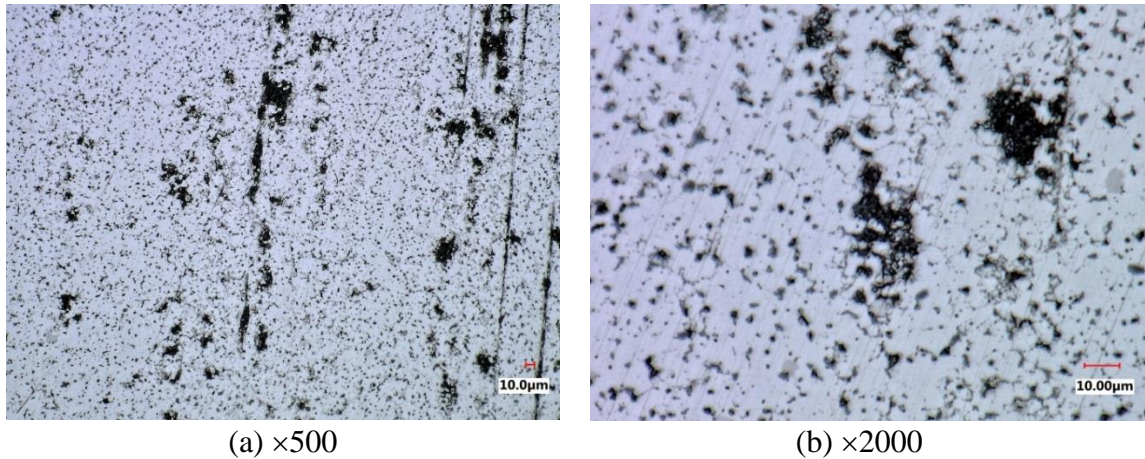


Fig. 2.21. Microstructure of sintered permanent magnet material.

2.5.5 System Cost Analysis for Traction Machine

The manufacturing cost of an electric machine is a synthesis of production volume, design requirement, manufacturing type and equipment, labor cost and machine hourly cost. The assessment of the cost structure for electric machine is an estimation of the main cost part which is prepared for present electric machine cost mathematically in the optimization model.

Despite the cost uncertainty of rare-earth materials in recent years, brushless permanent magnet (PM) machines are still a favored candidate technology for electric vehicle traction machines. Many papers have considered designs for traction applications, with the interior permanent magnet (IPM) topology gaining preference to date, while surface magnet (SPM) topologies seem less favorable [19, 87, 88]. Further, there has been much published on the choice of machine stator topology in terms of distributed versus concentrated winding implementations [19, 37].

The subsequent Chapter will consider various machine designs referenced to an industrial benchmark. Although no direct cost calculations are made, costs can be inferred by considering the various component volumes and mass.

2.6 Summary

This Chapter discusses the fundamentals of electrified vehicle BLPM traction machines in terms of modeling, design and manufacturing, provides the basis of Chapters 3 to 5, defining parameter choice, slot and pole combinations, rotor topologies, winding types and how they influence the performance and manufacturing process of the machine. The Nissan Leaf IPM machine is taken as a benchmark machine design in Chapter 3 where the specifications are studied and presented.

Chapter 3

Benchmark Machine Studies

3.1 Introduction

Much data is already published on the 2011 Nissan Leaf IPM traction machine [89-96], a distributed winding, IPM topology. Hence this machine is used as a reference benchmark against which a number of machine variations are compared. The various machine designs are compared at a number of key operating points on the Nissan Leaf IPM machine traction torque-speed characteristic and data presented for performance indicators. The study is used to inform on the design and production options faced by the industry when considering the manufacturing of high volume components. The manufacturability of the proposed designs will also be discussed in this thesis.

The benchmark machine is analyzed and the FEA model is created based on the published information. Meanwhile, the consistence between FEA results and published test data also validate the simulation results and additional measured back-EMF and phase current data supplied by Dr. Tim Burress of Oakridge Labs.

3.2 Overview of Nissan Leaf Machine

The specification and efficiency map of Nissan Leaf Machine are shown in Table. 3.1 and Fig. 3.1 respectively. The dimensions of the machine are obtained from the Oakridge reports [91], as well as slot/pole number, number of turns per coil, number of strands per hand, torque, efficiency information and system DC link voltage. The materials for stator, rotor iron, and permanent magnet, are applied to make sure the Nissan Leaf machine

model can match the published performance information. Many trial and error simulations have been undertaken to build a FEA model in commercial software that can satisfy all the published performance data within 5% error.

Based on the torque-speed information of the Nissan Leaf machine, four representative points are selected to capture the key features of the torque-speed specification, referring to 3.1, the first coordinate point is 0rpm, 280Nm, which shows the maximum torque at low speed region. The second coordinate point is 2100rpm, 280Nm, which is the maximum speed point to achieve maximum torque. The position of the third coordinate point is 3000rpm, 254.65Nm, at which the specified nameplate power of 80kW maximum is reached. The fourth coordinate point is 10000rpm, 76.4Nm, 80kW, which is the top speed point requiring torque at maximum speed. Following the motor efficiency map, the inverter efficiency map and combined inverter and motor efficiency map are shown in Fig. 3.2 and Fig. 3.3 respectively. We can see that the combined inverter and motor can acquire 90% efficiency and above in a large operation region.

Fig. 3.4 shows some Nissan Leaf machine thermal test runs from which it is observed that the machine is capable of operating at 80kW continuously at 7,000 rpm with stator temperatures leveling out at about 135°C. When the stator temperature is stable at 135°C, the rotor temperature reaches 120°C conservatively. So 120°C is chosen to be the operation temperature in the magnetic performance simulation for all the machines in this thesis without specific demonstration.

The Nissan Leaf machine design adopts a full pitched integer slot, single layer, distributed winding with two neutral points joined via an interconnecting link. The detail winding connection is sketched according to the winding information and DC link voltage. For this three phase machine, there are 8 coils per phase and three possible connections, (i) 8 coils that are all serially connected, (ii) every 4 coils are serially connected to form a group and then the two groups are connected parallel, and (iii) every 2 coils are serially connected to form a group and the four groups are parallel connected. Combining the simulation results for each possible connection and the maximum 375V DC link voltage, it is deduced that the winding in the Nissan Leaf machine is connected every 2 coils in series and then the 4 branches connected in parallel to form each phase.

The winding connection for 48 slots is shown in Fig. 3.5 and the connection for 8 coils in each phase is shown in Fig. 3.6.

Table 3.1. Details of 2012 Nissan Leaf machine [89-96].

Description	Nissan Leaf IPM machine
Outer diameter of stator (mm)	200
Inner diameter of stator (mm)	131
Stack length of stator (mm)	151
Number of slot	48
Winding type	Full pitch single layer distributed winding
No. of turns per coil	8
No. of strands per turn	15
Diameter of copper wire (mm)	0.812
Outer diameter of rotor (mm)	130
Inner diameter of rotor (mm)	45
Active axial length (mm)	151
No. of poles	8
Large magnet dimensions (mm)	3.79 (DOM) × 28.85 × 8.36*
Small magnet dimensions (mm)	2.29 (DOM) × 21.3 × 8.34*
Total magnet mass (kg)	1.8954
Pole arc/pole pitch ratio	0.9765
Skew angle (degrees mech.)	3.75
Performance	
Top speed	10,000 RPM
DC-link voltage	375 V
Stator excitation	Three-phase AC
Peak phase current amplitude (A)	625A

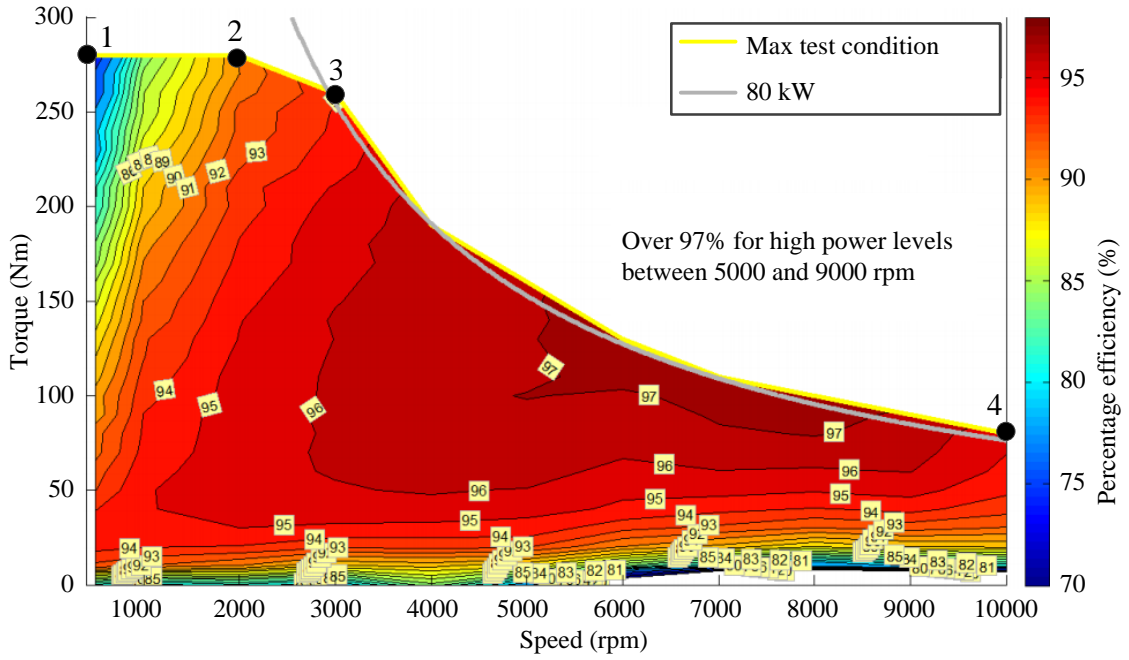


Fig. 3.1. Efficiency map of 2012 Nissan Leaf Machine [91].

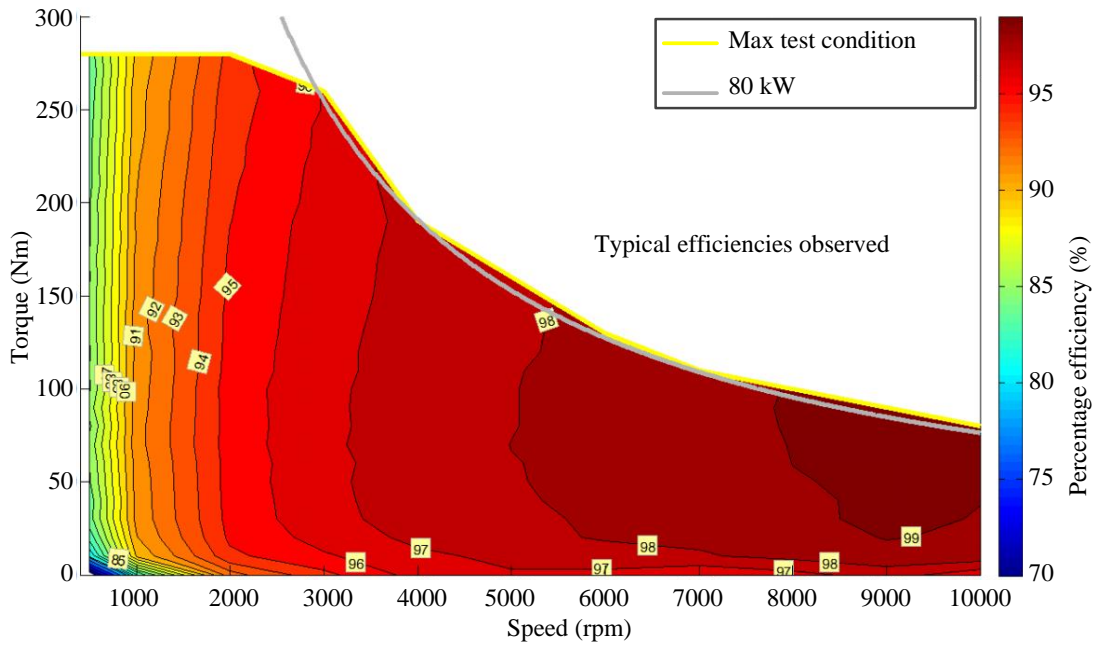


Fig. 3.2. Inverter efficiency map [91].

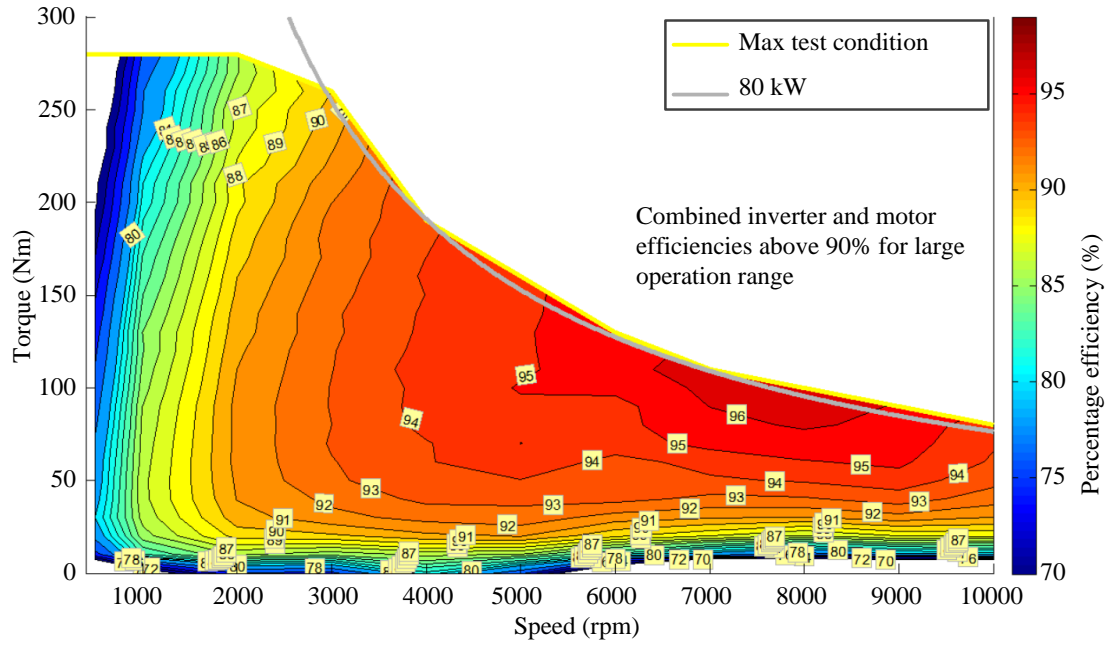


Fig. 3.3. Combined inverter and motor efficiency map [91].

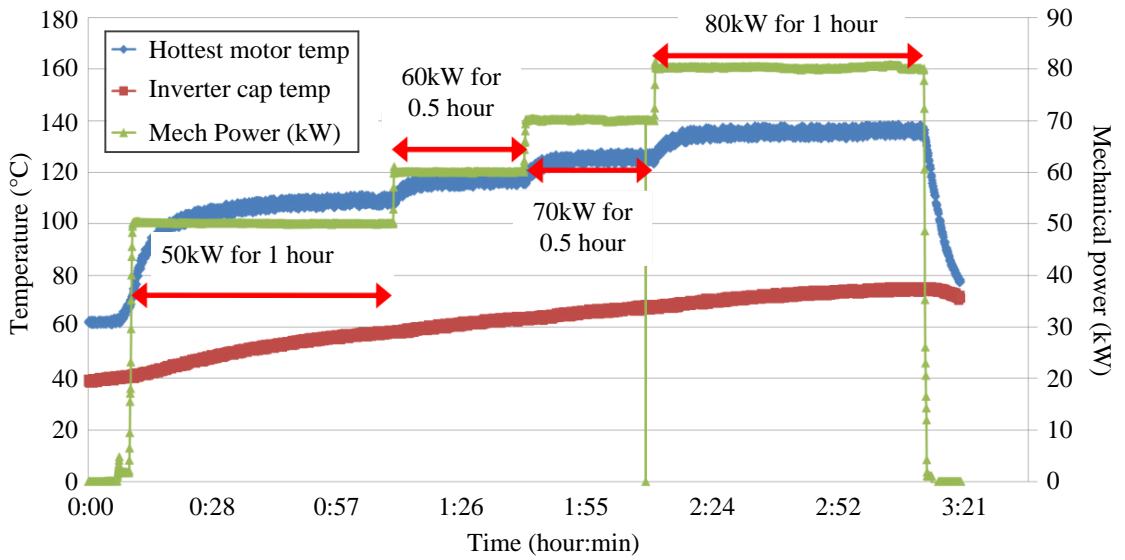


Fig. 3.4. Continuous test results [91].

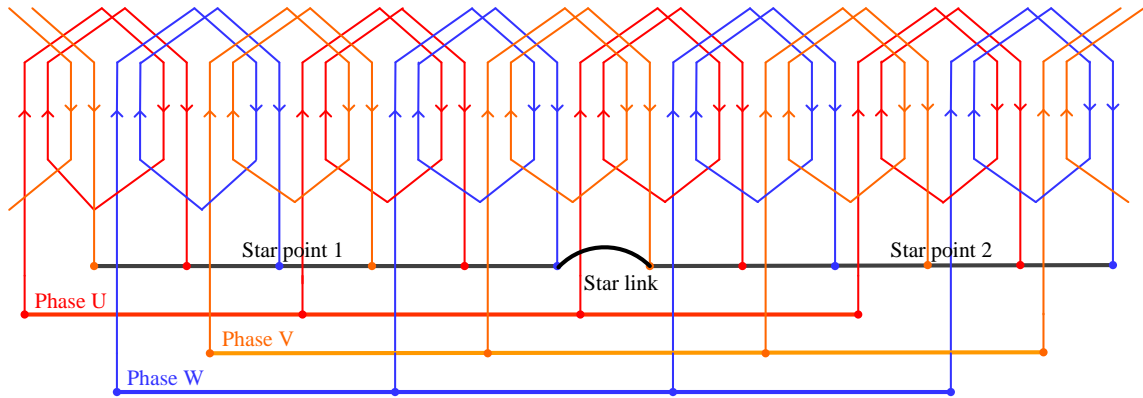


Fig. 3.5. Winding connection of Nissan Leaf Machine.

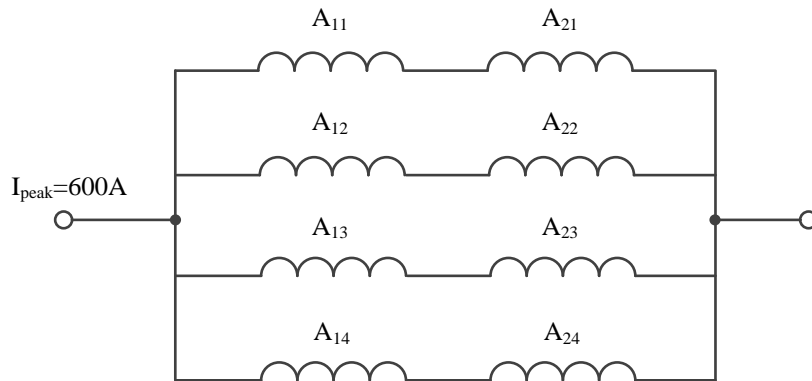


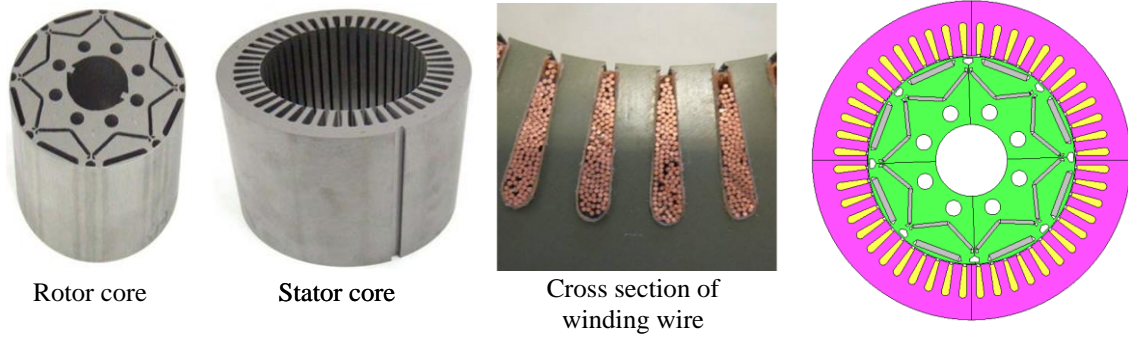
Fig. 3.6. Coil connection of 2011 Nissan Leaf Machine.

3.3 Nissan Leaf Machine FEA Model Creation

The mechanical model of the Nissan Leaf machine is created in the commercial FEA software JMAG on the basis of published structure data. Fig. 3.7 shows the Nissan Leaf rotor, stator, cross section of winding wire and the 2D model created in JMAG. Due to the repetitive characteristics, one quarter model, i.e. 1 pole-pair, is sufficient for the numerical calculation with acceptable accuracy and consecutive magnetic flux lines. Although one eighth, 1 pole, model consumes less time than the pole-pair model, the inconsistency of magnetic flux lines happens occasionally on the antiperiodic boundary. Fig. 3.8 shows an example of the magnetic flux line distribution in one eighth and one quarter model highlighting the antiperiodic boundary inconsistency of the model. This is not a software problem, but due to asymmetry in the solution at same rotor positions and under some (but not all) excitation conditions.

After the model, materials are a key issue for the FEA model. In addition, there is no specific material name and characteristics for the iron and permanent magnet. So the materials need to be decided according to the published performance.

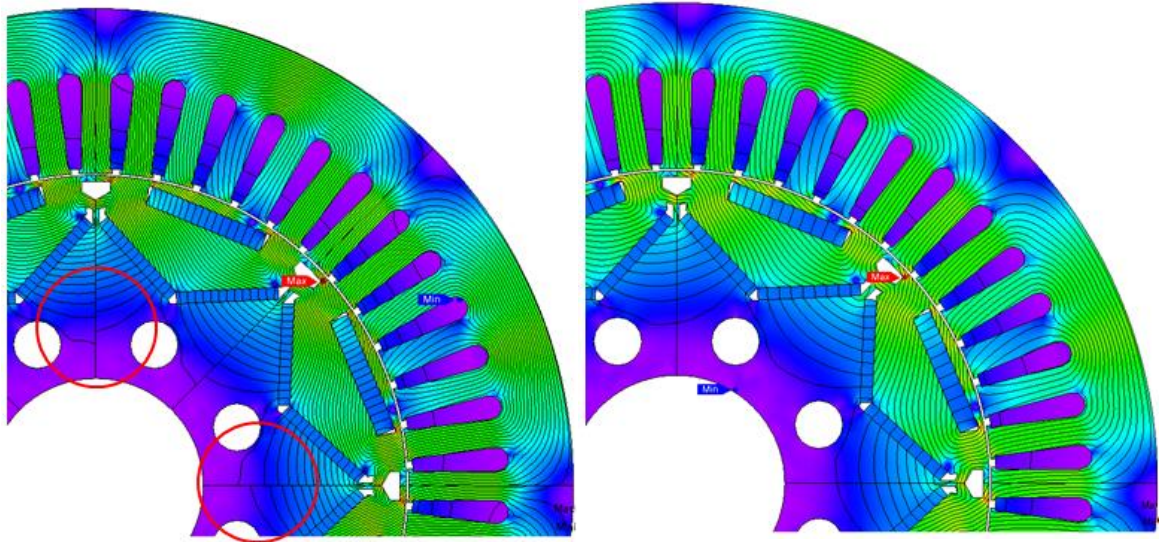
The permanent magnet material is selected based on the back-EMF information. Several permanent magnet materials are tried to tie up with the back-EMF at 10,000rpm due to the linear relationship between rotation speeds and back-EMF. For instance, N40UH, N48H, N36Z. Fig. 3.9 shows the back-EMF of 2011 Nissan Leaf machine with N28AH in different temperatures at 10,000rpm. The temperature coefficients of induction is $-0.120\%/^{\circ}\text{C}$ and of coercivity is $-0.393\%/^{\circ}\text{C}$. The back-EMF also decreases linearly when the temperature rises. So the N28AH is selected to be the permanent magnet material and the error is within 5% compared to the test back-EMF at 10,000rpm and 20°C , which is 198V_{rms} . This error is acceptable since there is also inevitable experimental error during test. Besides, the demagnetization characteristics need to be considered as well so that the magnets would not be demagnetized during the whole working region.



(a) Structure of Nissan Leaf machine [89]

(b) 2D model in JMAG

Fig. 3.7. Nissan Leaf machine and its 2D model in JMAG.



(a) 1/8 model

(b) 1/4 model

Fig. 3.8. Flux lines distribution in 1/8 and 1/4 model under same operation condition.

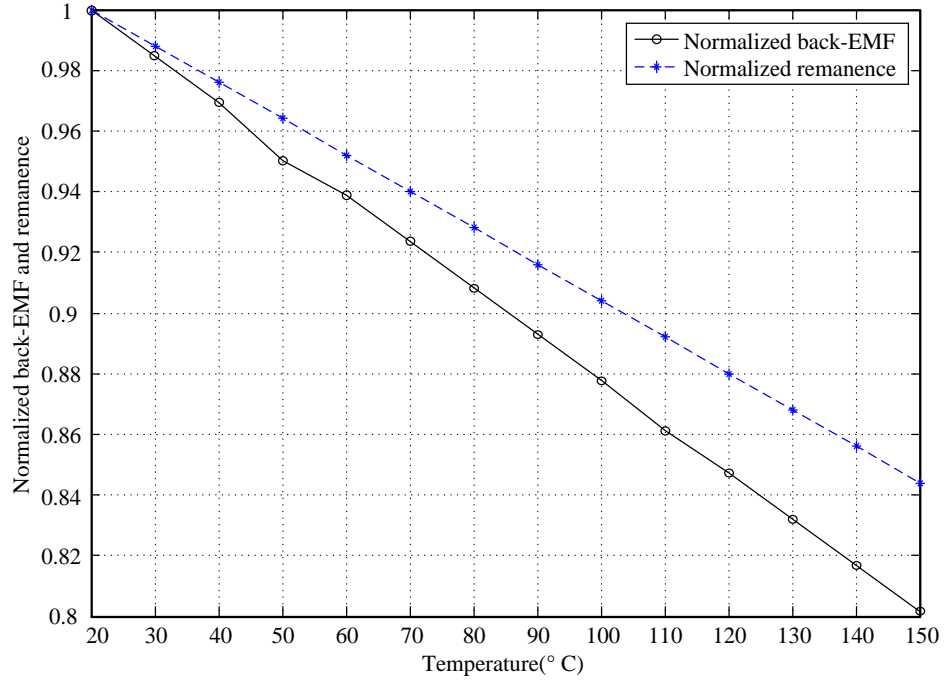


Fig. 3.9. Normalized back-EMF and remanence of N28AH in different temperatures at 10,000rpm.

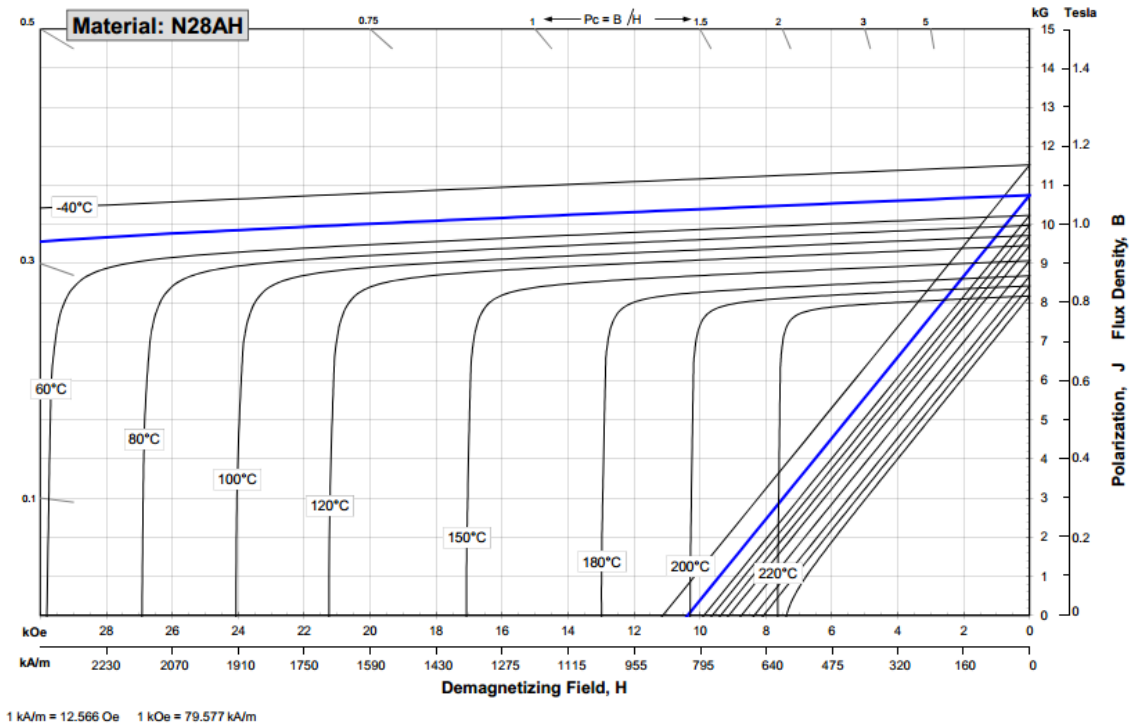


Fig. 3.10. Demagnetization curve of N28AH.

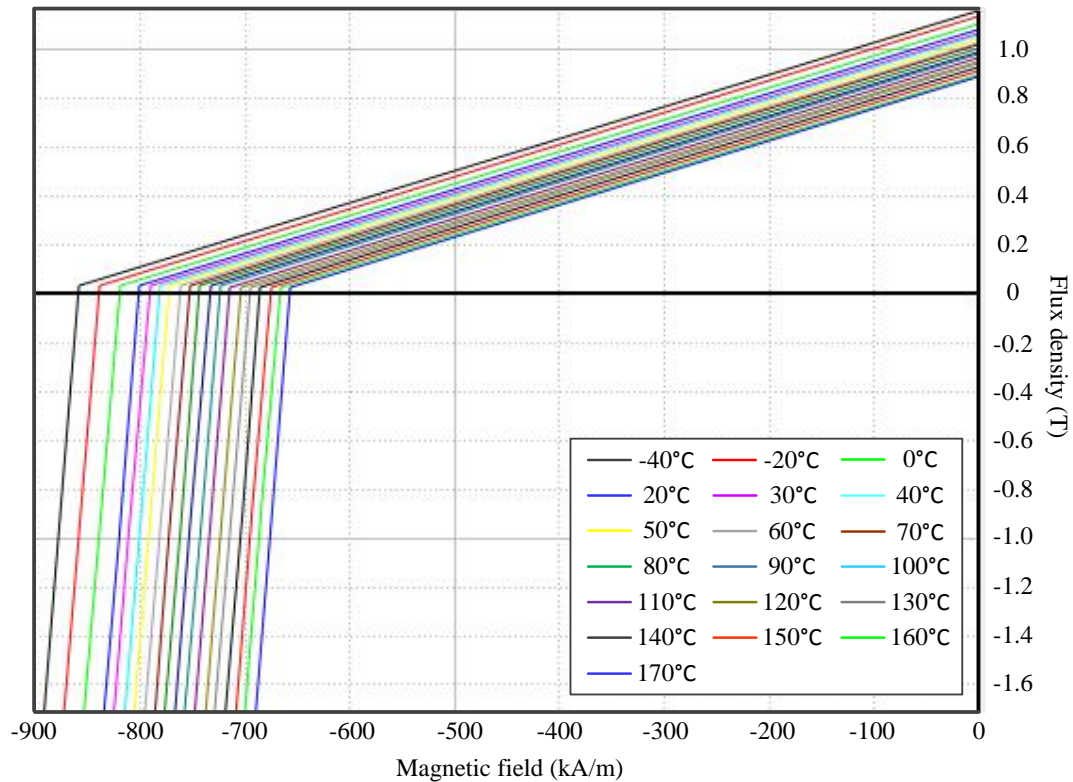


Fig. 3.11. Demagnetization curve of N28AH as defined in JMAG.

The demagnetization curve of N28AH is shown in Fig. 3.10 [97] and the JMAG self-defined demagnetization curves at different temperatures of N28AH are shown in Fig. 3.11. As mentioned before, the operation temperature for Nissan Leaf machine is set as 120°C and the maximum temperature is 170°C.

The 35JNE250 silicon steel is utilized to the stator and rotor iron to achieve low iron loss and high torque due to its low loss and high permeability feature. All the electrical, magnetic, mechanical, and loss information are included in the JMAG material library and can be applied to FEA simulation directly. Besides, the coating information is not included in the FEA simulation process and there is only one copper material in JMAG. The electric circuit and coils connections are built in FEA model based on Fig. 3.6. In this thesis, the sinusoidal current excitation is applied to all the permanent magnet machines.

To complete the FEA model, the phase resistance needs to be calculated. The copper wire in the specification in Nissan leaf is quoted as ~20AWG having an outer diameter of 0.812mm. However, using this figure yields an incorrect value for calculated resistance

and copper mass when compared to quote values. However, according to the technique data from P.A.R. (Insulations & Wires) Ltd [98], an outer wire diameter of 0.816mm yield a copper wire diameter of 0.71mm for grade 3 insulation. With this value of copper diameter, the calculated phase resistance and total copper mass agree with the Oakridge published data to within 0.4% and 9.69% error respectively. Each winding coil has 15 strands and comprises of 8 turns per coil. So the copper area per slot is:

$$A_{copper} = \frac{\pi}{4} \times 0.71^2 \times 15 \times 8 = 47.510 \text{ (mm}^2\text{)} \quad (3.1)$$

The slot area in the stator model is $A_{slot} = 77.377 \text{ (mm}^2\text{)}$. So the fill factor of the Nissan leaf motor is:

$$k_f = \frac{A_{copper}}{A_{slot}} = 61.401\% \quad (3.2)$$

This fill factor will be utilized to calculate the phase resistance of all the following distributed winding machine design candidates. Suppose the copper wire of distributed winding wire was wound like a half circle in the end winding part, as shown in Fig. 3.12.

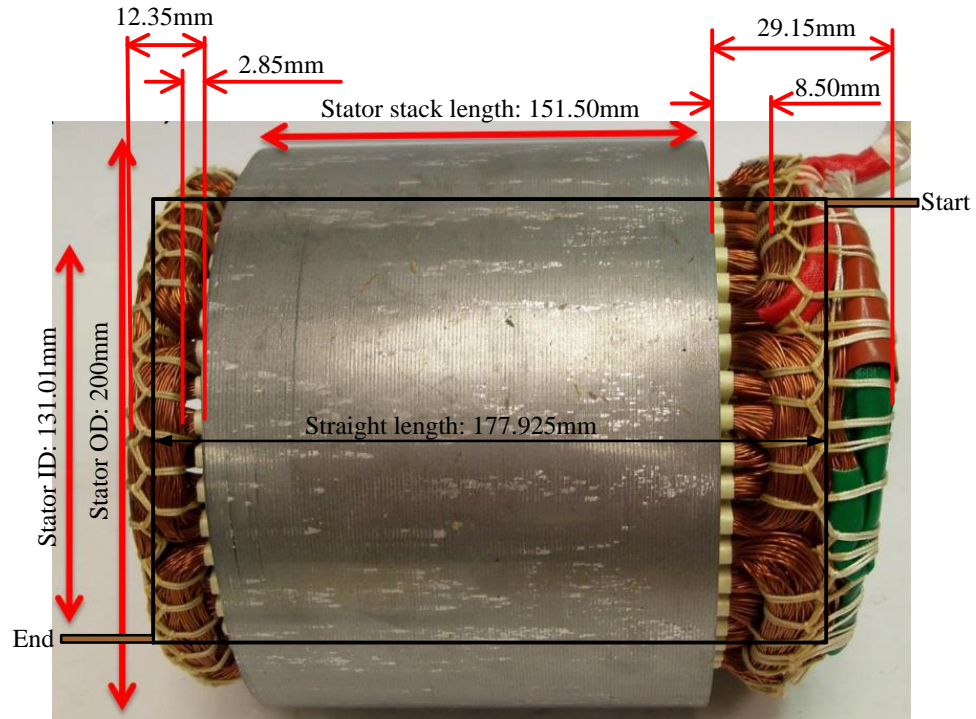
In this case, the coil distance is:

$$d_{coil} = 76.738 \times (44.132 / 180) \times \pi = 59.107 \text{ mm} \quad (3.3)$$

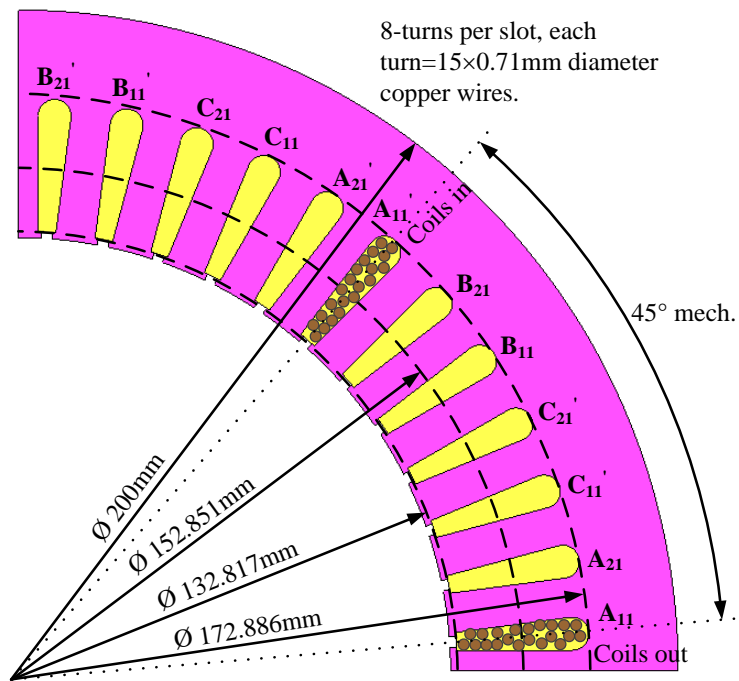
The density of the copper in JMAG is 8960 kg/m^3 . So the copper mass of the Nissan Leaf is 5.12kg. There is only 9.69% difference with the copper mass, 5.616kg, in the Oakridge report [93].

The resistivity of copper in JMAG is $1.673 \times 10^{-8} \text{ ohm}\cdot\text{m}$. So the resistance of the winding in the 20°C is 5.668 mohm , which is just 0.4% difference with the measured phase resistance 5.67 mohm in Oakridge report [93].

As shown in Fig. 3.4, the stator temperature in the normal operation condition is 135°C. Considering the $0.00393 \text{ mohm}/^\circ\text{C}$ temperature coefficient, the phase resistance at 135°C is 8.21 mohm .



(a) Dimensions from Oakridge report [91].



(b) Inter connection between two slots.

Fig. 3.12. Estimated winding length of 2011 Nissan Leaf Machine.

3.4 Validation of Nissan Leaf Machine FEA Model

(a) Validation of locked rotor test

To verify the FEA model, first the DC phase current excitation results are compared with the locked rotor test results published by Oakridge report. In Fig. 3.13, the black line shows the torque variation along one electric cycle at 615A peak phase current and it match well with the locked rotor test when the peak phase current is 625A. Even though there is a slight difference for the peak phase current amplitude between FEA and real test, the difference is within 5% error region. Besides the locked rotor test results comparison, the back-EMF, and excitation current amplitude for the whole speed region are further validated.

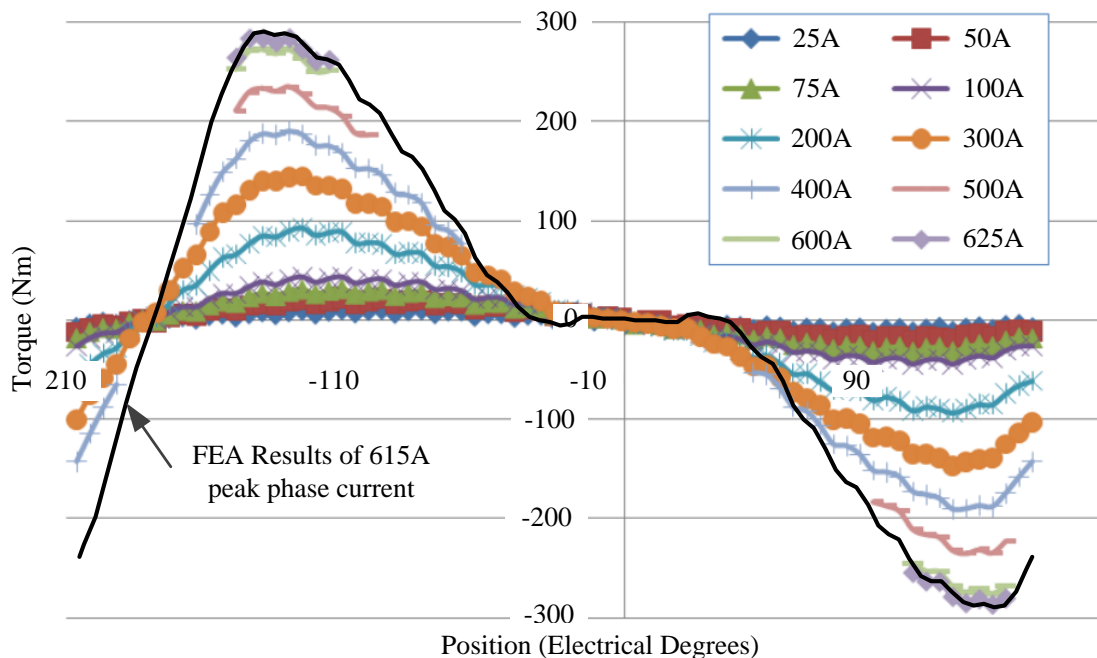


Fig. 3.13. Locked rotor test results and simulation results.

(b) Validation of back-EMF

The back-EMF comparison of Oakridge group test and simulation results at 20°C from 0rpm up to 10,000rpm is shown in Fig. 3.14. The simulation results are close to the test results in each point. Although the back-EMF slope of simulation results is a little smaller

than the test, the biggest gap between test result and simulation is 5.47V and within the 5% test error. So the back-EMF validates the FEA model of Nissan Leaf machine.

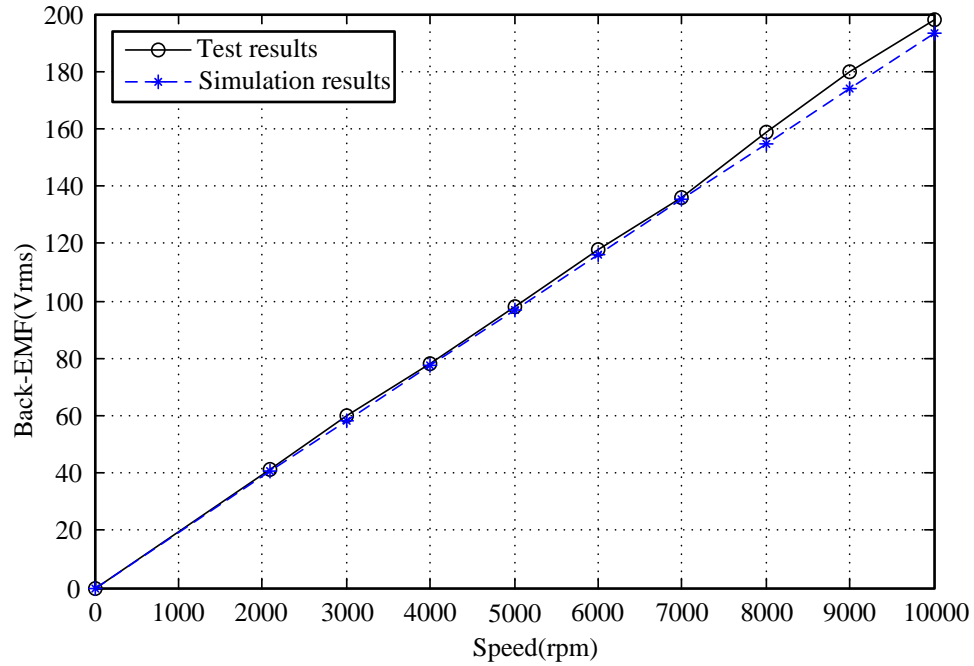


Fig. 3.14. Nissan Leaf machine back-EMF comparison between test data and FEA results at 20°C.

(c) Validation of excitation current for whole speed region

The excitation current for torque requirement at each speed has been tested by Oakridge and the comparison between the test data and simulation are shown in Table 3.2 and Fig. 3.15. The phase excitation current in simulation is very close to the test result and shows the accuracy of the FEA model of Nissan Leaf machine is within 5% error range.

Table 3.2. Comparison of phase current between Nissan Leaf machine test results and FEA simulation.

Speed (rpm)	2100	3000	4000	5000	6000	7000	8000	9000	10000
Phase current(I_{peak}) of test	640	599	425	363	297	238	242	247	253
Phase current(I_{peak}) of FEA simulation	615	600	425	365	300	245	250	250	251

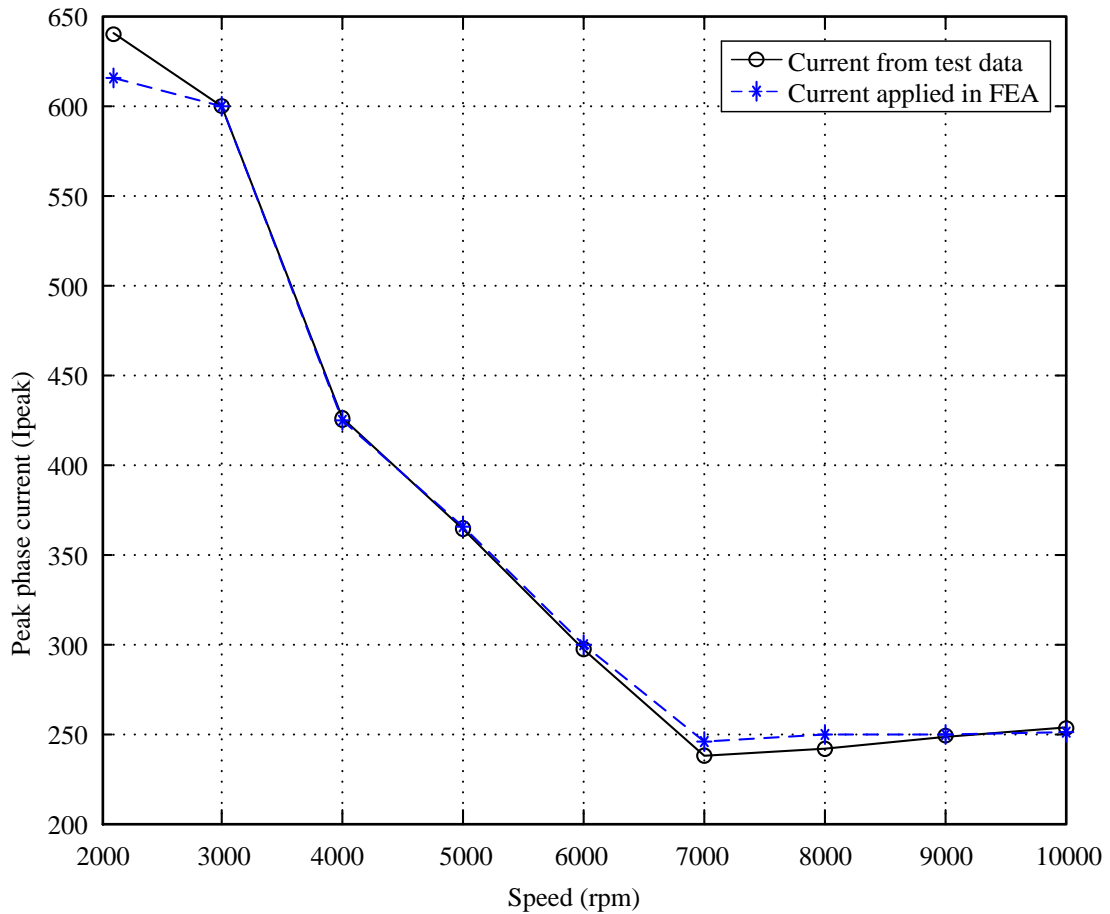


Fig. 3.15. Peak phase current comparison between test data and FEA simulation.

3.5 Assessment Criteria

To assess the Nissan Leaf machine and the following new designs, some criteria are proposed based on the characteristics of traction machines and listed below:

(a) Torque, power, speed.

In this case, the torque-speed and power-speed envelope is shown in Fig. 3.16. The maximum torque at low speed is 280Nm and the maximum speed is 10,000 rpm. The torque at maximum speed is 76.40Nm. The maximum power is 80kW.

(b) Cogging torque.

Cogging torque is the torque produced in the no load condition and the peak to peak value (maximum to minimum) is used to evaluate it as shown in Fig. 3.17. Since cogging torque is a key component of torque ripple, it is usually desired to minimize by design. During all the speed range, the amplitude or waveform shape of the cogging torque does not change but the frequency varies depending on the rotation speed.

(c) Excitation torque ripple.

Excitation torque ripple is defined as the difference between maximum torque and minimum torque divide the average torque. Excitation torque ripple is an important index to access the quality of the torque and usually presented by the percentage form. In addition, there is a close relationship between torque ripple and noise and vibration. So the torque ripple reduction is a popular topic in machine design area and several effective methods have been applied, for example, add skew angles on rotor, stator or both, appropriate slot/pole combination [99-101]. Traction machines often have a torque ripple requirement for a certain speed or speed range due to the variation in different operation conditions. In this thesis, the excitation torque ripple of Nissan Leaf model is set as one design target of the SPM machine distributed and concentrated winding machines.

(d) Thermal performance.

Thermal limits are the most important issue for a machine design and needs to be considered for both rotor and stator sides. Overheated machines may suffer rotor

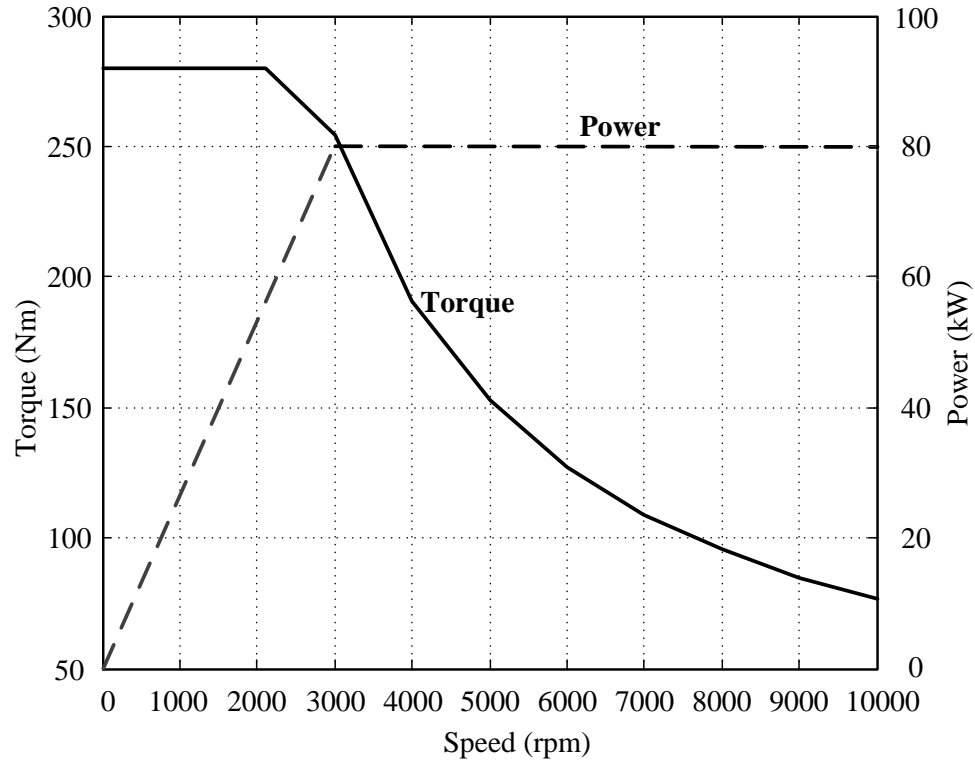


Fig. 3.16. Torque, power, and speed specification of Nissan Leaf machine.

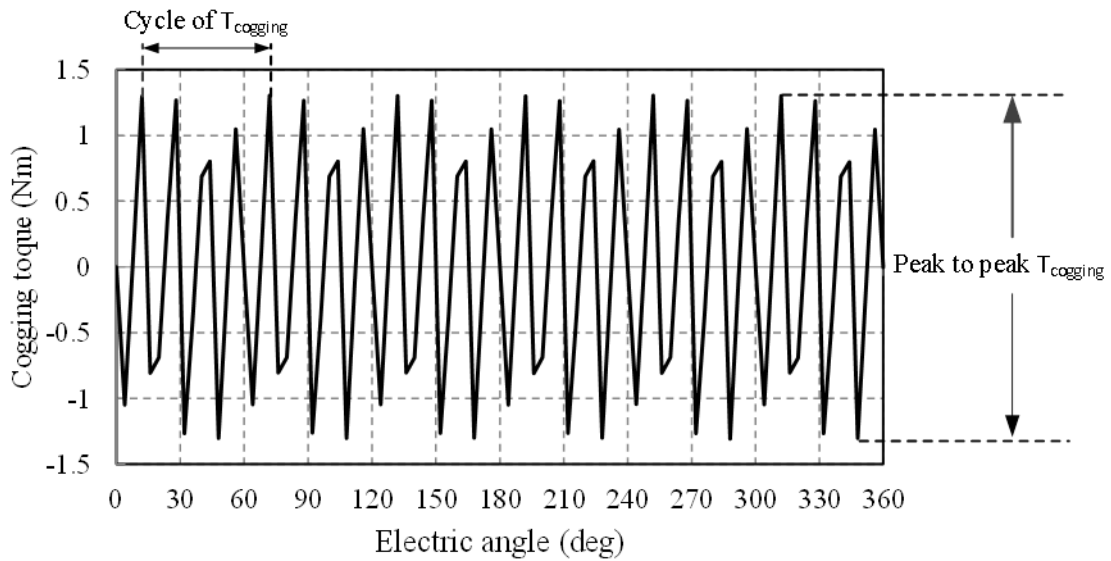


Fig. 3.17. Cogging torque waveform.

performance decrease and even damaged the machine. At the design stage, all kinds of loss needs to be evaluated carefully to make sure the elevated temperature is in requirement and the proper insulation materials has to be selected according to the power rating and loss disputation. In this thesis, the loss in rotor and stator iron and copper loss are the main comparative parts. The mechanical loss is roughly evaluated by an empirical formula and just related to the rotation speed. However, the temperature is kept constant in each FEA simulation.

(e) Voltage and current levels.

The voltage and current levels of electric machines determines the specification of power electronics as well as the machine performance. In constant torque range, the current levels limit the maximum torque and the iron loss, copper loss. In constant power range, the voltage levels limit the torque and excitation current. In this thesis, the voltage and current levels of Nissan Leaf machine is set up as a benchmark and other designs' voltage and current levels cannot exceed the benchmark.

(f) Demagnetization.

Demagnetization is the phenomenon that the permanent magnet loses its permanence permanently during operation. The demagnetizing ratio is used in FEA simulation to quantitatively analyze the demagnetization level and defined as the amount of demagnetization from the standard specified magnetization as given by Equation. (3.4) [102].

$$\text{Demagnetization ratio (\%)} = 100 \cdot \left(1 - \frac{B_2}{B_1} \right) \quad (3.4)$$

where B_1 is the residual magnetic flux density of the specified step and B_2 is the residual magnetic flux density of the step that is displayed.

The demagnetization ratio just reflects the demagnetization condition in one element in FEA. To make sure no element in magnet experiences it, the demagnetization ratio needs to be confirmed to 0 for every magnet element. In experimental test, the torque does not

increase linearly when current increase in certain operation temperature, then the demagnetization happens and the turning point is the boundary.

(g) Mechanical strength.

The mechanical stress on rotor is a normal issue for high speed machines. The maximum stress on rotor outer surface needs to be less than the material's yield stress to avoid the mechanical damage and meanwhile the deformation also needs to be verified not affecting the air-gap flux density distribution or even over through the air gap. In addition, the safety factor of 2 and 20% over speed is introduced during the mechanical analysis when considering fatigue and worst scenario in real case. In this thesis, the mechanical strength also applied to sleeve design for SPM rotor.

(h) Mass.

Mass of the traction machines is not only an important component of cost, but also the weight consumes energy when the EVs' driving. To gain high torque and power density with low cost, several design adjustments are implemented on rotor and stator sides in this thesis.

(i) Volume.

Volume is the whole space a machine occupies. Usually the outer diameter (OD) of housing, active stack length and the end winding length define the volume. In this thesis, the OD of stator, active stack length and the end turn length are considered synthetically to evaluate the machine volume since all the designs have the same power rating and there is only a subtle difference in housing.

(j) Manufacturability and cost issues.

The manufacturability is important for the industry application and volume commercialization. Since the Nissan Leaf machine has been volume produced, the manufacturability evaluation for the all the designs in this thesis are based on both volume production and laboratory prototypes. Besides, both the material cost and manufacturing cost are compared to study the cost issues.

3.6 Design Parameter Studies

DC-link voltage and temperature variations are critical issues when designing an electric vehicle traction system. For BLPM machines, ambient temperature variation impacts on the performance of the rotor PM material and hence machine operation [103, 104], a feature that should be considered at the PM traction machine design stage. The Nissan Leaf machine is evaluated and performance assessed by considering DC-link voltage and temperature variations in this part. Moreover, the high back-EMF also needs to be paid attention to in case the power electronic damage during loss of power to the inverter above base speed.

3.6.1 DC-Link Voltage

When the DC-link is directly connected to the battery, the DC-link voltage varies during the loading cycles due to the state-of-charge (SoC) and internal impedance voltage drop of the battery [105]. This voltage variation impacts on the performance capability of the traction machine and also impacts on the inverter voltage and current. This variation in DC-link voltage limits the machine controllable region (considering minimum battery terminal voltage) or excessive regenerating current (considering maximum equivalent machine voltage). In addition, the magnitude of DC-link voltage determines the voltage and current ratings for the power converter devices and the traction machine. Adding SCs in parallel with the battery is one way to improve the DC-link voltage transient variation; however the voltage still drops with battery discharging. Implementing a bidirectional DC/DC converter between the battery and DC-link to maintain voltage stability ensures best utilization of the traction machine and power converter, as will be discussed here.

While electric vehicle power-trains have been discussed extensively, the impact of maintaining a fixed DC-link supply to the vehicle traction system has not been assessed in terms of the traction machine and associated power electronic inverter specification requirements. Authors in [106, 107] discussed the traction machine torque control methods and field-weakening strategies by considering DC-link voltage variation. To reduce the DC-link voltage variation and hence extend the vehicle range, the combination

of battery pack and SCs are studied in [108]. Additionally, the benefits of adding a DC/DC converter have been reported. Firstly, with the DC/DC converter, the battery pack and traction machine can be designed independently [109]. Then, it is claimed that the implementation of a DC/DC converter improves the machine torque ripple and increases the system efficiency at low speeds and partial load, although additional converter losses are leading to advantages for the system without DC/DC converter at high speed operation [110-112]. Moreover, in the Toyota Hybrid System II (THS II), the DC/DC converter can boost the system voltage and increase the electrical power input of the inverter for the same current level which, combined with the machine rotor optimization, results in a higher machine power output than the last generation of THS [113, 114]. The boost converter also enables to reduce the number of battery modules connected in series [115] although the impact on reduced battery energy is not made clear. The impact of temperature variation on permanent magnet materials is reported in [103, 104]. However, there is no available study in EV traction system design based on the impact of DC-link voltage and ambient temperature variations.

According to [116], the model predictions for Nissan Leaf EV driving range and battery energy consumption rate show good agreement with the Argonne experimental tests for US06 driving cycle. In addition, the battery terminal voltage variation or DC-link voltage variation over repetitive US06 driving cycles is illustrated in Fig. 3.18. The corresponding battery current is shown in Fig. 3.19. For this case, the DC-link voltage follows the battery open-circuit voltage versus SoC variation, as shown in Fig. 3.20, with additional voltage variation due to the battery internal impedance voltage drop. It can be noticed that as the vehicle range increases, the vehicle DC-link voltage reduces due to SoC from 403V to 240V.

According to Fig. 3.18, there is an about 40% DC-link voltage reduction due to battery cumulative discharge and vehicle acceleration (battery regulation), which will impact on the traction system performance. The Nissan Leaf benchmark IPM machine is modeled by FEA software and the FEA model is validated by comparing the simulation results with the Oakridge test results presented earlier in Chapter 3.4, measured at a fixed DC-link voltage of 375V, as illustrated in Fig. 3.20. The IPM machine is capable to develop a

torque-speed envelope approaching the measured data with the same DC-link supply. Thus, the FEA analysis tool is applied with confidence to investigate the machine performance under the issues related to DC-link voltage variation and temperature extremes and validate the machine design consideration.

According to Fig. 3.21, the FEA simulation indicates that when the IPM machine operates at the minimum DC-link voltage, i.e. 240V, its field weakening capability is limited. By adjusting the phase current magnitude, it is still not capable to satisfy the specification in terms of torque and power requirements. Especially during the machine top speed operation at 10000 rpm, the torque can only reach 40% of the required value.

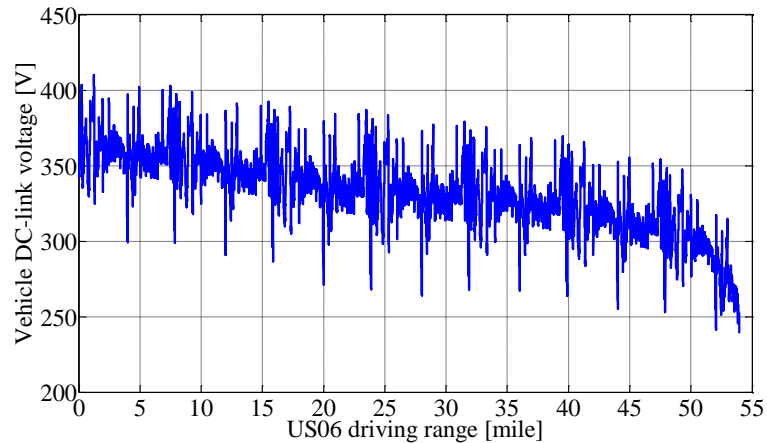


Fig. 3.18. DC-link voltage of the Nissan Leaf electric vehicle.

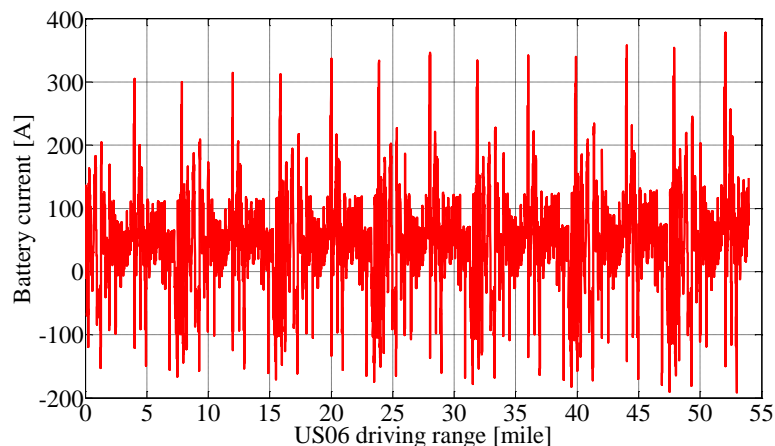


Fig. 3.19. Battery current of the Nissan Leaf electric vehicle.

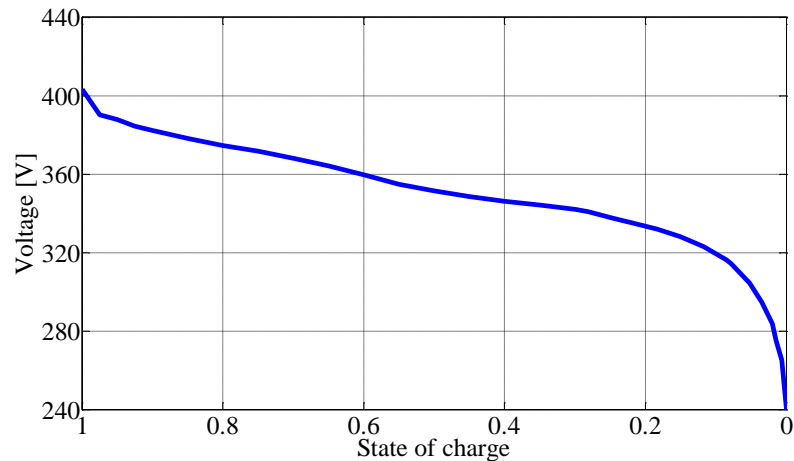


Fig. 3.20. Open circuit EMF of lithium-ion battery.

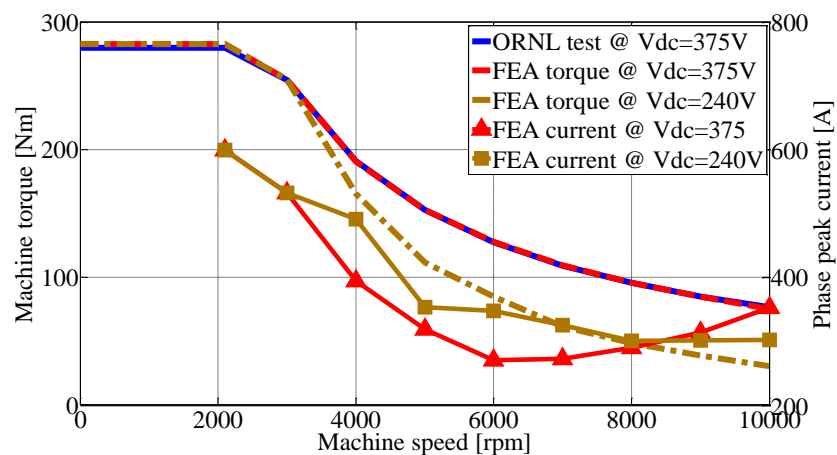


Fig. 3.21. Nissan Leaf machine FEA and ORNL test results at a fixed DC-link voltage of 375V.

3.6.2 Temperature

In order to analyze the Nissan Leaf brushless IPM machine and assess the main design parameters impacting on the machine field-weakening capability, a linear electromagnetic model of the machine, coupled with a numerical direct search algorithm, is developed. This model is implemented in a classical linear d-q two axis approach, as discussed in Chapter 2 and Equations. (2.21) and (2.27):

$$T_e = 3p \left(k_o I_s \cos \gamma + \frac{L_q - L_d}{2} I_s^2 \sin 2\gamma \right) \quad (2.21)$$

The machine torque consists of two items, i.e. excitation torque due to the permanent magnets and reluctance torque. For both IPM and SPM machines, k_o and I_s mainly impact on the electro-magnetic torque performance. In the field-weakening region, the current excitation angle is increased towards 90 degrees. If the phase resistance is neglected, the machine maximum achievable speed is given by:

$$\omega_{r(\max)} = \frac{V_s}{p |k_o - L_d I_s|} \quad (2.27)$$

It can be noticed that if the machine k_o equals to product of L_d and I_s , the maximum achievable speed is theoretically infinite. According to the FEA results, the benchmark IPM machine has been designed to make k_o approach the product of L_d and I_s to achieve wide constant power range. Generally, due to DC-link voltage reduction, the machine will require larger phase current to maintain the 80 kW constant power output in the field-weakening region. However, increasing phase current enlarges the difference between k_o and the product of L_d and I_s , resulting in a further fall-off in high speed torque.

Temperature variation is another issue impacting on the traction machine performance. According to the B-H characteristics analysis of typical PM materials [105, 106], magnet remnant flux density for a sintered NdFeB grade, Br, varies by typically 0.12% per degree C, which directly relates to variation of k_o . According to Equations. (2.21) and (2.27), lower magnet temperature boosts the machine low speed torque. However, a high value of k_o may impact on the machine field-weakening capability, which then requires some necessary adjustment (increase) of phase current magnitude, as detailed in Table 3.3 for the benchmark IPM and the SPM design detailed in Chapter 4 with 12 turns per phase (12t) and a variant with 8 turns per phase (8t). The design process and detail of the 12 and 8-turn SPM machines will be discussed in Chapter 4.

All of the Oakridge data is presented at a fixed DC link voltage of 375VDC, similarly with published data from other sources. No publications assess machine performance at minimum or maximum DC link voltage or with regard to typical automotive temperature variations. Clearly from the results of Fig 3.21 and Table 3.3, these are important issues

that are more pronounced at the high operating speeds of the traction torque-speed specification requirement and suggest the necessity of an intermediate DC-DC converter between the battery and system voltage source inverter – a feature that is missing in the Nissan Leaf powertrain.

Table 3.3. Machine peak phase current (A) requirements at 2100rpm and 10,000rpm for voltage and temperature extremes.

	2100RPM		10000RPM	
	375V	240V	375V	240V
IPM (-40°C)	535	535	393	*
IPM (+120°C)	600	600	354	303*
SPM-12t (-40°C)	390	390	481	600*
SPM-12t (+120°C)	480	480	392	500*
SPM-8t (-40°C)	590	590	435	747
SPM-8t (+120°C)	720	720	335	600

*Cannot realise torque specification

3.6.3 High Back-EMF Precaution

In the benchmark powertrain system, the traction motor inverter converts DC power from the Li-ion battery to AC power, and drives the traction motor. Traction motor inverter drives traction motor accurately with the motor controller installed inside the traction motor inverter. The motor controller receives the rotor rotation angle from the traction motor resolver and the traction motor current value from the current sensor, and creates the pulse signal for driving the Insulated Gate Bipolar Transistor (IGBT). During deceleration, the traction motor inverter drives the traction motor to function as a generator based on the regenerative torque command signal, converting the vehicle kinetic energy into electrical energy to charge the battery. At the same time, the regenerative torque can be used as braking force.

However, the fault behavior of inverter may cause serious consequence to the powertrain system. If IGBTs malfunction or the controller breaks down, the inverter will turn to an uncontrollable rectifier. In this case, if the vehicle operates at high speed, the traction machine will potentially generate high magnitude back-EMF which will be rectified to be

high magnitude DC voltage. Once the DC voltage magnitude is higher than the battery terminal voltage, the regenerative energy will feed back to the system without control. The worst case occurs when the machine is running at the maximum speed and battery voltage is dropped to its minimum. As an example, Fig. 3.22 shows the battery transient current when the battery voltage is 240V and the 8-turn SPM is rotating at 10,000 RPM with magnet temperature of +120°C. It can be observed that once the failure occurs, the positive DC-link current is immediately changed to large negative value, which will be worse if the machine operates at lower temperature. Although mechanical relays are installed in the system, it is difficult for them to immediately switch off during the full load condition. In this circumstance, the vehicle starts to operate with uncontrollable braking, which could lead to safety issues. In addition, the large transient current would result in further damage to the power-train system in terms of battery, DC-link capacitor and traction inverter. Therefore, installing PE switches or a DC/DC converter between the battery and DC-link would be necessary to avoid system uncertainty caused by the inverter failure issue, as illustrated in Figure 3.23.

3.7 Summary

In this Chapter, a brushless permanent magnet machine having an IPM rotor topology is studied and a model developed based on the Nissan Leaf IPM traction machine. The model results are compared with published data from a series of Oakridge National Laboratories reports and additional test data provided by Dr. Tim Burress of Oakridge Labs. The model and published data are found to be in good agreement and hence the FEA model and simulation tool can be taken forward with confidence to predict machine design variations in Chapters 4, 5 and 6.

The impact of DC link voltage and temperature variations commensurate with automotive applications is studied and shown to have a major impact on the realizable traction characteristic of a machine design based on a fixed DC link voltage and operating temperature. These considerations are not explored further in this thesis but recommended as an area of future research in Chapter 7.

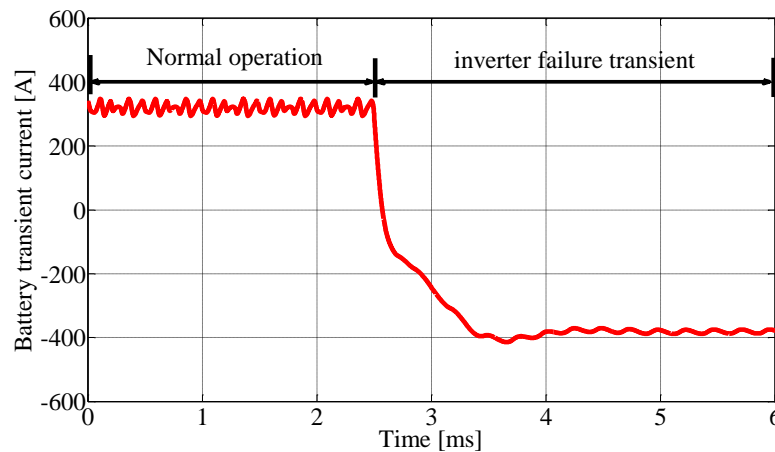
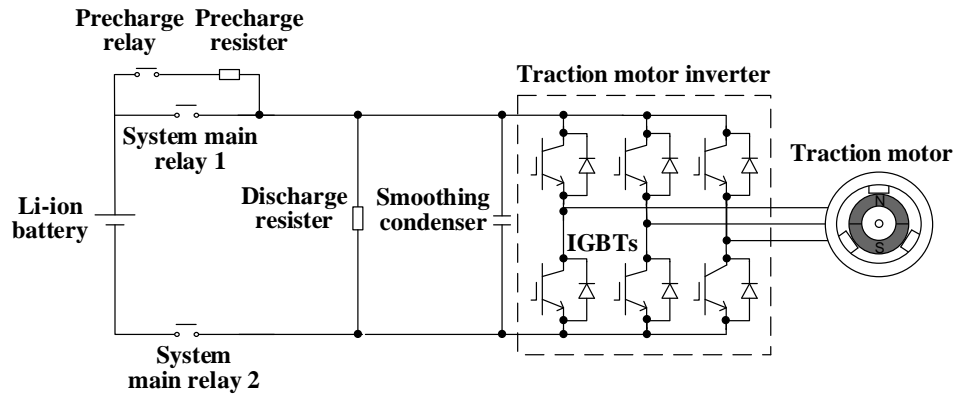
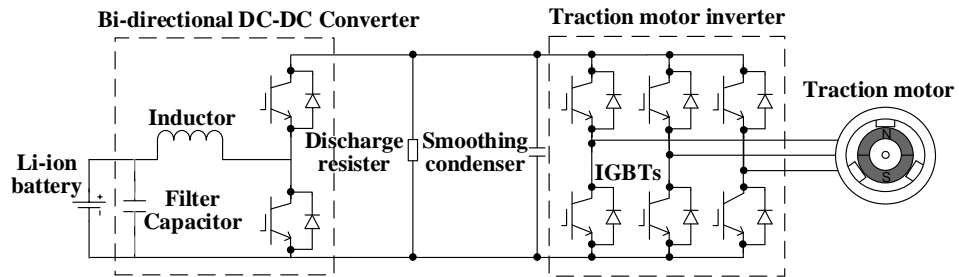


Fig.3.22. DC-link current during fault.



(a) Nissan Leaf power-train system diagram [116].



(b) Nissan Leaf powertrain system with DC/DC converter.

Fig. 3.23. Nissan Leaf powertrain system without and with DC/DC converter.

Chapter 4

Rotor Design for Volume Manufacturing

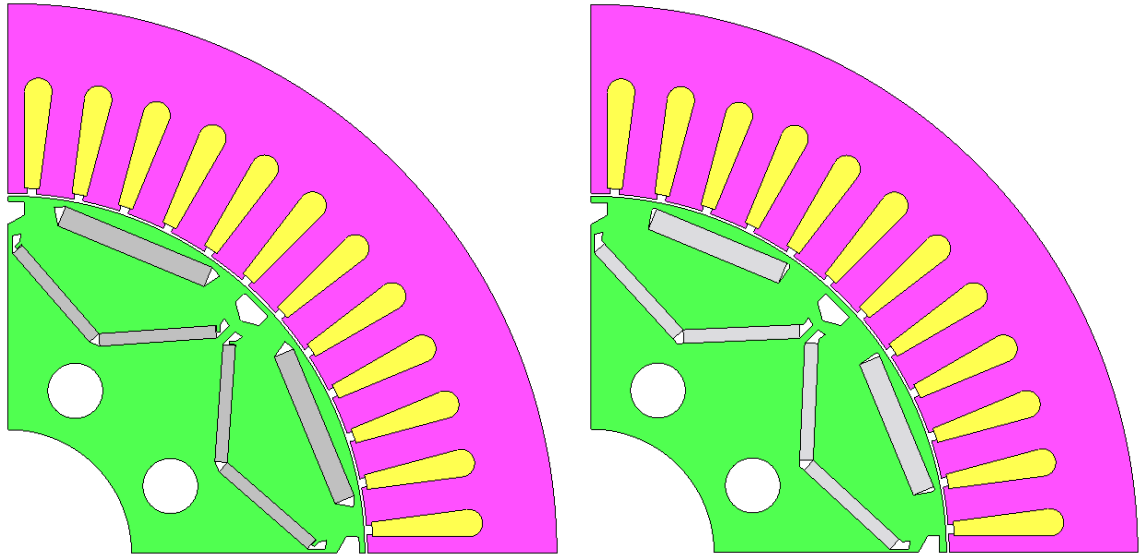
4.1 Introduction

In this Chapter, an overview of different rotor topologies and power electronics interface for traction machine applications is presented to propose new rotor topologies with high performance and low power electronics requirement for the EV's applications. Both permanent magnet (PM) machines and zero permanent magnet machines, for instance, synchronous machines, are designed and compared based on Nissan Leaf benchmark machine described in Chapter 3. The new grain boundary permanent magnet material is also investigated to improve machine performance.

4.2 Comparative Study of Modified and Original Benchmark Machine

As mentioned in Chapter 3, the over modulation control in high speed region stimulate the excitation torque ripple for Nissan Leaf machine. So a new IPM rotor is proposed to obtain the whole torque-speed curve without over modulation based on the Nissan Leaf machine IPM rotor. The modified machine utilizes the same stator, similar amount of permanent magnet material with slightly different magnet size, and simplified flux barrier. The 2D geometries of two machines are listed in Fig. 4.1 and the difference in magnet size and weight is listed in Table 4.1. The slight change in magnet size and position results in a considerable improvement in performance.

Although no over modulation, that is the constant peak phase voltage limit for the field weakening region, the modified design can meet the torque-speed profile and the power-speed profile published in the Oakridge report and shown in Fig. 4.2 and Fig. 4.3.



(a) Nissan Leaf IPM machine (b) Modified design based on Nissan Leaf
Fig. 4.1. Geometry comparison of Nissan Leaf machine and the modified one.

Table 4.1. Magnet comparison of Nissan Leaf IPM and the Modified Design.

Description	Nissan Leaf IPM machine	Modified design
Large magnet dimensions (mm)	3.79 (DOM)×28.85×8.36*	4.00 (DOM)×25.77×8.36*
Small magnet dimensions (mm)	2.29 (DOM)×21.30×8.34*	2.50 (DOM)×21.30×8.34*
The V-shape angle (deg)	127	130
Total magnet mass (kg)	1.962	1.988

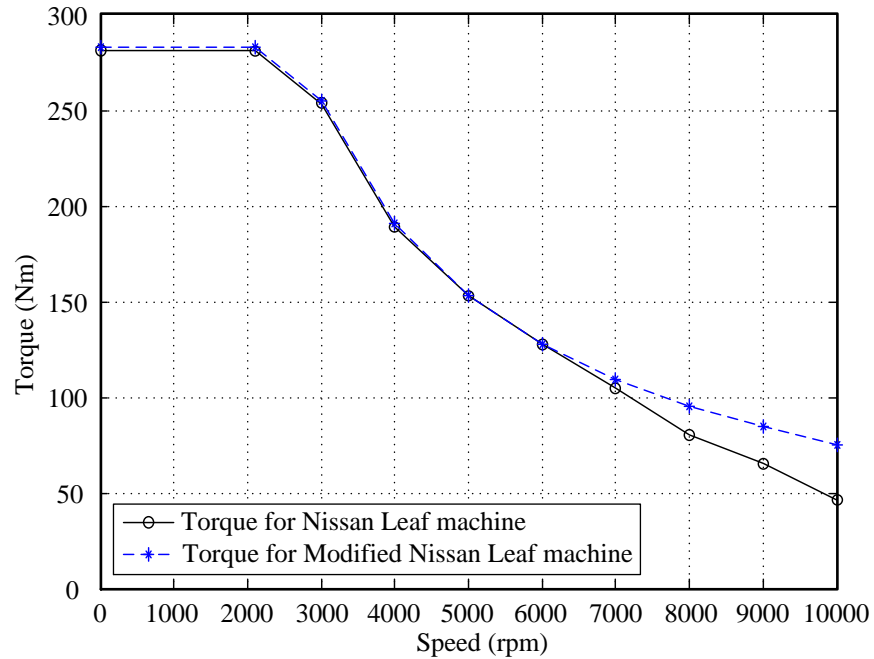


Fig. 4.2. Torque performance comparison of Nissan Leaf machine and the modified one with sinusoidal phase current.

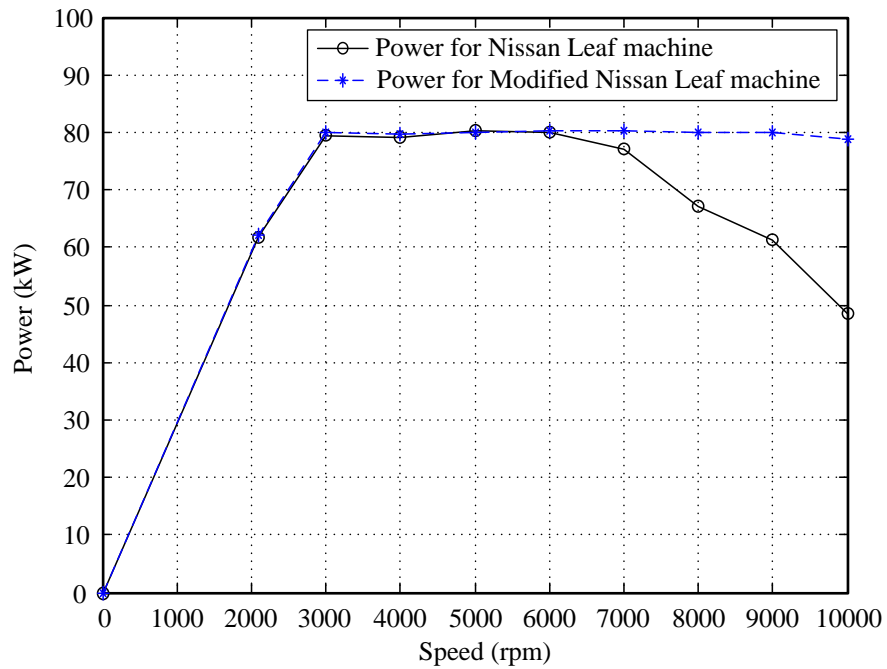


Fig. 4.3. Power performance comparison of Nissan Leaf machine and the modified one with sinusoidal phase current.

4.3 Comparative Study of PM Traction Machine Topologies for EV's

Interior permanent magnet (IPM) synchronous machines are popular in commercial hybrid- or all-electric vehicles (HEVs/EVs), such as the Toyota Prius, GM Chevy Volt, Lexus LS, Nissan Leaf, for example. This section presents the findings of a comparative study assessing the design and performance attributes of IPM machines when compared to other design options. The Nissan Leaf IPM traction machine has been widely analyzed and there is much public domain data for the machine. Hence, this machine is chosen as a representative benchmark design against which other permanent magnet (PM) machine topologies are assessed. Much is claimed of IPM topologies in terms of their saliency torque contribution, minimum magnet mass, demagnetization withstand, wide flux-weakening capability and high operational efficiencies. These attributes are assessed and compared for surface mounted permanent magnet machines (SPMs) for both distributed and concentrated stator winding designs. The study illustrates and concludes that both the IPM and SPM topologies have very similar capabilities with only subtle differences between the design options, subtleties that may be exploited when considering the traction application requirements, for example, predominant low, medium or high speed operations.

IPM machines appear to be the favored topology choice for electric vehicle traction machine applications because of their saliency torque contribution, minimum magnet mass, demagnetization withstand, wide flux-weakening capability and high operational efficiencies [15-17]. Due to the same inductance on the direct- and quadrature-axes, there is essentially no reluctance torque generated by SPM machines, although they can operate in a flux-weakening mode if appropriately designed [18-19]. Both rotor topologies have been explored with distributed and concentrated stator windings [17-19] with various justifications for either implementation. However, to-date, no paper has directly identified and justified the technical aspects of the various design choices. This research aims to address this via a comparative study of different machine implementation topologies, a subsequent qualification of design rules and finally quantified results from analysis underpinned via experimental test data published in [17].

Jahns et al [19] designed IPM and SPM machines with fractional-slot concentrated windings (FSCW) against the same vehicle traction specification, same slot-pole combination and same materials, presenting results in terms of flux weakening capability, overload capability, efficiency, loss, demagnetization, etc. However, the airgap and active axial lengths were varied, diluting the comparison. The results show that the IPM machine design needed slightly less permanent magnet material but required a higher phase current with similar machine torque and efficiencies over the whole speed range. Pellegrino et al [20] compared an IPM and SPM machine, but with different winding configurations and airgap diameter. Chlebosz and Ombach [118] studied the demagnetization properties of IPM and SPM traction machines and concluded that SPM machines required permanent magnets with higher coercivity or demagnetization withstand. However, the compared machines had different pole numbers, magnet material and geometries; hence the conclusions cannot be deemed general.

Although studies have compared the two rotor topology options for brushless PM machines, the compared designs always tend to have varied machine parameters, making a quantifiable comparison difficult, if somewhat arbitrary, and closely linked to the personal preference of the machine designer. To-date, no paper has directly identified and justified the technical aspects of the two rotor topologies. This study aims to address this deficiency via the comparison of a published electric vehicle traction machine design having a distributed stator winding and an IPM or SPM rotor while maintaining the mechanical air-gap and stator lamination.

The Nissan Leaf IPM traction machine is chosen as a benchmark design since there is much published technical and experimental test data available to validate the machine analysis tools utilized in the study [90, 91]. Detailed finite element analysis (FEA) is performed on the Nissan Leaf machine design and computed data compared with published experimental test data [91] and shown to be in good agreement in Chapter 3. Thus, the FEA analysis tool and design procedure is applied to the SPM design with confidence in the final calculated predictions. The torque and extended speed capability of both machine topologies are explored and a SPM rotor design presented that

embellishes sensible and reasonable manufacturing rules commensurate with high volume manufacture of such machines.

4.3.1 SPM Rotor Design

This thesis will consider IPM and SPM rotors with distributed and concentric stator windings. In the part, a SPM machine with distributed winding is designed according to the specification of Nissan Leaf IPM machine and compared with it to study the difference in machine and how the difference affects the performance. To keep the comparatively as much as possible, the SPM rotor inherits the outer diameter, permanent magnet material, rotor iron material, and total magnet mass from Nissan Leaf IPM machine. The torque performance of radially (or sectioned fixed) magnetized SPM machine is mainly affected by the magnet topology and material properties, air gap length and key magnet dimensions. Those design parameters will be determined for the radially magnetized SPM rotor respectively.

During the design process, tons of iterations have been done to search the optimal rotor design with minimum magnet mass. The mechanical air-gap is the same with the Nissan Leaf machine and the thickness of rotor iron is 10% more of the distance between coil edge and stator back iron edge of Nissan Leaf stator. Fig. 4.4 shows the design process of the SPM rotor. The design parameters are initialized by the IPM machine and then the machine performance are estimated by the FEA within the current and voltage limit. If the performance cannot satisfied the IPM performance, the design parameters are adjusted until the torque and power specification is met. Then the mechanical stress is analyzed to check the mechanical strength. In this application, the velocity of the rotor surface at top speed is very high and the glue method cannot hold the magnet. So the sleeve is decided to be introduced for permanent magnet retainment. Both the material and thickness of sleeve need to be selected according to the mechanical and electrical performance. Generally, the thickness sleeve is minimized on the basis of mechanical requirement to obtain better electromagnetic performance. Indeed, the sleeve thickness increases the magnetic air-gap in the machine and all the design parameters have to be modified again.

The process and principles of the main design parameters are discussed in detail in the following section.

(a) Pole-arc to pole-pitch ratio

As a design example, Fig. 4.5(a) illustrates the relationship between the air-gap flux-density and magnet length, while Fig. 4.5(b) shows the relationship between peak cogging torque and magnet pole-arc to pole-pitch ratio, a parameter that plays a significant role in cogging torque and total torque ripple. Due to complex electromagnetic relationships, there is no explicit expression between cogging torque and pole-arc ratio. In the beginning, the pole-arc to pole-pitch ratio of Nissan Leaf machine is applied and the cogging torque is around 5Nm. However, the FEA simulation results of the SPM machine design based on the Nissan Leaf IPM major dimensions displays a minimum cogging torque at a pole-arc ratio of 0.85 (for this design), as shown in Fig. 4.5(b). The add-on sleeve does not affect the relationship between cogging torque and pole-arc to pole-pitch ratio, so the ratio of 0.85 is determined for the SPM rotor.

(b) Sleeve thickness

High speed machine is normally defined as when the peripheral velocity of the rotor is above 100m/s [119]. At 10,000RPM the SPM machine rotor peripheral velocity 68.07 m/s, which allows nearly 20% over speed, to the 100m/s limit, a typical industrial requirement. Since the SPM magnets are not contained within the rotor iron structure as with the IPM, the magnet or rotor tensile stress is a key design factor. Magnet companies do not usually quote the tensile strength of sintered permanent magnets since it cannot be guaranteed due to manufacturing inconsistencies in the material microstructure. Both the IPM and SPM rotors suffer from the tensile stress during high speed operation mainly caused by centrifugal force [120, 121]. For the IPM, the thin bridge of the rotor iron is the weakest point due to stress concentration. While the failure of the permanent magnet is the concern for SPM rotor designs. Hence, an air-gap sleeve is introduced to protect the permanent magnet in high speed region.

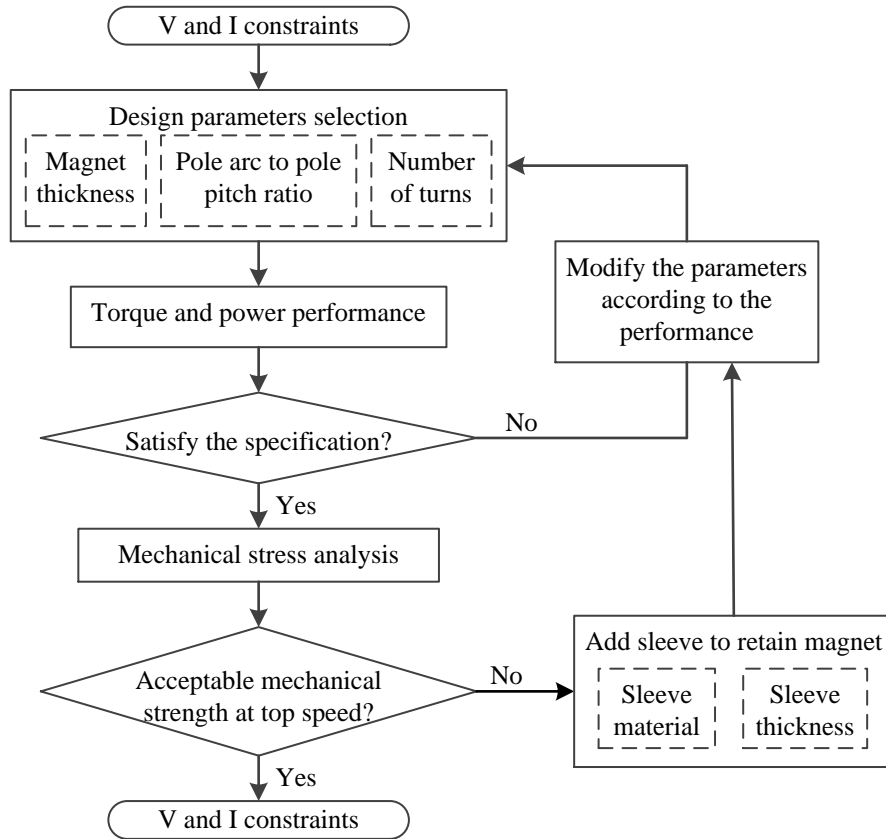
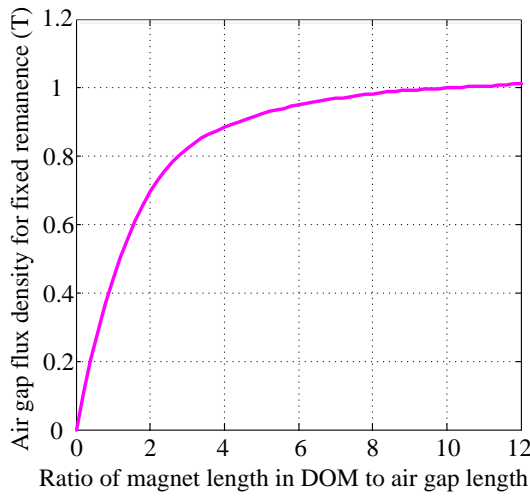
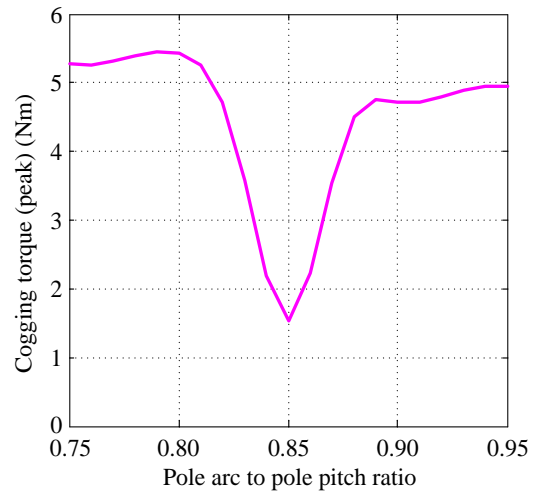


Fig. 4.4. Design process of SPM rotor.



(a) SPM Air-gap flux density versus ratio of magnet to air-gap lengths.



(b) Peak cogging torque versus pole-arc to pole-pitch ratio.

Fig. 4.5. Example SPM machine FEA design results.

Binder and Schneider also verified the bending failure of the SPM would happen if the filling material of the inter pole gap don't have similar mechanical properties to permanent magnets. The SPM rotor can be considered as a thick disk. Compared with the

hoop stress and radial stress generated by centrifugal force, the shear stress caused by the angular momentum is negligible. During design stage, the Von Mises Stress, which is an equivalent stress combining radial and tangential stress, is calculated and compared to yield stress or the strength in certain direction.

The sleeve is introduced to protect the permanent magnet in the SPM machine, especially in high speed region. The popular materials for the sleeves can be classified to non-conductive, low conductive, and conductive materials. The eddy current loss in the conductive sleeves needs to be considered, like high strength steel. The eddy current loss in the low conductive and non-conductive sleeve, for instance, carbon fiber and glass fiber, can be ignored. Table 4.2 shows the property of prevalent sleeve materials [107]. Compared with hardening stainless steel and high strength alloy, composite materials have higher tensile strength, which means thinner thickness of sleeve, lower eddy current loss, and poor heat dissipation performance. However, the maximum allowable stress of composite material is just 10% to 33% of the fiber's tensile strength due to the fabrication, air humidity, temperature rise, and fatigue failure. Besides, the tensile strength of carbon fiber is anisotropic in different direction and the strength is dependent on the temperature as shown in Table 4.3 and the mechanical property for iron rotor, permanent magnet and sleeve is shown in Table 4.4.

Based on the velocity of the SPM rotor and low requirement on thermal dissipation, carbon fibre is selected as the sleeve material for the SPM rotor. According to [109], the thickness and interference of between the sleeve and magnets need to satisfy the following conditions:

- (1) The Von Mises stress in sleeve under worst scenario cannot exceed maximum allowable stress of carbon fibre at 150°C, which is 1100 MPa.
- (2) The permanent magnets cannot in tension status and the tensile stress equals to compressive stress at 20% overspeed.
- (3) Both the parallel and perpendicular strength of carbon fibre need to be confirmed in the allowable stress at 150°C.

Table 4.2 Property of popular sleeve materials and the recommending ranges.

Materials	Density ρ (g/cm ³)	Tensile strength $\sigma_{t,max}$ (MPa)	Resistivity (Ωm)	Thermal conductivity K (W/(m.K))	Recommending velocity v_{max}
Glass fibre/ Kevlar fibre	1.44-2.54	2920-3447	$<4.0 \times 10^{12}$	<1.0	50-100
Hardening stainless steel	8.0	520-720	7.20×10^{-7}	16.2	75-125
Incenel 718 (GH4169)	8.2	1100	1.25×10^{-6}	11.4	100-200
High Strength Alloy	8.4	414-2200	9.86×10^{-7}	11.2	150-250
Carbon fibre	1.76	3500-6350	1.5×10^{-5}	5.0	100-500

Table 4.3 Property of carbon fiber.

Property	Circumferential direction	Radial direction
Young's Modulus	164 GPa	9.5 GPa
Maximum allowable stress at 20°C	2100 MPa	80 MPa
Maximum allowable stress at 150°C	1100 MPa	35 MPa

Table 4.4. The mechanical properties of the iron steel, permanent magnet and sleeve.

Description	Iron steel	Permanent magnet	Sleeve
Yield intensity/MPa	450	80	1070
Density (kg/m ³)	7650	7400	8240
Elastic module /GPa	200	150	187.5 (150°C)
Poisson ratio	0.30	0.24	0.28
Thermal expansion coefficient ($\times 10^{-6}/^{\circ}C$)	12	-4.6~-5.0 (Normal) 3.2~3.6 (Parallel)	13.25

In the high speed region, there are three main sources contributing to the stress in sleeve, which are centrifugal force, thermal expansion, and interference fit. Here, the centrifugal force not only includes the centrifugal force in sleeve itself, but also the magnet centrifugal force acting on the sleeve. After simplification, the rotor iron, permanent magnets and sleeve can be seen as a three layers concentric circle. The model and the force analysis is shown in Fig. 4.6.

The maximum centrifugal force on the sleeve appearing on the inner surface, which is:

$$\sigma_{t[\max]} = \frac{\rho\omega^2}{8} (R_1^2 + 7R_2^2) \quad (4.1)$$

where σ_t is the tensile force, ρ is the sleeve material density, ω is the rotation speed, R_1 is the inner diameter of the sleeve, R_2 is the outer diameter of the sleeve.

The tensile stress in sleeve produced by the centrifugal force by the magnet is:

$$\sigma_m = \frac{P}{R_2 - R_1} = \frac{\rho_m\omega^2}{3R_1(R_2 - R_1)} (R_1^3 - 7R_0^3) \quad (4.2)$$

where σ_m is the tensile stress along the sleeve thickness, R_0 is the outer diameter of the rotor.

The thermal stress generated by the temperature arise can be regarded as the tensile stress on the circumferential direction. Compared to the thermal expansion of sleeve, the one in rotor iron and magnet is very small. So the thermal stress in sleeve is:

$$\sigma_{\Delta T} = E \cdot \varepsilon_{\Delta T} = E \cdot \alpha \cdot \Delta T \quad (4.3)$$

where E is the Young's modulus, α is the thermal expansion coefficient, $\varepsilon_{\Delta T}$ is the strain caused by thermal stress.

The total strain in the sleeve should be no less than the strain induced by the interference fit between sleeve and magnets. So the mathematical expression is:

$$\varepsilon_{pre} \geq \varepsilon_{\Delta T} + \varepsilon_m + \varepsilon_{t[\max]} = \frac{\sigma_{\Delta T} + \sigma_m + \sigma_{t[\max]}}{E} \quad (4.4)$$

where ε_{pre} is the strain caused by the interference fit, ε_m is the strain led to by the centrifugal force of magnets, $\varepsilon_{t[\max]}$ is the strain generated by centrifugal force of sleeve itself. So the minimum interference δ is $\varepsilon \cdot R_1$.

The matlab code is developed based on Equation (4.1) to (4.4) and some published SPM sleeves have been tested and all the designed sleeve obtain a safety factor bigger than 2 [121-124]. For the SPM rotor we are working on, Table 4.5 shows 0.5mm, 1.0mm, and 1.5mm thickness sleeve and their corresponding maximum stress, safety factor, magnet mass, and magnet mass ratio to Nissan Leaf motor. Here the safety factor are all larger than 2. The 0.5 mm sleeve can help the SPM rotor achieve best electromagnetic

performance in Table 4.5 and is selected to be the sleeve thickness. The magnet thickness is supposed to 4.5mm at this stage and will be adjusted later on.

(c) Number of turns per coil

The number of turns per coil affects the peak phase current at constant torque region, as well as the performance at flux weakening region since the inductance will also be affected. So the torque performance at 2100rpm and 10,000rpm are checked to make sure the design can satisfy the whole operation range. The number of turns per coil for Nissan Leaf IPM machine is 8 and the same number is used to initialize the SPM machine design as well. Table 4.6 shows the designs with different number of turns, sleeve thickness and the required peak phase current at 2100 rpm and 10,000rpm. In this table, the N36Z permanent magnet material is utilized and the magnet thickness is 4.5mm because the trend can be observed.

In the 1.0mm thickness sleeve SPM machine, the peak phase current amplitude for constant torque region decreases when the number of turns per coils increases. The 10 turns SPM design hits peak phase current constraints. Since the remanence of N36Z is higher than N28AH, the current will increase when the magnet material changes back to N28AH. The 15 turns design cannot meet the torque specification at 10,000rpm and was wiped out. So the 12 turns per coil is determined to be the adopted for the SPM rotor. To keep the same fill factor with Nissan Leaf IPM, the 12 turns needs 50% more slot area on stator.

Winding copper loss is proportional to square of phase current and square of number of turns. For the SPM design, copper loss will change due to change in number of turns and current conducted per slot. Therefore, copper loss for SPM design will be:

$$SPM \text{ copper loss} = IPM \text{ copper loss} \times \left(\frac{12}{8}\right)^2 \times \left(\frac{\text{Phase current for SPM}}{\text{Phase current for IPM}}\right)^2 \quad (4.5)$$

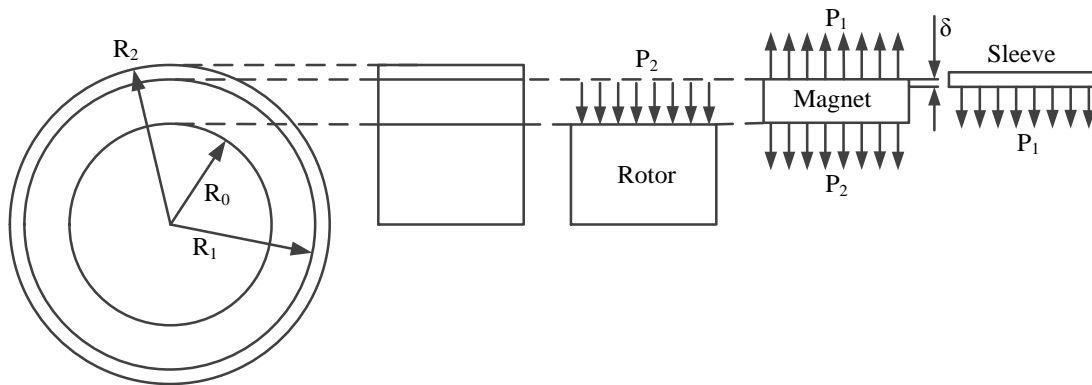


Fig. 4.6. Rotor model and its force analysis

Table 4.5 Mechanical performance comparison of SPM machines with different sleeves.

Thickness of the sleeve (mm)	Maximum stress in sleeve (MPa)	Safety factor	Magnet mass (kg)	Magnet mass ratio to Nissan Leaf motor
0.5	478.167	2.3005	1.751	0.9238
1	262.8462	4.185	1.7369	0.9164
1.5	191.0762	5.7569	1.7229	0.909

Table 4.6 Performance comparison between IPM and SPM at base and at top speed (N36Z and 4.5mm magnet thickness).

Sleeve thickness (mm)	IPM	0	0.5	1.0mm				1.5mm
Number of turns per coil	8	12	12	8	10	12	15	12
Current at 2100 rpm (A)	600	400	460	750	600	500	400	550
Current at 10,000 rpm (A)	440	400	440	310	380	400	400*	370

*cannot meet the torque requirement, the maximum torque is 71.3 Nm.

In the constant torque region, the peak phase current for IPM is 600A and the peak phase current for SPM is around 495A. So the SPM copper loss is 53.14% more than the IPM copper loss. The copper loss factor is denoted as the relationship between SPM copper loss and IPM copper loss. In this case, the copper loss factor for SPM is 1.53.

To achieve equitable copper loss between the Nissan Leaf IPM and SPM design, the SPM stator slot area is increased by the increase in copper loss factor:

$$SPM \text{ slot area} = 77.377 \times 1.5314 = 118.496 \text{mm}^2 \quad (4.6)$$

Thus, maintaining the same back iron thickness, the new stator outer diameter becomes 214mm. The SPM stator tooth width is maintained the same as the IPM tooth width so

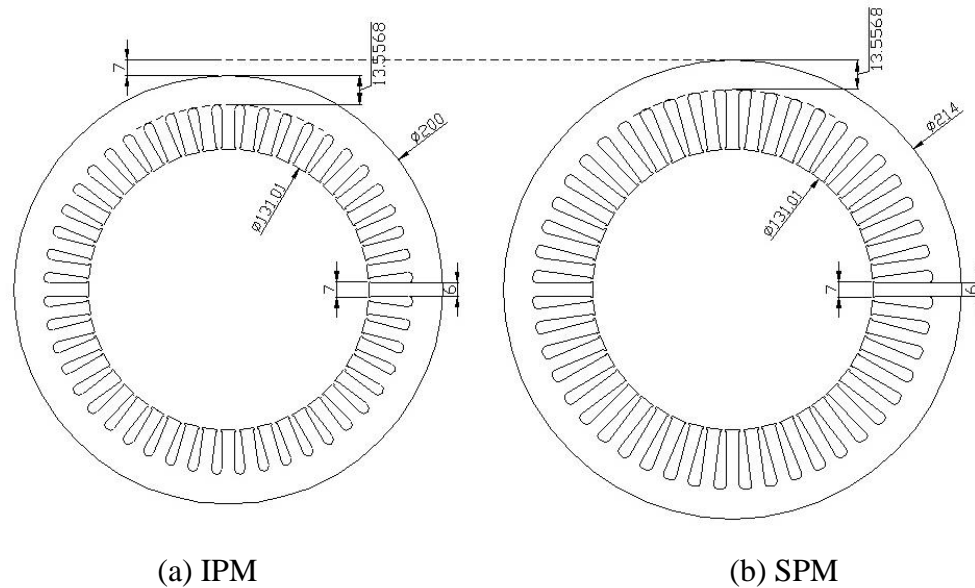


Fig. 4.7 Stator Comparison of IPM and SPM.

that the change of stator flux density is minimized. The slot bottom diameter is increased until the new slot area is realised. Fig.4.7 shows the stator difference between IPM and SPM.

(d) Magnet thickness

After the pole-arc to pole-pitch ratio has been decided, the magnet thickness determines the magnetic and mechanical performance. Table 4.6 shows four magnet thickness choices and the corresponding maximum stress, magnet mass, required current for constant torque region and the maximum torque the design can gain in this current. Those magnet thicknesses are all selected according to the air-gap flux density variation along magnet thickness to air-gap ratio in Fig. 4.5(a). When the ratio is larger than 4.5, the air-gap flux density increase speed slows down. So the peak phase current does not drop significantly when the magnet thickness increases from 4.5mm to 5.33mm. In order to guarantee the safety factor is no less than 2, the sleeve thickness is increased to 0.6 mm when the magnet thickness is 7.54mm. However, the adding in sleeve thickness mitigates

the ratio of magnet to air-gap length for the largest magnet thickness. Despite more than 30% magnet usage, the performance of last row in Table 4.6 is not competitive compared the first three rows. Combining the magnetic flux density saturation condition at 2100rpm full load operation, the 4.8862mm magnet thickness is decided to be the final result, which satisfied the performance requirements with slight saturation and same amount of magnet usage as Nissan Leaf IPM machine.

Table 4.7 Mechanical and electrical performance comparison of SPM machines with different magnet and sleeves thickness. (N28AH for magnet material and 12 turns)

Sleeve thickness (mm)	Magnet thickness (mm)	Maximum stress in sleeve (MPa)	Safety factor	Magnet mass (kg)	Magnet mass ratio to Nissan Leaf motor	Peak phase current @2100rpm	Torque @2100rpm (Nm)
0.5	4.5	478.17	2.3005	1.751	0.9238	500A	278.96
0.5	4.8862	511.73	2.1496	1.8954	1.0000	490A	277.36
0.5	5.33	549.76	2.0009	2.0601	1.0869	480A	277.84
0.6	7.54	549.59	2.0015	2.4990	1.3185	470A	276.15

4.3.2 Comparative Studies

Both the Nissan Leaf IPM machine and the SPM machine share the same stator, magnet volume, axial stack length, and outer rotor diameter. The information of Nissan Leaf motor is shown in Table 3.1.

For a radial field machine design, excitation torque can be derived from first principles by considering the force acting on a current carrying conductor in a magnetic field, resulting in an expression for torque that is a function of the machine geometry and electromagnetic quantities:

$$T = \frac{\pi}{2} D^2 L_a B Q \quad (4.7)$$

where D is the mean airgap diameter, L_a is the active axial length and B and Q the magnetic and electrical loadings respectively, as discussed in Chapter 2.

The torque produced by IPM machines is contributed to by excitation torque and a salient torque component, as will be shown later. However, Equation (4.7) still represents the basic sizing approach where the magnetic and electrical loadings (BQ) incorporate both torque producing components. Essentially, the saliency element is included in the electro-magnetic parameters.

So often in comparisons of machine technologies and topologies, the differences in design are hidden or masked by changes in key geometrical parameters of the machine, namely the diameter and active axial length. Similarly, different pole number creates an unnecessary complication when trying to make a comparison. Consequently, for this study, the machine active axial length, mechanical air-gap length and air-gap mean diameter are maintained constant. To maintain equitable thermal performance, the outer diameter of the SPM stator is allowed to increase by 7% (14mm) to accommodate the additional turns required for the design, Table 4.8. This change does not contravene the torque equation, although some may argue that a more optimized split ratio (stator outer-to-inner diameter ratio) may have been chosen.

The torque produced by IPM machine comes from two parts, magnetic torque and salient torque, as shown in Equation (4.8). In order to get high torque output and low loss, for the same pole numbers and power supply, the topology and material of the rotor are designed to provide large flux-linkage and inductance difference in the d- and q-axes. The way to embed permanent magnets in the rotor iron reduces the flux-linkage but leads to the inductance difference in two axes.

If the embedded position is closer to the air gap, more torque can be produced due to larger flux-linkage while bigger torque ripple can be introduced because of worse smooth flux variation. The design procedure is to find a proper structure based on the requirements.

$$T = \frac{3}{2} p [\psi_m i_{sq} - i_{sq} i_{sd} (L_q - L_d)] \quad (4.8)$$

where i_{sd} and i_{sq} are the d- and q-axis stator currents, L_d and L_q are the d- and q-axis inductances, p is the number of pole pairs, and ψ_m is the PM flux-linkage.

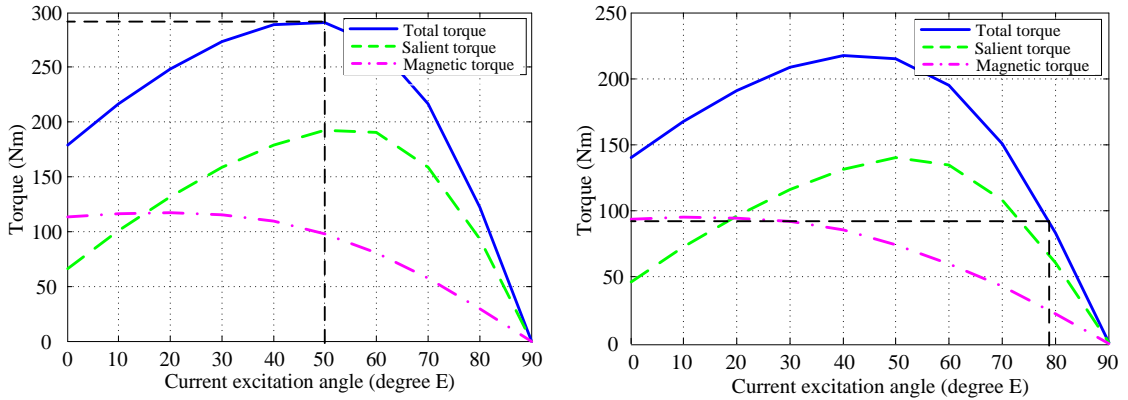
Table 4.8. Details of Nissan Leaf IPM and example SPM machine design; distributed winding.

Description	Nissan Leaf IPM machine	Example SPM machine design
Outer diameter of stator (mm)	200	214
Inner diameter of stator (mm)	131	
Stack length of stator (mm)	151	
Number of slot	48	
Winding type	Full pitch single layer distributed winding	
No. of turns per coil	8	12
No. of strands per turn	15	
Diameter of copper wire (mm)	0.812	
Outer diameter of rotor (mm)	130	
Inner diameter of rotor (mm)	45	93
Active axial length (mm)	151	
No. of poles	8	
Large magnet dimensions (mm)	3.79 (DOM) × 28.85 × 8.36*	4.8862 (DOM) × 8.35mm*
Small magnet dimensions (mm)	2.29 (DOM) × 21.3 × 8.34*	
Total magnet mass (kg)	1.8954	
Pole arc/pole pitch ratio	0.9765	0.85
Skew angle (degrees mech.)	3.75	
Stator and rotor iron material	35JNE250	
Permanent magnet material	N28AH	
Nominal Performance at a DC-link voltage of 375 V _{DC}		
Torque, zero to base speed	280Nm	
Power, base to maximum speed	80kW	
Thermal rating	80kW at 7000 RPM	
Peak phase current, 3 phases	615A	495A

*18 pieces per active axial length

For the IPM, the topology and material of the rotor are designed to provide permanent magnet (PM) flux-linkage and an inductance difference in the d - and q -axes. Generally, embedding the PM material in the rotor iron reduces the PM flux-linkage but leads to an inductance difference between the two axes. By way of example, torque segregation of the Nissan Leaf IPM design has been analysed, the results of which are illustrated in Fig. 4.8. For this design, the saliency component of torque is higher than the excitation

component of torque at full load torque and between zero and base speed, Fig. 4.8(a) and also at the extended speed operating point, Fig. 4.8(b), by a factor of about 2/3rds in both cases. The saliency torque arises from the difference between the d - and q -axis inductances, a factor which varies with load current or saturation in the machine stator and rotor, as shown in Fig. 4.9.



(a) 2,100 RPM; 600A peak phase current; excitation angle = 50°

(b) 10,000 RPM; 370A peak phase current; excitation angle = 78.2°

Fig. 4.8. IPM machine torque segregation at base and top speed.

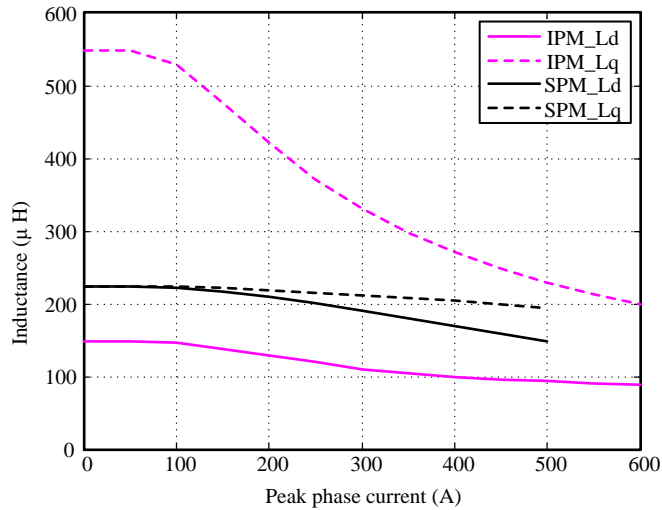


Fig. 4.9. Nissan Leaf IPM and SPM machine inductance comparison.

In constant torque region, the IPM works in the maximum torque per ampere (MTPA) condition. After going into constant power region, the q- axis current increases to weaken the flux produced by permanent magnet due to the voltage limit in power inverter. Hence the operation point locates on the large excitation angle area and the magnetic torque is much smaller than the salient torque. Therefore, the big difference between d- and q- axis inductance is conducive to the extension of IPM machines' speed range.

Relating the 2-axis currents to actual phase current, Equation (4.8) can be expressed in terms of the machine parameters, phase current, I_s , and the current excitation angle, γ , which is the controlled angle between phase current and the machine induced back-EMF:

$$T = 3p \left[\psi_m I_s \cos(\gamma) + \frac{(L_q - L_d)}{2} I_s^2 \sin(2\gamma) \right] \quad (4.9)$$

For SPM machines, the current excitation angle, γ , is held at zero from zero speed to base speed, where it is then progressively increased to field-weaken the machine for operation at speeds above base speed. For IPM machines, an optimum current excitation angle exists below base speed depending on the required load torque. In the case analyzed, the optimum current excitation angle is 50° electrical upon base speed, increasing to 78.2° electrical at maximum speed, as shown in Fig. 4.8(a) and (b) respectively.

Clearly from Fig. 4.8, it can be seen that the IPM rotor saliency provides the main torque contribution. This is also the case for other published IPM designs [15].

However, when assessing designs, it may be worth considering the utilization of the permanent magnet material, since this is a major cost component. Referring to Equation (4.9) the permanent magnet excitation torque component of the IPM is not fully utilized below base speed, being approximately only 64.3% effective at a current excitation angle of 50° electrical, i.e.:

$$T_{excitation} = 3p \left[\psi_m I_s \cos(50^\circ) \right] = 0.643(3p\psi_m I_s) \quad (4.10)$$

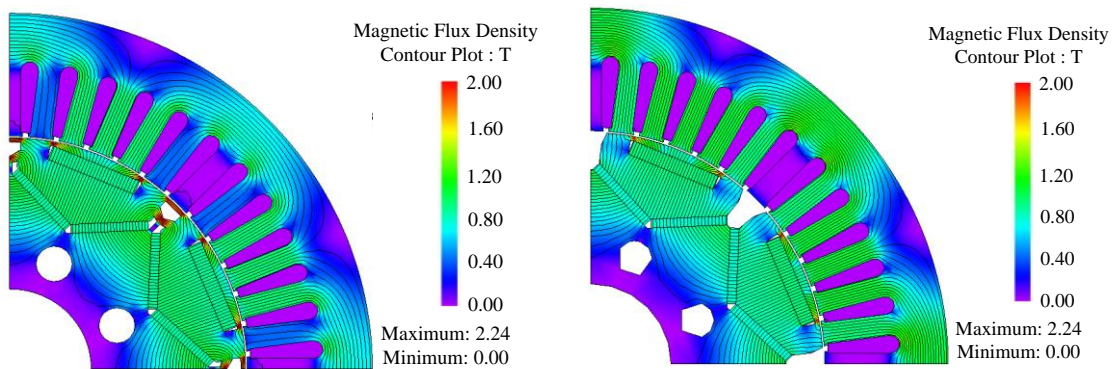
This is an over estimate since Equation (4.9) assumes an idealized sinusoidal machine design, which is not the case. Comparing the peak excitation torque and that at a current

excitation angle of 50° electrical from Fig. 4.7(a), the reduction can be estimated at 0.833 per unit.

Further, the rotor implementation necessitates flux barriers that result in some loss of magnet flux via leakage, as illustrated in Fig. 4.10(a) via the highly saturated ($+2T$) thin sections between rotor poles. These barriers are required for mechanical integrity, but nevertheless, compromise the idealized magnetic design. Fig. 4.10(b) shows the FEA solution of the benchmark machine with a modified idealized rotor design comprising of air sections to guide flux as opposed to flux barriers.

Until the discovery or invention of a flux insulator, this is purely an academic exercise to try to assess the reduced performance introduced by the rotor barriers, or flux short circuit paths. In the case studied, the idealized induced RMS back-EMF is reduced by a factor of 0.772 and peak back-EMF reduced by a factor of 0.893, the actual torque element lying somewhere between these two bounds. Thus, one might postulate that the PM utilization could be between 0.643 (i.e. 0.772×0.833) and 0.744 (i.e. 0.893×0.833).

For the proposed SPM design the peak stator current, at maximum torque-base speed, is 0.825 per unit of the IPM. Thus, the improvement in PM utilization is probably closer related to the current excitation angle than the leakage factor.



(a) Nissan Leaf IPM.

(b) Modified model.

Fig. 4.10. Lines of equal vector magnetic potential and flux-density contours for Nissan Leaf IPM and modified model.

4.3.3 Design and Comparison of two example machines

In order to study the IPM and SPM machine rotor topologies, an example SPM machine is designed within the Nissan Leaf stator lamination constraint and compared. The geometry and specifications of the machines are listed in Table 4.7 along with FEA calculated performance comparison results in Table II for the IPM and Table III for the SPM from the nominal base speed of 2,100 RPM to the top speed of 10,000 RPM.

To achieve extended speed capability, the machine parameters of the SPM are modified from those of the IPM to increase the direct-axis armature reaction flux to be closer in magnitude to the PM flux-linkage as suggested by [61]:

$$\omega_{\max} = \frac{V_s}{\psi_m - L_d I_s} \quad (4.11)$$

where V_s is the stator phase terminal voltage and ω_{\max} the achievable top speed within the power specification.

The increase in mechanical air-gap to accommodate the rotor sleeve along with choice of magnet radial length, Fig. 4.5(a), reduces the PM flux-linkage. Increasing turns then increases PM flux-linkage back to its desired value (proportional to turns) and direct-axis inductance proportional to turns squared resulting in a net increase of the direct-axis armature reaction flux-linkage.

This would result in an increase in stator resistance and hence copper loss compromising the machine efficiency and thermal performance. Hence, the stator slot depth is increased; and by keeping the back-iron thickness unchanged the machine outer diameter increases by 7%. Note, the stator winding loss is not kept as per the IPM machine. Since the stator current magnitude and iron losses are reduced for the IPM, some additional copper loss at higher speeds can be managed. The SPM design has slightly better efficiencies at full load across the full speed spectrum.

Each of the SPM poles is made from 6 circumferential blocks having fixed magnetization to realize a near radial air-gap magnetization. The SPM is designed to have the same magnet mass as the IPM. Both machines have full demagnetization withstand at the

operating points of Tables 4.9, 4.10 and 4.11 and at a rotor temperature of 120°C. The simplified SPM rotor design requires less iron, although the stator iron mass is increased due to the increase in outer diameter. Similarly, the stator copper mass is increased for the SPM as discussed. Table 4.12 details the materials mass audit for the two machine designs showing 1.5% net increase for the SPM, which is negligible.

Much is claimed of IPM topologies in terms of their saliency torque contribution, minimum magnet mass, demagnetization withstand, wide flux-weakening capability and high operational efficiencies. These attributes are assessed and compared for surface mounted permanent magnet machines (SPMs) for both distributed stator winding designs. The study illustrates and concludes that both the IPM and SPM topologies have very similar capabilities with only subtle differences between the design options, subtleties that may be exploited when considering the traction application requirements, for example predominant low, medium or high speed operation. All the performance difference between IPM and SPM can be concluded as the following six points:

- (a) The back-EMF of SPM machine is more than 50% higher than the IPM machine, which shows IPM machine is better in fault withstand as discussed in Chapter 3.6.3. Fig. 4.11(a) and (b) shows the back-EMF profile of IPM and SPM machine at 10,000rpm and the difference is obvious.
- (b) Flux-weakening range increased in SPM machine design. Fig. 4.11 shows that the field weakening range of Nissan Leaf IPM is from 6000 rpm to 10,000 rpm. While for SPM machine, the flux weakening range is enlarged to 4000 rpm to 10,000 rpm. However, the excitation current for SPM machine is much larger than the IPM machine.
- (c) The rotor active material mass for SPM machine reduced by 45.35%. However, the SPM rotor needs a sleeve to maintain enough mechanical strength. The stator active material mass for SPM machine increase by 28.48%. But the total iron mass of SPM is still 8% less.
- (d) The excitation torque ripple of SPM machine is less than the IPM machine. Fig. 4.12(c) and (d) shows the torque profile of IPM and SPM machine at 10,000rpm.

- (e) An interesting observation is the reduced peak phase current requirement (600 to 480A) for the SPM design, which is a significant reduction in power electronics.
- (f) Even though Fig. 4.12(e) and (f) shows no demagnetization, the IPM and SPM machine suffers different demagnetization if the permanent magnet material is not properly selected. Fig. 4.13 shows the torque-current relationship if the coercivity of the permanent magnet is very low, assuming 311kA/m at 180°C. The demagnetization starts at around 400A for SPM machine while 500A for IPM. As mentioned in Chapter 3.5, this torque-current curve is used to judge if the magnet is demagnetized in experiments.

Table 4.9 Performance information of Nissan leaf IPM over whole speed range.

Speed (RPM)	2100	3000	4000	5000	6000	7000	8000	9000	10000
Back-EMF (Vrms)	34.61	49.44	65.92	82.40	98.87	115.35	131.83	148.31	164.79
Back-EMF (Vpeak)	49.92	71.35	95.10	118.96	142.67	166.44	190.31	213.95	237.87
Torque (Nm)	280.70	255.09	191.47	153.29	127.30	108.40	95.49	85.05	75.84
Torque ripple (%)	10.65	15.16	13.72	16.42	16.55	15.78	20.06	23.23	26.40
Vphase_RMS	62.70	79.53	101.25	112.73	132.82	160.48	155.92	158.08	159.57
Vphase_peak	96.86	132.89	166.31	192.55	218.06	247.02	246.03	256.59	271.01
Iphase_peak (A)	615	600	425	365	300	245	250	250	251
Current excitation angle (γ)	50	49.2	43.35	47.88	55	48	58.5	63.25	67
Stator iron loss (W)	277.00	437.23	601.55	789.80	988.69	1228.24	1368.30	1576.47	1759.95
Rotor iron loss (W)	52.60	104.11	147.98	168.98	188.34	199.86	244.93	298.89	342.38
Iron loss (W)	329.60	541.34	749.53	958.78	1177.03	1428.10	1613.23	1875.35	2102.33
Copper loss (W)	4657.84	4433.40	2224.40	1640.67	1108.35	739.21	769.69	769.69	775.86
Mechanical loss (W)	17.15	35.00	62.22	97.22	140.00	190.56	248.89	315.00	388.89
Total loss (W)	5004.59	5009.74	3036.15	2696.67	2425.38	2357.86	2631.81	2960.04	3267.08
Efficiency (%)	92.50	94.12	96.35	96.75	97.06	97.12	96.81	96.44	96.05
Peak-peak Tcogging (Nm)	2.61								

Table 4.10 Performance information of modified Nissan leaf IPM over whole speed range.

Speed (RPM)	2100	3000	4000	5000	6000	7000	8000	9000	10000
Back-EMF (Vrms)	33.53	47.89	63.86	79.82	95.79	111.75	127.72	143.68	159.65
Back-EMF (Vpeak)	48.93	69.89	93.23	116.57	139.87	163.22	186.60	209.88	233.18
Torque (Nm)	283.01	254.89	190.56	152.70	127.85	109.42	95.61	84.87	75.15
Torque ripple (%)	8.54	7.63	9.76	9.49	10.26	17.12	23.18	29.37	38.13
Vphase_RMS	65.49	93.04	114.67	141.02	162.85	144.02	134.62	126.78	116.65
Vphase_peak	99.88	134.94	159.21	187.60	216.38	212.48	217.12	214.67	216.76
Iphase_peak (A)	600.00	532.50	395.00	319.00	271.00	273.00	290.50	314.00	353.5
Current excitation angle (γ)	50.00	45.00	45.00	39.60	38.20	58.30	66.80	72.40	77.25
Stator iron loss (W)	259.25	439.37	620.00	849.70	1067.51	1144.86	1305.93	1536.38	1881.76
Rotor iron loss (W)	38.92	62.81	86.33	116.87	135.22	167.47	209.17	269.46	364.29
Iron loss (W)	298.17	502.17	706.34	966.57	1202.73	1312.33	1515.09	1805.84	2246.06
Copper loss (W)	4433.40	3492.00	1921.45	1253.19	904.43	917.82	1039.27	1214.21	1538.91
Mechanical loss (W)	17.15	35.00	62.22	97.22	140.00	190.56	248.89	315.00	388.89
Total loss (W)	4748.72	4029.17	2690.01	2316.97	2247.15	2420.71	2803.25	3335.05	4173.86
Efficiency (%)	92.91	95.21	96.74	97.18	97.28	97.07	96.62	96.00	94.96
Peak-peak Tcogging (Nm)	1.26								

Table 4.11 Performance information of SPM design candidate over whole speed range.

Speed (RPM)	2100	3000	4000	5000	6000	7000	8000	9000	10000
Back-EMF (Vrms)	64.42	92.04	122.73	153.39	184.07	214.72	245.43	269.95	306.83
Back-EMF (Vpeak)	76.97	109.96	146.64	183.28	219.94	256.60	293.26	322.56	366.60
Torque (Nm)	282.59	254.61	192.02	152.93	128.67	109.73	95.25	84.77	76.21
Torque ripple (%)	5.51	5.40	4.70	5.56	6.80	8.94	11.19	12.79	15.85
Vphase_RMS (V)	85.75	116.54	141.28	127.98	130.10	125.59	121.84	117.76	112.89
Vphase_peak (V)	126.34	171.09	207.08	204.36	216.16	216.74	216.68	214.51	210.74
Iphase_peak (A)	480.00	428.00	316.70	306.00	305.00	326.00	345.00	362.00	392.00
Current excitation angle (γ)	0	0	0	35	46.3	56.35	63	62	71.36
Stator iron loss (W)	189.88	299.47	397.60	354.32	386.07	411.12	449.37	488.22	558.73
Rotor iron loss (W)	0.28	0.27	0.53	0.43	0.33	0.47	0.53	0.99	0.64
Iron loss (W)	190.16	299.74	398.13	354.75	386.39	411.59	449.90	489.21	559.37
Copper loss (W)	4079.77	3243.70	1776.02	1658.04	1647.22	1881.86	2107.61	2320.44	2720.98
Mechanical loss	17.15	35.00	62.22	97.22	140.00	190.56	248.89	315.00	388.89
Total loss (W)	4287.07	3578.44	2236.38	2110.01	2173.62	2484.01	2806.40	3124.65	3669.23
Efficiency (%)	93.55	95.72	97.29	97.43	97.38	97.00	96.60	96.24	95.60
Peak-peak Tcogging (Nm)	0.27								

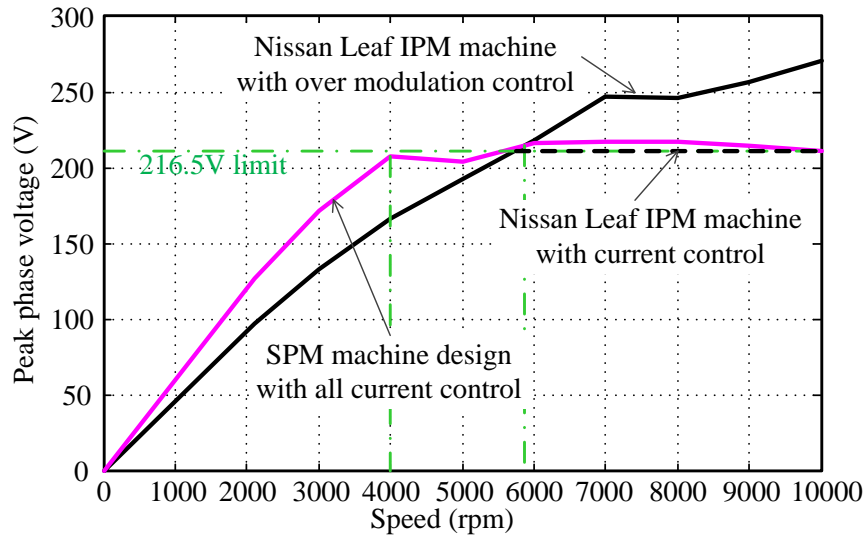
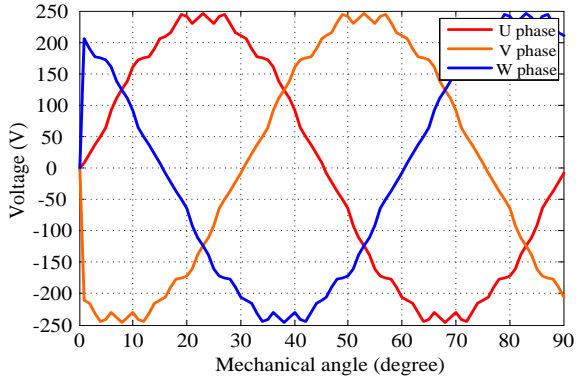


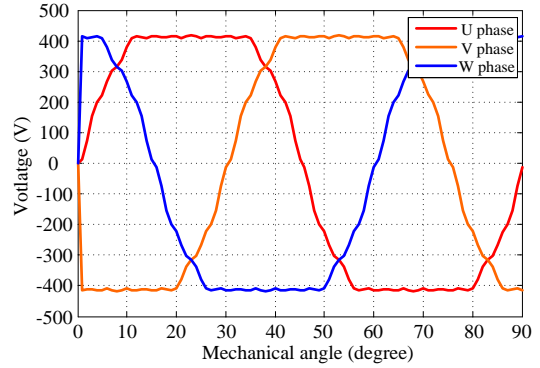
Fig. 4.11. Flux weakening range comparison of SPM design and Nissan Leaf IPM.

Table 4.12. Mass comparison between IPM and SPM at base and at top speed.

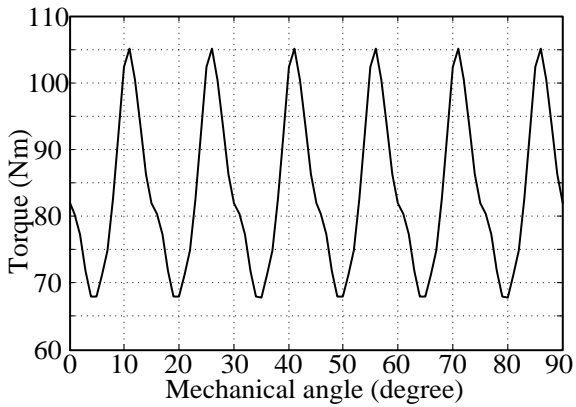
Unit (kg)	Stator iron	Rotor iron	Total iron	Copper	Magnet	Total machine
Nissan Leaf IPM	16.35	10.55	26.90	5.12	1.96	34.01
Modified Nissan Leaf IPM	16.35	10.55	26.90	5.12	1.99	34.04
SPM	19.4	5.6	24.9	7.71	1.92	34.53



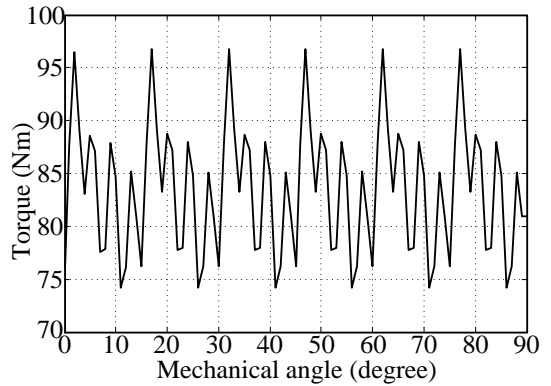
(a) Open circuit back-EMFs at 10,000rpm - IPM



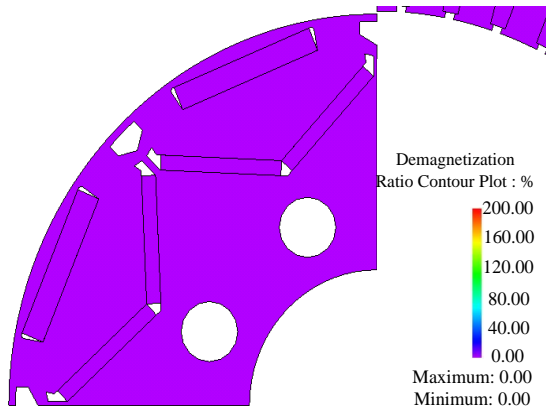
(b) Open circuit back-EMFs at 10,000rpm - SPM



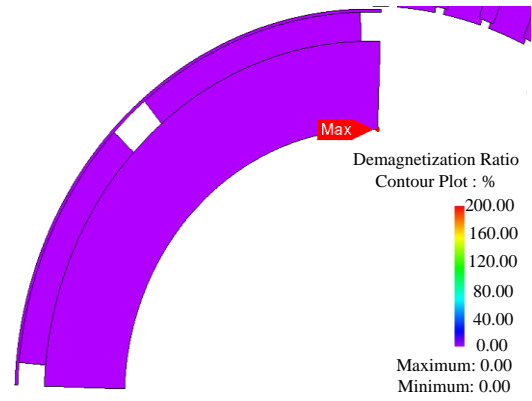
(c) Torque versus angle - IPM



(d) Torque versus angle at 10,000rpm - SPM



(e) Demagnetization ratio - IPM



(f) Demagnetization ratio - SPM

Fig. 4.12. Performance results comparisons between IPM and SPM machines at 10,000rpm.

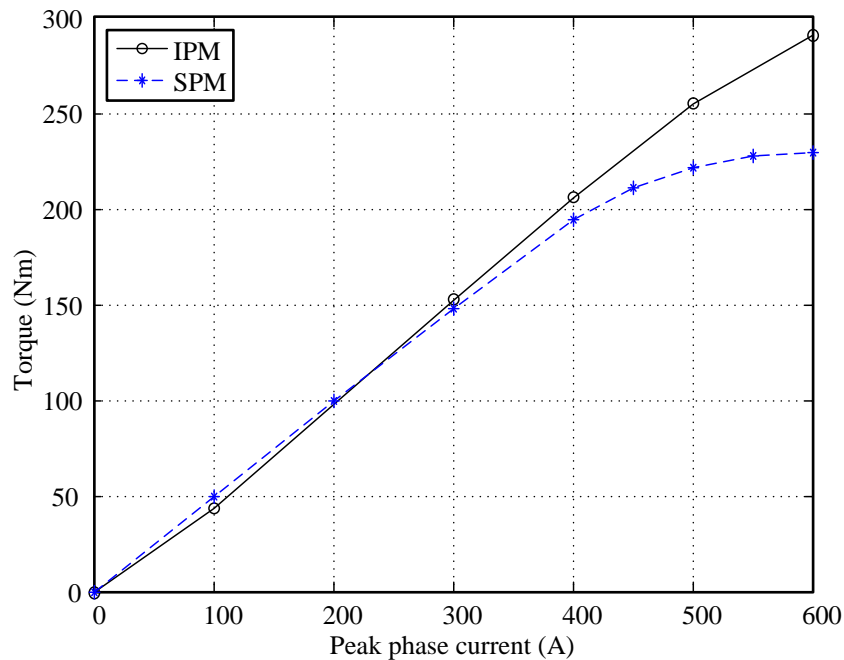


Fig. 4.13. Torque-current comparisons between IPM and SPM machines with 311kA/m coercivity permanent magnet at 2100rpm, 180°C.

4.3.4 Manufacturing Comparison of Two Example Machines

The Nissan Leaf machine has been commercialized and mass produced. Compared to the IPM rotor, the SPM rotor has simpler rotor lamination structure with radially magnetized arc magnets and carbon fiber sleeve. So it is not easy to judge which rotor is easier to be fabricated. But the good news is that both the arc shape permanent magnet with radial magnetization and SPM rotor with carbon fiber sleeve have been widely applied in industry before [122-124].

Much is claimed of IPM topologies in terms of their saliency torque contribution, minimum magnet mass, demagnetization withstand, wide flux-weakening capability and high operational efficiencies. These attributes are assessed and compared for well documented IPM design and a SPM design. The study illustrates and concludes that both the IPM and SPM topologies have very similar capabilities with only subtle differences between the design options, subtleties that may be exploited when considering the traction application requirements, for example predominant low, medium or high speed operation, and power train integration.

4.4 Rotor Stress Analysis

The hoop stress is the force exerted circumferentially (perpendicular both to the axis and to the radius of the object) in both directions on every particle in the cylinder wall.

The von Mises hypothesis, also called maximum-distortion-energy hypothesis, assumed that the material state becomes critical when the energy needed for the “distortion” of a material element (volume remains unchanged) reaches a critical value and the equivalent stress is called von Mises stress. Since the von Mises stress agrees well with experiments on ductile materials, it is preferably used to characterize the onset of plastic flow. In this case, a material is said to start yielding when its von Mises stress reaches a critical value known as the yield strength.

In order to understand how the stress operates on the rotating rotors, an SPM rotor is taken as an example to initially calculate stress analytical and then confirm via more detailed FEA studies. One general element of the rotor is considered. The forces acting on the element are shown in Fig. 4.14.

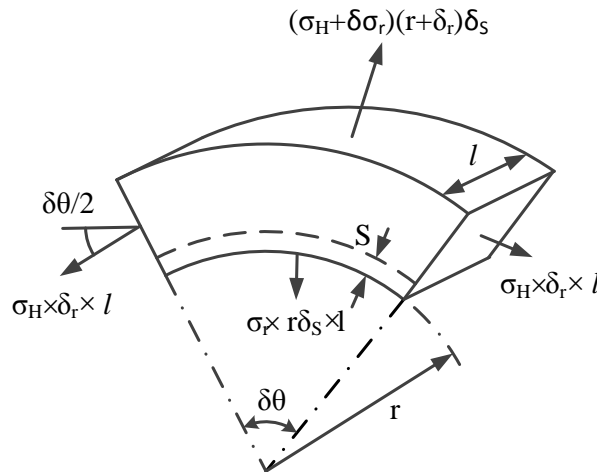


Fig. 4.14. Forces acting on general element in a rotating solid disc.

Because of the symmetry of the rotor structure and forces, the deformation will not twist the rotor and there is no shear force on both cut-off sections. The tangential tensile stress on each cut-off section is given by [125], which is

$$\text{Tensile strength per unit axial length} = \sigma_H \cdot \delta_r \quad (4.12)$$

The radial tensile stress acting on the inner surface of the rotor is σ_r , and $\sigma_r + \delta\sigma_r$ on the outer surface of the rotor. The volume of the element per unit length is

$$V_u = r \cdot \delta\theta \cdot \delta r \quad (4.13)$$

The element mass per unit length is

$$m_u = \rho \cdot r \cdot \delta\theta \cdot \delta r \quad (4.14)$$

Therefore, the centrifugal force acting on the element is

$$F_c = m\omega^2 r = \rho r \delta\theta \delta r \omega^2 r = \rho r^2 \omega^2 \delta\theta \delta r \quad (4.15)$$

From the equilibrium of the radial forces acting on the element,

$$2\delta\sigma_H \delta r \sin \frac{\delta\theta}{2} + \sigma_r r \delta\theta - (\sigma_r + \delta\sigma_r)(r + \delta r) \delta\theta = \rho r^2 \omega^2 \delta\theta \delta r \quad (4.16)$$

if $\delta\theta$ is small,

$$\sin \frac{\delta\theta}{2} = \frac{\delta\theta}{2} \quad (4.17)$$

and as $\delta r \rightarrow 0$, $\delta\sigma_r \rightarrow 0$

so the Equation 4.17 can be reduced to

$$\delta\sigma_H - \sigma_r - r \frac{d\sigma_r}{dr} = \rho r^2 \omega^2 \quad (4.18)$$

If there is a radial movement or “shift” of the element by an amount s , the radial strain can be expressed as:

$$\varepsilon_r = \frac{ds}{dr} = \frac{1}{E} (\sigma_r - \mu\sigma_H) \quad (4.19)$$

The diametric strain is equal to the circumferential strain, so the strain can be presented as

$$\frac{s}{r} = \frac{1}{E} (\sigma_H - \mu\sigma_r), \therefore s = \frac{r}{E} (\sigma_H - \mu\sigma_r) \quad (4.20)$$

The differential of deformation s is:

$$\frac{ds}{dr} = \frac{1}{E}(\sigma_H - \mu\sigma_r) + \frac{r}{E} \left(\frac{d\sigma_H}{dr} - \frac{\mu d\sigma_r}{dr} \right) \quad (4.21)$$

Simplifying Equation 4.20 and Equation 4.21, we can get

$$(\sigma_H - \sigma_r)(1 + \mu) + r \frac{d\sigma_H}{dr} - \mu r \frac{d\sigma_r}{dr} = 0 \quad (4.22)$$

Substituting for $(\sigma_H - \sigma_r)$ from Equation 4.19, we can get

$$\left(r \frac{d\sigma_r}{dr} + \rho r^2 \omega^2 \right) (1 + \mu) + r \frac{d\sigma_H}{dr} - \mu r \frac{d\sigma_r}{dr} = 0 \quad (4.23)$$

After simplification, the Equation 4.12 will be

$$\frac{d\sigma_r}{dr} + \frac{d\sigma_H}{dr} = -\rho \omega^2 r (1 + \mu) \quad (4.24)$$

The integration of Equation 4.13 will be

$$\sigma_r + \sigma_H = -\frac{\rho \omega^2 r^2 (1 + \mu)}{2} + 2A \quad (4.25)$$

where $2A$ is the convenient constant of integration.

Subtracting Equation 4.9 from Equation 4.14 leads to

$$2\sigma_r + r \frac{d\sigma_r}{dr} = -\frac{\rho \omega^2 r^2 (3 + \mu)}{2} + 2A \quad (4.26)$$

Since

$$2\sigma_r + r \frac{d\sigma_r}{dr} = \frac{1}{r} \cdot \frac{d}{dr} (r^2 \sigma_r) \quad (4.27)$$

Equation 4.26 can be rewrite as

$$\frac{d}{dr} (r^2 \sigma_r) = \left(2\sigma_r + r \frac{d\sigma_r}{dr} \right) r = \left[-\frac{\rho r^2 \omega^2}{2} (3 + \mu) + 2A \right] r \quad (4.28)$$

After integration,

$$r^2 \sigma_r = -\frac{\rho r^4 \omega^2}{8} (3 + \mu) + Ar^2 - B \quad (4.29)$$

and

$$\sigma_r = A - \frac{B}{r^2} - (3 + \mu) \frac{\rho r^2 \omega^2}{8} \quad (4.30)$$

Substitute Equation 4.19 to Equation 4.14, the tangential tensile stress can be got.

$$\sigma_H = A + \frac{B}{r^2} - (1 + 3\mu) \frac{\rho r^2 \omega^2}{8} \quad (4.31)$$

For a solid rotor, when $r = 0$, if $B \neq 0$, from Equation 4.30 and 4.31, the stress will be infinite, which is not real in practice. So B has to be zero.

There is a shaft hole in our rotor with radius of R_1 , so the integration constant B is not zero. But the stress at both inner and outer surface without shaft is zero. The outer radius of the rotor is R_2 . The stress at inner and outer surface is

$$\begin{aligned} \sigma_{r=R_1} &= A - \frac{B}{R_1^2} - (3 + \mu) \frac{\rho R_1^2 \omega^2}{8} = 0 \\ \sigma_{r=R_2} &= A - \frac{B}{R_2^2} - (3 + \mu) \frac{\rho R_2^2 \omega^2}{8} = 0 \end{aligned} \quad (4.32)$$

Both A and B can be solved as

$$\begin{cases} A = (3 + \mu) \frac{\rho \omega^2 (R_1^2 + R_2^2)}{8} \\ B = (3 + \mu) \frac{\rho \omega^2 R_1^2 R_2^2}{8} \end{cases} \quad (4.33)$$

Equation 4.19 and 4.20 can be rewritten as

$$\begin{cases} \sigma_r = (3 + \mu) \frac{\rho \omega^2}{8} \left[R_1^2 + R_2^2 - \frac{R_1^2 + R_2^2}{r^2} - r^2 \right] \\ \sigma_H = \frac{\rho \omega^2}{8} \left[(3 + \mu) \left(R_1^2 + R_2^2 + \frac{R_1^2 + R_2^2}{r^2} \right) (1 + 3\mu) r^2 \right] \end{cases} \quad (4.34)$$

so the maximum hoop stress occurs at the inner surface of the rotor, where $r = R_1$

$$\sigma_{H \max} = \frac{\rho \omega^2}{4} \left[(3 + \mu) R_2^2 + (1 - \mu) R_1^2 \right] \quad (4.35)$$

So for the case considered:

$$R_1 = 46.5 \text{ mm}, R_2 = 61.2 \text{ mm}, \rho = 7.65 \times 10^3 \text{ kg} \cdot \text{m}^{-3}, \mu = 0.3, \omega = 10,000 \text{ rpm} = 1256 \text{ rad} \cdot \text{s}^{-1},$$

$$\text{Hence } \sigma_{H \max} = 48.38 \text{ MPa}.$$

$$\text{when } r = R_2, \sigma_{H \min} = 29.438 \text{ MPa}$$

To find the maximum radial stress, we need to make $\frac{d\sigma_r}{dr} = 0$, the result is $r = \sqrt{R_1 R_2}$.

The maximum radial stress is:

$$\sigma_{r \max} = (3 + \mu) \frac{\rho \omega^2}{8} (R_2 - R_1)^2 = 1.07572 \text{ MPa} \quad (4.36)$$

Thus, compared with hoop stress, the radial stress can be ignored.

The researcher J. Jung, etc. [126] stated that the maximum centrifugal force is reached when the rotor suffering high angular momentum, instead of the constant speed. However, there is no else paper considering the stress caused by the angular momentum during rotor stress analysis [127-130]. So the stress produced by the angular acceleration is calculated to verify if the angular momentum needs to be considered.

According to [130], the maximum shear stress occurs at the inner radius and can be expressed as:

$$\sigma_{s \max} = -\dot{\omega} \cdot R_2^2 \cdot \rho \cdot \frac{R_2^4 - R_1^4}{4 \cdot R_1^2 R_2^2} = -2.4818 \dot{\omega} \text{ Pa} \quad (4.37)$$

Compared with the hoop stress and radial stress generated by centrifugal force, the shear stress caused by the angular momentum is negligible unless the angular acceleration can reach the level of $10^6 \text{ rad} \cdot \text{s}^{-2}$, which is impossible for the machine operation.

$$T = \frac{3}{2} p [\psi_m i_{sq} - i_{sq} i_{sd} (L_q - L_d)] \quad (4.38)$$

The calculated maximum stress of single rotor is at inner surface, 48.38MPa, the minimum stress is at the outer surface, 29.438MPa.

4.5 Zero Magnet Machine Designs

As an aside to the IPM and SPM studies, a magnet-less machine topology was considered based on the same stator active axial length of the Nissan Leaf machine (151mm), the same rotor outer diameter and stator inner diameter and an 8-pole rotor configuration. To maximize the machine saliency ratio, a concentrated winding topology was considered. Hence, the 12-slot and 15-slot reluctance machines with zero magnets are designed and excited with the winding connections are shown in Table 4.13 and 4.14. In order to obtain higher torque, the 12 degree choice is selected to be both the SPM and IPM 15 slot machine because of the highest winding factor among all the possible connections. Both 3-phase sinusoidal and square wave current are applied to the 12-slot synchronous machine. The 5-phase sinusoidal current is used to excite the 15-slot synchronous machine.

The 12-slot machine is also simulated as excited via a conventional 3-phase asymmetric SR machine converter, as illustrated in Fig. 4. 15 showing the machine geometry (a), asymmetric inverter (b) and applied phase currents (c). Fig. 4.18 shows the resulting torque waveform for the three configurations considered. Although the average torque are all lower than that of the Nissan Leaf machine (for the same peak inverter current) the sinusoidally excited machines show a better average than the asymmetrically driven SR machine. The synchronous machines have an average torque of 200Nm compared to the 280Nm of the Nissan Leaf machine (71.4%). However, the machines have zero magnet content and the 5-phase implementation has extremely good electro-magnetic torque ripple, far superior to the 12-8 topologies and comparable with the IPM and SPM designs considered throughout this thesis. Actually, the torque ripple for the 15-8, 5-phase synchronous reluctance machine is 16.35% without skew, which is comparable to the Nissan Leaf IPM machine, which is 10.65% after skew and 29.00% without skew.

In order to make the torque at constant torque region meet the torque requirement of Nissan Leaf machine, the stack length of 15-8, 5-phase synchronous reluctance machine is increased to 213.6 mm. The structure comparison of new synchronous machine and Nissan Leaf machine is shown in Fig. 4.19. Although the total end-winding length of

synchronous machine is 9.75 mm less than that of Nissan Leaf machine, the total length is 52.85 mm longer. The design parameters comparison of Nissan Leaf machine and synchronous reluctance machine are shown in Table 4.15. The curb weight of Nissan

Table 4.13 Three-phase concentrated winding connection for 12-slot machine.

3-Phase, 12 teeth			0 degree choice	
Tooth	Mech angle	Elect angle	Tooth	Coil
1	0	0	1	A1
2	30	120	2	B1
3	60	240	3	C1
4	90	0	4	A2
5	120	120	5	B2
6	150	240	6	C2
7	180	0	7	A3
8	210	120	8	B3
9	240	240	9	C3
10	270	0	10	A4
11	300	120	11	B4
12	330	240	12	C4

Coils are wound in the same sense, 1+, 1-, 2+, 2-, 3+, 3-, etc.

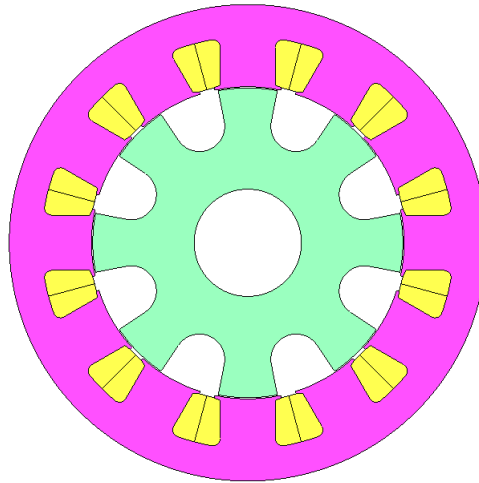
Leaf S vehicle is 1481 kg. The mass of Nissan Leaf IPM and the 15-slot synchronous machine are just 2.30% and 3.07% respectively of the total vehicle mass. So the mass increase of 15-8, 5-phase synchronous reluctance machine is acceptable. In conclusion, the non-permanent magnet synchronous machine with 5-phase voltage source inverter is potential to be applied for traction machines when the magnet prices or the supply becomes an issue.

Further work on this topology is time limited and hence reported in Chapter 7 as future work. However, an invention disclosure of this topology has been made and reported as an outcome of this thesis study.

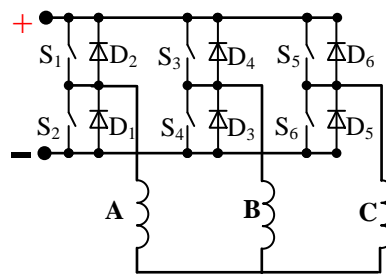
Table 4.14. Five-phase connections for the 15 slots.

5-Phase, 15 teeth (12)			12 Degrees choice		24 Degree choice	
Tooth	Mech angle	Elect angle	Tooth	Coil	Tooth	Coil
1	0	0	1	A1	1	A1
2	24	96	2	B3	2	B2
3	48	192	3	-A2	3	C3
4	72	288	4	E1	4	E1
5	96	24	5	A3	5	A2
6	120	120	6	-E2	6	B3
7	144	216	7	D1	7	D1
8	168	312	8	E3	8	E2
9	192	48	9	-D2	9	A3
10	216	144	10	C1	10	C1
11	240	240	11	D3	11	D2
12	264	336	12	-C2	12	E3
13	288	72	13	B1	13	B1
14	312	168	14	C3	14	C2
15	336	264	15	-B2	15	D3

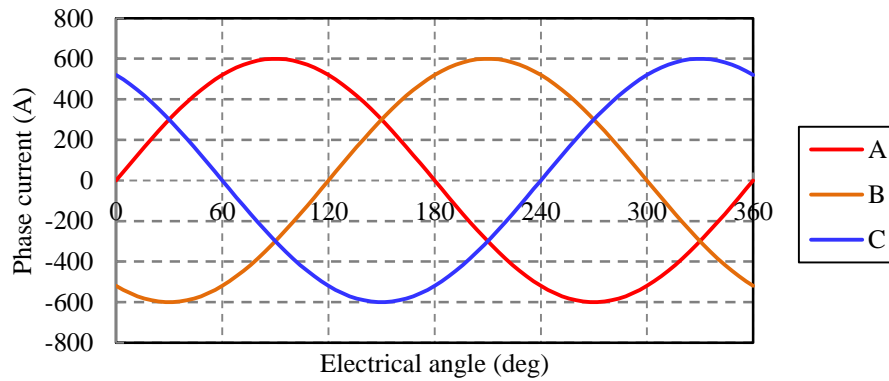
Coils are wound in the same sense, 1+, 1-, 2+, 2-, 3+, 3-, etc.



(a) Geometry of 12-slot machine

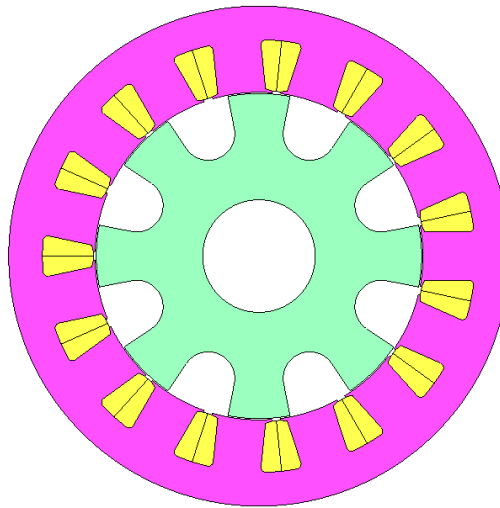


(b) 3-phase Voltage source inverter; 3-phase, star connected winding.

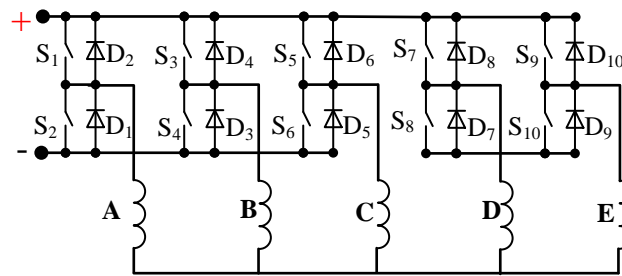


(c) Applied phase current

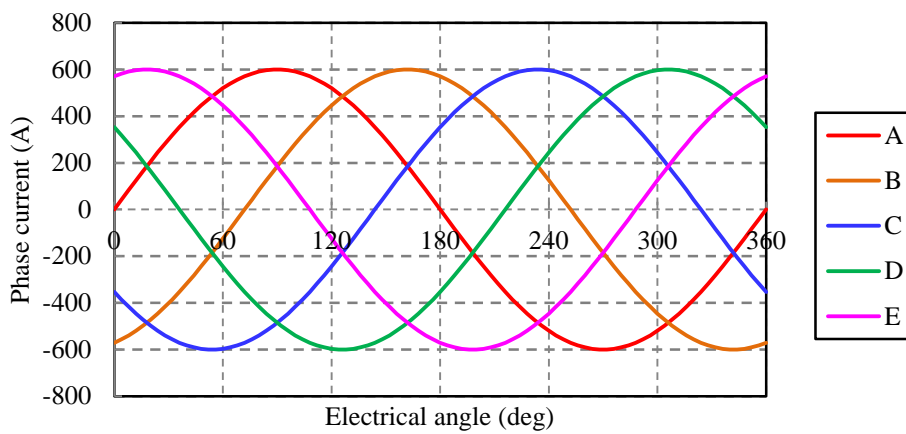
Fig. 4.15. 12-slot SR machine with sine wave current excitation.



(a) Geometry of 15-slot machine

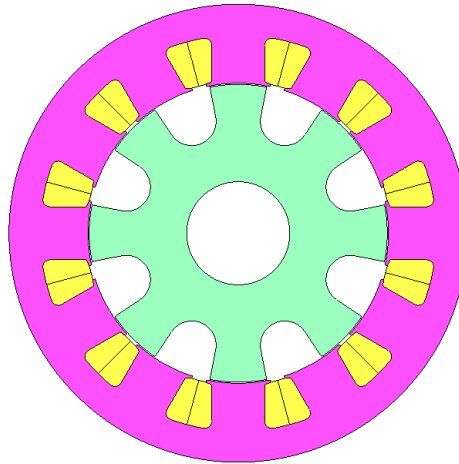


(b) 5-phase Voltage source inverter, star connected winding

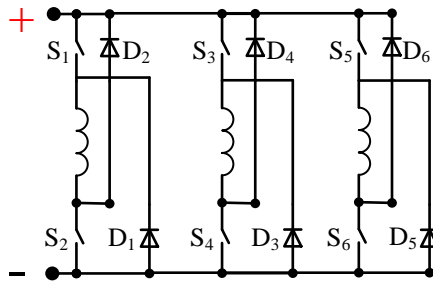


(c) Applied phase current

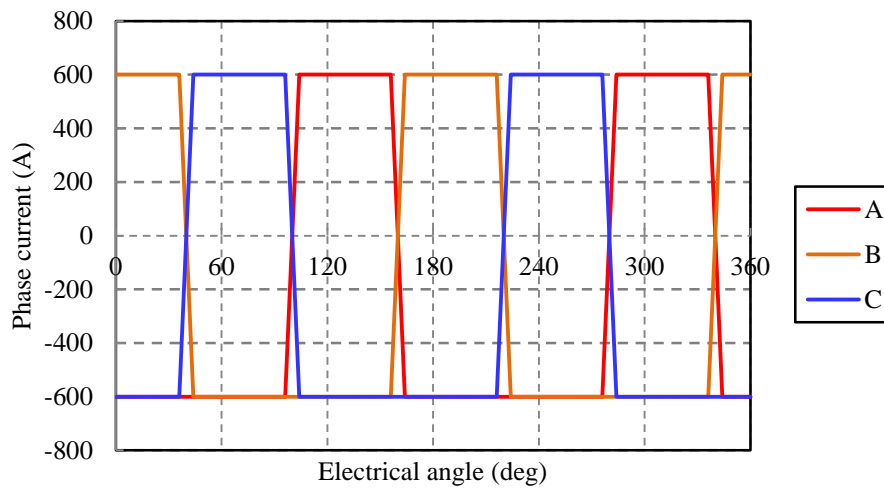
Fig. 4.16. 15-slot SR machine with square wave current excitation



(a) Geometry of 12-slot machine



(b) 3-phase Asymmetric inverter, 3-phase, 6-leadout connected winding



(c) Applied phase current

Fig. 4.17. 12-slot SR machine with square wave current excitation.

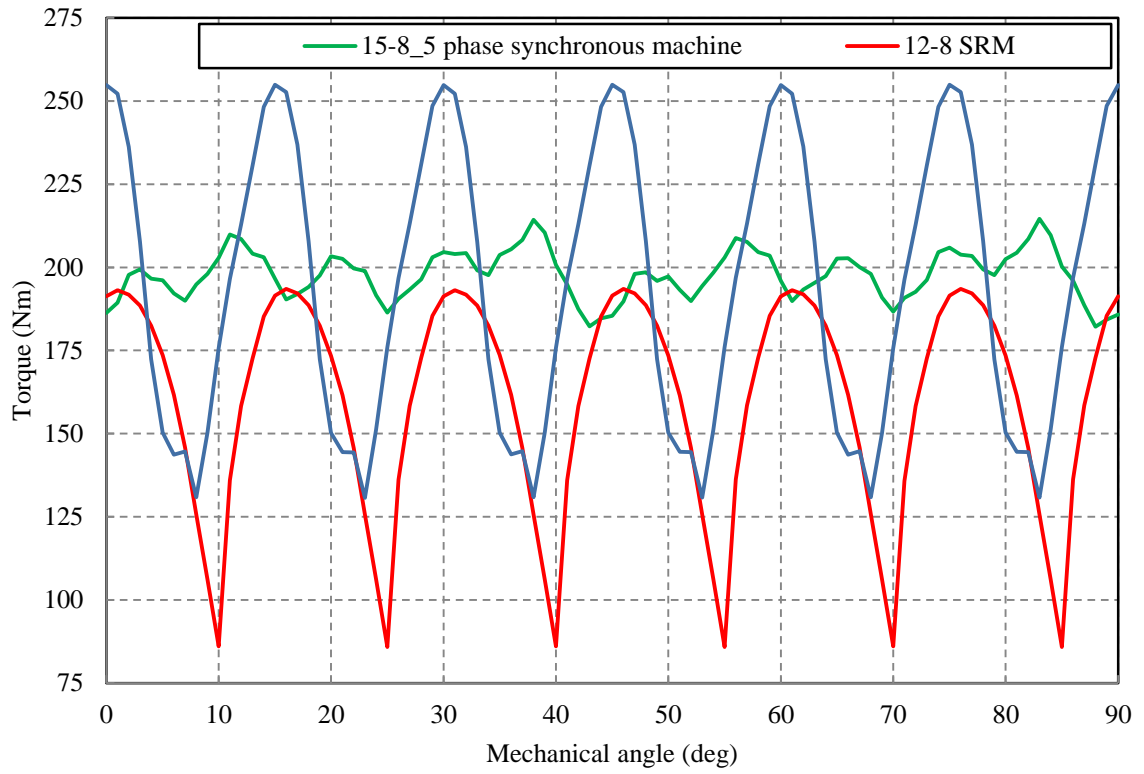
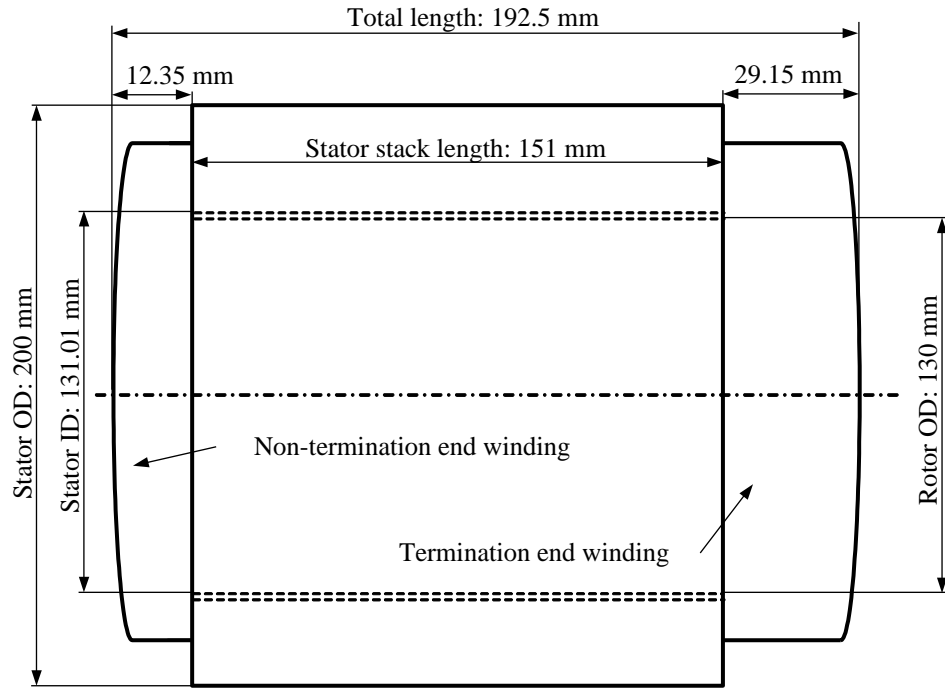
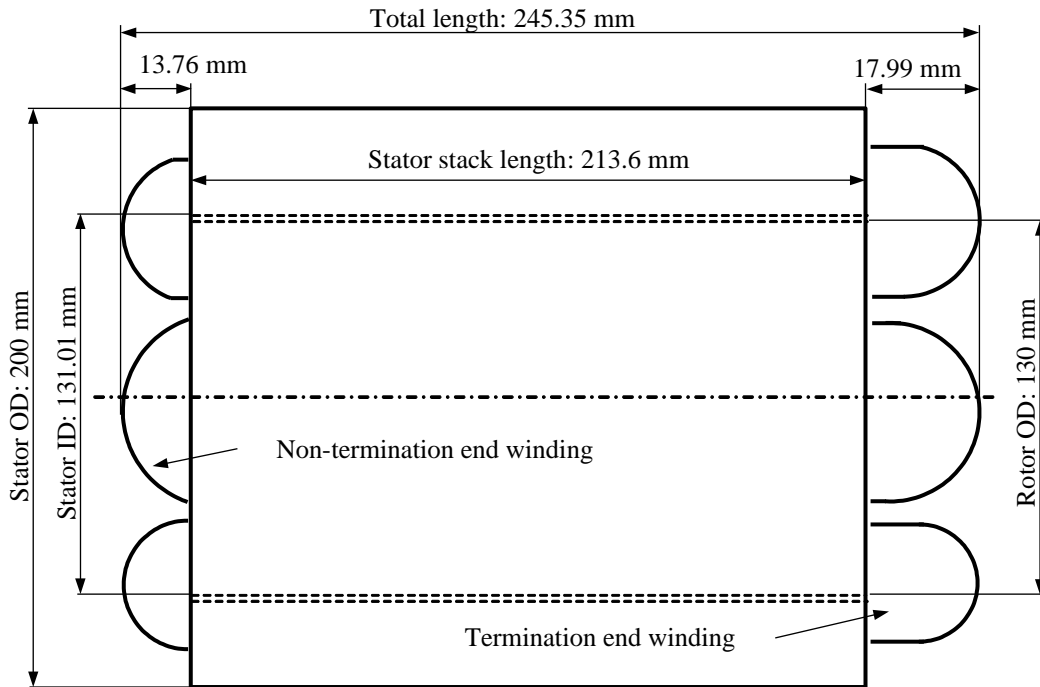


Fig. 4.18. Torque comparison of SR machines.



(a) Nissan Leaf machine



(b) 15-8 synchronous reluctance machine

Fig. 4.19. Structure comparison between Nissan Leaf machine and synchronous reluctance machine.

Table 4.15. Design parameters comparison between Nissan Leaf machine and synchronous reluctance machine.

Description		Nissan Leaf Machine	15-slot synchronous machine
Active stack length (mm)		151	213.6
Total length of end winding (mm)		41.5	31.75
Total length of machine (mm)		192.5	245.35
Number of turns per coil		8	8
Phase resistance at 20°C (mΩ)		5.67	10.11
Phase resistance at 135°C (mΩ)		8.21	14.64
Total slot area (mm ²)		3703.87	3800.71
Machine mass audit (kg)			
Stator iron		16.35	23.03
Stator copper	Active length	3.09	7.27
	End winding	1.77	1.36
	Interconnections	0.27	0.20
Total stator copper		5.12	8.83
Total stator		21.47	26.61
Rotor iron		10.55	13.54
Rotor magnets		1.99	0
Total rotor		12.54	13.54
Total iron		26.90	36.58
Total machine		34.01	45.41

4.6 Comparative study of IPM with conventional and GBDP Magnet

Grain boundary diffusion processed magnets provide advantages when applied in permanent magnet machines subject to high load and high temperature operating scenarios by preventing or reducing the onset of demagnetization. To investigate how grain boundary magnets affect the performance of interior permanent magnet (IPM) machines, one of the challenges is to model the magnet with grain boundary characteristics, in this case by assigning different material properties to individual magnet pieces within a discretized magnet pole. In this paper, scripts using commercial magnetic simulation software have been created to automatically generate the grain boundary magnets and define the material properties accordingly. Then, the performance of an IPM machine having a delta-shape rotor topology was analyzed with conventional and grain boundary magnets and results were compared. Further, demagnetization of the magnets was analyzed to verify the advantage of grain boundary magnets, illustrating that IPM machines with grain boundary magnets can realize torque and maintain efficiency at high loads while being less prone to demagnetization.

Since they were developed in 1984 [132], Neodymium Iron Boron (NdFeB) based magnets have attracted tremendous research focusing on improving their remanence and coercivity, so that the NdFeB based magnets can be downsized with lower cost while enhancing the machine performance. Adding HRE material such as Dy and Tb can enhance the coercivity because of the increase of magnetic anisotropy field. However, the remanence is lowered at the same time, since the uniformly distributed HRE increases the magnetic anisotropy field of grain boundaries and inner grain evenly [133]. In 2005, a new method named “Grain Boundary Diffusion Process (GBDP)” was proposed by Nakamura et al [134]. This process coated the HRE oxide or fluoride powders to the NdFeB sintered magnet. Then, heat-treatment is applied, so that Nd replaced HREs in Nd-rich phase and HREs diffused into the grain boundaries to form HRE-rich shells around Nd-riched phases. Fig. 4.20 (a) illustrates the GBDP with Dy source. In addition, Nagata employed vacuum technology to generate metal Dy vapor in a vacuum and diffused Dy to the crystal grain boundary [134].

GBDP has two distinct advantages compared to conventional binary alloy method. First, it can effectively improve the coercivity of NdFeB magnet without lowering the remanence. For example, the magnet produced by GBDP with TbF_3 improves the coercivity by more than 400kA/m and almost has the same remanence, as shown in the Fig. 4.20.(b). The specialized vapor deposition/diffusion technology invented by Hitachi metals can even increase remanence by 40mT while preserving the same intrinsic coercivity [136]. Second, GBDP reduces the amount of HREs used in permanent magnets. Nagata reports that, the amount of Dy in his process is just one-tenth of the Dy used in conventional magnets. Hidaka also announces that his “Homogeneous High Anisotropy field Layer (H-HAL)” process achieve 20% lower Dy content with the coercivity no less than 2.4MA/m [134].

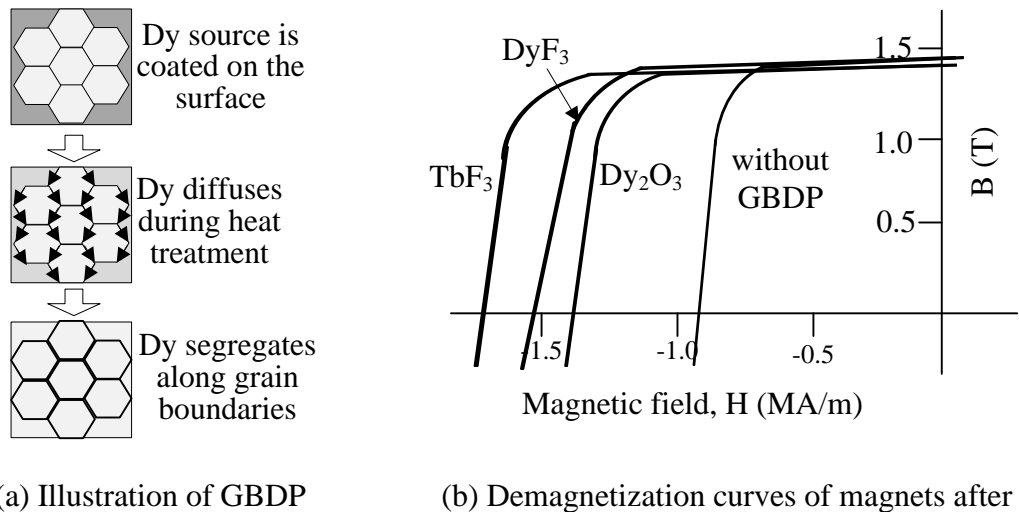


Fig. 4.20. GBDP and demagnetization curves comparison between GBDP and without GBDP[135].

4.6.1 Design process of PM machines with GBDP magnets.

GBDP permanent magnets can improve on the demagnetization limits provided by more conventional magnet grades. The machine design process is shown in Fig. 4.21. The original design is modeled with conventional magnets first and then analyzed to confirm whether the design can meet the performance requirements. Then the demagnetization analysis is performed and the maximum magnetic field strength, H , is recorded for all

working conditions, especially extreme conditions like the heaviest load and highest magnet operating temperature. Next, the GBDP magnets are selected based on the maximum H, with a tolerance to ensure the coercivity of the GBDP magnets is larger than the conventional magnets when the magnets work in the non-demagnetization region. Finally, the GBDP magnet design is modeled to verify that it meets the design requirements.

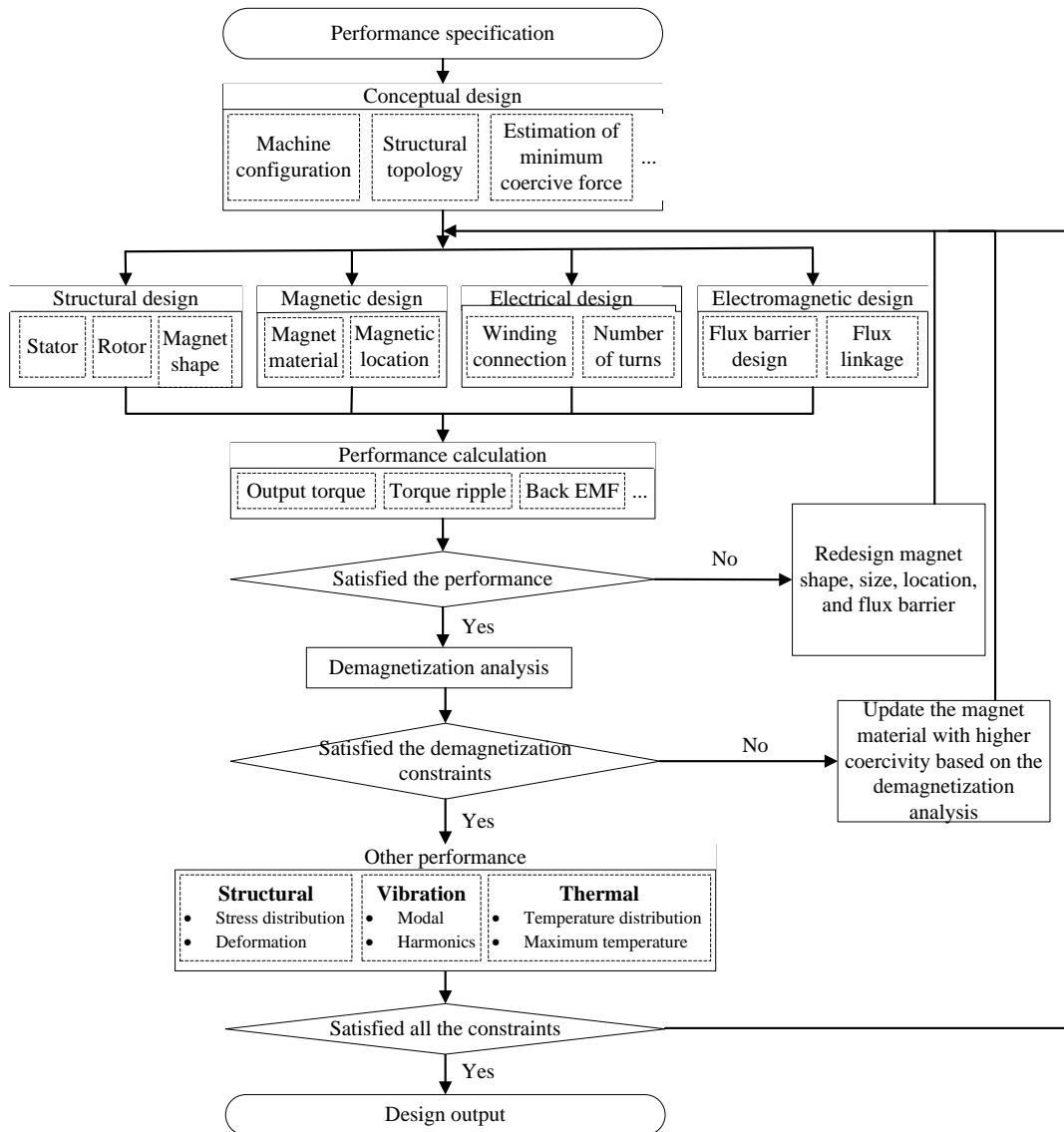


Fig. 4.21. Flow chart for the design process of permanent magnet machines using GBDP permanent magnets.

4.6.2 GBDP Magnet Modelling Process and Specification

Finite element analysis (FEA) is used to analyse an example automotive IPM machine with grain boundary and standard magnets. In the modelling process, all the machine parts except for the magnets can be created through drawing commands in the geometry editor while the grain boundary magnets need to be modelled with a certain scripting procedure. This section shows the grain boundary magnet modelling and material definition process in detail.

The magnetic characteristics of permanent magnet materials in the second quadrant reflect how they operate in an electric machine and, hence, determine machine performance. Fig. 4.22 illustrates typical magnetic characteristics of a high-energy-density rare-earth NdFeB permanent magnet. The intrinsic curve stands for the total magnetic flux potential that can be produced by the magnet material while the normal curve represents the magnetic flux which can be measured and used in the magnetic field of the electric machine. When selecting permanent magnets, one would choose materials that have high remanence and coercivity at the same time. However, from Fig. 4.22, it can be observed that the magnetic characteristic curves are sensitive to temperature for NdFeB magnets higher temperature degrades the magnetic performance in terms of the remanence and the coercivity which typically change by -0.11 and -0.6% per °C respectively. If the magnet encounters strong exterior magnetic fields or is exposed to high temperatures, the magnet will work below the knee point of the magnetization curve and operate in its nonlinear region. Hence, magnetic performance will be lost and the performance of the machine would degrade since the recoil permeability lines have lower magnetic flux density for the same coercivity [137].

In grain boundary magnets, the coercivity varies through the magnet cross-section and, hence, the magnets are modeled in a piece-wise fashion. The segmentation of the magnet is a trade-off between accuracy of the analysis and computation time. In this section, each rotor pole is comprised of three magnet pieces arranged in a delta configuration, as illustrated in Fig. 4.23. For FEA, each magnet piece is sub-divided into 0.5mm×1.0mm rectangular pieces. The N48H GBDP magnet is selected from magnet manufacturer and

the coercivity distribution for each magnet piece is defined based on the manufacturing properties, as illustrated in Fig. 4.22. The coercivity distribution in the modelled N48H GBDP magnet is at 180°C.

As discussed, coercivity distributes unevenly in the grain boundary magnet. Hence, each magnet is divided into smaller sections, and coercivity and direction of magnetization are assigned for each section.

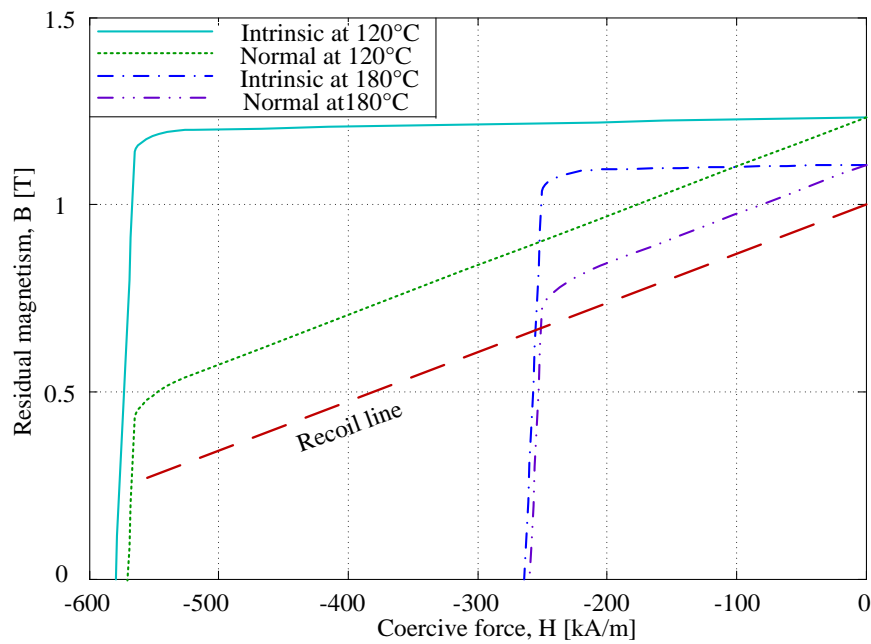


Fig. 4.22. Intrinsic and normal curves for a permanent magnet at 120 and 180 degrees centigrade and an example recoil permeability curve.

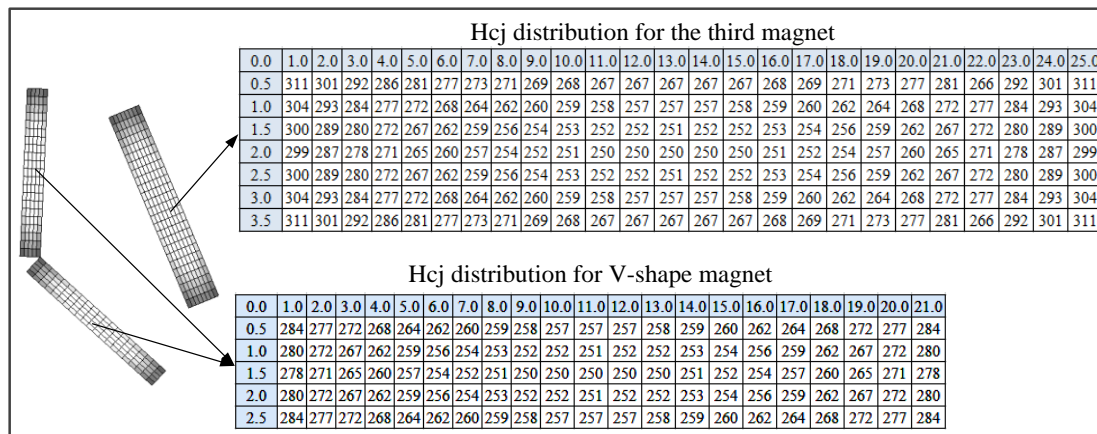


Fig. 4.23. Coercivity definition of grain boundary magnet (Unit: kA/m, 180°C).

Fig. 4.24 shows the flowchart for the programming process of the grain boundary magnet model. A coercivity distribution table that defines magnet coercivity distribution, typically provided by a grain boundary magnet manufacturer, is created in a spreadsheet. Then a conventional electric machine geometry is created in the FEA solver geometry editor. After the geometry modeling process, the electric machine with segmented magnet model is imported into the FEA solver, the main project interface for material and conditions pre-processing. The defined magnet characteristic curves are then assigned to each magnet piece with a name based on the magnet coercivity. The material defining and assigning process are then repeated until all the magnet pieces are defined. The remaining steps are assigning materials to other parts of IPM machines and assigning simulation conditions as is the case in conventional machine simulations.

The specification and finite element model for 1-pole of the example IPM machine are presented in Fig. 4.25 [91]. The machine is an 8 pole, 48 slot IPM machine with 151 mm active axial stack length. The rated base speed of 3,000 rpm is selected as an example for comparison. Both the conventional and GBDP sintered NdFeB magnets were modeled. Thus, the only difference between the two machines is their magnet coercivity distribution.

The coercivity in the conventional magnet is at the minimum value in each magnet in Fig. 4, which is -250kA/m for all three magnets. The demagnetization effect due to the stator winding is investigated to compare the performance of the two machines. The demagnetization analysis is composed of three stages: before current excitation, during current excitation, and after current excitation [102]. The current is applied in the winding only in the second stage, while in the first and third stages the machine is working under open circuit conditions. After completing the three steps, both the magnetic flux density and field strength are recorded and depicted on the B-H curve of the magnet. The demagnetization ratio, permeance coefficient distribution, induced voltage waveforms, etc. can be obtained and compared for each of the three stages.

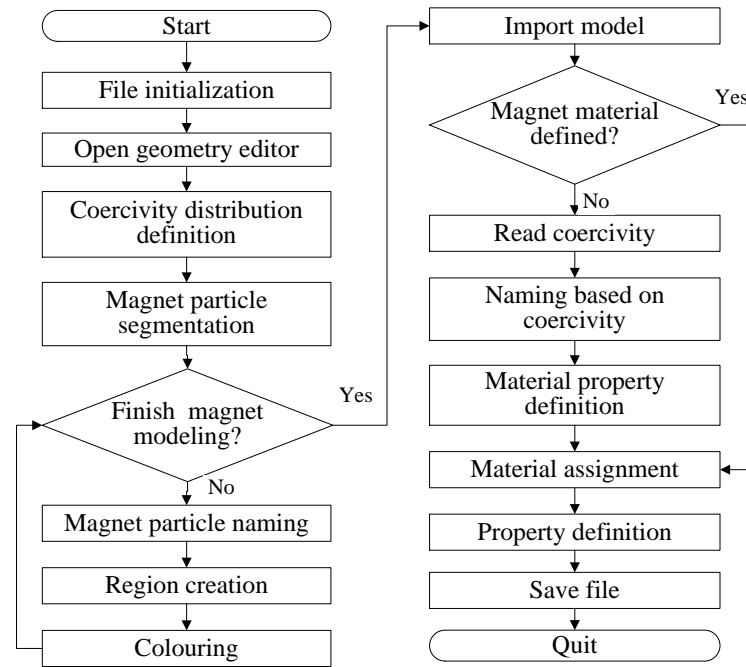


Fig. 4.24. Grain boundary magnet programming flowchart.

4.6.3 Results and comparison

In order to study the performance of grain boundary magnets comprehensively, torque analysis, loss and efficiency calculations, demagnetization analysis, magnetic operating point analysis and magnetic flux-density analysis have been conducted in FEA. Each aspect will be discussed in this section.

(a) Torque, loss, and efficiency study.

The comparison between the conventional and grain boundary magnet machines has been investigated for winding peak excitation currents ranged from 100A to 200A, as shown in Table 4.16. When operating in the linear region of the magnet's B-H characteristics at 180°C, which is 100A current amplitude, the grain boundary magnet does not provide obvious advantages when compared to the conventional magnet. However, the advantage becomes more apparent at higher currents as shown in Table 4.16. When the peak winding current increases above 140A, the GBDP magnet machine shows better performance than the conventional magnet machine, in terms of torque performance, iron

loss, and efficiency, while it performs nearly equivalently as the conventional magnet with higher coercivity.

(b) Operating Points Study.

After projecting flux-density and field strength into the magnetization direction of the magnets, the magnet operating points can be plotted on the material B-H curve. Fig. 4.24 shows the operating points with 100A and 200A peak current excitation. In Fig. 4.26 (a), all the magnetic operating points stay on the magnetization characteristic for the open circuit working conditions. No point goes into the non-linear region of the B-H characteristics; hence there is no demagnetization at this load current and operating temperature. On the contrary, under 200A peak current excitation, the magnetic operating points cross the knee point of the B-H characteristics as shown in Fig. 4.26 (b). After removing the load current, the operating points cannot go back to their original characteristic and instead operate on the recoil permeability line, which is parallel, but has smaller magnetic flux-density values. This phenomenon shows that the magnets are demagnetized when the peak phase excitation current value is at 200A and the rotor operating temperature is 180°C. For the design considered, 140A is deemed the peak rated current at 180°C.

(c) Demagnetization ratio study.

The demagnetizing ratio is defined as the amount of demagnetization from the standard specified magnetization as given by Equation (3.4) in Chapter 3.5.

The demagnetization ratio results for the conventional and grain boundary magnets machines at 100 and 200A peak phase current are shown in Fig. 4.27, other conditions being the same as in Table 4.11. It can be observed that the grain boundary magnets prevent demagnetization on the corners and edges of the magnets, compared to the demagnetization experienced by the conventional magnets. For conventional magnets, the whole magnet shares the same coercivity. Demagnetization happens where the magnetic field is strong, typically in the corners and edges of the magnets. Nevertheless, the grain boundary magnets have different coercivity distribution, where the corners and outer edges exhibit higher coercivity, than the center part. Therefore, the higher coercivity in

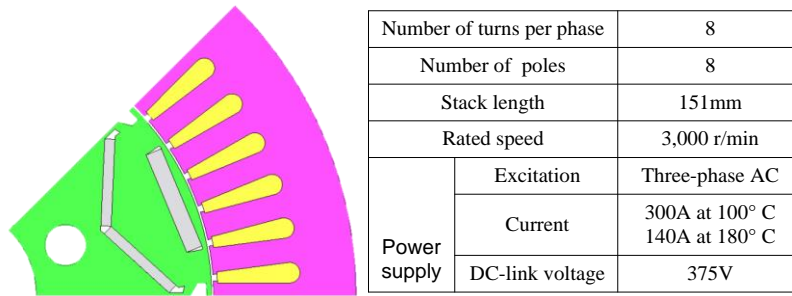


Fig. 4.25. Geometry and specifications of the IPM machines model [91].

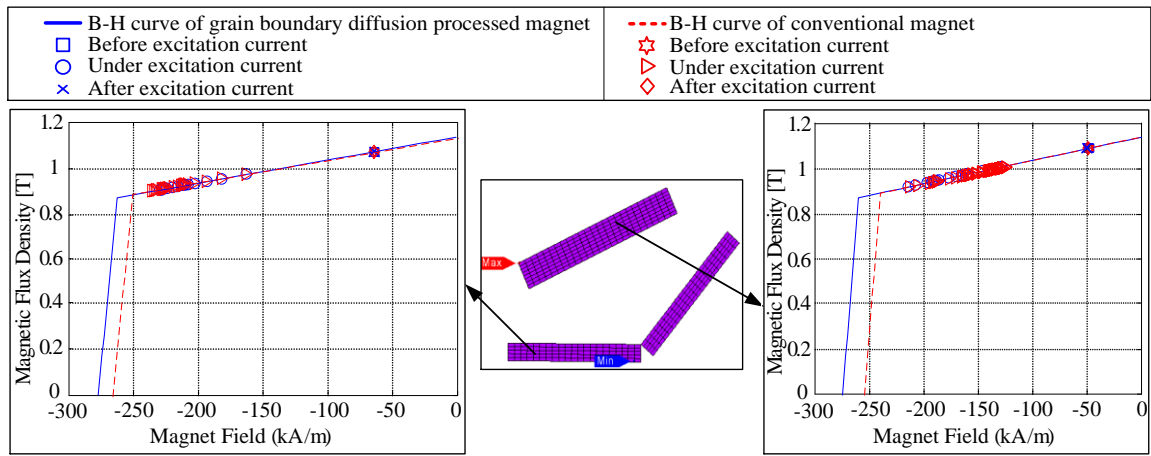
Table 4.16: Performance comparison between grain boundary magnet motor and conventional motors.

Performance	Conventional magnet	GBDP magnet
Peak phase excitation current, 100A		
Average torque (Nm)	205.76	206.06
Iron loss (W)	436.93	451.20
Efficiency (%)	97.38	97.37
Peak phase excitation current, 140A		
Average torque (Nm)	243.60	250.37
Iron loss (W)	528.03	516.74
Efficiency (%)	96.17	96.28
Peak phase excitation current, 200A		
Average torque (Nm)	244.94	254.88
Iron loss (W)	641.26	643.52
Efficiency (%)	93.04	93.29

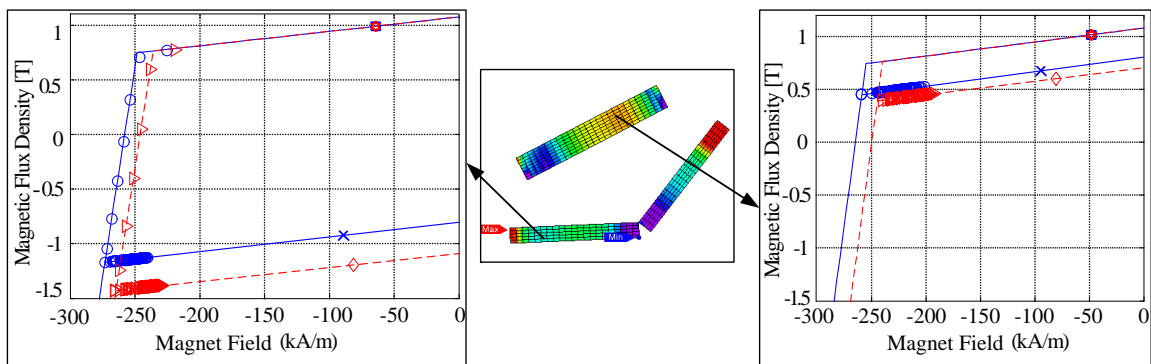
the corners and outer edges counteract the strong external magnetic field, preventing demagnetization in these regions.

Grain boundary diffusion process increases the coercivity of permanent magnets in regions subject to high demagnetization field while reducing the amount of rare-earth materials (Dysprosium). In this paper, the grain boundary magnets have been modeled automatically by running both MATLAB and FEA scripts. The performance of delta shape rotor topology IPM machines with conventional and grain boundary magnets have

been analyzed and compared based on the results of parallel FEA simulations. It is concluded that GBDP magnets have similar characteristics with conventional magnets in the linear region. However, in the nonlinear magnet B-H region, grain boundary magnets have better demagnetization performance thanks to their higher coercivity distribution on the corners and edges of the magnets. So IPM machines operating at elevated rotor temperature with grain boundary magnets can achieve better performance, such as higher average torque and higher efficiency, than machines with conventional magnets.



(a) Permanent magnet working points when peak current value is 100A



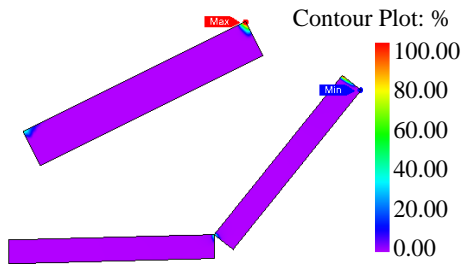
(b) Permanent magnet working points when peak current value is 200A

Fig. 4.26. Permanent magnet working points when current peak value is 100A and 200A.

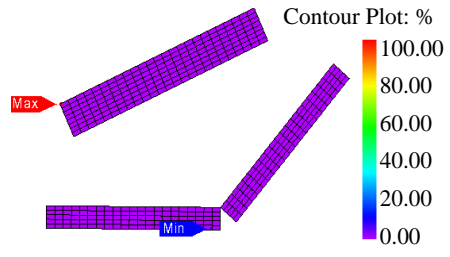
4.7 Summary

In this Chapter, different machine topologies and permanent magnet materials for traction machines are proposed. The redesigned Nissan Leaf machine rotor can achieve the performance specification for whole operation range by supplying sinusoidal phase current. The IPM and SPM machine comparative study shows that the SPM machine can obtain the IPM machine performance with the same permanent magnet material and 7% more stator OD but 20% less silicon usage in power electronics. Then the non-permanent magnet synchronous machine is proposed to study the potential of its application for traction machines.

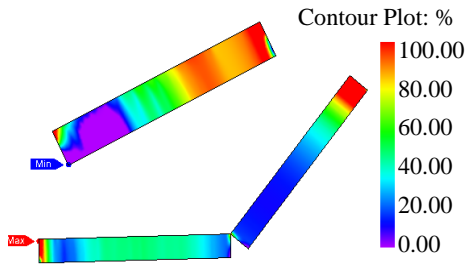
In the last section, the electric machine with grain boundary magnets are analyzed and exhibits that the grain boundary magnets are more capable to withstand the demagnetization in high temperature or high load condition than the conventional permanent magnet material.



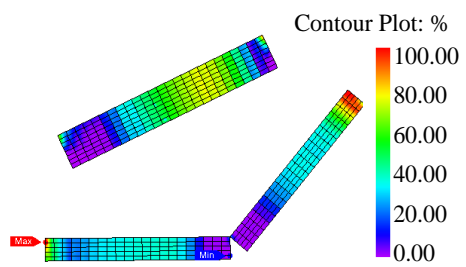
(a) Conventional magnet at 100A.



(b) GBDP magnet at 100A.



(c) Conventional magnet at 200A.



(d) GBDP magnet at 200A.

Fig. 4.27. Demagnetization ratio when current peak value is 100A and 200A.

Chapter 5

Stator Design for Volume Manufacturing

5.1 Introduction

In this Chapter, various stators are designed and compared in terms of performance and manufacturing. Both IPM and SPM rotors are compared for 48-slot distributed and 9-, 10-, 12- and 15-slot concentrated 8 pole winding schemes. The results are compared for the same performance specification in terms of supply (voltage and current), material requirements, and manufacture cost for prototype and volume production.

5.2 Fundamentals of Stator Windings

The object of winding is to produce a magnetic field in the machine that is used to create torque. As a designer, the goal is to control the magnetic field by managing the winding, i.e., position, shape, movement etc.

According to different winding construction, winding can be classified to distributed and concentrated winding. Each type of winding can have different layers, i.e. single layer, double layer, and even multiple layers. The more layers a winding has, the harder to manufacture it. Distributed windings are mainly used in the stator of AC machines, including induction and synchronous machines. It can create a sinusoidal rotating magneto motive force (MMF) distribution and magnetic field in the air-gap. Distributed windings are common on all machines, while, concentrated windings can be machine wound and widely adopted in low power or low cost machines. Further, multi-phase

windings are applied to improve the harmonic content of the air-gap MMF. i.e. make it more sinusoidal.

Specific winding has its particular characteristics. It is reported that bar-wound windings usually have larger fill factor than the stranded windings, which means bar-wound windings can provide higher torque. However, the eddy current induced in the inductor of the bar increase the copper loss and the temperature of the machine, which will be more severe in the high speed region [87]. Compared with the distributed windings, concentrated windings are claimed to have shorter end winding [85]. If the axial stack lengths are the same, short end winding results in lower copper material and less copper loss. In addition, concentrated winding is easier to be automatic wounded while the slot fill factor will be lower if automatized [138]. The number of winding layer is not only determined by the manufacturability, but the performance. The Table 5.1 shows different performance between single and double-layer concentrated windings.

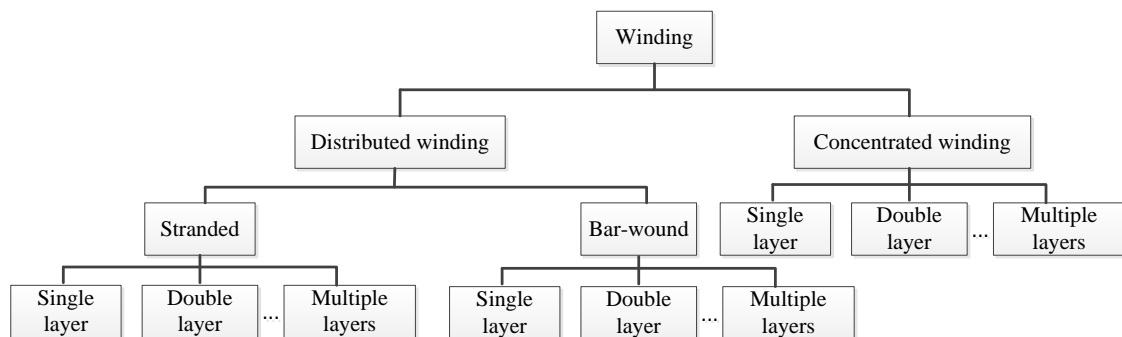


Fig. 5.1. Stator Winding classification.

Table 5.1. Comparison between single and double-layer concentrated windings [46][85].

Description	Single-layer	Double-layer
Fundamental winding factor	higher	lower
End-windings	longer	shorter
Slot fill factor	higher	lower
Mutual-inductance	lower	higher
EMF	more trapezoidal	more sinusoidal
Harmonic content of MMF	higher	lower
Eddy current losses in the PM	higher	lower
Overload torque capability	higher	lower

The concentrated winding can be classified to two major kinds. One is overlapping concentrated winding, also denoted as fractional slot concentrated winding. The other is non-overlapping concentrated winding, which means the coil is wound on each tooth separately. Single and double layer windings are popular non-overlapping concentrated winding, shown in the following figure. And the winding factors are different in these two types of winding for the same slot/pole combination.

To study the magnetic performance affected by the winding, the field solution is studied and the results are shown in Fig. 5.2. In this case, the rotor is set up as a solid cylinder with same dimension and magnetic material property. The 48 slots single layer distributed winding has evenly distributed magnetic field for both stator and rotor side. The penetration of the magnetic field on rotor is relatively deep compared with other windings. The field solution of 9 slot-8pole combination exhibits the unbalanced pull, which is not favored. The 12 slot machine has the strongest localized magnetic field on the rotor side which leads to higher rotor loss among those five designs.

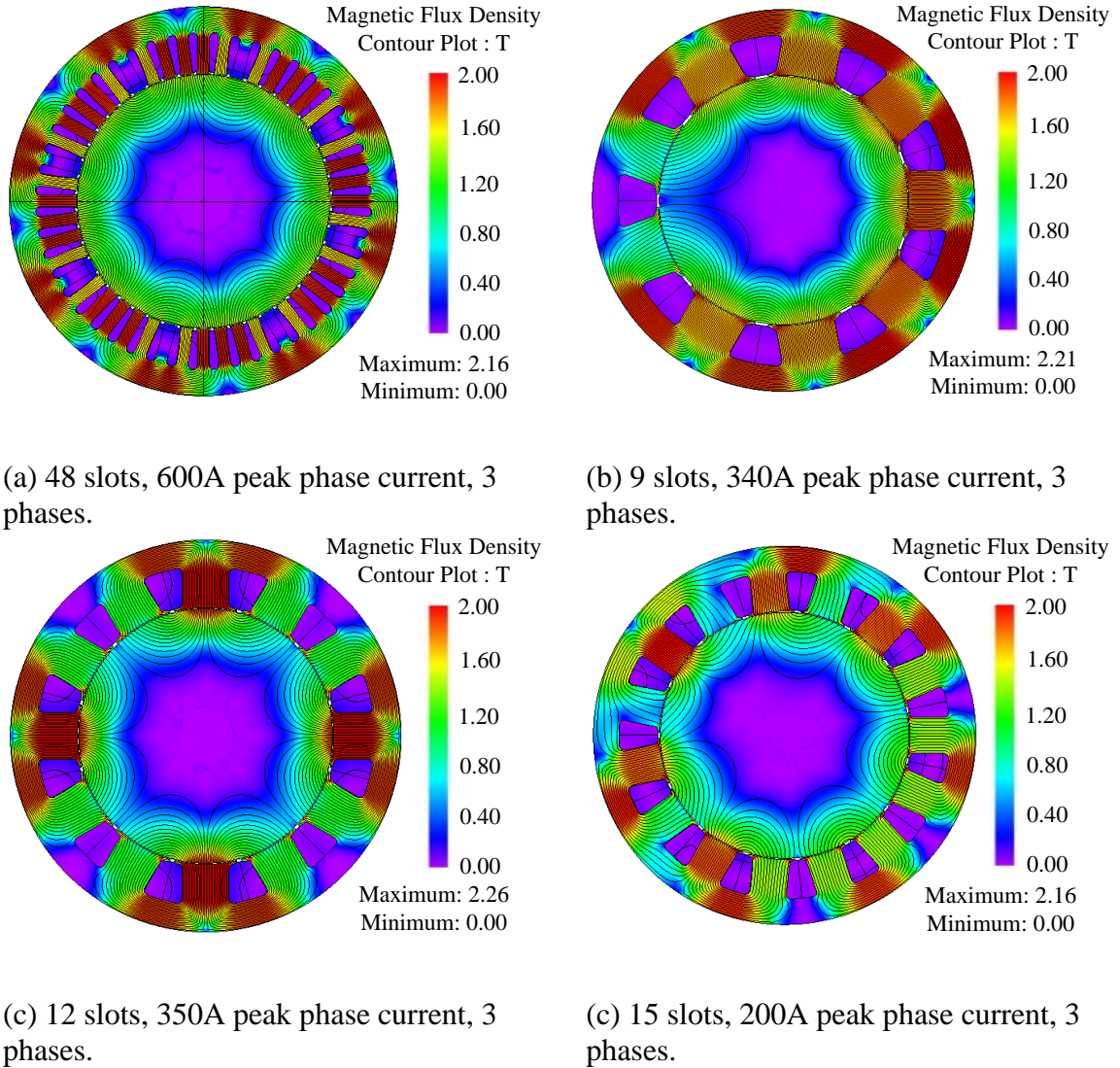


Fig. 5.2. Filed solution at 2100 rpm of different slot numbers with 8 poles, 8 turns per coil, 151mm stack length at the edge of demagnetization.

5.3 Winding Layout procedure

5.3.1 Terminologies Needs for Winding Layout

- (a) **Coil span**, also known as coil pitch, is the circumferential width of a coil, should be as close to 180° as possible but seldom exceed it to maximize the flux linked to the coil and therefore maximizes the back EMF induced in the coil. Coil span can be defining by the number of slot per magnet pole as Equation (5.1).

$$N_{sm} = \frac{N_s}{N_m} \quad (5.1)$$

where N_s is the number of slots, N_m is the number of phase. The nominal coil span in slots is the integer portion of the Equation (5.1), or the equation (5.2)

$$S^* = \max \left\{ \text{fix} \left(\frac{N_s}{N_m} \right), 1 \right\} \quad (5.2)$$

where the $\max(\cdot, \cdot)$ returns the maximum of its two arguments and the function $\text{fix}(\cdot)$ returns the integer portion of its argument.

- (b) **Pole pitch** is the distance that a magnetic pole covers in the air-gap. It can be defined as a function of the bore diameter, D or the number of slots per pole as shown in Equation (5.3)

$$\tau_p = \frac{\pi D}{p} \text{ or } \tau_p = \frac{N_s}{p} \quad (5.3)$$

where p is the pole number.

- (c) **Number of slot per pole per phase**, denominated as q , is defined as Equation (5.4):

$$q = \frac{N_s}{N_m p} \quad (5.4)$$

A very high value of q means a more sinusoidal current linkage, but it also leads to a higher number of coils and higher manufacturing cost. In practice, two to four coils per pole per phase are usually desirable in medium-size machines.

(d) **Winding factor** contributes a lot to the torque production and can be expressed as Equation (5.5).

$$k_{wn} = k_{dn} \cdot k_{pn} = \frac{\sin\left(\frac{mnp\beta}{2}\right)}{m \sin\left(\frac{np\beta}{2}\right)} \cdot \cos\left(\frac{np\alpha}{2}\right) \quad (5.5)$$

where, $k_{dn} = \frac{\sin\left(\frac{mnp\beta}{2}\right)}{m \sin\left(\frac{np\beta}{2}\right)}$ is distribution factor, $k_{pn} = \cos\left(\frac{np\alpha}{2}\right)$ is short pitch factor. β is

slot angle. $\beta = \frac{360}{N_s}$. m is the phase band, which is the group of adjacent slots of the same phase. n is the n th order of harmonic field. α is an integer multiple of the slot angle, β , $\alpha = k \cdot \beta = k \cdot \frac{2\pi}{N_s}$. p is the number of pole pairs

If magnitude of the n -th harmonic mmf produced by concentrated fully-pitched winding is F_n , the magnitude of n -th harmonic mmf produced by distributed short-pitched winding is $F_n k_{dn} k_{pn} = F_n k_{wn}$. The effect of distributing the winding is to modify the magnitude of n -th harmonic produced by our basic concentrated winding by k_{dn} , which would increase the torque in electric machines. Short-pitch can be used to reduce the length of the end windings, which can be particularly significant in 2-pole machines.

(e) **Phase offset.** The phase offset of k_0 slots leads to a 120° E offset between phase A and phase B, shifting the coils in phase C by k_0 slots from those of phase B produces another 120° E offset, thereby creating a balanced winding. The angle of k^{th} slot is shown as Equation (5.6).

$$\theta_{sl}(k) = k \frac{N_m}{2} \cdot \frac{360}{N_s} = k \frac{N_m}{N_s} 180^\circ e \quad \text{for } k = 1, 2, \dots, N_{s-1} \quad (5.6)$$

$$\text{or } \theta_{sl}(k) = \text{rem} \left(k \frac{N_m}{N_s} 180^\circ e, 360^\circ e \right) = 120^\circ e$$

There will be multiple solutions and any solution works equally well for Equation (5.6), so the smallest is usually chosen. The Equation (5.6) can be simplified to equation (5.7).

$$\text{rem} \left(k_0 \frac{3N_m}{2N_s}, 3 \right) = 1 \quad (5.7)$$

where $k_0 = \frac{2N_s}{3N_m} (1 + 3q)$, is a valid phase offset if the equation for an integer value of q in the range 1 to $\left(\frac{N_m}{2} - 1 \right)$ produces an integer results.

5.3.2 Assumptions for the Winding Layout Procedure

- (1) Three phases.
- (2) All slots are filled.
- (3) There are two coil sides in each slot. That is, the winding can be classified as a double layer winding.
- (4) Balanced winding.
- (5) The numbers of slots per pole per phase is less than or equal to 2.
- (6) All coils have the same number of turns and all span the same number of slots.

5.3.3 Integer Slot Winding Layout Procedure

The integer slot winding layout procedure is shown as Fig. 5.3. The phase offset K_0 needs to be found first and then the nominal coil span S^* , number of coils per phase N_{ph} will be

calculated. Then the first coil will be placed in phase A and angular offset will be listed. Next choose a minimum total angular spread of N_{ph} coils to be the coils for phase A and phase B and phase C will be determined by the coil offset right after. An example of 48 slots, 8 poles, 3 phases winding layout demonstrates how this procedure work.

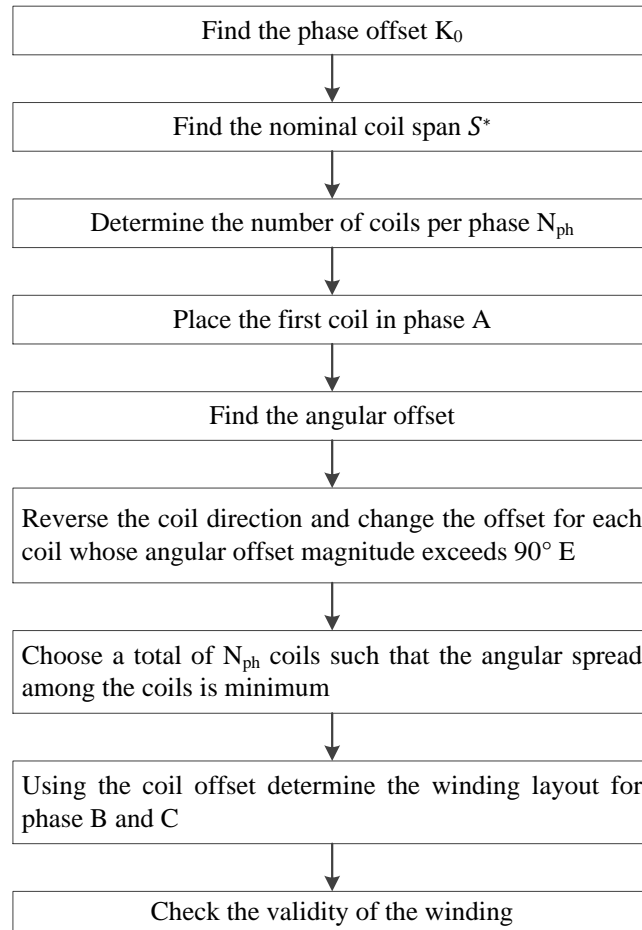


Fig. 5.3. Flowchart of integer slot winding layout procedure.

For example:

$$N_s=48, N_m=8, p=3.$$

$$\text{Phase offset is } k_0 = \frac{2N_s}{3N_m}(1+3q) = 8$$

$$q \text{ in the range 1 to 3, so coil span is } S^* = \max \left\{ \text{fix} \left(\frac{N_s}{N_m} \right), 1 \right\} = 6$$

$$\text{Number of coils per phase is } N_{ph} = 48/3=16$$

Angular slot pitch is $\theta_s = \frac{N_m}{N_s} \cdot 180^\circ e = 30^\circ e$

If the angles extend the range $-180^\circ \leq \theta \leq 180^\circ$, find the principle angle by applying the Equation (5.8).

$$\theta = \text{rem}(\theta + 180^\circ, 360^\circ) - 180^\circ \quad (5.8)$$

So the angle, in and out direction for each coil are listed in Table 5.2.

Table 5.2. Coil angle, in and out direction for each coil.

Coil	1	2	3	4	5	6	7	8	9	10	11	12
Angle	0	30	60	90	120	150	180	-150	-120	-90	-60	-30
In	1	2	3	4	5	6	7	8	9	10	11	12
Out	7	8	9	10	11	12	13	14	15	16	17	18
Coil	13	14	15	16	17	18	19	20	21	22	23	24
Angle	0	30	60	90	120	150	180	-150	-120	-90	-60	-30
In	13	14	15	16	17	18	19	20	21	22	23	24
Out	19	20	21	22	23	24	25	26	27	28	29	30
Coil	25	26	27	28	29	30	31	32	33	34	35	36
Angle	0	30	60	90	120	150	180	-150	-120	-90	-60	-30
In	25	26	27	28	29	30	31	32	33	34	35	36
Out	31	32	33	34	35	36	37	38	39	40	41	42
Coil	37	38	39	40	41	42	43	44	45	46	47	48
Angle	0	30	60	90	120	150	180	-150	-120	-90	-60	-30
In	37	38	39	40	41	42	43	44	45	46	47	48
Out	43	44	45	46	47	48	1	2	3	4	5	6

Changing the coil angle by 180° and the coil direction is reversed as listed in Table 5.3.

Table 5.3. Coil angle, in and out direction for each coil after applying Equation 4.8.

Coil	1	2	3	4	5	6	7	8	9	10	11	12
Angle	0	30	60	90	-60	-30	0	30	60	-90	-60	-30
In	1	2	3	4	11	12	13	14	15	10	11	12
Out	7	8	9	10	5	6	7	8	9	16	17	18
Coil	13	14	15	16	17	18	19	20	21	22	23	24
Angle	0	30	60	90	-60	-30	0	30	60	-90	-60	-30
In	13	14	15	16	23	24	25	26	27	22	23	24
Out	19	20	21	22	17	18	19	20	21	28	29	30
Coil	25	26	27	28	29	30	31	32	33	34	35	36
Angle	0	30	60	90	-60	-30	0	30	60	-90	-60	-30
In	25	26	27	28	35	36	37	38	39	34	35	36
Out	31	32	33	34	29	30	31	32	33	40	41	42
Coil	37	38	39	40	41	42	43	44	45	46	47	48
Angle	0	30	60	90	-60	-30	0	30	60	-90	-60	-30
In	37	38	39	40	47	48	1	2	3	46	47	48
Out	43	44	45	46	41	42	43	44	45	4	5	6

Choose those coil angles closest to 0° for phase A and minimizing the total spread of angles will generally maximize motor performance. The chosen coils and angle is listed in Table 5.4.

Table 5.4. Chosen coils for phase A.

Coil	1	2	7	8	13	14	19	20	25	26	31	32
Angle	0	30	0	30	0	30	0	30	0	30	0	30
In	1	2	13	14	13	14	25	26	25	26	37	38
Out	7	8	7	8	19	20	19	20	31	32	31	32

So the winding layout of the 48-slots, 8-poles, 3-phases machine is shown as Table 5.5.

Table 5.5. Winding layout of the 48-slots, 8-poles, 3-phases machine.

Slot	Phase A	Phase B	Phase C
1	In & In		
2	In & In		
3		Out & Out	
4		Out & Out	
5			In & In
6			In & In
7	Out & Out		
8	Out & Out		
9		In & In	
10		In & In	
11			Out & Out
12			Out & Out

Note: 13-48 slot repeat the winding layout in 1-12 slot for four times.

The harmonics produced by conductor density can be used to judge the quality of winding layout. The fundamental harmonics needs to be maximized to get the larger output torque and the summation of other harmonics excluding the fundamental should be as small as possible to minimize the loss.

During Fourier transform, both positive and negative frequencies will be obtained. Since the negative frequency does not exist, this part will be converted to the negative region by the complex conjugate. When the frequency domain signals are converted to the time domain, the negative frequency will be considered to reproduce the original time domain signals.

5.4 Comparative Study between Concentrated and Distributed Windings for EV's

In this section, various winding types are discussed and compared in terms of performance and manufacturing. Both IPM and SPM rotors are compared for 48-slot distributed and 9-, 10- and 15-slot concentrated pole winding schemes. The results are compared for the same performance specification in terms of supply (voltage and current) and material requirements.

5.5.1 Winding Connection Design

Similar with distributed windings, the connection of concentrated windings affect the machine performance significantly. In order to get the maximum torque with minimum loss, the connections with maximum winding factor is selected. Table 5.6 and Table 5.7 show the concentrated winding connections for 9- and 15-slot 8-pole combination. The winding connection for 12-slot 8-pole combination has been shown in Table 4.10 in Chapter 4.5.

Table 5.6 Three phase concentrated winding connection for 9 slot machine.

3-Phase, 9 teeth			0 degree choice	
Tooth	Mech angle	Elect angle	Tooth	Coil
1	0	0	1	-A1
2	40	160	2	A2
3	80	320	3	B3
4	120	120	4	-B1
5	160	280	5	B2
6	200	80	6	C3
7	240	240	7	-C1
8	280	40	8	C2
9	320	200	9	A3

Table 5.7 Three phase concentrated winding connection for 15-slot machine.

3-Phase, 15 teeth			0 degree choice	
Tooth	Mech angle	Elect angle	Tooth	Coil
1	0	0	1	A1
2	24	96	2	B4
3	48	192	3	-A2
4	72	288	4	-B5
5	96	24	5	A3
6	120	120	6	B1
7	144	216	7	C4
8	168	312	8	-B2
9	192	48	9	-C5
10	216	144	10	B3
11	240	240	11	C1
12	264	336	12	A4
13	288	72	13	-C2
14	312	168	14	-A5
15	336	264	15	C3

5.5.2 Preliminary Design of Concentrated Winding Machines

This is the primary step to have a rough idea of how the performance of IPM with concentrated winding. For all the concentrated windings machines, the same slot area with Nissan Leaf machine is adopted although there is a slight difference among Nissan leaf machine, 9-, 12-, and 15-slot stator during the specific cases. So in this step, the stack length, number of turns and phase resistance are kept the same with the Nissan leaf winding. The stack length for 9-slot and 12-slot are all 151mm, the number of turns is 8, and the phase resistance is 0.00821Ω . One thing needs to be pointed out is that both the 9-slot and 12-slot IPM concentrated winding machine are all on the edge of demagnetization and the peak phase current is limited by the demagnetization, so as the maximum output torque.

The performance of 9-slot and 12-slot IPM machine with concentrated windings at base speed (2100rpm) is shown in Table 5.8. From Table 5.8, we can see that the 9-slot machine generates lower torque with lower cogging torque and torque ripple compared to

12-slot machine. However the most severe problem of these two machines is that there is a high spike in the phase voltage, which means these IPM concentrated winding machines cannot provide required torque performance with the same inverter of Nissan leaf machine.

Then the SPM rotor is introduced to the 9-, 12-, 15-slot concentrated winding and preliminary performance tests are also done with 151mm stack length, 8 turns per coil, and 0.00821Ω phase resistance. The results are shown in Table 5.9. The terminal voltage of those SPM machines is much smoother than the IPM. Fig. 5.5, 5.6, and 5.7 shows the phase voltage waveforms of 9-, 12-slot and 15-slot IPM and SPM machines and their corresponding flux density distribution. It can be seen that the local saturation on stator and rotor causes the high spike on the phase voltage. From machine design side, this issue can be solved by change the design parameters. It has been noted in this thesis that the SPM rotor help get rid of the problem in this situation. Meanwhile, Zhu et al also pointed out that the change of slot and pole number combination can also reduce the distortion in the phase voltage waveform [139-141].

Table 5.8. Performance comparison among 9-slot, 12-slot and 15-slot IPM machine with concentrated winding at base speed (120°C).

Description		Base speed 2100rpm		
		9-slot	12-slot	15-slot
Open circuit back EMF (V)	RMS	51.857	61.923	63.73
	Peak	84.106	93.754	91.48
Maximum average torque (Nm)		169.664	185.116	166.92
Excitation torque ripple* (%)		4.637	18.310	6.57
$V_{\text{phase_RMS}}$ (V)		119.514	126.108	117.16
$V_{\text{phase_peak}}$ (V)		300.798	217.297	174.43
$I_{\text{phase_peak}}$ (A)		300	230	200
Current excitation angle (Electrical)		25	35	35
Peak-peak T_{cogging} (Nm)		0.392	3.972	0.13

Table 5.9. Performance comparison among 9-slot, 12-slot and 15-slot SPM machine with concentrated winding at base speed (120°C).

Description		Base speed 2100rpm		
		9-slot	12-slot	15-slot
Open circuit back EMF (V)	RMS	61.997	76.959	78.76
	Peak	77.484	102.955	125.04
Maximum average torque (Nm)		197.110	250.564	225.79
Excitation torque ripple* (%)		3.038	7.985	2.59
$V_{\text{phase_RMS}}$ (V)		90.272	116.094	106.76
$V_{\text{phase_peak}}$ (V)		134.108	175.838	146.98
$I_{\text{phase_peak}}$ (A)		340	350	310
Current excitation angle (Electrical)		0	0	0
Peak-peak T_{cogging} (Nm)		0.873	7.221	0.63

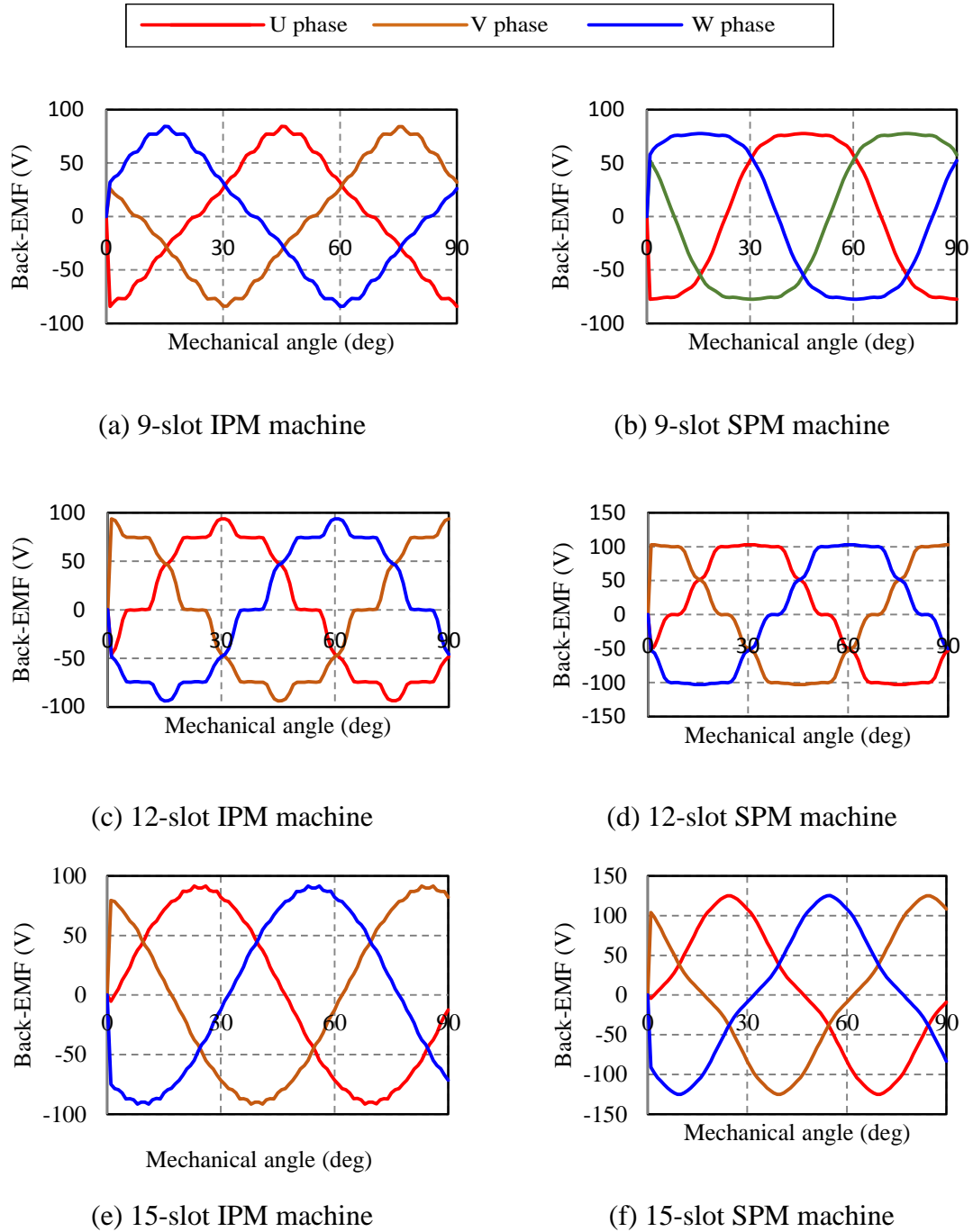
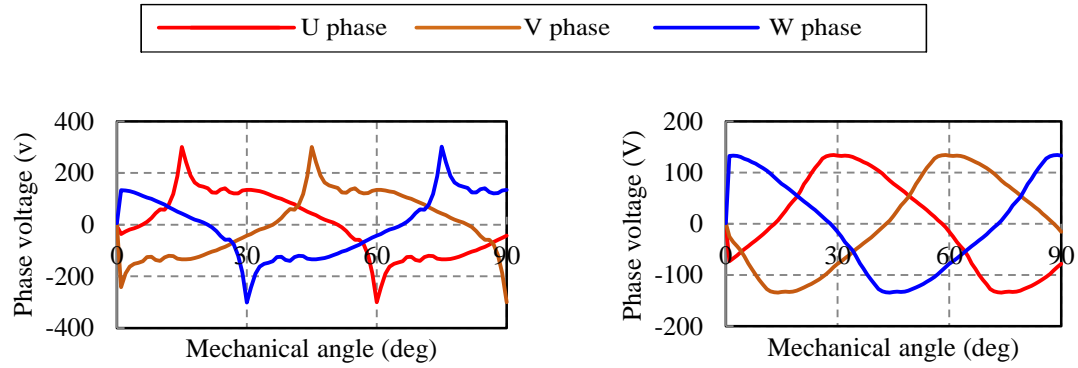
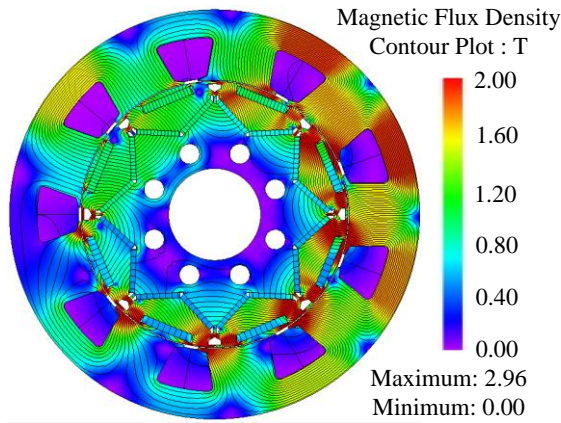


Fig. 5.4. Back-EMF of 9-, 12-, 15-slot IPM and SPM machine at 2100rpm.

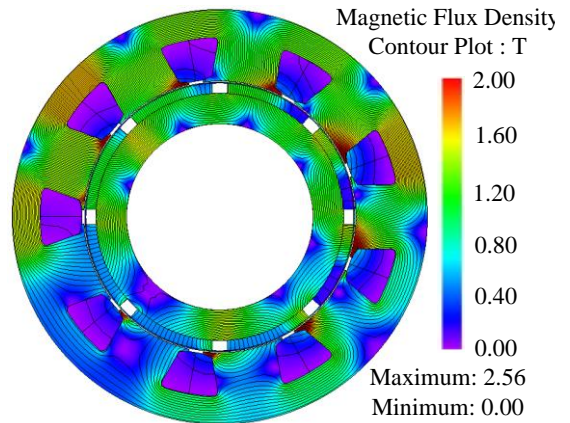


(a) Phase voltage of 9-slot IPM machine

(b) Phase voltage of 9-slot SPM machine

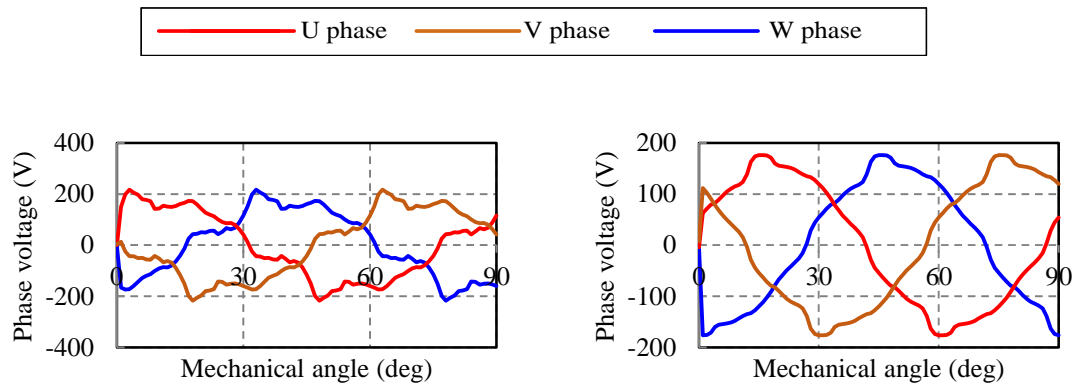


(c) Flux density distribution of 9-slot IPM machine



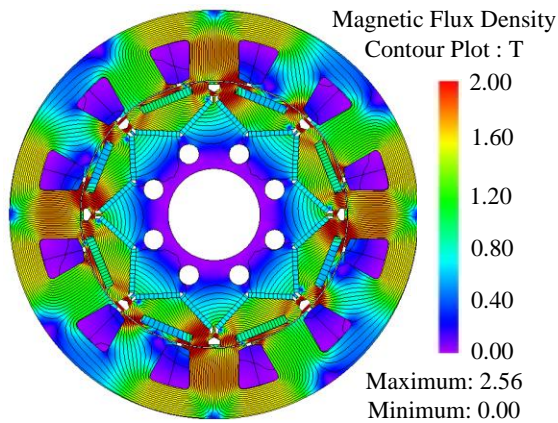
(d) Flux density distribution of 9-slot SPM machine

Fig. 5.5. Phase voltage and magnetic flux density distribution of 9-slot IPM and SPM machine at 2100rpm, full load.

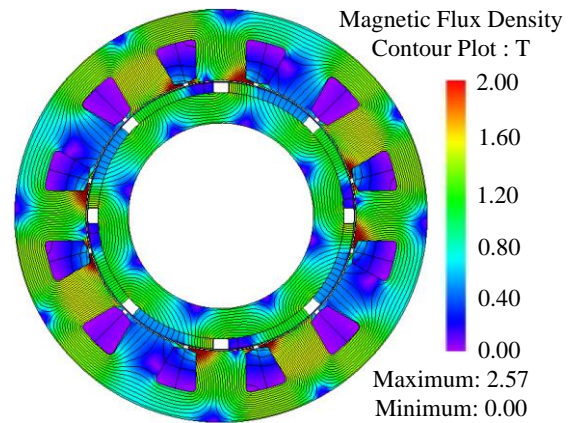


(a) Phase voltage of 12-slot IPM machine

(b) Phase voltage of 12-slot SPM machine

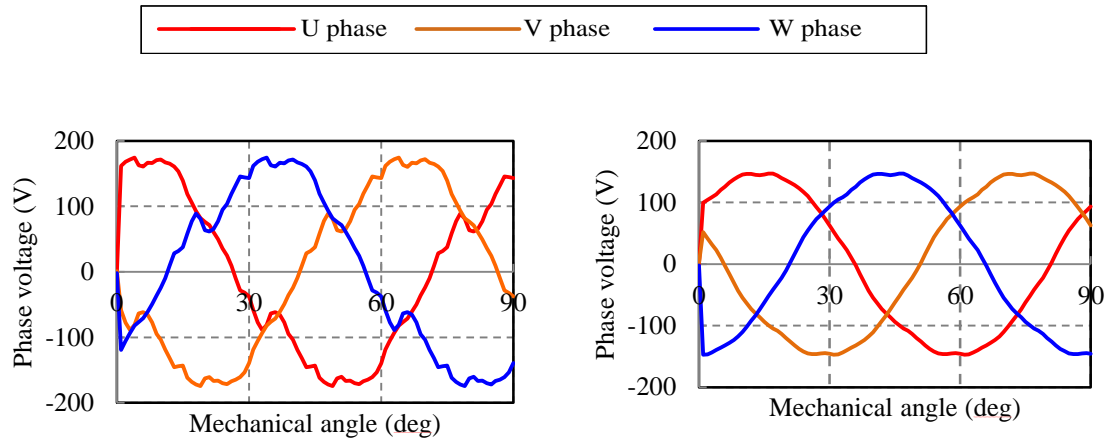


(c) Flux density distribution of 12-slot IPM machine



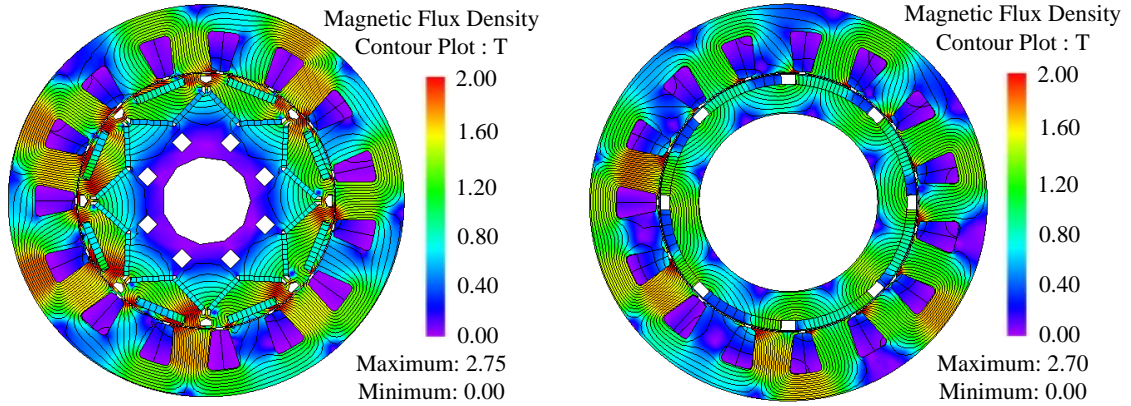
(d) Flux density distribution of 12-slot SPM machine

Fig. 5.6. Phase voltage and magnetic flux density distribution of 12-slot IPM and SPM machine at 2100rpm, full load.



(a) Phase voltage of 15-slot IPM machine

(b) Phase voltage of 15-slot SPM machine



(c) Flux density distribution of 15-slot IPM machine

(d) Flux density distribution of 15-slot SPM machine

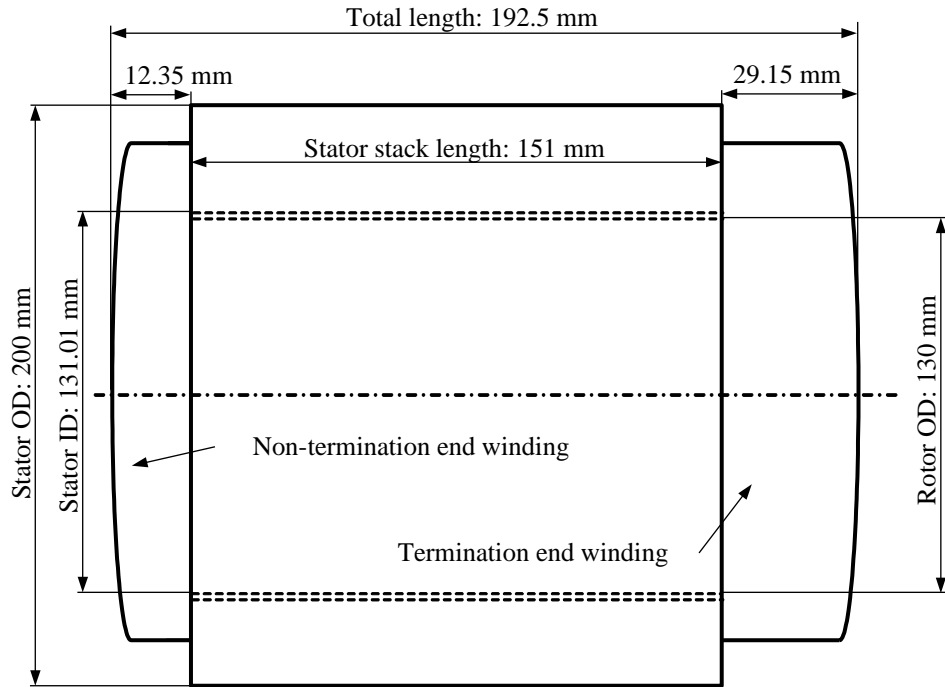
Fig. 5.7. Phase voltage and magnetic flux density distribution of 15-slot IPM and SPM machine at 2100rpm, full load.

5.5.3 Concentrated Winding SPM Machine Design and Performance

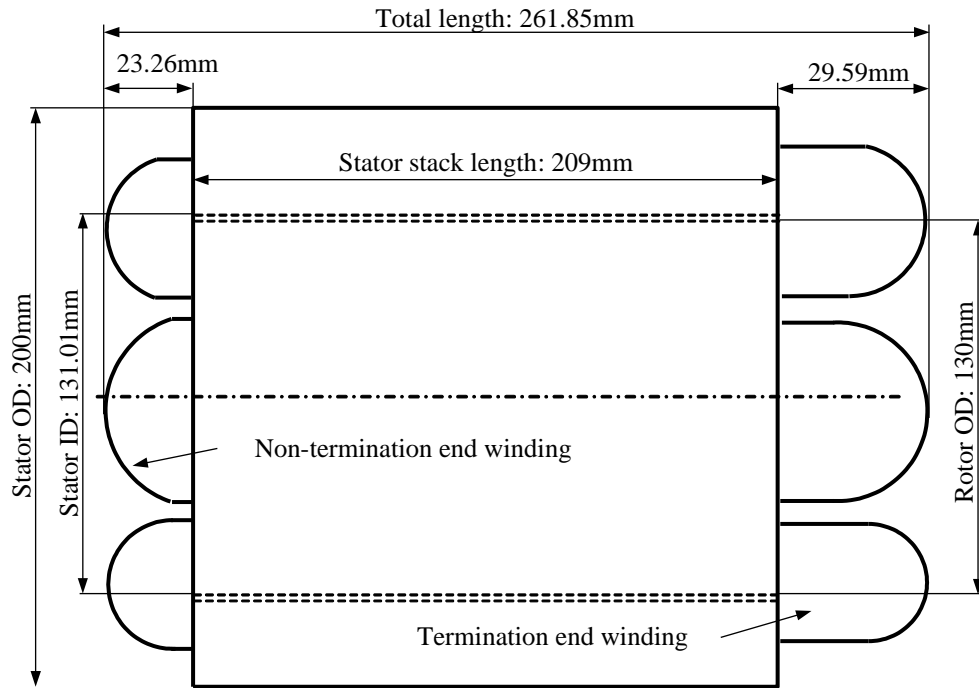
The SPM machines with concentrated windings are selected as design candidates to be redesigned to meet the requirements of Nissan leaf machine. The design parameters, including stack length and number of turns, are adjusted. The final design parameters are

shown in Table 5.10. Compared to distributed integer slot Nissan Leaf machine, the concentrated winding SPM consumes more materials due to the increased active stack length. However, the end-turns length is shorter, so the total machine length is very similar. The concentrated winding can obtain higher slot fill factor than the distributed winding. In this paper, 0.8 is supposed to all the concentrated winding design candidates since it is normal for automatically wound tooth. Here, the ampere turns in preliminary design is applied to each machine to keep the demagnetization on edge. In addition, the torque at low speed and high speed need to be satisfied with the similar peak phase voltage in low speed and DC link voltage limit in high speed. The fill factor of each machine is also kept the same. After redesigned, the stack lengths of 9-, 12- and 15-slot concentrated winding machine are increased. The end winding lengths also change due to the different winding arrangement and layout compared to the distributed winding. The machine structure and dimensions compared to Nissan leaf machine are shown respectively in Fig. 5.8, 5.9 and 5.10. For the 9-slot concentrated winding machine, both the stack length and total end winding length is longer than the Nissan Leaf distributed winding machine. So the end winding length of concentrated winding machines are not always shorter than distributed winding machines. It is determined by both the winding type and the machine geometry and dimensions. The total end-winding lengths of 12- and 15-slot concentrated winding machine are shorter than the Nissan Leaf distributed winding machine, which is commonly stated in the published literatures.

The machine performance of 9-, 12- and 15-slot concentrated windings is presented in Table 5.11. Among those three machine, the 9-slot one need smallest current and smaller cogging torque and excitation torque ripple, while the 12-slot one produce less core loss. One thing needs to be noted that there are unbalanced magnetic pull in 9-slot 8-pole machines which may lead to noise and vibration in real application. Fig. 5.5 (c) and (d) shows that the magnetic flux density distributes unevenly in 9-slot machine causing the unbalanced magnetic pull.

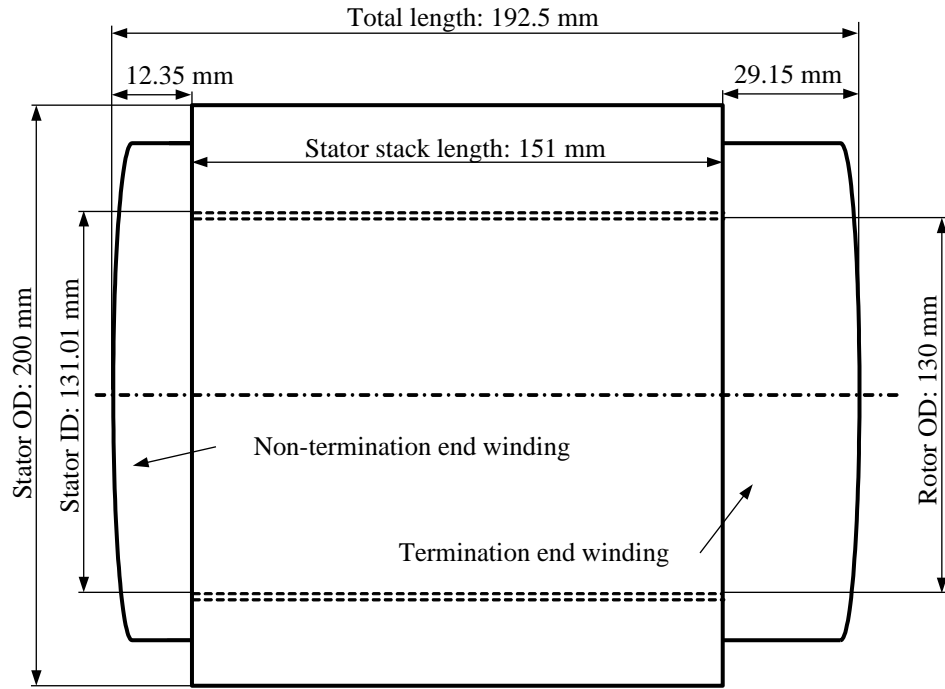


(a) Nissan Leaf machine

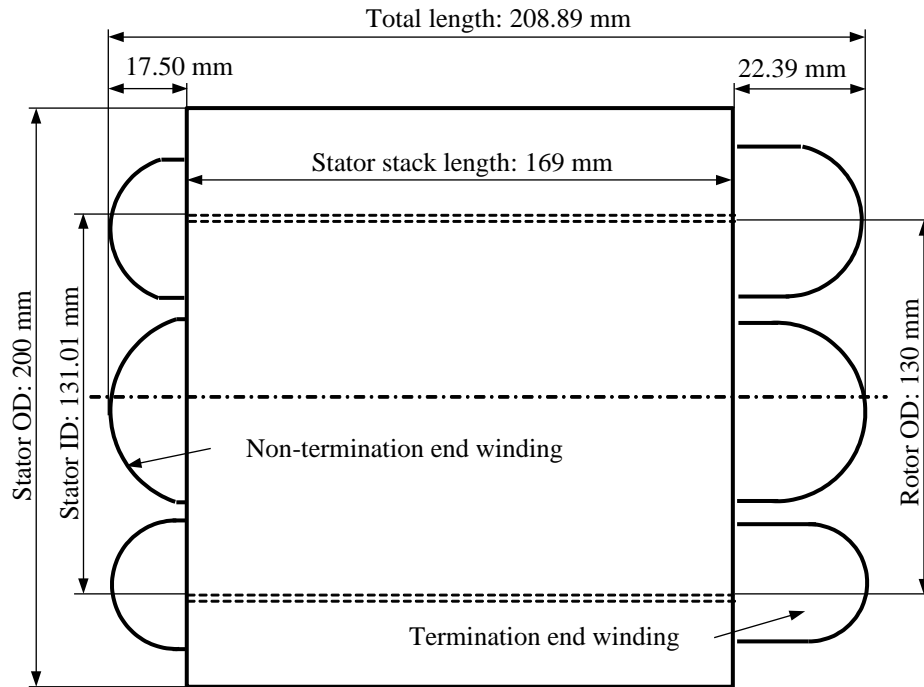


(b) 9-slot concentrated winding machine

Fig. 5.8. Structure comparison between Nissan Leaf machine and 9-slot concentrated winding machine.

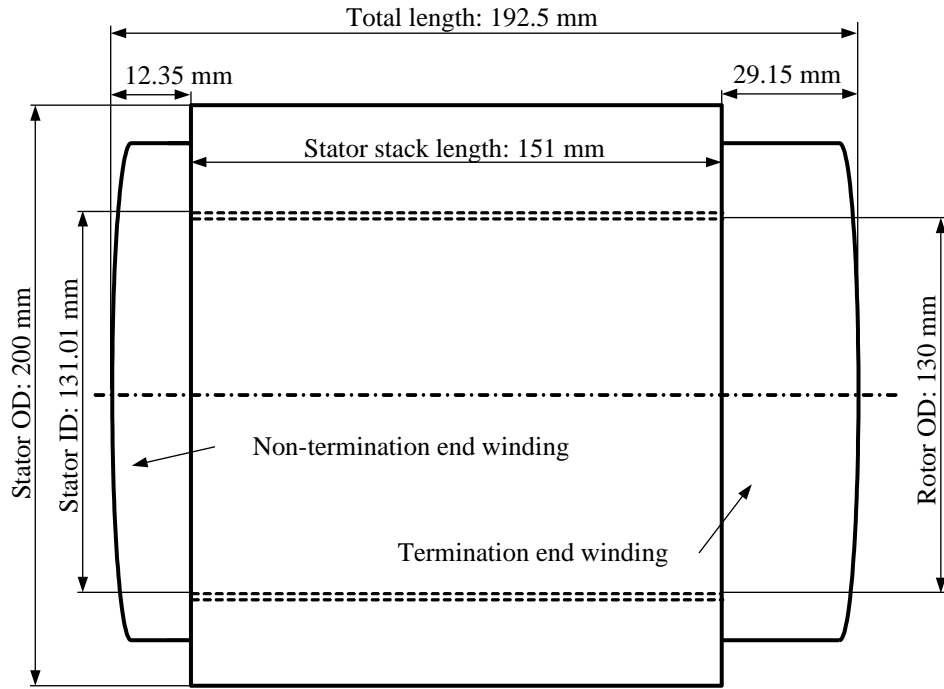


(a) Nissan Leaf machine

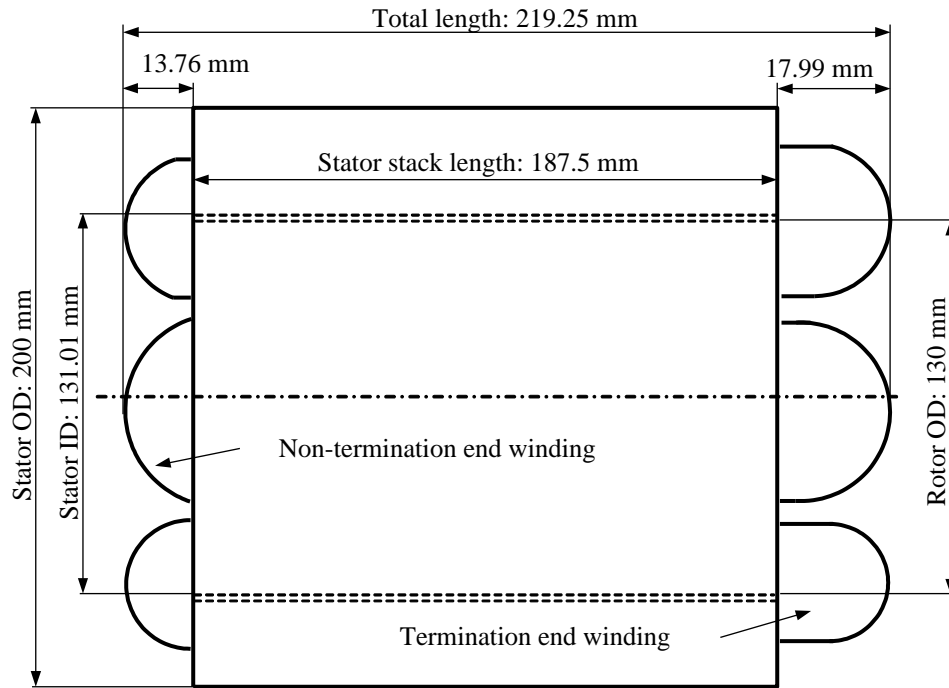


(b) 12-slot concentrated winding machine

Fig. 5.9. Structure comparison between Nissan Leaf machine and 12-slot concentrated winding machine.



(a) Nissan Leaf machine



(b) 15-slot concentrated winding machine

Fig. 5.10. Structure comparison between Nissan Leaf machine and 15-slot concentrated winding machine.

Table 5.10. Design parameter comparison between 3 phase 9 slot, 12 slot and 15 slot SPM machine with concentrated winding.

Description	9-slot SPM machine	12-slot SPM machine	15-slot SPM machine	Nissan Leaf Machine	48-slot SPM machine	
Active stack length (mm)	209	169	187.5	151	151	
Total length of end winding (mm)	52.85	39.89	31.75	41.5	41.5	
Total length of machine (mm)	261.8	208.9	219.2	192.5	192.5	
Number of turns per coil	7	5	5	8	12	
Phase resistance at 20°C (mΩ)	8.37	6.66	10.11	5.67	8.15	
Phase resistance at 135°C (mΩ)	12.12	9.65	14.64	8.21	11.80	
Total slot area (mm ²)	3907.74	3742.99	3800.71	3703.87	5694.90	
Machine mass audit (kg)						
Stator iron	22.33	18.32	20.22	16.35	19.40	
Stator copper	Active length	5.87	4.53	5.13	3.09	4.73
	End winding	2.33	1.68	1.36	1.77	2.71
	Interconnections	0.12	0.37	0.20	0.27	0.27
Total stator copper	8.33	6.58	6.69	5.12	7.71	
Total stator	30.66	24.90	26.61	21.47	27.11	
Rotor iron	7.73	6.25	6.93	10.55	5.60	
Rotor magnets	2.66	2.15	2.38	1.99	1.92	
Total rotor	10.39	8.40	9.31	12.54	7.52	
Total machine	41.05	33.30	35.92	34.01	34.63	

In terms of the cost, the manufacturing cost of lamination is pretty close for the volume progressive die stamping. Compared with IPM rotor, the manufacturing of SPM rotor cost more due to the magnets retainment. The manufacturing process cost for distributed and concentrated windings are also similar for the automated winding methods. So the material cost contributes a big portion to the total manufacturing cost. From Table 5.12, we can see that the 9-slot SPM machine uses 11.07% more steel, 33.65% more magnet, but 12% less copper material compared to the Nissan Leaf machine. The 12-slot SPM

machine needs 9.20% less steel, 25% less copper, and 8.10% more permanent magnet material. Among all the materials, permanent magnet material is the most expensive material. Concentrated windings are easier to be automated, but only if the stator is segmented. A non-segmented stator lamination design would result in lower slot packing factor for an automated winding design.

Table 5.11. Performance comparison among 9 slot, 12 slot and 15 slot SPM machine with concentrated winding at base and at top speed (120°C).

Description		Base speed 2100rpm			Top speed 10,000rpm		
		9 slot	12 slot	15 slot	9 slot	12 slot	15 slot
Open circuit back EMF (V)	RMS	75.08	53.83	61.12	357.54	256.35	291.06
	Peak	93.84	72.02	97.04	446.86	342.97	462.04
Average torque (Nm)		280.31	280.43	279.86	76.69	76.41	76.30
Excitation torque ripple (%)		3.03	7.98	2.59	5.22	17.65	3.04
$V_{\text{phase_RMS}}$ (V)		110.75	84.63	83.91	139.13	148.16	141.82
$V_{\text{phase_peak}}$ (V)		164.95	126.92	115.81	214.12	213.79	211.02
$I_{\text{phase_peak}}$ (A)		400	560	495	279.50	280.00	320
Current excitation angle (Electrical)		0	0	0	66	55.50	63.7
Peak-peak T_{cogging} (Nm)		1.21	8.80	0.79	1.21	8.08	0.79
Stator iron loss (W)		225.45	204.53	199.78	613.35	592.88	606.89
Rotor iron loss (W)		74.18	7.04	18.94	438.16	17.40	117.98
Iron loss (W)		299.63	211.57	218.72	1051.51	610.28	724.86
Copper loss (W)		2908.80	4539.36	5380.75	1420.23	1134.84	2248.70
Mechanical loss (W)		17.15			388.89		
Total loss (W)		3225.58	4768.08	5616.62	2860.62	2134.01	3362.46
Efficiency (%)		95.03	92.82	91.64	96.56	97.40	95.96

5.5 Aluminum Stator Winding Design

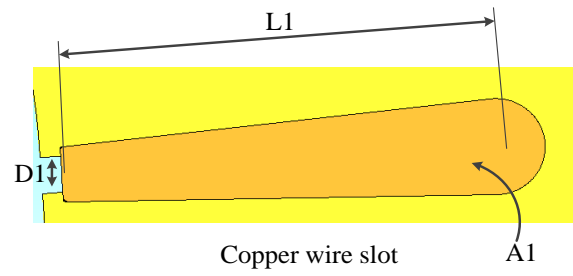
The increase in hybrid and electric vehicle traction machines may pose a challenge to future copper resources. Here, an aluminum winding configuration is considered to investigate the impact on machine design for such a material change.

Assume that the aluminum conductors can be manufactured as per the copper conductors, i.e. 0.71mm diameter aluminum wires electrically insulated from each other, 15 wires for one turn and 8 turns per slot. Hence, 15×8 wires are electrically connected at the machine phase and star-point terminals. The challenges for the aluminum windings are:

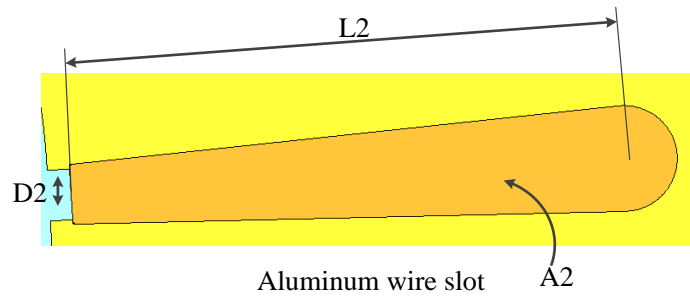
- (a) The manufacture and handling of the small diameter separately insulated aluminum wire.
- (b) Transposition (axial twist) of the 15 wires as the 8 turns is wound.
- (c) Jointing of the terminal connections.
- (d) The issue of durability during repetitive electrical pulse cycling.

The benchmark Nissan Leaf machine is again used for comparison. The rotor geometry remains unchanged, while the stator slot for the aluminum wound machine is extended to increase winding surface area and maintain stator Joule loss to be equitable for the two designs. Fig. 5.11 shows the slot geometry comparison between copper winding and aluminum winding and Table 5.12 presents the main dimensions. This longer stator tooth and back iron volume results in an increase in stator iron volume and mass. But the net winding loss is reduced. Thus the aluminum wound machine demonstrates a 4% net increase in specific power (kW/kg) due to a reduced total active mass of 2kg but a 15% reduction in power density (kW/liter) based on the Nissan Leaf machine and peak power rating of 80kW.

Although the reduction in power density looks quite detrimental, it is actually an increase in machine outer diameter from 200mm to 220mm, which is a relatively small increase (10%) in dimension.



(a) Copper wire slot



(b) Aluminum wire slot

Fig. 5.11. Machine slot geometries.

Table 5.12. Comparison between copper and aluminum wire slot.

Description	Copper wire	Aluminum wire
D (mm)	D1=1.88	D2=2.4
L (mm)	L1=22	L2=25.3
Area (mm ²)	A1=96.2	A2=105.8
Winding mass (kg)	5.67 ^[69]	3.603
Outer diameter of stator (mm)	200	220

5.6 Comparative Study between Stranded and Bar Wound Windings for EV's

Nowadays, although the stranded windings are popular in EV's traction motor, bar wound windings are also applied in some commercial EV vehicles, for example, GM Chevy Volt [142] and Toyota Prius 4th generation [143]. According to GM and Toyota's published information, the proper designed bar wound winding machine can provide torque requirements from low speed up to maximum speed with competitive efficiency compared with stranded windings. So a bar wound winding is designed based on the Nissan Leaf stator. Fig. 5.12 shows two options for layer arrangement of the bar wound windings. Because of the limitation of skin effect, the 8-layer arrangement is selected to be this bar wound winding connection.

The phase resistance of bar wound winding is $11.45\text{m}\Omega$, which is 39.46% more than the stranded windings. So the copper loss of bar wound winding machine is 39.46% higher than the stranded winding machine with same peak phase current amplitude. The performance comparison between stranded and bar wound IPM machine at corner speed and top speed is shown at Table 5.13. The efficiency of bar wound machine decrease due to higher iron loss and copper loss compared to stranded winding machine.

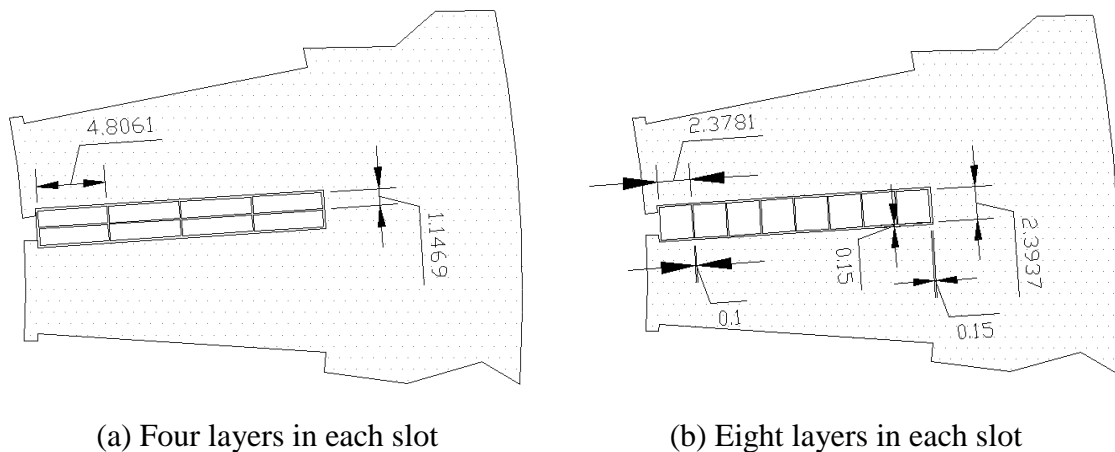


Fig. 5.12. Options for bar wound winding.

5.7 Summary

This Chapter discusses how different winding designs and winding layout affect the performance, manufacturability and material cost of the machines. The 9-, 12-, and 15-slot concentrated winding IPM machine have higher peak phase voltage than the concentrated SPM machine due to higher saturation in rotor and stator iron. Compared to Nissan Leaf IPM machine, the concentrated winding machines utilize more magnet material and have longer stack length, but lower excitation torque ripple and peak phase current in constant torque region. The aluminum winding design and investigation indicates that the aluminum winding can reduce the winding weight with same thermal and electromagnetic performance. However, the mechanical strength of transposition and terminal joint still a concern. The bar wound winding design based on the Nissan Leaf stranded winding stator can gain slightly higher torque than the stranded winding in the low speed region while the copper loss and iron loss increase more.

Table 5.13. Performance comparison between stranded and bar wound distributed winding IPM machine at corner and top speed (120°C).

Description		Base speed 2100rpm		Top speed 10,000rpm	
		Stranded	Bar wound	Stranded	Bar wound
Open circuit back EMF (V)	RMS	33.53	33.45	159.65	159.31
	Peak	48.93	49.03	233.18	233.69
Maximum torque (Nm)		283.01	288.59	75.15	67.44
Excitation torque ripple* (%)		8.54	10.32	38.13	39.33
$V_{\text{phase_RMS}}$ (V)		65.49	72.52	116.65	121.73
$V_{\text{phase_peak}}$ (V)		99.88	109.62	216.76	220.15
$I_{\text{phase_peak}}$ (A)		600.00	600	353.5	316
Current excitation angle (Electrical degrees)		50.00	45.00	77.25	76.60
Peak-peak T_{cogging} (Nm)		1.26	1.319	1.26	1.319
Stator iron loss (W)		259.25	330.02	1881.76	2015.94
Rotor iron loss (W)		38.92	66.06	364.29	804.75
Iron loss (W)		298.17	396.08	2246.06	2820.68
Copper loss (W)		4433.40	6183.00	1538.91	1715.03
Mechanical loss (W)		17.15		388.89	
Total loss (W)		4748.72	6596.23	4173.86	4924.60
Efficiency (%)		92.91	90.58	94.96	93.48

Chapter 6

Multiphase Machine Design and Study

6.1 Introduction

In this Chapter, multiphase machines with concentrated and distributed windings will be designed to satisfy the Nissan Leaf machine performance and comparative studies between multiphase machines and three phase machines will be discussed as well. The 2×3-, 5-, and 9-phase machines are designed and evaluated from both machine and power electronics sides, as well as material audit.

6.2 2×3-Phase Machine Design with Distributed Winding

Based on the advantages of multiphase machine mentioned above, the 2×3 phase is selected to compare the performance with the Nissan Leaf benchmark machine. The machine structures are exactly same. The only difference is the winding connection, which actually the difference in current source. Unlike the conventional three phase machine, the 2×3 phase machine needs two inverters with 30 degree electric shift. The current requirement for each inverter is downsized to half of the three phase machine. The FEA results of the 2×3 phase machine are shown in Table. 6.1. The maximum torque at base speed of 2×3 phase machine is 5.04% higher than the conventional three phase machine. However, the phase voltage exceeds the voltage limit and cannot meet the torque requirement in the high speed region.

The winding connections are shown as Fig. 6.1 and 6.2. Instead of the 2 slot winding per pole per phase, the 2×3-phase connection becomes 1 slot per pole per phase and two three phase current supply having a 30 electric degree shift. And the current amplitude is divided to two half parts. Fig. 6.3 explains the winding connection relationship of 2×3-phase machine. Assuming the length of A21 to A24 and A11 to A14 are all 1.0 p.u., so the length of A_{total} will be 1.9318 p.u., which is 3.5% less than 2. So the back-EMF of 2×3-phase is around 3.5% higher than that of 3-phase. Fig. 6.4 shows the Inverter comparison between 3- and 2×3-phase machines. It is obvious that the inverter size of 2×3-phase machine is doubled compared to 3-phase machine, but the current in each inverter leg is just half of that of 3-phase machine inverter. So the current handling capability of the higher phase number machine is much better than the 3-phase machine.

In order to meet the 280Nm requirement of low speed region, the 2×3 phase machine can be redesigned to save cost. From the inverter side, the excitation current can be reduced 6.17% to 565A so that the current requirement of inverter can be reduced. If considering the machine, the stack length can be decreased 6.17% to 142mm so that the 2×3 phase machine can meet the low speed torque specification. The two redesign ideas are also verified by the FEA results and shown in Table 6.2. The results provide two options for the machine designer or researchers in related field. However, none of 2×3-phase IPM machine can achieve the required torque specification at top speed within the voltage constraint.

Similar to 2×3-phase IPM machine, the 2×3-phase SPM machine is also designed and the results are shown in Table 6.3 and 6.4. If the same excitation current is applied to the 2×3-phase and 3-phase SPM machine design, the 2×3-phase machine can gain 2.59% more torque at 2100RPM than the 3-phase SPM machine as shown in Table 6.3. Unfortunately, the 2×3-phase SPM cannot realize the requiring torque at top speed within the voltage constraint. So the 2×3-phase SPM machine is redesigned to use either less excitation current for same active stack length with 3-phase SPM machine or same excitation current but shorter active stack length than the 3-phase SPM machine. Table 6.4 shows that 464A peak phase current is needed to excite the 151mm active stack length

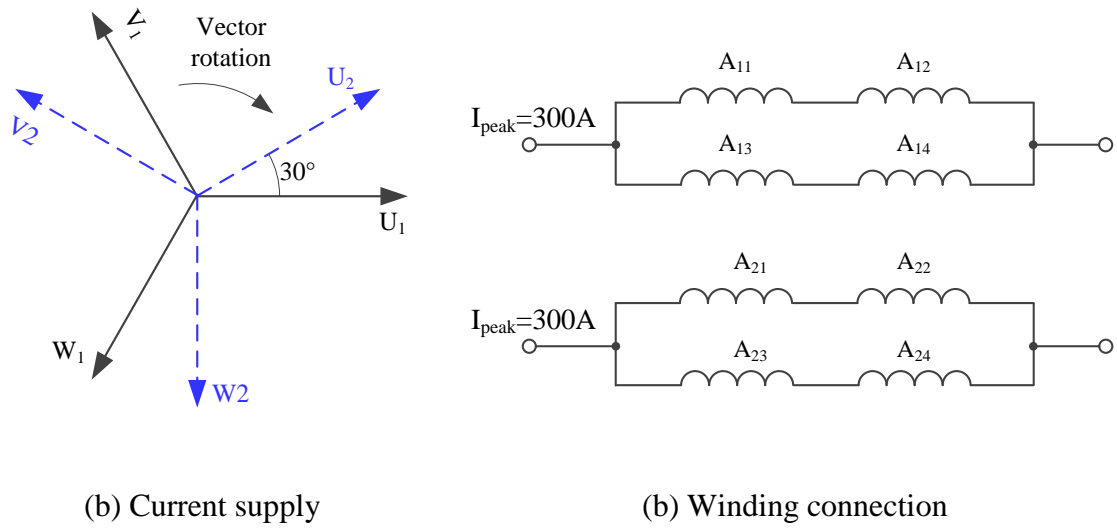


Fig. 6.1. 2x3 phase machine winding set.

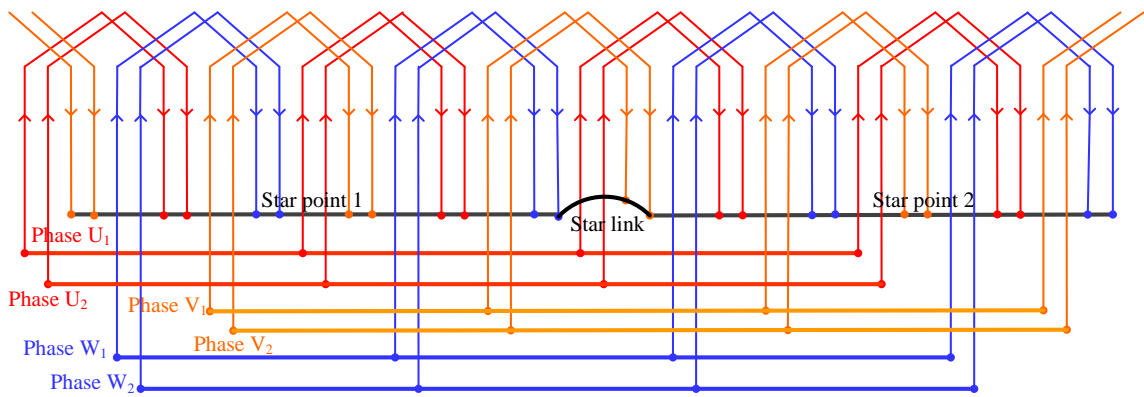


Fig. 6.2. Winding connection of 2x3-phase machine.

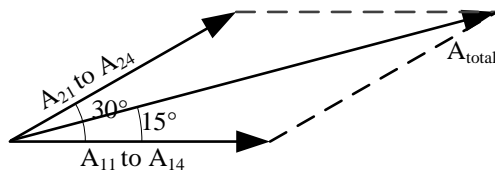
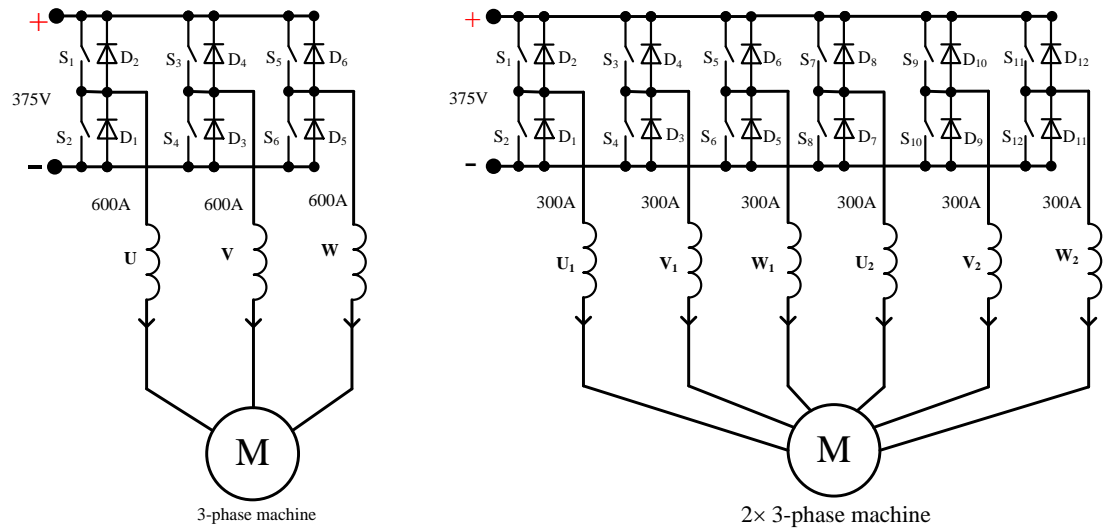


Fig. 6.3. Winding connection relationship of 2x3-phase machine.



(a) Inverter of 3-phase machine

(b) Inverter of 2×3-phase machine

Fig. 6.4. Inverter comparison between 3- and 2×3-phase machine.

Table 6.1. Performance comparison between 3-phase and 2×3-phase IPM machine with distributed winding at base and top speed (120°C).

Description		Base speed 2100rpm		Top speed 10,000rpm	
		3 phase	2×3 phase	3 phase	2×3 phase
Open circuit back EMF (V)	RMS	33.53	34.80	159.65	165.71
	Peak	48.93	49.24	233.18	234.68
Maximum torque (Nm)		283.01	297.28	75.15	76.33
Excitation torque ripple* (%)		8.54	5.47	38.13	7.87
$V_{\text{phase_RMS}}$ (V)		65.49	67.44	116.65	163.00
$V_{\text{phase_peak}}$ (V)		99.88	94.16	216.76	294.66*
$I_{\text{phase_peak}}$ (A)		600.00	600.00	353.5	260.80
Current excitation angle (Electrical degrees)		50.00	50.00	77.25	70.15
Peak-peak T_{cogging} (Nm)		1.26			
Stator iron loss (W)		259.25	258.87	1881.76	1642.19
Rotor iron loss (W)		38.92	36.63	364.29	219.78
Iron loss (W)		298.17	295.50	2246.06	1861.97
Copper loss (W)		4433.40	4433.40	1538.91	837.62
Mechanical loss (W)		17.15		388.89	
Total loss (W)		4748.72	4746.05	4173.86	3088.48
Efficiency (%)		92.91	93.23	94.96	96.28

*cannot realize required torque within voltage constraint.

Table 6.2. Redesign of 2×3-phase IPM machine with distributed winding (120°C).

Description		Base speed 2100rpm		Top speed 10,000rpm	
		151mm stack length	142mm stack length (-6%)	151mm stack length	142mm stack length
Open circuit back EMF (V)	RMS	34.80	32.72	165.71	155.83
	Peak	49.24	46.29	234.68	220.76
Maximum torque (Nm)		281.63	279.56	76.33	76.02
Excitation torque ripple* (%)		4.57	5.46	7.87	8.11
V _{phase_RMS} (V)		68.88	63.50	163.00	156.26
V _{phase_peak} (V)		93.33	88.63	294.66*	288.91*
I _{phase_peak} (A)		565.00 (-6%)	600.00	260.80	270
Current excitation angle (Electrical degrees)		45.00	50.00	70.15	70.10
Peak-peak T _{cogging} (Nm)		1.26	1.18	1.26	1.18
Stator iron loss (W)		265.03	243.44	1642.19	1602.58
Rotor iron loss (W)		34.72	33.96	219.78	216.41
Iron loss (W)		299.75	277.40	1861.97	1818.99
Copper loss (W)		3931.26	4433.40	837.62	904.43
Mechanical loss (W)		17.15		388.89	
Total loss (W)		4248.16	4727.95	3088.48	3112.31
Efficiency (%)		93.58	92.86	96.28	96.24

*cannot realize required torque within voltage constraint.

2×3-phase SPM machine and 146mm active stack length can achieve the 280Nm torque at 2100RPM for 480A peak phase current excitation. But the torque at top speed cannot be realized within the voltage constraint for either design candidate.

Since the winding connection of 2×3-phase IPM and SPM machine is similar to the 3-phase machine, so the end winding length of 2×3-phase machine is also 41.5mm, the same with 3-phase machine. The overall length of 142mm active stack length IPM design is 183.5mm, which is 4.68% shorter than the overall length of Nissan Leaf machine. While the overall length of 146mm active stack length IPM design is 187.5mm, which is 3.10% shorter than the overall length of Nissan Leaf machine.

Table 6.3. Performance comparison between 3-phase and 2×3 phase SPM machine with distributed winding at base and top speed (120°C).

Description		Base speed 2100rpm		Top speed 10,000rpm	
		3 phase	2×3 phase	3 phase	2×3 phase
Open circuit back EMF (V)	RMS	64.42	68.98	306.83	321.60
	Peak	76.97	77.27	366.60	366.63
Maximum torque (Nm)		282.59	289.90	76.21	76.11
Excitation torque ripple* (%)		5.51	1.97	15.85	9.62
V _{phase_RMS} (V)		85.75	91.59	112.89	119.52
V _{phase_peak} (V)		126.34	129.62	210.74	236.67*
I _{phase_peak} (A)		480	480	392	450
Current excitation angle (Electrical degrees)		0	0	71.36	69.3
Peak-peak T _{cogging} (Nm)		0.27			
Stator iron loss (W)		189.88	242.44	558.73	636.33
Rotor iron loss (W)		0.28	0.21	0.64	0.27
Iron loss (W)		190.16	242.65	559.37	636.59
Copper loss (W)		4079.77	4079.77	2720.98	3585.73
Mechanical loss (W)		17.15		388.89	
Total loss (W)		4287.07	4339.56	3669.23	4611.22
Efficiency (%)		93.55	93.63	95.60	94.53

*cannot realize required torque within voltage constraint.

In summary, the 2×3-phase IPM and SPM machines can gain slightly higher torque in constant torque region but cannot achieve required torque at top speed within voltage constraint. When compare the 2×3-phase IPM and SPM machines, the 2×3-phase IPM can realize the torque at low speed region with 4mm shorter active stack length, while the peak phase voltage of 2×3-phase SPM machine at top speed is 23.76% smaller than that of IPM machine. But the rotor topology is not optimized in this study so the further study can be carried on in the future work.

Table 6.4. Redesign of 2×3-phase SPM machine with distributed winding (120°C).

Description		Base speed 2100rpm		Top speed 10,000rpm	
		151mm stack length	146mm stack length	151mm stack length	146mm stack length
Open circuit back EMF (V)	RMS	68.98	66.70	321.60	310.95
	Peak	77.27	74.70	366.63	354.45
Maximum torque (Nm)		281.72	280.30	76.11	76.34
Excitation torque ripple* (%)		1.95	1.97	9.62	9.29
V _{phase_RMS} (V)		90.42	88.59	119.52	117.95
V _{phase_peak} (V)		128.64	125.37	236.67*	233.45*
I _{phase_peak} (A)		464	480	450	450
Current excitation angle (Electrical degrees)		0	0	69.3	68.7
Peak-peak T _{cogging} (Nm)		0.15	0.14	0.15	0.15
Stator iron loss (W)		235.63	234.52	636.33	623.14
Rotor iron loss (W)		0.13	0.21	0.27	0.25
Iron loss (W)		235.76	234.73	636.59	623.39
Copper loss (W)		3812.31	4079.77	3585.73	3585.73
Mechanical loss (W)		17.15		388.89	
Total loss (W)		4065.22	4331.65	4611.22	4598.01
Efficiency (%)		93.84	93.43	94.53	94.56

*cannot realize required torque within voltage constraint.

6.3 Five-Phase Machine Design with Concentrated Winding

To study the advantages and disadvantages of five-phase machine, 10-slot and 15-slot stator is selected and the concentrated windings are applied. Both the IPM and SPM rotors are combined with the 10- and 15-slot stator to investigate the optimal 5-phase machine.

6.3.1 Winding Connection Design for 5-phase Machine

Five-phase winding connection of 10 teeth concentrated winding is shown in Table 6.5. The 5-phase winding connection for 15-slot concentrated winding has been given in Table 4.11 in Chapter 4.5.

Table 6.5 Five phase concentrated winding connection for 10-slot machine.

5-Phase, 10 teeth			0 degree choice	
Tooth	Mech angle	Elect angle	Tooth	Coil
1	0	0	1	A1
2	36	144	2	C1
3	72	288	3	E1
4	108	72	4	B1
5	144	216	5	D1
6	180	0	6	A2
7	216	144	7	C2
8	252	288	8	E2
9	288	72	9	B2
10	324	216	10	D2

The five phases are distributed uniformly in the space and there is a 72deg E between each neighboring phase as shown in Fig. 6.5 and the winding connections is shown in Fig. 6.6.

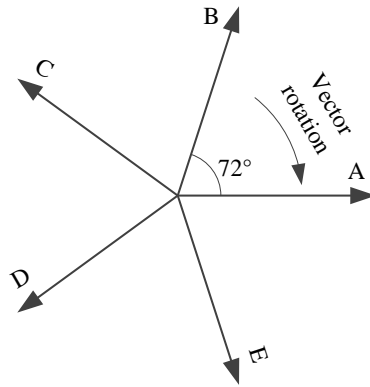


Fig. 6.5. Five phase winding set.

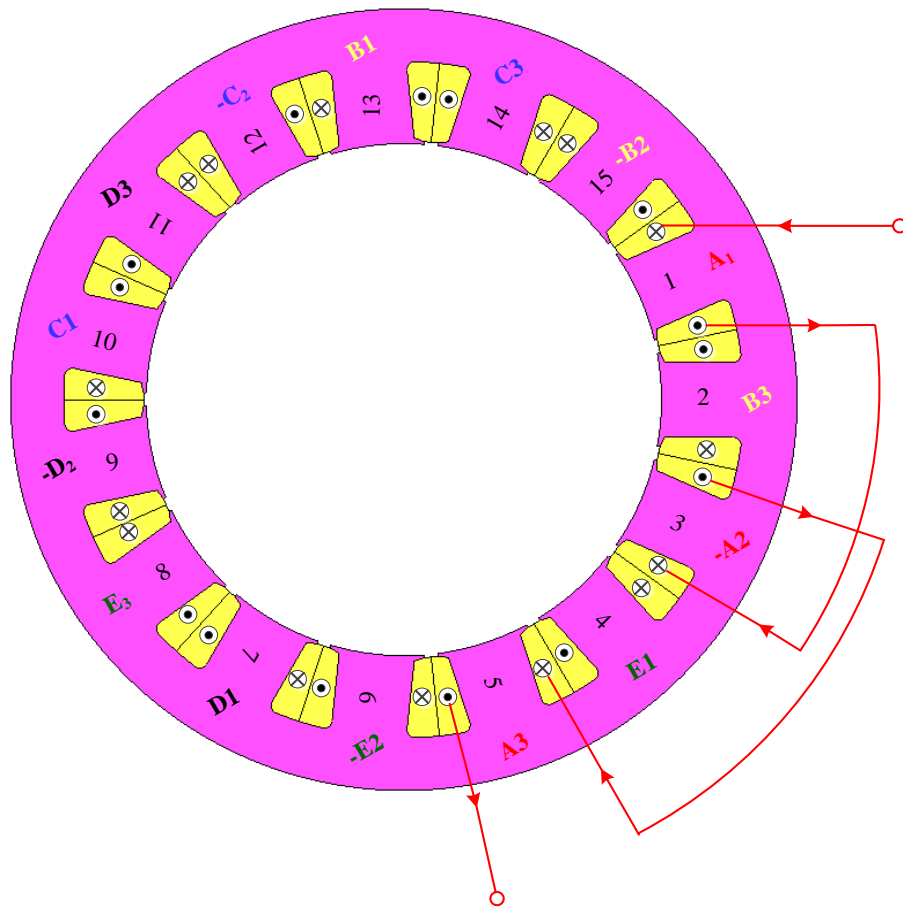


Fig. 6.6. Winding Connection of 5 phase 15 slot concentrated winding.

6.3.2 Preliminary Design of 5-phase Machine

After the winding layout and connections are sorted out, the FEA is adopted to verify the design and study the performance of each design candidate. Similar to 3-phase concentrated winding study, both IPM and SPM rotor are tried in the 5-phase concentrated winding stator. During the preliminary design, the 151mm active stack length, 8 turns per coil and 0.00821Ω phase resistance are applied in the FEA simulation. The performance at corner speed 2100rpm is shown in Table 6.6. For this design, the slot areas are consistent with the Nissan Leaf machine and the full load of every machine determined by the demagnetization edge.

Table 6.6. Performance comparison between 10-slot and 15-slot 5-phase preliminary design with concentrated winding at corner speed (120°C).

Description		Turning speed 2100rpm			
		With IPM rotor		With SPM rotor	
		10-slot	15-slot	10-slot	15-slot
Open circuit back EMF (V)	RMS	54.73	39.40	42.37	49.07
	Peak	81.76	55.92	52.28	76.28
Maximum average torque (Nm)		178.05	175.79	211.40	226.65
Excitation torque ripple* (%)		6.18	2.87	2.12	0.71
$V_{\text{phase_RMS}}$ (V)		110.46	73.60	63.51	68.45
$V_{\text{phase_peak}}$ (V)		217.12	118.98	99.78	96.33
$I_{\text{phase_peak}}$ (A)		180	200	320	300
Current excitation angle (Electrical)		30	40	0	0
Peak-peak T_{cogging} (Nm)		3.46	0.13	3.83	0.63

Compare the performance between 5-phase machine with IPM rotor and SPM rotor, both the IPM machines shows lower cogging torque, lower full load current and lower maximum torque. The lower cogging torque is because of the more sinusoidal back EMF of 5-phase IPM than the back-EMF of SPM machines as shown in Fig. 6.7. The lower full load current and lower maximum torque are caused by the high local saturation of magnetic flux. Meanwhile, the local saturation also leads to another big issue for the 10-slot IPM is that there is a high spike in the phase voltage as well similar to the 3-phase 9- and 12-slot machine. Fig. 6.8 and 6.9 shows the phase voltage waveform and the magnetic flux distribution of 10- and 15- slot, 5-phase IPM and SPM machines. From

Fig. 6.9 (c), we can see there is less magnetic saturation and no high spike on the voltage waveform in Fig. 6.9 (a). Compared to Fig. 6.9 (c), Fig. 6.9 (d) has less saturation area so that both 10-slot and 15-slot SPM machines are chosen for the final design of 5-phase machine.

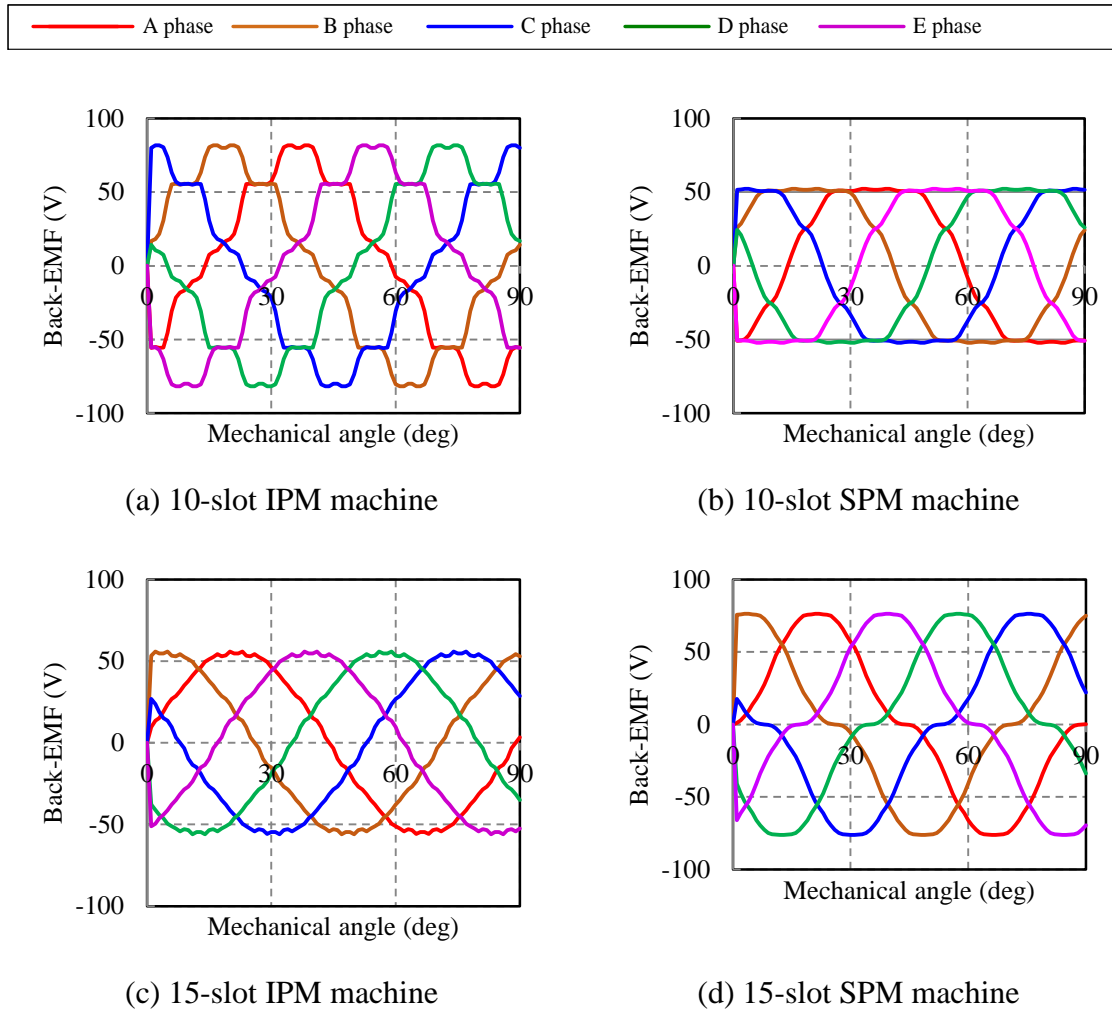
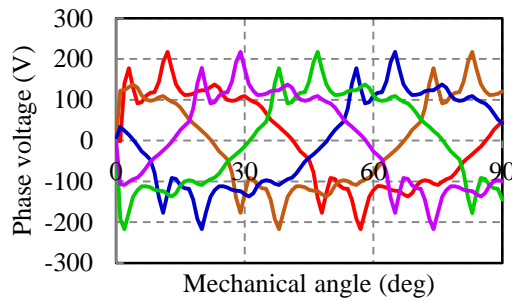
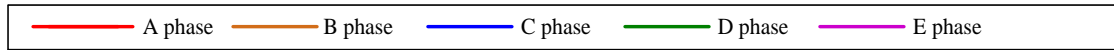
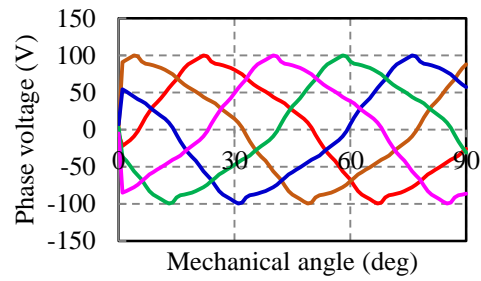


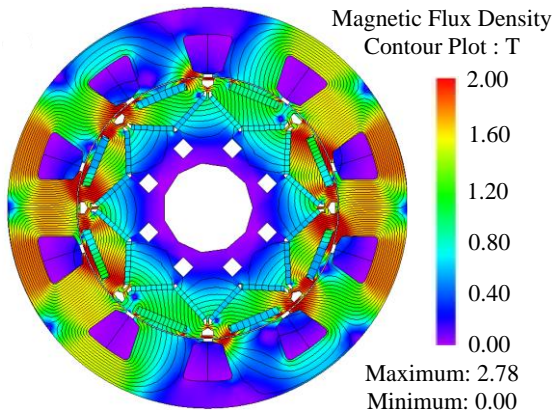
Fig. 6.7. Back-EMF comparison between 5-phase IPM and SPM machine at 2100rpm.



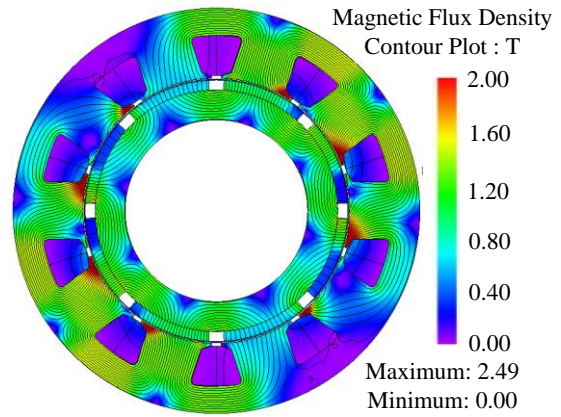
(a) Phase voltage of 10-slot IPM machine



(b) Phase voltage of 10-slot SPM machine

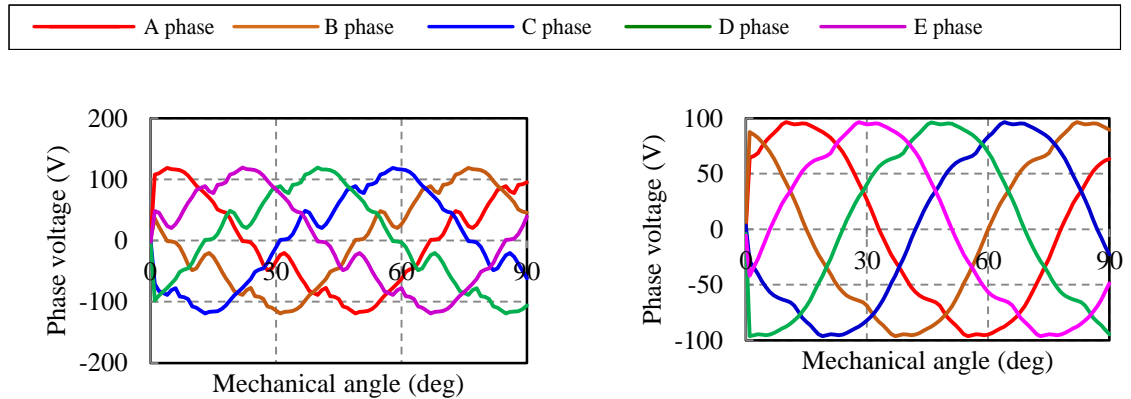


(c) Flux density distribution of 10-slot IPM machine



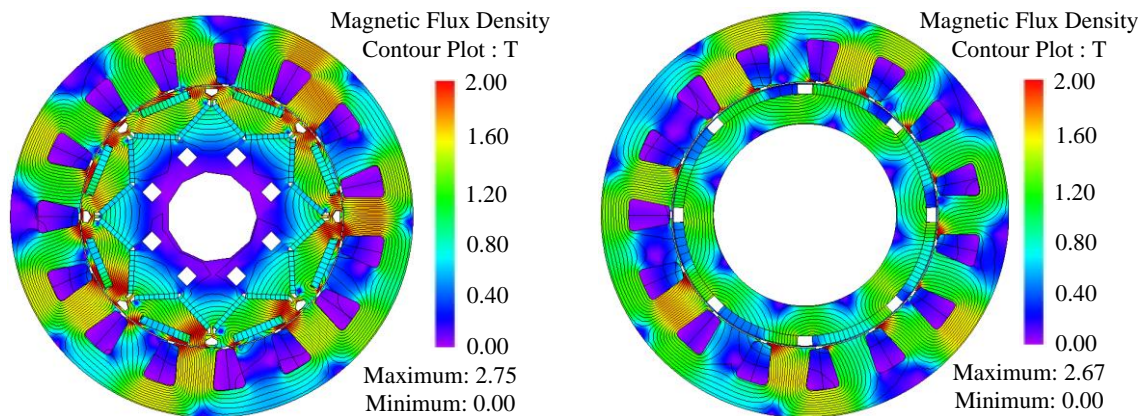
(d) Flux density distribution of 10-slot SPM machine

Fig. 6.8. Phase voltage and magnetic flux density distribution comparison between 10-slot, 5-phase IPM and SPM machine at 2100rpm, full load.



(a) Phase voltage of 15-slot IPM machine

(b) Phase voltage of 15-slot SPM machine



(c) Flux density distribution of 15-slot IPM machine

(d) Flux density distribution of 15-slot SPM machine

Fig. 6.9. Phase voltage and magnetic flux density distribution comparison between 15-slot, 5-phase IPM and SPM machine at 2100rpm, full load.

6.3.3 Final Design of 5-phase machine

The design parameters and results for 5 phase concentrated winding for 10 and 15 slot are shown in Table 6.7 and 6.8 respectively. Due to one turn less but 19.05% lower current in the maximum speed, which indicates the 10-slot 5-phase concentrated winding SPM machine has better flux weakening capability than the 15-slot 5-phase SPM machine. Although the end winding length of 15 slot SPM machine is 9.75mm shorter than Nissan

Leaf distributed IPM machine, the overall length is 26.20mm longer due to the longer active stack length.

Table 6.7. Design parameter comparison between 5-phase 10-slot and 15-slot SPM machine with concentrated winding.

Description	Active stack length (mm)	End winding length (mm)	Overall length (mm)	Number of turns	Total slot area (mm ²)	Phase resistance (mΩ)
10 slot SPM machine	200	47.81	247.81	7	3783.69	9.05
15 slot SPM machine	187	31.75	218.7	8	3800.71	22.12

Table 6.8. Performance comparison between 5 phase 10 slot and 15 slot SPM machine with concentrated winding at base and at top speed (120°C).

Description		Base speed 2100rpm		Top speed 10,000rpm	
		10 slot	15 slot	10 slot	15 slot
Open circuit back EMF (V)	RMS	49.05	60.77	233.56	289.40
	Peak	60.36	94.46	287.39	449.84
Maximum average torque (Nm)		283.05	280.68	75.71	76.233
Excitation torque ripple* (%)		2.12	0.71	15.04	3.60
V _{phase_RMS} (V)		73.93	83.94	148.99	136.82
V _{phase_peak} (V)		116.37	118.21	216.33	216.68
I _{phase_peak} (A)		370	300	170	210
I _{phase_reference to 3 phase}		616.67	500	283.33	350
Current excitation angle (Electrical degrees)		0	0	54.5	67.5
Peak-peak T _{cogging} (Nm)		4.39	0.79	4.83	0.79
Stator iron loss (W)		205.30	200.54	759.45	545.13
Rotor iron loss (W)		25.39	11.76	69.14	82.96
Iron loss (W)		230.69	212.29	828.59	628.10
Copper loss (W)		3097.36	4977.00	653.86	2438.73
Mechanical loss (W)		17.15		388.89	
Total loss (W)		3345.20	5206.44	1871.34	3455.71
Efficiency (%)		94.90	92.22	97.69	95.85

Once again, the 15-slot 5-phase SPM machine presents extraordinary advantage in low cogging torque and torque ripple and slight higher efficiency since low iron loss. In addition, the active length of 15-slot is 6.50% less than 10-slot and leading to 6.50% material cost in terms of steel, copper and permanent magnets. From all the performance information above, the 15-slot 5-phase SPM machine is recommended to be the comparative design with Nissan Leaf machine.

The performance data in Table 6.8 demonstrates that the 10-slot 5-phase SPM machine needs 23.33% higher current than the 15-slot 5-phase SPM machine in the constant region. Compared with three phase distributed Nissan Leaf machine, the five phase concentrated winding SPM machines reduce the torque ripple a lot, especially for 15 slot one. Fig.6.10 shows the torque profile comparison between modified Nissan Leaf machine and 5 phase machines. The torque ripple of 15-slot 5-phase SPM machine for base speed is 8.28% of the Nissan Leaf machine and 9.45% at the maximum speed. However, the 5 phase machines need 23.84% more materials to satisfy the torque requirement in the whole speed range as shown in Table 6.9. Although the current limit for each phase is reduced to half of the current for the three-phase Nissan Leaf machine, the increased phase number make the total energy just reduced by 16.67%. So the 5-phase 15-slot concentrated winding SPM machine provides an option for low torque ripple, high efficiency and less current supply.

Table 6.9. Material usage comparison between 5 phase 10 slot and 15 slot SPM machine with concentrated winding (kg).

Description	Rotor iron	Stator iron	Copper	Magnet	Total iron	Total mass
10 slot SPM machine	7.394	21.554	7.982	2.543	28.948	39.473
15 slot SPM machine	6.913	20.164	6.599	2.377	27.077	36.053

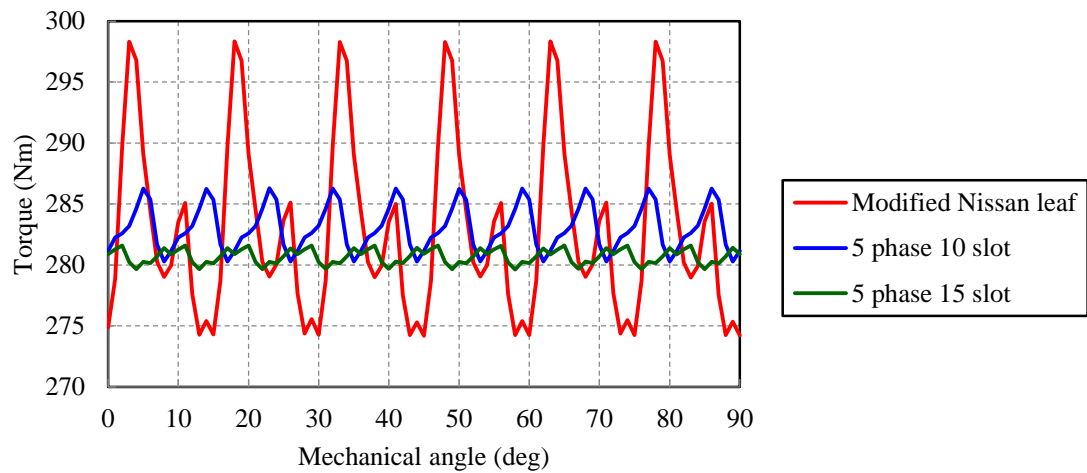


Fig. 6.10. Torque profile comparison between modified Nissan Leaf machine and 5 phase machines at 2100rpm, full load.

6.4 Nine-Phase Machine Design with Concentrated Winding

6.4.1 Winding Connection Design for 9-phase Machine

Different with 9-slot 3-phase machine winding layout, the 9-slot 9-phase machine has one slot per phase and the winding connection which can provide the maximum winding factor is selected as shown in Table 6.10. The 9 phase is evenly distributed in the space and the electric angle between each adjacent phase is 40deg electric. Fig. 6.11 shows the winding set for nine phase connection.

Table 6.10 Nine phase concentrated winding connection for 9 slot machine.

9-Phase, 9 teeth			0 degree choice	
Tooth	Mech angle	Elect angle	Tooth	Coil
1	0	0	1	A
2	40	160	2	E
3	80	320	3	I
4	120	120	4	D
5	160	280	5	H
6	200	80	6	C
7	240	240	7	G
8	280	40	8	B
9	320	200	9	F

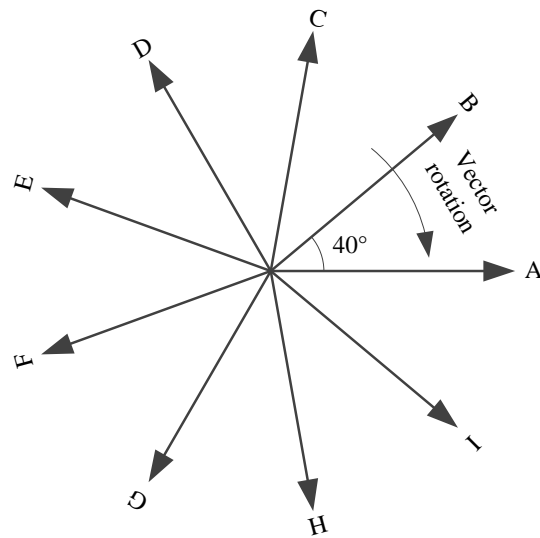


Fig. 6.11. Nine phase winding set.

6.4.2 Preliminary Design of 9-phase Machine

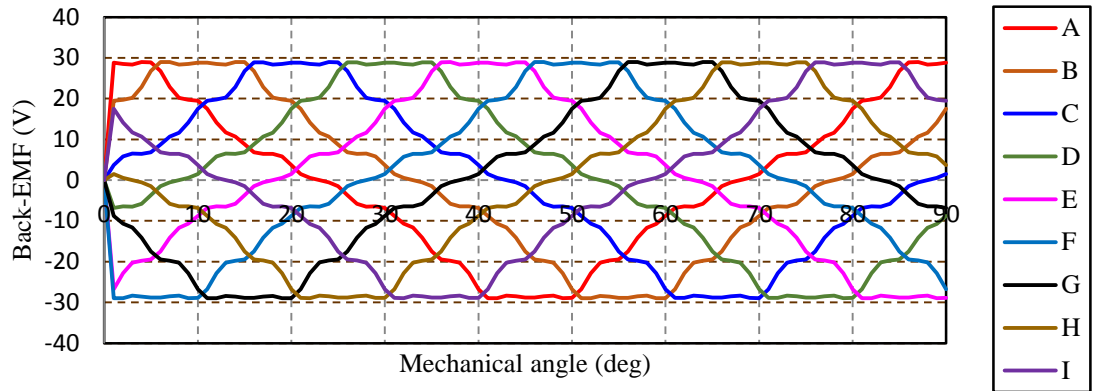
Both IPM and SPM rotor are tried in the 9-phase concentrated winding stator. During the preliminary design, the 151mm active stack length, 8 turns per coil and 0.00821Ω phase resistance are applied in the FEA simulation. The performance at speed 2100rpm is shown in Table 6.11. For this design, the slot areas are consistent with the Nissan Leaf machine and the full load of every machine determined by the demagnetization edge. The machine geometry is the same with the 3-phase 9-slot machine, just the winding reconnected to 9-phase machine.

Table 6.11. Performance comparison between 9-slot 9-phase preliminary design with concentrated winding at 2100rpm (120°C).

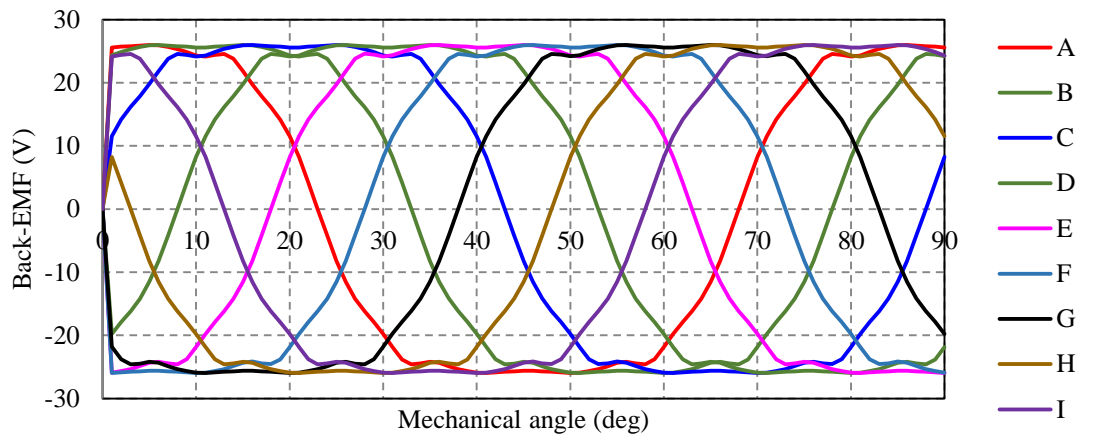
Description		2100rpm	
		With IPM rotor	With SPM rotor
Open circuit back EMF (V)	RMS	18.192	21.75
	Peak	28.942	25.97
Maximum average torque (Nm)		194.63	218.90
Excitation torque ripple* (%)		3.25	0.68
$V_{\text{phase_RMS}}$ (V)		42.104	33.100
$V_{\text{phase_peak}}$ (V)		86.397	52.243
$I_{\text{phase_peak}}$ (A)		335	360
$I_{\text{phase_peak}}$ reference to 3 phase (A)		1005	1080
Current excitation angle (Electrical)		30	0
Peak-peak T_{cogging} (Nm)		0.38	0.87

Compare the performance between 9-phase machine with IPM rotor and SPM rotor, the IPM machines shows lower cogging torque, lower full load current and lower maximum torque. The lower cogging torque is because of the more sinusoidal back EMF of 9-phase IPM than the back-EMF of SPM machines as shown in Fig. 6.12. The lower full load current and lower maximum torque are caused by the high local saturation of magnetic flux. However, the excitation phase current for all 9-phase is too high compared to 3-phase Nissan Leaf machine. So the number of turns needs to be adjusted to make the back-EMF and peak phase current similar to the Nissan Leaf machine.

Meanwhile, the local saturation also leads to higher phase voltage in IPM than the SPM machine. Fig. 6.13 shows the magnetic flux distribution of 9- slot, 9-phase IPM and SPM machines. The unbalanced magnetic pull still exists in the 9-phade 9-slot IPM and SPM machines. From Fig. 6.13, we can see that there is less magnetic saturation in SPM machine than the IPM machine. So the SPM machine is selected for the final design of 9-phase machine.



(a) 9-slot IPM machine



(b) 9-slot SPM machine

Fig. 6.12. Back-EMF comparison between 9-phase IPM and SPM machine at 2100rpm.

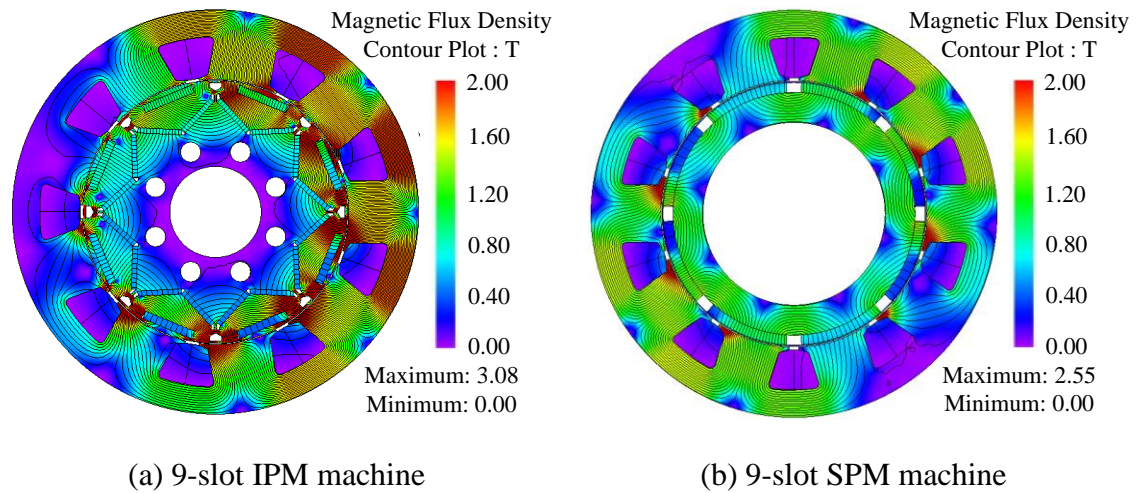


Fig. 6.13. Flux density distribution comparison between 9-phase IPM and SPM machine at 2100rpm, full load.

6.4.3 Final Design of 9-phase machine

The design parameters and results for 9 phase concentrated winding for 9-slot are shown in Table 6.12 and Table 6.13 respectively. Due to low back-EMF at 2100rpm, 8 turns, 11 turns and 21 turns are tried to test the performance in top speed. Same to 5-phase machined design, the slot area is also roughly the same with the Nissan Leaf IPM machine to maintain the same thermal rating.

The results in Table 6.14 exhibit that the longer stack length can reduce the current requirement. Thus the silicon can be reduced in the power electronic side. So it is an option for designer to decide to use more material in machine side or power electronic side combined with Table 6.15, which presents the material usage for the 200mm and 209mm 9-phase SPM machine design candidates. Fig. 6.14 shows the phase voltage and flux density distribution of 9-phase, 21 turns, 200mm stack length SPM machine at 2100rpm. The peak phase current of this 9-phase machine design candidate is still much higher than the 3-phase SPM machine design but the saturation is reduced a lot by increasing the number of turns.

Table 6.12. Design parameter comparison for 9-phase, 9-slot SPM machine with concentrated winding.

Description	Active stack length (mm)	End winding length (mm)	Overall length (mm)	Number of turns	Total slot area (mm ²)	Phase resistance (mΩ)
Candidate 1	193.5	52.85	246.3	8	3907.74	4.90
Candidate 2	193.5	52.85	246.3	11	3907.74	9.27
Candidate 3	200	52.85	252.8	21	3907.74	34.58
Candidate 4	209	52.85	261.8	21	3907.74	35.68

Table 6.13. Performance comparison between 9 phase 9 slot SPM machine with 8 turns and 11 turns at base and at top speed (120°C).

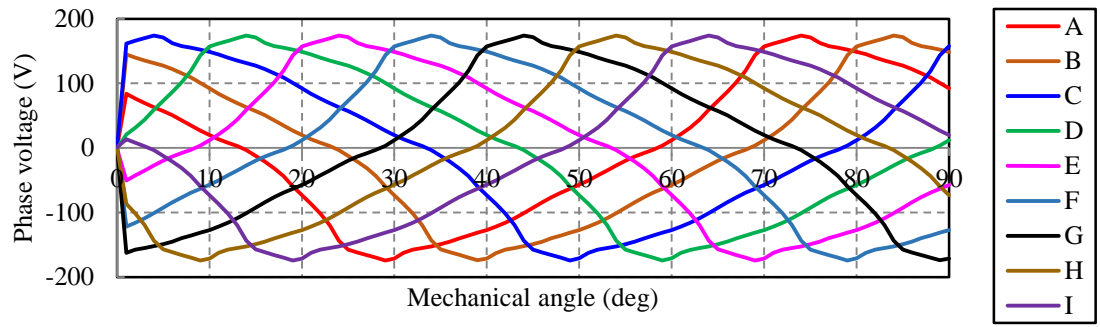
Description		Base speed 2100rpm		Top speed 10,000rpm	
		8 turns	11 turns	8 turns	11 turns
Open circuit back EMF (V)	RMS	27.87	38.32	132.72	182.49
	Peak	33.28	45.76	158.46	217.91
Maximum average torque (Nm)		280.50	280.69	76.67	76.744
Excitation torque ripple* (%)		0.68	0.68	2.44	3.06
V _{phase_RMS} (V)		42.00	56.82	138.400	157.72
V _{phase_peak} (V)		66.59	90.77	188.586	215.76
I _{phase_peak} (A)		360	262	96	82
I _{phase_peak} reference to 3 phase (A)		1080	786	288	246
Current excitation angle (Electrical degrees)		0	0	0	30.5
Peak-peak T _{cogging} (Nm)		1.12			

Table 6.14. Performance comparison between 9 phase 9 slot SPM machine with 200mm and 209mm stack length at base and at top speed (120°C, 21 turns).

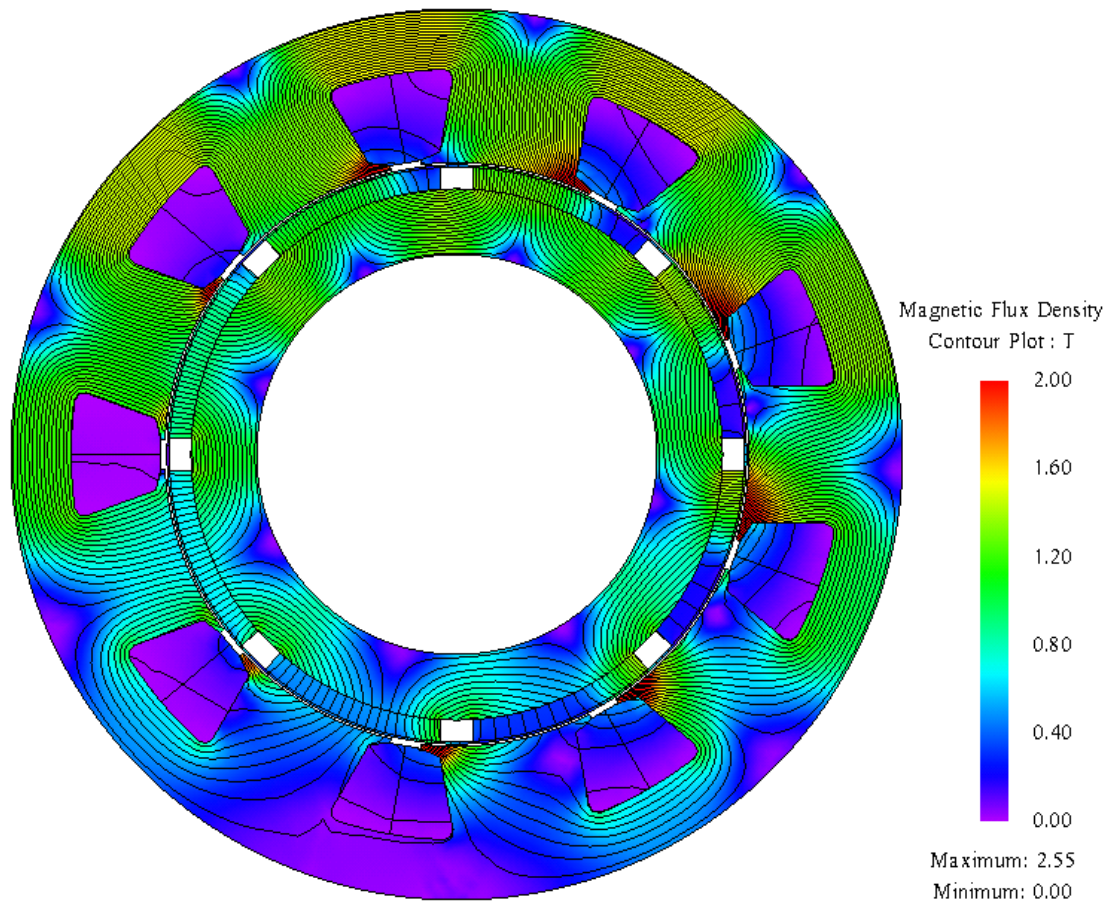
Description		Base speed 2100rpm		Top speed 10,000rpm	
		200mm	209mm	200mm	209mm
Open circuit back EMF (V)	RMS	75.62	79.02	360.09	376.29
	Peak	90.28	94.35	429.92	449.27
Maximum average torque (Nm)		281.74	281.89	76.69	76.32
Excitation torque ripple* (%)		0.72	0.77	4.02	4.41
V _{phase_RMS} (V)		108.92	111.34	128.93	136.14
V _{phase_peak} (V)		174.13	176.77	215.50	222.15
I _{phase_peak} (A)		133	127	100	96
I _{phase_peak} reference to 3 phase (A)		399	381	300	288
Current excitation angle (Electrical degrees)		0	0	67.35	67.6
Peak-peak T _{cogging} (Nm)		1.16	1.21	1.16	1.21
Stator iron loss (W)		183.24	184.12	486.20	509.48
Rotor iron loss (W)		28.85	27.74	166.24	159.98
Iron loss (W)		212.09	211.86	652.44	669.45
Copper loss (W)		2752.59	2589.67	1556.10	1479.72
Mechanical loss (W)		17.15		388.89	
Total loss (W)		2981.82	2818.68	2597.43	2538.06
Efficiency (%)		95.41	95.65	96.87	96.92

Table 6.15. Material usage comparison between 200mm and 209mm stack length of 9-phase SPM machine with concentrated winding (kg).

Description	Rotor iron	Stator iron	Total iron	Magnet	Copper	Total mass
200mm stack length	7.39	21.36	28.75	2.54	7.95	39.24
209mm stack length	7.72	22.33	30.05	2.66	8.20	40.91



(a) 9-slot SPM machine phase voltage at 2100rpm (21 turns).



(b) 9-slot SPM machine flux density distribution

Fig. 6.14. Phase voltage and flux density distribution of 9-phase, 21 turns, 200mm stack length SPM machine at 2100rpm.

6.5 Distributed Winding Multiphase SPM Machine Design

The one slot per pole per phase single layer distributed winding 5-, 7- and 9-phase SPM machine are designed based on the 3-phase SPM machine. The rotor, stack length, and stator outer diameter are all the same with the 3-phase SPM machine. Fig. 6.15 illustrates the phase winding set for 7-phase machine. Other phase implementations have been shown in Fig. 6.5 and 6.11. Fig. 6.16 illustrates the 5-phase (a), 7-phase (b) and 9-phase (c) SPM machine cross section and the winding connection for one pole-pair of the 5- (d), 7- (e) and 9-phase SPM (f) respectively with the maximum winding factor. Table 6.16 and 6.17 present materials usage and design parameters for the 5-, 7- and 9-phase design respectively. Table 6.18 presents the performance comparison results for the 5-, 7- and 9-phase designs at 2100rpm and 10000rpm. Compared to 3-phase SPM, the phase peak current for 5-, 7- and 9-phase machine is too high and the peak phase voltage are all beyond the 375V DC link voltage. So the number of turns needs to be adjusted to make the design candidates meet the torque requirement at 10,000rpm within the 375V DC link voltage.

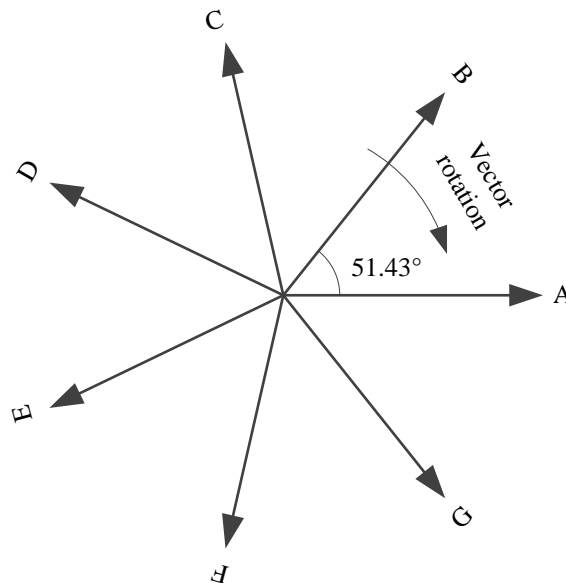
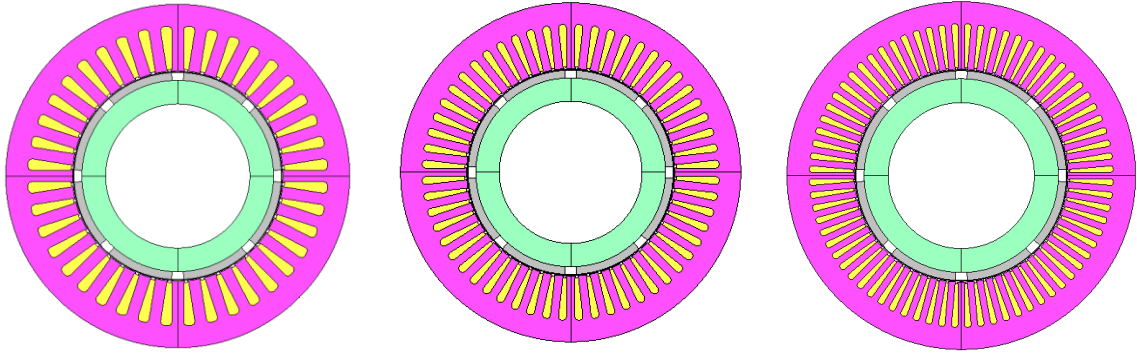


Fig. 6.15. Seven phase winding set.



(a) 5-phase SPM machine

(b) 7-phase SPM machine

(c) 9-phase SPM machine

Slot	Coil
1	A+
2	C-
3	E+
4	B-
5	D+
6	A-
7	C+
8	E-
9	B+
10	D-

Note: 11-40 slot repeat the winding layout in 1-10 slot for four times.

Slot	Coil
1	A+
2	D-
3	G+
4	C-
5	F+
6	B-
7	E+
8	A-
9	D+
10	G-
11	C+
12	F-
13	B+
14	E-

Note: 15-56 slot repeat the winding layout in 1-14 slot for four times.

Slot	Coil
1	A+
2	E-
3	I+
4	D-
5	H+
6	C-
7	G+
8	B-
9	F+
10	A-
11	E+
12	I-
13	D+
14	H-
15	C+
16	G-
17	B+
18	F-

Note: 19-72 slot repeat the winding layout in 1-18 slot for four times.

(d) Winding connection for 5-phase SPM machine

(e) Winding connection for 7-phase SPM machine

(f) Winding connection for 9-phase SPM machine

Fig. 6.16. Geometry and winding connection of 5-, 7-, 9- phase SPM machine with single layer integer slot distributed winding.

Table 6.16. Material usage comparison between 5-, 7- and 9- phase SPM machine with

single lager integer slot distributed winding (kg).

Description	Rotor iron	Stator iron	Total iron	Magnet	Copper	Total mass
5-phase SPM	5.58	19.36	24.94	1.92	7.64	34.50
7-phase SPM	5.58	19.39	24.97	1.92	7.60	34.49
9-phase SPM	5.58	19.33	24.91	1.92	7.67	34.50

The end winding length of the 5-, 7- and 9-phase distributed winding machine is 41.5mm, the same as the 48-slot 3-phase machine, and as well as the overall length, 192.5mm. As shown in Table 6.16, even rotor, stator and copper mass are very similar. So there is almost no difference in the material usage for 5-, 7- and 9-phase distributed winding machine design and the performance is the only aspect needs to be considered.

When the number of turns increases, the back-EMF will increase and the inductance as well. Hence less current may need to weaken the flux at the top speed. However, if the number of turns drops, the back-EMF will decrease as well as the inductance, which may cause less current at the top speed, too. Both 26 and 22 turns are tried for 9-phase machine and the results show that the 22 turns-9-phase machine design candidate can satisfy the torque at 10,000rpm within the 375V DC link voltage. So the 23 turns are applied to for the 5- and 7- phase machine design candidates and meet the torque and voltage requirements at the same time. But the phase current increases in the constant torque region correspondingly. The results are shown in the Table 6.19. Now the three designs can achieve torque at 10000rpm within the voltage limit, however, the excitation phase current is very high compared to the 392A for that of 3-phase SPM machine design. The excitation phase current of 5-, 7- and 9-phase distributed winding designs already similar to or even slightly higher than the 480A for the 3-phase SPM machine design. If the number of turns decreases, the current for low speed increase again although the current for high speed reduce, which indicates the power electronic size has to be enlarged for the 5-, 7- and 9-phase distributed winding designs. From this performance side, the 5- and 9-phase concentrated winding design candidates are better than that of distributed winding in terms of lower phase current requirements at both low and high speed and lower torque ripple but more material usage due to longer axial stack length.

Table 6.17. Design parameter comparison for 5-, 7- and 9-phase SPM machine with distributed winding.

Description	Slot number	Number of turns	Total slot area (mm ²)	Phase resistance (Ω)
5-phase SPM	40	24	5647.91	19.41
7-phase SPM	56	24	5623.72	27.31
9-phase SPM	72	24	5675.80	34.81

Table 6.18. Performance comparison between 5-, 7- and 9-phase SPM machine with distributed winding at base and at top speed (120°C).

Description		Base speed 2100rpm			Top speed 10,000rpm		
		5-phase	7-phase	9-phase	5-phase	7-phase	9-phase
Open circuit back EMF (V)	RMS	68.64	68.97	80.12	326.84	328.45	329.51
	Peak	77.31	77.31	119.17	368.11	368.21	367.63
Maximum average torque (Nm)		281.62	281.12	281.13	76.42	76.39	76.96
Excitation torque ripple* (%)		2.66	5.49	3.53	73.11	60.65	11.93
V _{phase_RMS} (V)		94.60	94.16	90.40	149.34	153.55	146.84
V _{phase_peak} (V)		135.39	134.09	130.05	224.85*	232.86*	240.19*
I _{phase_peak} (A)		276	196	151.5	320	240	180
I _{phase_peak} (A)_reference to 3-phase		460	457.33	454.5	533.33	560	540
Current excitation angle (Electrical degrees)		0	0	0	76.15	79.30	72.00
Peak-peak T _{cogging} (Nm)		6.14	3.63	2.68	6.14	3.63	2.69
Stator iron loss (W)		278.35	282.48	269.28	766.61	882.46	906.65
Rotor iron loss (W)		0.28	0.44	0.25	1.51	1.59	1.18
Iron loss (W)		278.63	282.92	269.53	768.12	884.04	907.84
Copper loss (W)		3696.20	3672.54	3595.62	4968.63	5506.52	5278.23
Mechanical loss (W)		17.15			388.89		
Total loss (W)		3991.97	3972.61	3882.30	6125.64	6779.45	6602.36
Efficiency (%)		93.94	93.96	94.09	92.89	92.19	92.39

*cannot realize the torque without over modulation.

Table 6.19. Performance comparison between 5-, 7- and 9-phase SPM machine with distributed winding at base and at top speed (120°C).

Description		Base speed 2100rpm			Top speed 10,000rpm		
		5-phase	7-phase	9-phase	5-phase	7-phase	9-phase
Open circuit back EMF (V)	RMS	65.78	66.10	63.43	313.23	314.77	302.05
	Peak	74.09	74.08	70.76	352.81	352.80	336.93
Maximum average torque (Nm)		281.62	281.09	280.72	76.41	76.58	76.53
Excitation torque ripple* (%)		2.66	5.49	3.53	72.37	59.36	13.21
$V_{\text{phase_RMS}}$ (V)		90.75	90.30	82.93	140.64	141.89	138.37
$V_{\text{phase_peak}}$ (V)		129.86	128.57	119.30	218.41	215.83	216.11
$I_{\text{phase_peak}}$ (A)		288	204.5	165	330	245	200
$I_{\text{phase_peak}}$ (A)_reference to 3-phase		480	477.17	495	550	571.67	600
Current excitation angle (Electrical degrees)		0	0	0	76	79	72.3
Peak-peak T_{cogging} (Nm)		6.14	3.63	2.68	6.14	3.63	2.69
Stator iron loss (W)		278.29	282.54	268.69	747.01	849.34	933.53
Rotor iron loss (W)		0.33	0.41	0.30	1.33	1.75	1.71
Iron loss (W)		278.62	282.95	268.99	748.35	851.09	935.24
Copper loss (W)		3700.50	3676.04	3592.49	4858.52	5276.26	5278.23
Mechanical loss (W)		17.15			388.89		
Total loss (W)		3996.27	3972.61	3878.64	5995.75	6516.23	6602.36
Efficiency (%)		93.94	93.96	94.09	93.03	92.48	92.39
Description		23 turns	23 turns	22 turns	23 turns	23 turns	22turns

6.6 Summary

In this Chapter, different phase numbers and stators are designed for both IPM and SPM rotors. Compared with 3-phase machine, the 2×3 phase machine can obtain higher torque at low speed but a slightly lower torque in the top speed due to higher phase voltage. The redesigned 2×3 phase machine provides two options for the future application. The five phase machine designs can satisfy the performance specification with much lower torque ripple than the Nissan Leaf machine but higher material mass. The 15-slot, 5-phase machine design shows lower excitation current and torque ripple and less material than the 10-slot, 5-phase machine design. Compared with distributed multiphase machine candidates, the concentrated winding multi-phase machine design candidates can meet the performance specification with lower current. Especially for 9-phase concentrated winding candidate, the excitation torque ripple at both low and top speed is comparable with 5-phase 15-slot concentrated winding but the current requirement reduces 20%. But the active axial stack length of 9-slot 9-phase machine is 6.95% more than the 5-phase 15-slot design candidate. Compared to the 5- and 9-phase distributed winding multiphase design, the 5- and 9-phase concentrated winding design candidates are better in terms of lower phase current requirements at both low and high speed and lower torque ripple but more material usage due to longer axial stack length.

Chapter 7

Conclusions, Future Research Work and Publications

7.1 Conclusions

Different traction machine design candidates satisfying the Nissan Leaf machine specification are proposed and discussed in this thesis. The design and manufacturing issues for traction machine are analyzed and the design improvements have been investigated. The comparative studies of rotor topologies, winding types and phase numbers provide reference information for machine designers and engineers.

In Chapter 3, The FEA modal of Nissan Leaf benchmark machine is built and verified. The FEA results shows that the Nissan Leaf machine can achieve its announced performance when the over modulation is applied after 6000rpm.

In Chapter 4, the comprehensive rotor topology design is conducted. The modified Nissan Leaf machine rotor is proposed to meet the whole operation range with sinusoidal phase current excitation. Then a SPM design is proposed and compared for well documented IPM design. The study illustrates and concludes that both the IPM and SPM topologies have very similar capabilities with only subtle differences between the design options, subtleties that may be exploited when considering the traction application requirements, for example, predominant low, medium or high speed operation, and power train integration. In addition, the SPM machine also reduces 20% silicon in power electronics compared to the Nissan Leaf machine. A new synchronous machine structure with 5 phase sine wave current excitation is proposed in the rotor design part. The torque ripple produced by the new machine can be controlled within 20%. It is concluded that GBDP magnets have similar characteristics with conventional magnets in the linear region. So

IPM machines operating at elevated rotor temperature with grain boundary magnets can achieve better performance, such as higher average torque and higher efficiency, than machines with conventional magnets.

In Chapter 5, different types of windings are studied and discussed. The results shows the the SPM machines with concentrated windings can achieve higher torque at low speed than the IPM machines due to less saturation in rotor and stator iron. The 12-slot concentrated winding machine can achieve the Nissan Leaf machine specification with 12% more magnet and iron material but 20% less copper and 6.67% less silicon in power electronics. The aluminum stator winding design provides an opportunity to reduce the machine's weight with the same thermal and magnetic performance. However, the risk of mechanical strength in transposition parts and difficulties of terminal joints are significant issues for aluminum stator windings. The bar wound winding design based on Nissan Leaf machine stator exhibits that the higher copper loss and iron loss in bar wound winding is a considerable aspect needs to be managed in the design stage.

In Chapter 6, the study of multiphase machine designs shows that the increase of phase numbers may not cause the performance improvement or material saving, but can decrease the torque ripple. The 2×3-phase connection of Nissan Leaf machine obtain 5% higher torque in constant region and 2.67% less torque at top speed. Similar to 3-phase concentrated winding machines, the 5- and 9-phase machine with SPM rotor gain more torque at low speed than the machine with IPM rotor. The 10-slot SPM 5-phase machine achieve 3% and 1% higher efficiency than the 15-slot machine in low speed and high speed respectively but 11.76% more magnet and iron material and 23% more silicon in power electronics. Another exciting discovery is that the 15-slot, 5-phase machine can acquire amazing low excitation torque ripple, for example, 0.70% at 2100rpm and 3.60% at 10,000rpm. The 9-phase machine design consumes 31% more silicon and 28.15% more magnet and iron material than the 3-phase machine but also very low torque ripple. The multiphase machine is an option for fault tolerance and high quality torque requirements.

7.2 Future Research Work

Following recommendations are suggested for future work:

- (a) More investigation can be done to find out the reason why the industry prefers IPM machine design than SPM machine design. The manufacturing cost of IPM and SPM machine can be a possible answer.
- (b) The impact of system DC link voltage and temperature variations on machine capability requires further study to reduce the impact on the realizable traction characteristics.
- (c) The high noise and vibration and low torque density of the 5-phase synchronous machines need to be studied further. Further detail analysis and prototype validation need to be done to validate the design.
- (d) The inductance comparison and how this affects the machine performance of concentrated winding and distributed winding can be further studied. Assembly of concentrated and distributed winding designs and its impact on manufacturing techniques and time per stator will be an interesting topic.
- (e) As discussed in Chapter 6 that the excitation torque ripple is reduced for the higher phase number machine design. It would be interesting to quantify the benefits of this torque ripple in terms of the total machine noise and vibration. This work is currently being investigated by colleagues at MARC.

7.3 Publications

This Ph.D. study has resulted in following publications to-date:

Journal Paper:

Yinye Yang, Sandra Castano, **Rong Yang**, Michael Kasprzak, Berker Bilgin, Anand Sathyan, Hossein Dadkhah, and Ali Emadi, “Design and comparison of Interior Permanent Magnet Topologies for Traction Applications”, Accepted and to be published in *IEEE Transactions on Transportation Electrification*.

Conference Papers:

1. Nan Zhao, Nigel Schofield, **Rong Yang** and Ran Gu, “An Investigation of DC-Link Voltage and Temperature Variations on EV Traction System Design”, *IEEE Energy Conversion Congress and Exposition (ECCE 2016), Milwaukee, MI, September 18-22, 2016*.
2. **Rong Yang**, Nigel Schofield, and Ali Emadi, “Comparative Study between Interior and Surface Permanent Magnet Traction Machine Designs”, *The IEEE Transportation Electrification Conference and Expo (ITEC), Dearborn, Michigan, USA, June 27-29, 2016*.
3. **Rong Yang**, Yinye Yang, Berker Bilgin, Nigel Schofield, Anand Sathyan, Hossein Dadkhah, Stephen C. Veldhuis, and Ali Emadi, “Analysis of an IPM machine with grain boundary diffusion processed magnet”, *The 8th IET international conference on Power Electronics, Machines and Drives (PEMD 2016), Glasgow, Scotland, UK, April 19-21, 2016*.

Patents:

1. Berker Bilgin, **Rong Yang**, Nigel Schofield, Ali Emadi, “Alternating-Current Driven, Salient-Teeth Reluctance Motor with Concentrated Windings”, 2016. (submitted, internal reference number is 17-019).
2. Berker Bilgin, Yinye Yang, **Rong Yang**, Anand Sathyan, Hossein Dadkhah, Ali Emadi, “Permanent Magnet Machine Design for Higher Resistivity against Demagnetization of Permanent Magnets”, submitted to FCA in October, 2014.

References

- [1] A. Emadi, *Advanced Electric Drive Vehicles*, Boca Raton, FL: CRC Press, Oct. 2014.
- [2] Mehrdad Ehsani, Yimin Gao, and Ali Emadi, *Modern Electric, Hybrid Electric and Fuel Cell Vehicles Fundamentals, Theory and Design*, second edition, New York: Taylor and Francis Group, LLC, 2010.
- [3] Y. Yang and A. Emadi, "Hybrid and plug-in hybrid vehicles," in *Wiley Encyclopedia of Electrical and Electronics Engineering*, John Wiley & Sons, 2013, pp. 1-22.
- [4] Y. Yang, K. Arshad-Ali, J. Roeleveld, and A. Emadi, "State-of-the-art electrified powertrains: hybrid, plug-in hybrid, and electric vehicles," *International Journal of Powertrains*, vol. 5, no. 1, pp. 1-29, 2016.
- [5] B. Bilgin and A. Emadi. "Electric motors in electrified transportation: A step toward achieving a sustainable and highly efficient transportation system," *IEEE Power Electronics Magazine*, volume. 1, no. 2, pp. 10-17, (2014).
- [6] B. Bilgin, P. Magne, P. Malysz, Y. Yang, V. Pantelic, M. Preindl, A. Korobkine, W. Jiang, M. Lawford, and A. Emadi, "Making the case for electrified transportation," *IEEE Transactions on Transportation Electrification*, vol. 1, no. 1, pp. 4-17, 2015.
- [7] Z.Q. Zhu and David Howe, "Electrical machines and drives for electric, hybrid, and fuel cell vehicles," in *Proceedings of the IEEE*, vol. 95, no. 4, pp. 746-765, 2007.
- [8] Automotive industry, [Online]. Available: https://en.wikipedia.org/wiki/Automotive_industry.

- [9] J. A. Cook, J. Sun, J. H. Buckland, I. V. Kolmanovsky, H. Peng and J. W. Grizzle, "Automotive powertrain control-a survey," *Asian Journal of Control*, vol. 8, no. 3, pp. 237-260, Sep. 2006.
- [10] C. Lin, H. Peng, J. W. Grizzle, and J. Kang, "Power management strategy for a parallel hybrid electric truck," *IEEE Transactions on Control Systems Technology*, vol. 11, no. 6, pp. 839-849, Nov. 2003.
- [11] V. Freyermuth, E. Fallas, and A. Rousseau, "Comparison of powertrain configuration for plug-in HEVs from a fuel economy perspective," *SAE International*, 2007.
- [12] J. Liu, "Modeling, configuration and control optimization of power-split hybrid vehicles," Ph.D. dissertation, Horace H. Rackham School of Graduate Studies, The University of Michigan, Ann Arbor, MI, United States, 2007.
- [13] K. C. Bayindir, M. A. Gozukucuk and A. Teke, "A comprehensive overview of hybrid electric vehicle: Powertrain configurations, powertrain control techniques and electronic control units," *Energy Conversion and Management*, 52(2011), pp. 1305-1313, 2011.
- [14] D. Sherman, We build the chevy spark EV's AC permanent-magnet motor, [Online]. Available: <http://blog.caranddriver.com/we-build-the-chevy-spark-ev%E2%80%99s-ac-permanent-magnet-motor/>, last accessed September, 2016.
- [15] D. G. Dorrell, A. M. Knight, L. Evans and M. Popescu, "Analysis and design techniques applied to hybrid vehicle drive machines—assessment of alternative IPM and induction motor topologies," *IEEE Transactions on Industrial Electronics*, Vol. 59, No. 10, pp. 3690-3699, Oct. 2012.
- [16] M. Li, J. He, and N. Demerdash, "A flux-weakening control approach for interior permanent magnet synchronous motors based on z-source," in *IEEE Transportation Electrification Conference and Exhibition Conference*, Detroit, US, 2014.

- [17] J. Wang, X. Yuan and K. Atallah, "Design optimization of a surface-mounted permanent-magnet motor With concentrated windings for electric vehicle applications," *IEEE Transactions on Vehicular Technology*, Vol. 62, No. 3, pp. 1053-1064, March 2013.
- [18] P. B. Reddy, Ayman. M. El-Refaie, K. Huh, J. K. Tangudu, and T. M. Jahns, "Comparison of interior and surface PM machines equipped with fractional-slot concentrated windings for hybrid traction applications", *IEEE Transactions on Energy Conversion*, Vol. 27, NO. 3, pp.593-602, September 2012.
- [19] A. M. EL-Refaie, T. M. Jahns, "Optimal flux weakening in PM surface machines using fractional-slot concentrated windings," *IEEE Transactions on Industry. Application*, Vol. 41, No. 3, pp. 790–800, May–June 2005.
- [20] G. Pellegrino, A. Vagati, P. Guglielmi, and B. Boazzo "Performance comparison between surface-mounted and interior PM motor drives for electric vehicle application", *IEEE Transactions on Industrial Electronics*, Vol. 59, No. 2, pp. 803-811, February. 2012.
- [21] W. Chlebosz and G. Ombach, "Demagnetization properties of IPM and SPM motors used in the high demanding automotive application", *The International Journal for Computation and Mathematics in Electrical and Electronic Engineering*, Vol. 32, No. 1, pp. 72 – 85, 2012.
- [22] P. Campbell. "System cost analysis for an interior permanent magnet motor," Ames Laboratory, Iowa State University, Ames, (2008). [Online]. Available: <http://www.osti.gov/scitech/servlets/purl/940187-ne49KO/>, last accessed September, 2016.
- [23] Y. Doi, T. Minowa, H. Nakamura, and K. Hirota. "Manufacturing method of a rotor in a machine comprising embedded permanent magnets", European Patent, EP2306623A2, (2011).
- [24] T. Nakada, S. Ishikawa, and S. Oki. "Development of an electric motor for a newly developed electric vehicle," *SAE International*, Volume 01, No. 1879, (2014).

- [25] W. T. Benecki, T. K. Clagett, and S. R. Trout. *Permanent Magnets 2010-2020: A Comprehensive Overview of the Global Permanent Magnet Industry*, Walter T. Benecki LLC, Highland Beach, Florida, (2010).
- [26] J Rowlatt, "Rare earths: Neither rare, nor earths," BBC NEWS, [Online]. Available: <http://www.bbc.com/news/magazine-26687605>.
- [27] A. M. EL-Refaie, "Fractional-slot concentrated-windings Synchronous permanent magnet machines: opportunities and challenges," *IEEE Transactions on Industrial Electronics*, Vol. 57, No. 1, pp. 107–121, January 2010.
- [28] P. Salminen, M. Niemela, H. Jussila, J. Pyrhonen, and J. Mantere, "Concentrated wound 45 kW, 420 rpm permanent magnet machine with embedded magnets," in *The 3rd IET International Conference on Power Electronics, Machines and Drives (PEMD)*, 2006, pp. 494-498.
- [29] P. M. Lindh, H. K. Jussila, M. Niemela, A. Parviainen, and J. Pyrhonen, "Comparison of concentrated winding permanent magnet motors with embedded and surface-mounted rotor magnets," *IEEE Transactions on Magnetics*, vol. 45, pp. 2085-2089, 2009.
- [30] L. Chong, R. Dutta, N. Q. Dai, M. F. Rahman, and H. Lovatt, "Comparison of concentrated and distributed windings in an IPM machine for field weakening applications," in *Universities Power Engineering Conference (AUPEC)*, 2010, pp. 1–5.
- [31] Y. Honda, T. Nakamura, T. Higaki, and Y. A. Takeda, "Motor design considerations and test results of an interior permanent magnet synchronous motor for electric vehicles," in *Thirty-Second IAS Annual Meeting on Industry Applications Conference*, 1997, pp. 75-82 vol.1.
- [32] F. Libert and J. Soulard, "Investigation on pole-slot combinations for permanent-magnet machines with concentrated windings," in *proceeding of the International Conference on Electrical Machines (ICEM)*, 2004.

- [33] H. Jussila, P. Salminen, M. Niemelä and J. Pyrhönen, “Guidelines for designing concentrated winding fractional slot permanent magnet machines,” in *International Conference on Power Engineering, Energy and Electrical Drives*, Setubal, Portugal, April, 2007.
- [34] J. Cros and P. Viarouge, “Synthesis of high performance PM motors With concentrated windings,” *IEEE Transactions on Energy Conversion*, Vol. 17, No. 2, pp. 248–253, June 2002.
- [35] F. Magnussen and C. Sadarangani, “Winding factors and Joule losses of permanent magnet machines with concentrated windings,” in *IEEE International Electric Machines and Drives Conference*, 2003, vol. 1, pp. 333–339.
- [36] A. M. EL-Refaie, T. M. Jahns, and D. W. Novotny, “Analysis of surface permanent magnet machines with fractional-slot concentrated windings,” *IEEE Transactions on Energy Conversion*, Vol. 21, No. 1, pp. 34–43, March 2006.
- [37] J. K. Tangudu and T. M. Jahns, “Comparison of interior PM machines with concentrated and distributed stator windings for traction applications”, in *2011 Vehicle Power and Propulsion Conference (VPPC 2011)*, Chicago, IL, USA, 2011.
- [38] A. M. EL-Refaie, T. M. Jahns, P. J. McCleer, and J. W. McKeever, “Experimental verification of optimal flux weakening in surface PM machines using concentrated windings,” *IEEE Transactions on Industrial Applications*, Vol. 42, No. 2, pp. 443–453, March-April 2006.
- [39] L. Chong and M. F. Rahman, “Comparison of d- and q-axis inductances in an IPM machine with integral-slot distributed and fractional-slot concentrated windings,” in *2008 International Conference on Electrical Machines (ICEM)*, September 2008.
- [40] A. Wang, C. Wang, and W. L. Soong, “Design and optimization of interior PM machines with distributed and fractional-slot concentrated windings for hybrid electric vehicles,” in *2014 IEEE Conference and Expo Transportation Electrification Asia-Pacific (ITEC Asia-Pacific)*, August-September 2014.

- [41] J. J. Lee, W. H. Kim, J. S. Yu, S. Y. Yun, S. M. Kim, J. L. Lee, and J. Lee, “Comparison between concentrated and distributed winding for IPMSM for traction application,” in *2010 International Conference on Electrical Machines and Systems (ICEMS)*, October 2010.
- [42] J. Goss, D. Staton, R. Wrobel, and P. Mellor, “Brushless AC interior-permanent magnet motor design: comparison of slot/pole combinations and distributed vs. concentrated windings,” in *2013 IEEE Energy Conversion Congress and Exposition (ECCE)*, September 2013.
- [43] M. Martinović, D. Žarko, S. Stipetić, T. Jerčić, M. Kovačić, Z. Hanić, and D. Staton, “Influence of winding design on thermal dynamics of permanent magnet traction motor”, *2014 International Symposium on Power Electronics, Electrical Drives, Automation and Motion (SPEEDAM)*, June 2014, pp. 397-402.
- [44] L. Chong, R. Dutta, and M. F. Rahman, “Design and thermal considerations of an interior permanent magnet machine with concentrated windings,” *2009 International Conference on Electrical Machines and Systems (ICEMS)*, November 2009.
- [45] N. Bianchi, S. Bolognani, M. D. Prè, and G. Grezzani, “Design considerations for fractional-slot winding configurations of synchronous machines,” *IEEE Transactions on Industrial Applications*, Vol. 42, No. 4, pp. 997–1006, July-August 2006.
- [46] A. M. EL-Refaie and T. M. Jahns, “Impact of winding layer number and magnet type on synchronous surface PM machines designed for wide constant-power speed range operation”, *IEEE Transactions on Energy Conversion*, Vol. 23, No. 1, pp. 53–60, March 2008.
- [47] A. Fatemi, D. M. Ionel, N. A. O. Demerdash, and T. W. Nehl, “Optimal design of IPM motors with different cooling systems and winding configurations,” *IEEE Transactions on Industry Applications*, Vol. 52, No. 4, pp. 997–1006, July-August 2016.

- [48] N. Schofield, X. Niu, and O. Beik, “Multiphase machines for electric vehicle traction,” *2014 IEEE Transportation Electrification Conference and Expo (ITEC)*, Dearborn, USA, June 2014.
- [49] J. Huang, M. Kang, J. Yang, H. Jiang, and D. Liu, “Multiphase machine theory and its applications,” *International Conference on Electrical Machines and Systems (ICEMS)*, Wuhan, China, Oct. 2008.
- [50] F. Barrero and M. J. Duran, “Recent advances in the design, modeling and control of multiphase machines—part 1,” *IEEE Transactions on Industrial Electronics*, Vol. 63, No. 1, pp. 449–458, Jan. 2016.
- [51] M. J. Duran and F. Barrero, “Recent advances in the design, modeling and control of multiphase machines—part 2,” *IEEE Transactions on Industrial Electronics*, Vol. 63, No. 1, pp. 459–468, Jan. 2016.
- [52] A. Baltatanu and M. L. Florea, “Multiphase machines used in electric vehicles propulsion,” *International Conference on Electronics, Computers and Artificial Intelligence (ECAI)*, Pitesti, Romania, June 2013.
- [53] E. Levi, F. Barrero, and M. J. Duran, “Multiphase machines and drives-revisited,” *IEEE Transactions on Industrial Electronics*, Vol. 63, No. 1, pp. 429–432, January, 2016.
- [54] B. Aslan, E. Semail, J. Korecki, and J. Legranger, “Slot/pole combinations choice for concentrated multiphase machines dedicated to mild-hybrid applications,” *37th Annual Conference on IEEE Industrial Electronics (IECON 2011)*, Nov. 2011.
- [55] H. Kim, K. Shin, S. Englebretson, N. Frank, and W. Arshad, “Analytical model of multiphase permanent magnet synchronous machines for energy and transportation applications,” *2013 IEEE Electric Machines & Drives Conference (IEMDC)*, May. 2013.

- [56] J. Riveros, B. Bogado, J. Prieto, F. Barrero, S. Toral, and M. Jones, “Multiphase machines in propulsion drives of electric vehicles,” *2010 14th International Power Electronics and Motion Control Conference (EPE/PEMC)*, Sept. 2010.
- [57] R. Bojoi, A. Cavagnino, A. Tenconi, A. Tassarolo, and S. Vaschetto, “Multiphase electrical machines and drives in the transportation electrification,” *2015 IEEE 1st International Forum on Research and Technologies for Society and Industry Leveraging a better tomorrow (RTSI)*, Sept. 2015.
- [58] H. Kim, K. Shin, S. Englebretson, N. Frank, and W. Arshad, “Multiphase machines in propulsion drives of electric vehicles,” *14th International Power Electronics and Motion Control Conference (EPE/PEMC)*, Sept. 2010.
- [59] H. Kim, K. Shin, S. Englebretson, N. Frank, and W. Arshad, “Multiphase machines in propulsion drives of electric vehicles,” *14th International Power Electronics and Motion Control Conference (EPE/PEMC)*, Sept. 2010.
- [60] N. Schofield, “Brushless permanent magnet traction machines with extended speed capability ” Ph.D. dissertation, department of Electronic and Electrical Engineering, The University of Sheffield, 1995.
- [61] N. Schofield, *Lecture notes of ECE 787*, department of Electrical and Computer Engineering, McMaster University, 2014.
- [62] K. T. Kim, K. S. Kim, S. M. Hwang, T. J. Kim and Y. H. Jung, “Comparison of performances between IPM and SPM motors with rotor eccentricity”, *IEEE Transactions on Magnetics*, vol. 37, pp. 3448–3451, 2002.
- [63] J. Dong, Y. Huang, L. Jin and H. Lin. “Comparative study of surface-mounted and interior permanent-magnet motors for high-speed applications”, *IEEE Transactions on Applied Superconductivity*, vol. 26, Article: 5200304, 2016.
- [64] R. Schiferl and T. A. Lipo. “Power capability of salient pole permanent magnet synchronous motors in variable speed drive applications”, in *Proceeding of IEEE Industry Applications Society Annual Meeting*, pp. 23–31, 1988.

- [65] M. Ehsani, Y. Gao and S. Gay. “Characterization of electric motor drives for traction applications”, in *Proceeding of IEEE Conference IECON*, pp. 891–895, 2003.
- [66] M. Ehsani, Y. Gao and J. M. Miller. “Hybrid electric vehicles: architecture and motor drives”, in *Proceeding of the IEEE*, vol. 95, pp. 719–728, 2007.
- [67] X. Luo and T. A. Lipo. “A synchronous/permanent magnet hybrid AC machine”, *IEEE Transactions on Energy Conversion*, vol. 15, no. 2, pp. 203–210, June 2000.
- [68] Y. Amara, L. Vido, M. Gabsi, E. Hoang, A. H. Ben Ahmed and M. Lecrivain. “Hybrid excitation synchronous machines: energy-efficient solution for vehicles propulsion” *IEEE Transactions on Vehicular Technology*, vol. 58, pp. 2137–2149, 2009.
- [69] A.K. Sawhney, *A Course in Electrical Machine Design*, Dhanpat Rai and Sons, Delhi-Jullundur, USA, 1997.
- [70] G. Novak, J. Kokošar, A. Nagode and D. S. Petrovič, “Core-loss prediction for non-oriented electrical steels based on the Steinmetz equation using fixed coefficients with a wide frequency range of validity”, *IEEE Transactions on Magnetics*, vol. 51, no. 4, pp: , April 2015.
- [71] E. Dlala, M. Solveson, S. Stanton and A. Arkkio, “Improved model for the prediction of core loss in finite element analysis of electric machines,” in *proceeding of IEEE Electric Machines and Drives Conference IEMDC*, 2015.
- [72] K. Yamazaki and Y. Seto, “Iron loss analysis of interior permanent-magnet synchronous motors-variation of main loss factors due to drive condition”, *IEEE Transactions on Industry Applications*, vol. 42, no. 4, pp: 1045-1052, July/August 2006.
- [73] JAMG. Co, “JMAG Application Note- Analysis of the eddy current in the magnet of an IPM motor,” 2013. [Online]. Available: http://www.jmag-international.com/catalog/22_IPMMotor_MagnetLoss.html.

- [74] H. J. Warnecke and R. Bäbeler, "Design for Assembly - Part of the Design Process," *Annals of the CIRP*, pp. 1-4, 1988.
- [75] D. M. Anderson, *Design for Manufacturability & Concurrent Engineering*, Cambria, California: CIM Press, 2004.
- [76] Peter Groche, Wolfram Schmitt, Andrea Bohn, Sebastian Gramlich, Stefan Ulbrich, Ute Günther, "Integration of manufacturing-induced properties in product design," *CIRP Annals*, pp. 163-166, 2012.
- [77] Sinya Regal Beloit Electrical Machine Co. Limited, 2010. [Online]. Available: <http://www.sinyamotor.com/>, last accessed September, 2016.
- [78] J. Hallberg, "Conceptual evaluation and design of a direct-driven mixer." Master thesis, Department of Mechanical Engineering, Linköpings University, Linköping, Sweden, 2005.
- [79] T. Mitsuhiro, "Manufacturing device for spiral laminated core." Patent JP1148046, 1989.
- [80] S. Lee, "Laminated body of motor and manufacturing method thereof." United States Patent Application 20050073211, 2005.
- [81] H. Akita, Y. Nakahara, N. Miyake, and T. Oikawa, "New core structure and manufacturing method for high efficiency of permanent magnet motors," in *Proceeding of IEEE Industry Applications Society Conference*, vol. 1, pp. 367-372, 2003.
- [82] B. Mecrow, A. Jack, J. Haylock, U. Hofer, and P. Dickinson, "Simplifying the manufacturing process for electrical machines," in *Proceeding of International Conference on Power Electronics, Machines and Drives (PEMD)*, vol. 1, pp. 169-174, 2004.
- [83] A. Jack, C. Mecrow, P. Dickinson, D. Stephenson, J. Burdess, N. Fawcett, and J. Evans, "Permanent-magnet machines with powdered iron cores and prepressed windings," *IEEE Transactions on Industry Applications*, vol. 36, no. 4, pp. 1077-1084, 2000.

- [84] T. Yamada, T. Kawamura, N. Mizutani, T. Sato, K. Miyaoka, and M. Mochizuki, “Stator for dynamoelectric machine and method for making the same.” European patent application, EP 0871282, 1998.
- [85] F. Meier, “Permanent-magnet synchronous machines with non-overlapping concentrated windings for low-speed direct-drive applications,” Ph.D. dissertation, School of Electrical Engineering, Royal Institute of Technology, Stockholm, Sweden, 2008.
- [86] A Vertical Wind Generator from Washing Machine Motor, [online]. Available: <http://www.instructables.com/id/A-Vertical-Wind-Generator-from-Washing-Machine-Mot>.
- [87] A. M. EL-Refaie and T. M. Jahns, "Comparison of synchronous PM machine types for wide constant-power speed range operation," in *2005 IEEE Industry Applications Society Annual Meeting*, vol. 2, pp.1015-1022, 2005.
- [88] D. Evans, Z. Azar, L. J. Wu and Z. Q. Zhu, "Comparison of optimal design and performance of PM machines having non-overlapping windings and different rotor topologies," in *2010 IET Power Electronics, Machines and Drives Conf. (PEMD 2010)*, 2010, pp. 1-7.
- [89] Y. Sato, S. Ishikawa, T. Okubo, M. Abe, and K. Tamai, "Development of high response motor and inverter system for Nissan LEAF electric vehicle," *SAE International*, doi: 10.4271/2011-01-0350, 2011.
- [90] T. Nakada, S. Ishikawa, and S. Oki, “Development of an electric motor for a newly developed electric vehicle,” *SAE International*, Vol. 01, No. 1879, 2014.
- [91] T. Burress, “Benchmarking of Competitive Technologies,” Oak Ridge National Laboratory, 2012, [Online]. Available: http://www1.eere.energy.gov/vehiclesandfuels/pdfs/merit_review_2012/adv_power_electronics/ape006_burress_2012_p.pdf, last accessed 16-Dec.-2015.
- [92] U.S. Department of Energy, “2011 Nissan Leaf – VIN 0356 Advanced Vehicle Testing – Baseline Testing Results,” [Online]. Available:

- http://energy.gov/sites/prod/files/2014/02/f8/2011_nissan_leaf_fs.pdf, last accessed on 16-Dec.-2015.
- [93] B. Ozpineci, “Oak Ridge National Laboratory annual progress report for the power electronics and electric machinery program,” Oak Ridge National Lab., Oak Ridge, TN, ORNL/SPR-2014/532, Nov. 2014.
- [94] T. Burress, “Benchmarking state-of-the-art technologies”, presented at the 2013 U.S. Department of Energy Hydrogen and Fuel Cells Program and Vehicle Technologies Program Annual Merit Review and Peer Evaluation Meeting.
- [95] Y. Sato, S. Ishikawa, T. Okubo, M. Abe, and K. Tamai, “Development of high response motor and inverter system for the Nissan LEAF electric vehicle,” presented at the SAE World Congress Exhibition, Paper 2011-01-0350, 2011.
- [96] T. Burress, "Benchmarking competitive technologies", presented at the 2012 U.S. Department of Energy Hydrogen and Fuel Cells Program and Vehicle Technologies Program Annual Merit Review and Peer Evaluation Meeting.
- [97] Arnold Magnetic Technologies, [Online] Available: <http://www.arnoldmagnetics.com/en-us/Products/Neodymium-Magnets>, Last accessed September. 2016.
- [98] P.A.R. (Insulations & Wires) Ltd, [Online] Available: <http://www.par.gb.com/files/0101%20Dimensions%20of%20Round%20Copper%20&%20Aluminium%20Wires.pdf>, Last accessed September. 2016.
- [99] W. Jiang, B. Bilgin, Y. Yang, A. Sathyan, H. Dadkhah, and A. Emadi, "Rotor skew pattern design and optimization for cogging torque reduction," *IET Electrical Systems in Transportation*, vol. 6, no. 2, 2016.
- [100] W. Jiang, B. Bilgin, Y. Yang, A. Sathyan, H. Dadkhah, and A. Emadi, "Rotor skew pattern design and optimization for cogging torque reduction," *IET Electrical Systems in Transportation*, vol. 6, no. 2, 2016.
- [101] S. Han, T.M. Jahns, and W.L. Soong “Torque ripple reduction in interior permanent magnet synchronous machines using stators with odd number of slots

- per pole pair,” *IEEE Transactions on Energy Conversion*, Vol. 25, No. 1, pp. 34–43, March 2010.
- [102] JMAG Co., “34-Demagnetization Analysis of an SPM Motor JMAG Application Catalogue. [Online]. Available: <http://www.jmag-international.com>.
- [103] M. Fasil, N. Mijatovic, B. B. Jensen and J. Holboll, “Performance variation of ferrite magnet PMSM motor with temperature,” *IEEE Transactions on Magnetics*, vol. 51, no. 12, article: 8115106, 2015.
- [104] A. Wang, H. Li, and C. Liu, “On the material and temperature impacts of interior permanent magnet machine for electric vehicle applications,” *IEEE Transactions on Magnetics*, vol. 44, no. 11, pp. 4329–4332, 2008.
- [105] N. Zhao, N. Schofield and W. Niu, “Energy storage system for a port crane hybrid power-train,” *IEEE Transactions on Transportation Electrification*, vol. PP, no. 99, 2016.
- [106] J. H. Lee, C. Y. Won, B. K. Lee, H. B. Kim, “IPMSM torque control method considering DC-link voltage variation and friction torque for EV/HEV applications,” in *Proceeding IEEE Conference VPPC.*, pp. 1063–1069, 2012.
- [107] J. H. Lee, J. H. Lee, J. H. Park, C. Y. Won, “Field-weakening strategy in condition of DC-link voltage variation using on electric vehicle of IPMSM,” in *Proc. IEEE Conf. ICEMS.*, pp. 1–6, 2011.
- [108] A. M. Jarushi and N. Schofield, “Battery and super capacitor combination for a series hybrid electric vehicle,” in *Proceeding of. IET Conference. PEMD.*, pp. 1-6, 2010.
- [109] T. Schoenen, M. S. Kunter, M. D. Hennen, R. W. De Doncker, “Advantages of a variable DC-link voltage by using a DC-DC converter in hybrid-electric vehicles,” in *Proceeding of IEEE Conference. VPPC*, pp. 1–5, 2010.
- [110] A. Najmabadi, K. Humphries, B. Boulet, “Implementation of a bidirectional DC-DC in electric powertrains for drive cycles used by medium duty delivery trucks,” in *Proceeding of IEEE Conference. ECCE*, pp. 1338–1345, 2015.

- [111] A. Najmabadi, K. Humphries, B. Boulet, “Application of a bidirectional DC-DC in an electric powertrain for medium duty delivery trucks,” in *Proceeding of IEEE Conference IEMDC*, pp. 866–871, 2015.
- [112] S. Tenner, S. Gimther, W. Hofmann, “Loss minimization of electric drive systems using a DC/DC converter and an optimized battery voltage in automotive applications,” in *Proceeding of IEEE Conference VPPC*, pp. 1–7, 2011.
- [113] J. O. Estima, A. J. M. Cardoso, “Efficiency analysis of drive train topologies applied to electric/hybrid vehicles,” *IEEE Transactions on Vehicular Technology*, vol. 61, no. 3, pp. 1021–1031, 2012.
- [114] Toyota Hybrid System THS II, [Online]. Available: <http://www.evworld.com/library/toyotahs2.pdf>, last accessed September, 2016.
- [115] M. Kamiya, “Development of traction drive motors for the Toyota hybrid system,” *IEEE Transactions on Industry Applications*, vol. 126, no. 4, pp. 473–479, 2006.
- [116] Nan Zhao, Nigel Schofield, Rong Yang and Ran Gu, “An Investigation of DC-Link Voltage and Temperature Variations on EV Traction System Design”, in *IEEE Energy Conversion Congress and Exposition (ECCE)*, September, 2016.
- [117] 2011 Nissan LEAF - Traction Motor System (TMS), [Online]. Available: <https://carmanuals2.com/nissan/leaf-2011-traction-motor-system-tms-47803>, last accessed September, 2016.
- [118] W. Chlebosz and G. Ombach, "Demagnetization properties of IPM and SPM motors used in the high demanding automotive application", *The international journal for computation and mathematics in electrical and electronic engineering*, Vol. 32 Iss 1 pp. 72 – 85, 2012.
- [119] A. Binder and T. Schneider, “High-speed inverter-fed AC drives in electrical machines and power electronics”, in *International Aegean Conference on Electrical Machines and Power Electronics (ACEMP)*, pp. 9-16, Bodrum, Turkey, September 2007.

- [120] Y. M. Rabinovich, V. V. Sergeev, A. D. Maystrenko, V. Kulakovsky, S. Szymura, H. Bala, “Physical and mechanical properties of sintered Nd-Fe-B type permanent magnets”. *Intermetallics*, Vol. 4, NO. 8, pp: 641–645, 1996.
- [121] J. Jung, B. Lee, D. Kim, J. Hong, J. Kim, S. Jeon, and D. Son, “Mechanical Stress Reduction of Rotor Core of Interior Permanent Magnet Synchronous Motor”, *IEEE Transactions on Magnetics*, Vol. 48, NO. 2, 911-914, February 2012.
- [122] J. Dong, Y. Huang, L. Jin, B. Guo, T. Zhou, H. Lin, and J. Dong, “Development of an air-cooled 150 kW high speed permanent magnet motor with Gramme ring windings for turbo blowers”, in *17th International Conference on Electrical Machines and Systems (ICEMS)*, Hangzhou, China, Oct. 22-25, 2014.
- [123] C. C. Hwang, S. S. Hung, C. T. Liu, and S. P. Cheng, “Optimal design of a high speed SPM motor for machine tool applications,” *IEEE Transactions on Magnetics*, vol. 50, no. 1, Jan. 2014.
- [124] J. An, A. Binder, and C. R. Sabirin, “Loss measurement of a 30 kW high speed permanent magnet synchronous machine with active magnetic bearings,” in *International Conference on Electrical Machines and Systems (ICEMS)*, October, 2013, pp. 905–910.
- [125] D. Hanselman, *Brushless Permanent Magnet Motor Design*, second edition, Lebanon: Magna Physics Publishing, 2006.
- [126] J. Jung, B. Lee, D. Kim, J. Hong, J. Kim, S. Jeon, and D. Song, “Mechanical stress reduction of rotor core of interior permanent magnet synchronous motor”, *IEEE Transactions on Magnetics*, vol.48, no.2, pp. 911-914, Feb. 2012.
- [127] E. C. Lovelace, T. M. Jahns, T. A. Keim, and J. H. Lang, “Mechanical design considerations for conventionally laminated, high-speed, interior PM synchronous machine rotors”, *IEEE Transactions on Industry Applications*, vol. 40, no. 3, pp. 806-812, May-June 2004.

- [128] L. Chen and C. Zhu, "Rotor strength analysis for high speed permanent magnet machines", in *17th International Conference on Electrical Machines and Systems (ICEMS)*, Oct. 22-25, 2014, Hangzhou, China
- [129] Z. Han, H. Yang, and Y. Chen, "Investigation of the rotor mechanical stresses of various interior permanent magnet motors," presented at *the Int. Conf. Elect. Mach. Syst. (ICEMS)*, Tokyo, Japan, Nov. 2009.
- [130] A. Binder T. Schneider, and M. Klohr, "Fixation of buried and surface-mounted magnets in high-speed permanent-magnet synchronous machines", *IEEE Transactions on Industry Applications*, vol. 42, no. 4, pp. 1031-1037, July-August 2006.
- [131] V. Vullo and F. Vivio, "Chapter 2, Constant thickness rotating disk", in *Rotors: Stress Analysis and Design*, Springer-Verlag Italia, 2013.
- [132] H. Onodera, Y. Yamaguchi, H. Yamamoto, M. Sagawa, Y. Matsuura, and H. Yamamoto. "Magnetic properties of a new permanent magnet based on a Nd-Fe-B compound (Neomax)," *Journal of Magnetism and Magnetic Materials*, volume 46, pp. 151-156, (1984).
- [133] K. Hirota, H. Nakamura, T. Minowa, and M. Honshima. "Coercivity enhancement by the grain boundary diffusion process to Nd-Fe-B sintered magnets," *INTERMAG 2006*, volume 42, no. 10, pp. 2909-2911, (2006).
- [134] H. Nakamura, K. Hirota, M. Shima, T. Minowa, and M. Honshima. "Magnetic properties of extremely small Nd-Fe-B sintered magnets," *IEEE Transactions on Magnetics*, volume 41, no. 10, pp. 3844-3846, (2005).
- [135] S. Sugimoto. "Current status and recent topics of rare-earth permanent magnets," *Journal of Physics D: Applied Physics*, volume 44, no. 064001, pp. 1-11, (2011).
- [136] Hitachi Metals. "Materials Magic Hitachi Metals," Hitachi Metals News Release June 26, (2008). [Online]. Available: <http://www.hitachi-etals.co.jp.htm>, last accessed December, 2015.

- [137] S. Constantinides and D. Gulick. "NdFeB for high temperature motor applications," in *SMMA (The motor and motion association) Fall Technical Conference*, November 3-5, (2004).
- [138] Jagadeesh K. Tangudu and T. M. Jahns, "Comparison of interior PM machines with concentrated and distributed stator windings for traction applications," in *IEEE Vehicle Power and Propulsion Conference*, Chicago, 2011.
- [139] D. Wu, Z. Q. Zhu, and X. Ge, "Effectiveness of terminal voltage distortion minimization methods in fractional slot surface-mounted permanent magnet machines considering local magnetic saturation", *IEEE Transactions on Energy Conversion*, Vol. 31, NO. 3, pp: 1090-1099, September 2016.
- [140] D. Wu, Z. Q. Zhu, and W. Chu, "Reduction of on-load terminal voltage distortion in fractional slot interior permanent magnet machines", *IEEE Transactions on Energy Conversion*, Vol. 31, NO. 3, pp: 1161-1169, September 2016.
- [141] Z. Q. Zhu, D. Wu, and X. Ge, "Investigation of voltage distortion in fractional slot interior permanent magnet machines having different slot and pole number combinations", *IEEE Transactions on Energy Conversion*, Vol. 31, NO. 3, pp: 1192-1201, September 2016.
- [142] S. Jurkovic, K. Rahman, B. Bae, N. Patel, and P. Savagian, "Next generation chevy volt electric machines; design, optimization and control for performance and rare-earth mitigation", in *2015 IEEE Energy Conversion Congress and Exposition (ECCE)*, September, 2015
- [143] S. Sano, T. Yashiro, K. Takizawa, and T. Mizutani, "Development of new motor for compact-class hybrid vehicles," in *EVS29 Symposium*, Montreal, Canada, June, 2016.